

# **Identification of Tire Dynamics Based on Intelligent Tire**

**Hojong Lee**

**Dissertation submitted to the faculty of the Virginia Polytechnic Institute and State  
University in partial fulfillment of the requirements for the degree of**

**Doctor of Philosophy  
In  
Mechanical Engineering**

**Saied Taheri Chair  
Corina Sandu  
Pablo Tarazaga  
Ronald Kennedy  
Kejing Li**

**September 14, 2017  
Blacksburg, Virginia**

**Keywords: intelligent tire, tire model, sensor, strain, system identification**

**© Copyright 2017  
Hojong Lee**

# Identification of Tire Dynamics Based on Intelligent Tire

*Hojong Lee*

## ABSTRACT

Sensor-embedded tires, known as intelligent tires, have been widely studied because they are believed to provide reliable and crucial information on tire-road contact characteristics e.g., slip, forces and deformation of tires. Vehicle control systems such as ABS and VSP (Vehicle Stability Program) can be enhanced by leveraging this information since control algorithms can be updated based on directly measured parameters from intelligent tire rather than estimated parameters based on complex vehicle dynamics and on-board sensor measurements. Moreover, it is also expected that intelligent tires can be utilized for the purpose of the analysis of tire characteristics, taking into consideration that the measurements from the sensors inside the tire would contain considerable information on tire behavior in the real driving scenarios. In this study, estimation methods for the tire-road contact features by utilizing intelligent tires are investigated. Also, it was discussed how to identify key tire parameters based on the fusion technology of intelligent tire and tire modeling. To achieve goals, extensive literature reviews on the estimation methods using the intelligent tire system was conducted at first. Strain-based intelligent tires were introduced and tested in the laboratory for this research.

Based on the literature review and test results, estimation methods for diverse tire-road contact characteristics such as slippages and contact forces have been proposed. These estimation methods can be grouped into two categories: statistical regressions and model based methods. For statistical regressions, synthetic regressors were proposed for the estimation of contact parameters such as contact lengths, rough contact shapes, test loads and slip angles. In the model-based method, the brush type tire model was incorporated into the estimation process to predict lateral forces. Estimated parameters using suggested methods agreed well with measured values in the laboratory environment.

By utilizing sensor measurements from intelligent tires, the tire physical characteristics related to in-plane dynamics of the tire, such as stiffness of the belt and sidewall, contact pressure distribution and internal damping, were identified based on the combination of strain measurements and a flexible ring tire model. The radial deformation of the tread band was directly obtained from strain measurements based on the strain-deformation relationship. Tire parameters were identified by fitting the radial deformations from the flexible ring model to those derived from strain measurements. This approach removed the complex and repeated procedure to satisfy the contact

constraints between the tread and the road surface in the traditional ring model. For tires with different specifications, identification using the suggested method was conducted and their results are compared with results from conventional methods and tests, which shows good agreements. This approach is available for the tire standing still or rolling at low speeds. For tires rolling at high speeds, advanced tire model was implemented and associated with strain measurements to estimate dynamic stiffness, internal damping effects as well as dynamic pressure distributions. Strains were measured for a specific tire under various test conditions to be used in suggested identification methods. After estimating key tire parameters step by step, dynamic pressure distributions was finally estimated and used to update the estimation algorithm for lateral forces. This updated estimation method predicted lateral forces more accurately than the conventional method.

Overall, this research will serve as a stepping stone for developing a new generation of intelligent tire capable of monitoring physical tire characteristics as well as providing parameters for enhanced vehicle controls.

# Identification of Tire Dynamics Based on Intelligent Tire

*Hojong Lee*

## GENERAL AUDIENCE ABSTRACT

Tires are very crucial components in a vehicle because they are only objects in contact with the road surface on which the vehicle drive. They support the weight of the vehicle and generate forces which make the vehicle drive, stop and turn. Thus, the improvement of vehicle performances such as handling, ride quality and braking can be achieved by understanding and by optimizing tire properties as well as improving the design of the vehicle itself.

These days, diverse vehicle control systems such as anti-lock braking and cornering stability control systems have been widely adopted to improve the stability of the vehicle when it is braked or turned. These stability controls usually require information about slippages and forces occurring between the tire and the road surface. These quantities can be indirectly estimated by monitoring vehicle motions, which are measured by sensors installed on the vehicle frame. Although these traditional methods have worked successively, the control algorithms can be improved further by directly sensing the tire behaviors using sensors embedded in the tire. These sensor-embedded tires are often called as 'intelligent tire' because tires themselves serve as the monitoring device on driving conditions as well as conduct traditional functions. Also, the measured quantities inside the tire can be effectively used to understand tire characteristics because they have valuable information on tires, especially, mechanism how the tire deforms and generate contact forces when it rolls over the road surface.

In this research, strains are measured at the inner surface of the tire during it rolling and cornering on the flat road surface under different loads on the indoor test rig. A strain represents the relative displacement between particles. Based on experimental results, estimation algorithms for test loads, contact lengths, cornering angles and

cornering forces are developed. These estimation methods can be incorporated in the vehicle control algorithm in the real driving scenario for improved vehicle controls.

A tire is a complex system comprising various composite materials, so their behaviors or characteristics show severe non-linearity which is difficult to understand. They have been simplified and modeled in various ways based on diverse physical principles to understand how they are deflected and generate forces and moments during rolling on the road surface under a vertical load. These models are called 'physical tire model'. To extract and analyze tire physical characteristics, measured strains at the inner surface are combined with these tire models. In this research, tires are modeled as a flexible ring which is supported by viscoelastic materials and this tire model is called a 'flexible ring model' which has been utilized to analyze vibration properties and contact phenomena of tires. Strain measurements were fed into the model and crucial tire characteristics are extracted such as tire stiffness, pressure distributions and internal damping. These properties can be used to analyze tire performance like wear, rolling resistance, ride qualities and the capacity of cornering forces. Since intelligent tire systems are applied for the real driving situation, tire characteristics extracted in this way would have closer links to vehicle performances rather than those measured in the laboratory.

Overall, this research will serve as a stepping stone for developing a new generation of intelligent tire capable of monitoring physical tire characteristics as well as providing parameters for enhanced vehicle controls.

## ACKNOWLEDGEMENT

During the entire four years spent at the Center for Tire Research, a very special gratitude goes out to my advisor, Dr. Taheri. He has served as a great teacher guiding me in the right track to the research goal, as well as a life mentor during my stay in America. I am grateful to members of my Ph.D. committee – Dr. Sandu, Dr. Tarazaga, Dr. Kennedy, Dr. Li – for their guidance and supports throughout the entire research effort.

I would like to extend my gratitude to all of my colleagues at the Center for Tire Research. Their advice to my research and friendship are greatly appreciated. Also, I would like to thank Korean friends of mine for their cheers and considerations. My life in America should have been monotonous and lonely without them.

I also would like to thank Hankook Tire Co. Ltd. for giving me the chance and the financial and experiment supports for this study. Special thanks go to Mintae Kim for conducting experiments and providing test data. All experimental data described in this research were provide by Hankook Tire Co. Ltd., Korea.

I am deeply grateful to my mother, sister and brother for their sacrifices dealing with family affairs during my absence in Korea. I was heavily indebted to them and promise to be better son and brother in the rest of my life

Finally, I would like to thank my wife Sunkyong Jung for her love, patience and sacrifice. It should have been difficult for her to live in foreign country taking care of two children without much help from his husband, who usually spent his time at a school. Without her support, this dissertation would have not been possible.

선경아, 4 년 동안 정말 고맙고, 고생 많았어.

## TABLE OF CONTENTS

<b>ABSTRACT</b> .....	<b>i</b>
<b>GENERAL AUDIENCE ABSTRACT</b> .....	<b>iii</b>
<b>ACKNOWLEDGEMENT</b> .....	<b>vi</b>
<b>TABLE OF CONTENTS</b> .....	<b>vii</b>
<b>LIST OF SYMBOLS</b> .....	<b>ix</b>
<b>LIST OF FIGURES</b> .....	<b>xii</b>
<b>LIST OF TABLES</b> .....	<b>xix</b>
<b>1 INTRODUCTION</b> .....	<b>1</b>
1.1 Background and Motivation .....	1
1.2 Problem Statement and Scope of Work .....	3
1.3 Main Contributions .....	6
1.4 Dissertation Outline .....	7
<b>2 LITERATURE REVIEW</b> .....	<b>8</b>
2.1 Type of Sensors and measured variables .....	8
2.1.1 <i>Sensors for identifying contact deformation</i> .....	10
2.1.2 <i>Sensors for identifying global deformation of tire</i> .....	13
2.2 Estimation Methods for Tire Characteristics .....	14
2.2.1 <i>Estimation based on acceleration measurement</i> .....	15
2.2.1.1 Estimation of contact features and its application .....	16
2.2.1.2 Signal processing for road differentiation.....	20
2.2.1.3 Lateral deflection by double integral of acceleration .....	23
2.2.1.4 Statistical approach .....	28
2.2.2 <i>Estimation based on strain measurement</i> .....	30
2.2.2.1 Estimation of contact features and its application .....	31
2.2.2.2 Signal amplitude as prediction parameter .....	35
2.2.2.3 Integral/Derivative of signal as prediction parameter .....	37
2.2.2.4 Other methods .....	41
2.2.3 <i>Estimation based on global deflection measurement</i> .....	44
2.3 Chapter Summary and Discussion .....	48
<b>3 STRAIN BASED INTELLIGENT TIRE AND EXPERIMENTATION</b> .....	<b>53</b>
3.1 Types and the Principle of Strain Gage Measurement .....	53
3.2 Sensor Arrangement inside Test Tire.....	55
3.3 Test Information .....	57
3.4 Data Processing.....	60
<b>4 ESTIMATION OF TIRE-ROAD CONTACT FEATURES USING STRAIN-BASED INTELLIGENT TIRE</b> .....	<b>63</b>
4.1 Estimation of tire-road contact features using statistical regressions .....	63
4.1.1 <i>Contact Length Estimation</i> .....	63
4.1.2 <i>Test Load Estimation</i> .....	66

4.1.3	<i>Slip Angle Estimation</i> .....	67
4.1.4	<i>Lateral Force Estimation</i> .....	71
4.1.5	<i>Slip Ratio Estimation</i> .....	79
4.2	Model Based Estimations of Lateral Force .....	82
4.3	Chapter Conclusion .....	88
<b>5</b>	<b>INVESTIGATION ON CIRCUMFERENTIAL CONTACT MECHANISM USING STRAIN MEASUREMENTS</b> .....	<b>90</b>
5.1	ESTIMATION OF RADIAL DEFORMATION OF THE TREAD BAND USING STRAIN MEASUREMENTS .....	93
5.1.1	<i>The relationship between deformations of tread band and strains at inner liner...</i> .....	93
5.1.2	<i>Estimation of radial deformation from strain measurement</i> .....	99
5.2	APPLICATION OF STRAIN MEASUREMENT FOR CIRCUMFERENTIAL CONTACT PROBLEMS .....	104
5.2.1	<i>Flexible Ring Model</i> .....	104
5.2.2	<i>Solving the contact problem using strain measurement</i> .....	108
5.3	Estimation Results for Tire Parameters and Characteristics .....	111
5.4	Discussions .....	117
5.5	Chapter Conclusion .....	120
<b>6</b>	<b>ESTIMATION OF TIRE DYNAMIC CHARACTERISTICS</b> .....	<b>122</b>
6.1	Flexible Ring Model for Rolling Tire .....	123
6.2	Boundary Condition for Tread-Road Contact .....	127
6.3	Implementation of Models .....	131
6.3.1	<i>Model response to general concentrated line forces</i> .....	131
6.3.2	<i>Tread compatibility model: radial deformation only</i> .....	133
6.3.3	<i>Tread compatibility model: normal and shear deformation</i> .....	138
6.4	Comparison of Simulation Results for Different Boundary Conditions .....	143
6.5	Estimation of Dynamic Pressure Distribution and Tire Parameters .....	147
6.5.1	<i>Estimation of Model Parameters</i> .....	149
6.5.1.1	Geometrical Parameters .....	149
6.5.1.2	Ring bending stiffness and tread stiffness .....	150
6.5.2	<i>Parameter Estimation using Strain Measurements</i> .....	152
6.5.2.1	Sidewall Stiffness.....	152
6.5.2.2	Damping coefficient .....	162
6.6	Application for Lateral Force Estimation .....	169
6.7	Chapter Conclusion .....	174
<b>7</b>	<b>CONCLUSIONS AND FUTURE WORK</b> .....	<b>175</b>
7.1	Research Summary .....	175
7.2	Research Contributions.....	178
7.3	Future works .....	179
	<b>REFERENCE</b> .....	<b>184</b>

## LIST OF SYMBOLS

$s$	1/mms	slope of peak strain rate over tread width
$CP1$		first compressive peak of strain during complete rotation of wheel
$CL$		indicator of contact length identified by peak to peak distance of strain rate
$\Omega$	rad/s	angular velocity of wheel
$R_{eff}$	m	effective rolling radius of wheel
$\alpha$	rad(or °)	slip angle
$F_z, F_y$	N	vertical or lateral force applied to contact patch
$F_{yp}$	N	peak lateral force
$c_{py}$	N/m	bristle stiffness in the lateral direction
$c_\alpha$	N/rad	cornering stiffness
$q_z$	N/m	one dimensional contact pressure (same as $\sigma$ )
$A$	m <sup>2</sup>	area of the cross section of the ring $A=bt_0$
$b$	m	width of the ring
$d_0$	m	overall tire vertical deflection
$EI$	Nm <sup>2</sup>	circumferential bending stiffness of the treadband
$f_x, f_z$	N	external forces acting at the wheel center in the x, z direction respectively
$f_x^*, f_z^*$	N	external forces acting at the wheel center in the rotating coordinate system
$t_0$	m	thickness of the ring
$I_r$	kgm <sup>2</sup>	moment of inertial of the wheel
$k_u, k_v$	N/m <sup>2</sup>	stiffness of the sidewall elastic foundation in the radial and tangential direction respectively, measured per unit length of the ring
$\lambda$		modal damping coefficient

$c$	Ns/m <sup>2</sup>	damping coefficient of the sidewall viscoelastic foundation, measured per unit length of the ring
$k_t$	N/m <sup>2</sup>	stiffness of the tire tread elements in the radial direction
$k_{ET}, k_{GT}$	N/m <sup>2</sup>	compression and longitudinal shear stiffness of tread elements
$m$	kg	mass of the wheel body
$m_t$	kg	Tire mass
$n$		mode number
$N$		number of modes used
$p_0$	N/m <sup>2</sup>	Tire inflation pressure
$q_u, q_v$	N/m	external distributed forces acting on the ring in the radial and tangential directions, respectively
$q_\beta$	Nm/m	moment intensity acting along the tread band axis
$\sigma, \tau$	N/m	contact pressure and tangential stress distribution acting along the contact patch
$R$	m	mean radius of the ring (treadband)
$r$	m	radius of a ring element $r=R + y$
$\bar{R}$	m	free radius of the tire $\bar{R} = R + \tau$
$R_e$	m	effective rolling radius
$R_l$	m	dynamic loaded radius
$T$	Nm	torque acting on the wheel
$w, v$	m	total displacements of the ring element in the radial and tangential directions, respectively
$w_r, v_r$	m	total displacements of the ring element relative to the wheel center in the radial and tangential directions, respectively
$\beta$	rad	rotating angle of the treadband's cross section
$\eta$	rad	inclination angle of the normal to treadband from the vertical
$x, z$	m	displacement of the wheel center in the longitudinal and vertical directions, respectively

$x^*, z^*$	m	displacement of the wheel center described in the rotating coordinate system
$y$	m	the distance of an element of the ring from the middle surface
$\vec{r}$	m	vector of a point on the middle surface of the ring with respect to the origin of the x-z coordinate system
$P, Q$		points located on the treadband axis and on the tread rubber surface of the deflected rotating tire, respectively
$P_0, Q_0$		points located on the treadband axis and on the tread rubber surface of the undeflected rotating tire, respectively
$\vartheta$	rad	central angle of a point on the ring with respect to the rotating coordinate system
$\vartheta_r$	rad	angular displacement of the wheel due to the variation of the rotating speed
$\varphi$	rad	angular coordinate of a point on the ring with respect to the non-rotating coordinate system
$\varphi_f, \varphi_r$	rad	fore and aft contact angles, respectively
$\rho$	kg/m <sup>3</sup>	density of the ring material
$\sigma_{\vartheta}^0$	N/m <sup>2</sup>	Pre-stress in the ring
$\tau$ (or $h_0$ )	m	thickness of the tire tread
$k$ (or $h$ )	m	deformed thickness of tire tread
$\omega_n$	rad/s	tire natural frequency
$V_s$	m/s	local sliding velocity of the tread rubber
$\mu$		coefficient of friction

## LIST OF FIGURES

Fig. 1-1 Expected application of intelligent tire system and its work flow. ....	4
Fig. 2-1 Schematic view of the tire lateral deflection when lateral force is applied: Left is front view of the tire, right is contact view from above .....	9
Fig. 2-2 (a) Sensor location. (b) Designed tire sensor. 1: elastic component, 2: sensor base, 3: slider mechanism, 4: elastic cantilever beam, 5: root of the cantilever beam [23].....	14
Fig. 2-3 FL parameter vs slip angle: (a) inner sensor and (b) central sensor as a function of tire load and camber. Adapted from F. Braghin et al., Measurement of contact forces and patch features by means of accelerometers fixed inside the tire to improve future car active control[4], © 2006 Taylor & Francis Publishing .....	16
Fig. 2-4 Effect of a longitudinal force variation. Adapted from S.M. Savaresi et al., New Regressors for the direct identification of tire deformation in road vehicles via ‘In-Tire’ accelerometers [29], © 2008 IEEE Publishing .....	17
Fig. 2-5 Determination of the contact length: (a) Full aquaplaning: vehicle velocity=90 km/h; (b) Partial aquaplaning: vehicle velocity=72 km/h; (c) Dry asphalt: vehicle velocity=74 km/h, tyre pressure=2.2 bars. Adapted from M. Matilainen et al., Tyre contact length on dry and wet road surfaces measured by three-axial accelerometer [27], © 2014 Elsevier Publishing. ....	19
Fig. 2-6 Acceleration waveform on different road surfaces: (a) Dry asphalt; (b) Ice; (c) Wet asphalt; (d); Snow [37] .....	21
Fig. 2-7 Power spectrum of the band-pass (2000–5000 Hz) filtered x-axis acceleration signal before contact (2.2 bars, 20 km/h) [36] .....	23
Fig. 2-8 Lateral (a) acceleration and (b) deflection simulations at different slip angles [32].....	24
Fig. 2-9 Features 1-5. [30].....	29
Fig. 2-10 Characteristics of tire strain time history. Adapted from H. Morinaga et al., The Possibility of Intelligent Tire (Technology of Contact Area Information Sensing) [37], © 2006 JSAE Publishing. ....	32
Fig. 2-11 Drawings of tire deformation. Adapted from H. Morinaga et al., The Possibility of Intelligent Tire (Technology of Contact Area Information Sensing) [37], © 2006 JSAE Publishing .....	33
Fig. 2-12 Contact length ratio at sensor position versus tire slip angle [39] .....	34

Fig. 2-13 Strain distribution when braking torque is applied at 0, 144 and 342 Nm. Wheel load $F_w$ is set to 500 N [42].....	36
Fig. 2-14 Axial strain waveform under tire braking, free rolling and traction from FEA [41].....	36
Fig. 2-15 Relationship between deformation of tread ring and deformation speed wave form at the time of entering in the leading edge [43] .....	38
Fig. 2-16 Cross-sectional deformation and strain distribution of a tire derived from a vertical load: (a) applied load, (b) strain distribution [44] .....	39
Fig. 2-17 Cross-sectional deformation and strain distribution of tire derived from the kinetic frictional force: (a) the applied load, (b) the strain distribution [44].....	39
Fig. 2-18 Strain components and total strain of the circumferential strain of the interior surface of a tire: (a) the strain components (b) the total strain [44].....	40
Fig. 2-19 Standardized shape of tire strain and strain differential and decisive parameters (dots) representing the overall strain shape. Adapted from S. J. Kim et al., Development of a tire model based on an analysis of tire strain obtained by an intelligent tire system[46], © 2015 KSAE Publishing. ....	42
Fig. 2-20 Strain sensor arrangement[14].....	43
Fig. 2-21 Lateral displacement of LED at different slip angles. Adapted from A. J. Tuononen, Optical position detection to measure tyre carcass deflections [17], © 2008 Taylor & Francis Publishing. ....	45
Fig. 2-22 Vertical displacement of LED. Adapted from A. J. Tuononen, Optical position detection to measure tyre carcass deflections [17], © 2008 Taylor & Francis Publishing.....	45
Fig. 2-23 The mean intensity and standard deviation before and after driving into the water at 110 km/h. Adapted from A. Tuononen et al., Optical position detection sensor to measure tyre carcass deflections in aquaplaning [16], © 2008 Inderscience Enterprise Publishing.....	47
Fig. 2-24 Possible applications with intelligent tire.....	51
Fig. 3-1 Structure of a foil strain gage .....	54
Fig. 3-2 Quarter-bridge system.....	54
Fig. 3-3 Intelligent tire system with five strain gage: sensor arrangement in the cross section of tire (left) and sensor attachment on the inner liner. ....	56
Fig. 3-4 Hardware setup for intelligent tire system.....	56
Fig. 3-5 Flat-Trac test rig.....	57

Fig. 3-6 Examples of Flat-Trac test conditions and force measurements. Upper left is slip angle time history and upper right is corresponding lateral forces. Lower left is slip ratio time history and lower right is corresponding longitudinal forces. ....	58
Fig. 3-7 Time history of circumferential strain under different test loads.....	61
Fig. 3-8 Strain and strain rate over the rotation angle under different test loads.....	62
Fig. 4-1 Strain measurements at $-4^\circ$ slip angle and schematic view of contact patch .....	64
Fig. 4-2 Estimated contact shapes for different slip angles at 100% $F_z$ .....	65
Fig. 4-3 Contact lengths variation at different slip angles (left) and % standard deviations of contact lengths over various slip angles.....	67
Fig. 4-4 Regression results between contact lengths and test loads: curve-fitting plot (left) and residual-fit plot (right) .....	67
Fig. 4-5 Regression results between in/out ratio of peak strain rate and slip angle: curve-fitting plot (left) and residual-fit plot (right) .....	68
Fig. 4-6 Strains at three channels (right) and their derivatives with the synthetic parameter (s) for slip angle estimation .....	69
Fig. 4-7 Regression results between slope of peak strain rate and slip angle: curve-fitting plot (left) and residual-fit plot (right) .....	70
Fig. 4-8 Slip angle estimation results for whole slip angles under different test loads .....	71
Fig. 4-9 Slip angle time history for test set 1 and 2 .....	72
Fig. 4-10 Combined effects of slip angle and test load on circumferential strain measured at ch3; slip angle: $0^\circ \rightarrow 2^\circ$ , $F_z$ :100% $\rightarrow$ 137.5%.....	72
Fig. 4-11 Six regressors for multi-variable regression study .....	74
Fig. 4-12 Regression model for test set 1 and fitting results.....	75
Fig. 4-13 Goodness of fit for test set 1 .....	75
Fig. 4-14 Regression results for lateral force estimation under different camber angles .....	77
Fig. 4-15 Conceptual shapes for contact patch subjected to slip and camber angles .....	78
Fig. 4-16 Combined effects of slip angle and camber angle on contact lengths.....	79
Fig. 4-17 Strain measurements under various rolling condition: braking (a), driving (b), free rolling (c).....	80
Fig. 4-18 Slip angle estimation by use of strain measurement .....	82
Fig. 4-19 Scheme for lateral force estimation based on Brush tire model.....	83
Fig. 4-20 Magic Formula fitting on measured lateral force with characteristic parameters .....	85

Fig. 4-21 Assumed one-dimensional pressure distributions at different test loads. ....	86
Fig. 4-22 Lateral force estimation results. ....	86
Fig. 4-23 Curve-fitting between cornering stiffness with estimated contact length (left) and peak lateral force and estimated contact length (right) .....	87
Fig. 5-1 The location of two neighboring points before and after ring deformation.....	93
Fig. 5-2 FEM simulation results for tire subjected to vertical force on the flat road .....	94
Fig. 5-3 Radial (a) and tangential (b) deformations of each tire layer .....	95
Fig. 5-4 Strains directly from FEM simulation and by calculating from U, V .....	96
Fig. 5-5 Strains at each layer of tire.....	97
Fig. 5-6 Strains calculated from IL deformations (U, V) and from BT1 deformations ( $u_b, v_b$ ) .....	97
Fig. 5-7 Comparison of strains calculated by using different equations. ....	99
Fig. 5-8 Flexible ring model including tread elements, adapted from [57] .....	100
Fig. 5-9 Discretization of radial deformation based at strain-measurement points.....	102
Fig. 5-10 Radial deformations at different vertical loads estimated from strain measurements.....	103
Fig. 5-11 Convergence of FDM solution at $F_z=5666N$ .....	103
Fig. 5-12 Flexible ring model subjected to a point load, adapted from [64] .....	104
Fig. 5-13 Flexible ring model when subjected to distributed load .....	106
Fig. 5-14 Flow chart to simulation for flexible ring model .....	108
Fig. 5-15 Realization of one dimensional pressure distribution for diverse shape factors: (a) effects of $n_p$ , (b) effects of $S_f$ .....	110
Fig. 5-16 Geometrical parameters of tire for simulation .....	112
Fig. 5-17 Radial deformations estimated by different methodologies: based on flexible ring model, strain measurement and optimization.....	112
Fig. 5-18 Comparison of contact lengths obtained from different methodologies .....	113
Fig. 5-19 Vertical deformations versus test load for rolling and static tire.....	114
Fig. 5-20 Comparison of contact lengths at reference test load for different tire specifications.....	115
Fig. 5-21 Estimated stiffness parameters for different tire specifications using different methodologies.....	115
Fig. 5-22 Estimated one dimensional pressure distribution under different test loads: (a) based on flexible ring model only, (b) based on optimization results (flexible ring model + strain measurements) .....	116

Fig. 5-23 Estimated pressure distributions at reference test load for different tire specifications: (a) based on flexible ring model only (b) based on optimization results (flexible ring model + strain measurements) .....	117
Fig. 5-24 Circumferential strains from simulation and measurements: (a) measured strain, (b) simulated strain from conventional flexible ring contact model (c) simulated strain from new method using strain measurements .....	118
Fig. 5-25 FEM simulation results for circumferential strains .....	119
Fig. 5-26 Cross-sectional deformation and strain distribution of a tire derived from the static frictional force: (a) the applied load (b) the strain distribution [44].....	119
Fig. 6-1 Flexible ring model for rolling tire with circumferential components .....	123
Fig. 6-2 Tread elements models as radial spring [50].....	128
Fig. 6-3 Distribution of friction force on the tread surface in contact with the roadway [68] ...	129
Fig. 6-4 Directions of shear stress for radial pneumatic tire compared to solid tire [69] .....	129
Fig. 6-5 The geometry of the treadband and tread rubber in undeformed and deformed state [61] .....	130
Fig. 6-6 Flow chart of flexible ring model simulation for free rolling tire (considering radial pressure distribution only) .....	137
Fig. 6-7 Validation of the implemented simulation results with those from literature: comparison with Yamagishi and Gong's results (a), comparison with Gong's results (b) .....	138
Fig. 6-8 Flow chart of flexible ring model simulation for free rolling tire (considering normal and tangential pressure distribution).....	142
Fig. 6-9 Normal and horizontal force distribution for different $d_0$ considering: (a) tread normal & shear deformation, (b) tread radial deformation only ( $d_0$ : 2.5, 3.5, 4.5 cm).....	144
Fig. 6-10 Circumferential strains at inner line considering: (a) tread normal & shear deformation, (b) tread radial deformation only ( $d_0$ : 2.5, 3.5, 4.5 cm).....	145
Fig. 6-11 Radial and tangential deformation a) tread normal & shear deformation, (b) tread radial deformation only ( $d_0$ : 3.5cm) .....	145
Fig. 6-12 Identifying contact edges using two different contact models: (a) tread normal & shear deformation, (b) tread radial deformation only ( $d_0$ : 2.5, 3.5, 4.5 cm) .....	146
Fig. 6-13 Measured and simulated strains: (a) measured for 195/65R15 tire (b) simulated using the tire parameters of Table 6-1 .....	147
Fig. 6-14 Geometrical model parameters .....	149

Fig. 6-15 Decomposition of the tire into five components [70].	150
Fig. 6-16 Natural frequencies from vibration test	151
Fig. 6-17 Optimization routing for parameterization	153
Fig. 6-18 Estimated sidewall stiffness	154
Fig. 6-19 Tire vertical stiffness ( $K_v$ ) and longitudinal stiffness ( $K_t$ )	155
Fig. 6-20 Comparison of $k_u$ , $K_v$ , and $K_t$ on various inflation pressure	156
Fig. 6-21 Error between set $F_z$ and estimated $F_z$ from optimization	157
Fig. 6-22 Estimated pressure distribution under various loads: (a) normal pressure distribution, (b) tangential stress distribution	158
Fig. 6-23 Estimated pressure distribution under various inflation pressures: (a) normal pressure distribution, (b) tangential stress distribution	158
Fig. 6-24 Pressure distribution using advanced contact model under various test loads ( $\lambda=0$ )	159
Fig. 6-25 Measured strains (a) and strain rate (b) under various test loads @ 2.1 bars	160
Fig. 6-26 Simulated strains (a) and strain rate (b) under various test loads @ 2.1 bars	160
Fig. 6-27 Measured strains (a) and strain rate (b) under various inflation pressures @ 4265.9N	161
Fig. 6-28 Simulated strains (a) and strain rate (b) under various inflation pressures @ 4265.9N	161
Fig. 6-29 Damping effect on pressure distributions and strains at ref. test condition. $\lambda=0$ (a), $\lambda=0$ (b), $\lambda=0$ (c)	162
Fig. 6-30 Test speeds effect on circumferential strains in 195/65R15 tire (a) and 205/55R16 tire (b)	163
Fig. 6-31 Strain and rotational speed time history	164
Fig. 6-32 Identification of contact angle offset in measured data	165
Fig. 6-33 Estimation of normalized damping coefficient	166
Fig. 6-34 Pressure distribution using model type I under various test loads ( $\lambda=0.09$ )	167
Fig. 6-35 Pressure distribution using model type II under various test loads ( $\lambda=0.09$ )	168
Fig. 6-36 Pressure distribution using model type II under various test loads ( $\lambda=0.09$ )	169
Fig. 6-37 Estimation of lateral force by use of BM and flexible ring model	170
Fig. 6-38 Lateral force estimations for various test loads using estimated pressure distributions	171

Fig. 6-39 Lateral force estimations for various inflation pressures using estimated pressure distributions.....	172
Fig. 6-40 Comparison of pressure distribution between estimated and parabolic-assumed.....	172
Fig. 6-41 Comparison of lateral force estimation results between suggested and conventional	173
Fig. 6-42 Comparison of lateral force estimation results between suggested and conventional	173
Fig. 7-1 Tread-road contact model: (a) radial-only-deformation of tread, (b) shear and normal deformation of tread.....	180
Fig. 7-2 Simulated strains: (a) radial-only-deformation of tread, (b) shear and normal deformation of tread.....	180
Fig. 7-3 Proposal of improved model for strain simulation.....	181
Fig. 7-4 In-plane tire deformations under different vertical forces with a rotational speed of 100 rad/s: (a) radial deformations and (b) tangential deformations.....	182

## LIST OF TABLES

Table 2-1 Estimated characteristics and related methods based on acceleration .....	15
Table 2-2 Estimated characteristics and related methods based on strain .....	30
Table 3-1 Flat-Trac test conditions for 235/55R19 tire (Test Set 1) .....	59
Table 3-2 Flat-Trac test conditions for P235/60R18 Tire (Test Set 2) .....	59
Table 3-3 Flat-Trac test conditions for P195/65R15 Tire (Test Set 3) .....	59
Table 4-1 Statistics table of regression for test set 1 .....	76
Table 4-2 Statistics table of regression for test set 2 .....	77
Table 6-1 Model parameters for implementation and comparison .....	143
Table 6-2 Estimated model parameters for test tire (P195/65R15) .....	152
Table 6-3 Comparison of stiffness parameters of flexible ring with those from literature .....	157

# 1 INTRODUCTION

## 1.1 Background and Motivation

The handling and braking performances of ground vehicles are mainly governed by the forces and moments generated at the contact between the tire and the road surface. Therefore, measuring or estimating tire force and moment is a key task to analyze and control the vehicle behavior. From the performance analysis viewpoint, tire forces and moments are investigated since they can be improved through tire design improvements leading to desirable vehicle performance. Then, tire simulation or experimentation can be used to propose modification to the tire design. When it comes to vehicle control, the electronic control unit (ECU) of vehicle dynamic control system, e.g., ABS, ESP (Electronic Stability Program), determines the control command based on the estimated force and moment available at the tire contact patch.

Both tasks face some difficulties. In the former task, measuring exact forces and moments in the real world is challenging. Usually tire forces and moments can be measured on the flat belt type test rig, e.g., Flat-Trac. Although these test rigs can apply the diverse combinations of driving conditions and measure the force and moment with enough accuracy, the test surface is usually limited to safety walks or steel belts. Because the characteristics of road surface plays a key role in the mechanism of friction generation between the tire and the road, this limitation could be critical in some applications such as an analysis of the vehicle performance on wet, snowy or icy conditions. To overcome this problem, outdoor test equipment such as skid trailers have been used. However, the reliability of test results is lower than indoor test rigs. Also, mimicking real-world driving conditions, i.e., changing test conditions in real-time, is near impossible. Although we can measure the tire forces for a moving vehicle directly with various types of wheel force transducers, the installation requires considerable time and efforts causing inefficiency in measurement.

In the second task of vehicle control, exact estimations of tire contact features in real-time are very demanding. Traditionally, tire force and slip are estimated with

observer-based techniques utilizing the data from the on-board vehicle sensors. These observers usually have adopted simple vehicle models for longitudinal and lateral dynamics to estimate tire variables and require a change in slip condition before they can process the data and estimate the friction. So, under the severe driving conditions accompanied with large combined slips and abrupt wheel load changes, the estimated values are unreliable. Also, considerable uncertainties can be accumulated during the estimation process, which can be due to the use of a simple vehicle model. Estimating reliable tire forces and slips in contact patch is very important considering that the performance of vehicle control algorithm is directly linked to the performance of the system and to the safety of drivers and passengers.

Sensor embedded tires, the so called intelligent tires, have been widely researched in the automotive industry because they are believed to provide more reliable and exact tire-road contact characteristics to vehicle active control systems than traditional indirect estimation methods. In intelligent tire systems, usually deformations and accelerations are measured at locations of interest inside the tire with corresponding sensors. These measurements contain abundant information about tire dynamic behaviors and by utilizing them, more reliable estimation of tire characteristics can be achieved. For these measurements to contain abundant information about the tire contact characteristics, the measured locations are determined as close to the contact area as possible. Through careful manipulation of these measurements utilizing diverse technologies such as sensor fusion, Wavelets, statistical regression, tire modeling, etc., tire parameters can be estimated directly without introducing observer based indirect methods. It is expected that intelligent tires reduce the risk of accidents by providing reliable tire-road contact parameters under various driving conditions. Moreover, it would be possible to simplify and optimize current control systems by eliminating uncertainty-adding procedures inherent to traditional, indirect estimation methods.

From tire designers' view point, tire contact forces estimated using the intelligent tire scheme is expected to have a closer relationship with vehicle performances because sensor measurements can be conducted in the real-world scenarios, i.e., a real vehicle

moving on the real road surface, rather than in the laboratory environment. The contact forces estimated from the real world possibly can explain the behavior of the vehicle better whereas the force and moment measured in the laboratory sometimes fail to describe it correctly.

Tire force and moment generation is mainly governed by the tire design characteristic such as tire stiffness, contact shapes, contact pressure distribution and so on. Therefore, tire designers usually make use of these parameters to tune tire forces and moments for the enhancement of vehicle performances and safeties. They are usually measured on indoor test rigs and under static test conditions. Of course, measuring these characteristics under dynamic test conditions on the real road surface is more desirable since measured tire characteristics are expected to have closer relationship with tire forces and moments. However, measurements in this way are challenging and even not possible. The intelligent tire can also play a role for this application. As mentioned previously, the sensor measurements inside the tire contain information on its deformations and behaviors when it is subjected to certain driving conditions. By interpreting these measurements based on the physical theories, valid tire characteristics can be found and used for the analysis of tire performances.

Overall, intelligent tire systems are expected to be used for advanced vehicle controls and analysis of tire performance characteristics.

## **1.2 Problem Statement and Scope of Work**

This research focuses on the application of intelligent tires for estimation of tire-road contact features and characterization of tire dynamics. Fig. 1-1 illustrates the application flow of intelligent tire system to achieve the research goals. As shown, appropriate sensors corresponding to intended measurements are attached to the tire innerliner where accelerations, strains or deformations can be measured. Based on these measurements, a diverse set of tire-road characteristics can be estimated, i.e., friction coefficient, contact forces, types of road surfaces and tire health status such as the amount of wear and pressure by using different estimation schemes. These estimated

quantities are finally used for the advanced vehicle control, performance analysis and ADAS (Advanced Driver Assistant System).

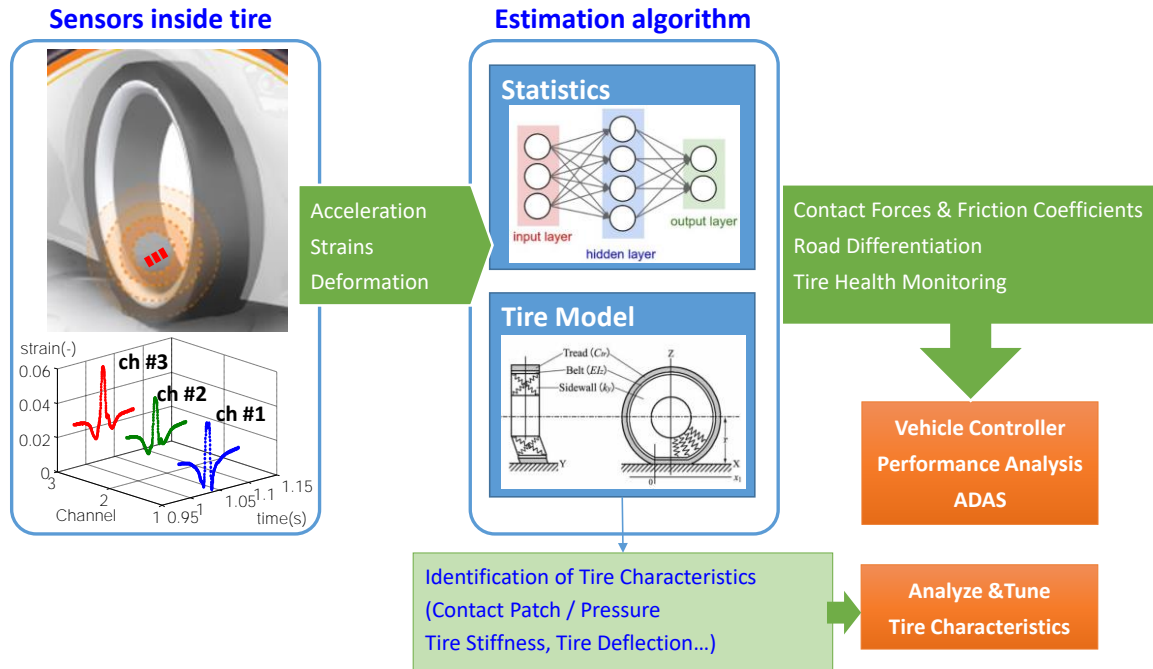


**Fig. 1-1** Expected application of intelligent tire system and its work flow.

Estimation algorithms can be grouped into two categories: statistical and model based methods.

In the statistical methods, features of measured signals are extracted as predictors based on the simple theories in tire-road contact mechanics. These characteristics are fed into statistical algorithms like simple/multivariable regressions or machine learning methods. These methods are expected to predict tire parameters more accurately as more test data sets are accumulated and do not require profound understandings of the complex tire mechanics.

In the model based methods, well-defined tire models are introduced into the estimation process, which can provide tire forces and moments based on physical theories. Tire models generally need tire parameters as their input and these parameters are identified using the sensor measurements in the estimation methods. Tire models

need to be developed by considering the types of measurements available from the intelligent tire and the driving conditions such as test loads, slip & camber angles, slip ratio, etc.

Model based methods usually demand less number of tests than statistical methods but require understanding of the complex tire mechanics. Sometimes new tire models need to be developed if there are no existing models which can utilize the sensor measurements. Moreover, the accuracy of the estimated values may be less than statistical methods because theoretical tire models are developed under considerable simplifying assumptions for limited test/environmental conditions. However, model based methods can provide understanding of the physical meaning of sensor measurements and to find useful predictors before applying statistical methods. Also, if we know the tire forces and moments from other methods, important tire characteristics such as tire contact features and stiffness can be extracted using inverse modeling methods.

From the expected applications of the intelligent tire, this dissertation is focused on formulating methods for:

- 1) The estimation of tire contact features such as forces and slippages for advanced vehicle chassis control systems, and
- 2) Identification of tire characteristics based on fusion technology of intelligent tire and tire model.

To achieve these goals, extensive literature survey on intelligent tires was conducted focusing on methodologies to estimate tire-road contact features. Based on the literature survey, an intelligent tire system was developed by specifying the measurement type and the locations of sensors considering their capabilities to provide data for estimation of crucial tire-road contact parameters as well as to explore tire dynamic behavior. The measurement type was determined as strains because they can be directly related to the tire deformation which is one of the most desirable quantities

to be used with the model based methods. Sensor measurements were collected while measuring the forces and moments of different tires simultaneously on the indoor rolling tire test machine under diverse test conditions.

The sensor measurements were closely investigated under various test conditions. Based on simple tire mechanics theories, promising parameters were extracted from measurements to be used as predictors in regression studies. Simple or multivariable regressions were conducted to estimate various tire characteristics. An analytical tire model was introduced to estimate lateral force using previously predicted parameters.

To figure out the physical meanings of the strain measurements and how they relate to tire deformation, an analytical model was developed. This simple and reliable model was validated using Finite Element Method (FEM). And then, this model was combined with the well-defined flexible ring model to simulate circumferential strains. The circumferential contact problem was solved and various tire dynamic characteristics were identified based on the combination of these models and strain measurements.

### **1.3 Main Contributions**

The contributions of this research are:

1. Explore the state of the art technologies in intelligent tire applications.
2. A multiple strain-based intelligent tire system was proposed by specifying the attachment position, directions or number of sensors. This proposed intelligent tire system is confirmed to be effective for the estimation of tire characteristics.
3. Important tire parameters were estimated based on fully statistical or model based methods. They are expected to provide more accurate parameters to control algorithms to achieve more reliable safety controls
4. The simulation method for circumferential strains was developed. This provided an insight into the physical meanings of strains measured inside the

tire. This can contribute to development of robust estimation algorithms based on the physical theories rather than on fully statistical methodologies.

5. The circumferential contact problem was solved by using strain measurements and flexible ring model. This method removes the complex tread-road contact models, which sometimes cause numerical difficulties in satisfying boundary conditions between the tire and the road simultaneously.
6. Tire parameters for dynamic rolling tire were identified based on the combination of strain measurements and dynamic flexible ring tire model. It is expected that parameters estimated using this methodology reflect more realistic features of tires when strains are measured in the real driving scenario.

Overall, this study will provide methodologies to estimate the tire-road contact parameters for advanced vehicle control programs and another analysis tool to identify tire characteristics which could be more closely related to the tire performance in the real driving scenarios.

#### **1.4 Dissertation Outline**

The rest of this document is organized as follows: Chapter 2 addresses the literature survey on the estimation methods by utilizing intelligent tire. The intelligent tire and experiments are explained in Chapter 3. Methodologies to estimate tire-road contact features are delivered in Chapter 4 followed by the identification of tire characteristics using the flexible ring model in Chapter 5 and Chapter 6. Conclusions, discussions as well as future works are provided in Chapter 7.

## 2 LITERATURE REVIEW

This chapter reviews the literature on estimation methods for tire dynamic characteristics based on the intelligent tire system. There are already some review articles in the subject of intelligent tire, but they usually have focused on tire sensors [1] with the purpose of friction estimation methods for optimized vehicle controls. This dissertation seeks to exploit the intelligent tire system as a tool to characterize tire dynamic features from the point of view of tire engineer. So, this literature review concentrates on the estimation methods of tire dynamics characteristics such as tire forces and contact characteristics. The chapter is organized as follows: Section 2.1 discusses the types of sensors and corresponding measurement values for application in intelligent tire system. Section 2.2 details the estimation algorithm to characterize tire features with each measurement type before summary and discussion are delivered in Section 2.3.

### 2.1 Type of Sensors and measured variables

The forces and moments between the tire and the road surface play a crucial role in the vehicle functional performances such as ride, handling and braking. These forces and moments are generated in the contact patch and are due to the deflection of the tire and the friction between tread rubber and road surface.

Fig. 2-1 shows a typical example of a loaded rolling tire deflection when slip angle is applied. Applied slip angle makes the tread ring, which comprises of tread elements and belt, deflect in the lateral direction resulting in a distorted contact shape and contact stress distribution. This asymmetric stress distribution generates a corresponding force in the vertical direction to the wheel plane (+y direction) in this described example. This lateral force ( $F_y$ ) also causes the carcass line to deflect in the lateral direction with respect to the rim. Similarly under braking or acceleration, nonzero slip ratio causes the contact stress distribution along the longitudinal direction, which generates the longitudinal force [2]. The contact patch moves back and forth with respect to the undisturbed position because of this longitudinal force.

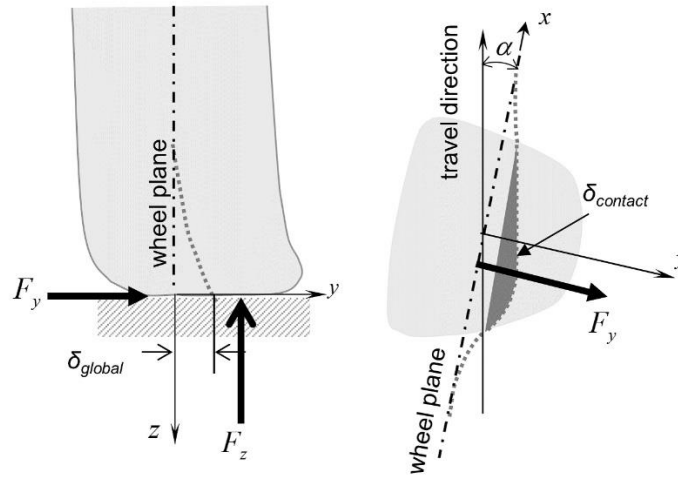


**Fig. 2-1 Schematic view of the tire lateral deflection when lateral force is applied: Left is front view of the tire, right is contact view from above**

As wheel load increases, more of the tread ring is straightened in the contact patch through bending deformation. Also, the radial distance between rim and contact patch decreases through sidewall deformations.

Therefore, if we intend to estimate the tire forces and slippage in the contact patch with sensors inside the tire, the measurement of tread ring deformation in the contact is crucial. Moreover, the measurement of deflection of tread ring out of contact should not be neglected. In this research, the local deformation of tread ring in the contact patch is defined as the ‘contact deformation’ ( $\delta_{contact}$  in Fig. 2-1), and the overall deformation of tread ring with respect to rim is defined as global deformation ( $\delta_{global}$  in Fig. 2-1)

After comprehensive review of this subject, it is revealed that contact deformations are usually identified with measurements of accelerations and strains from traditional sensors available in the market or newly developed sensors (usually for strain sensors) installed near the contact patch. The global deformation is directly measured with specially designed measurement devices such as optical sensors.

### 2.1.1 Sensors for identifying contact deformation

For the purpose of characterization of contact patch, generally accelerometers or strain sensors are attached to the innerliner of the tire on the tread portion. To locate the sensor as near to contact path as possible, sensors can be inserted into tire components like tread or belt package. APOLLO project [3] showed that due to severe relative movements of tire components during rolling, sensors cannot be inserted into tire structure. Also, it can cause durability issues. Therefore, sensors are usually attached to the inner linear on tread portion to secure durability, while they can still be located near the contact patch.

As to acceleration measurement, accelerometer based on microelectromechanical systems (MEMS) are used widely. This type of sensor assures signal linearity and stability over time and insensitivity to temperature change. Moreover, this accelerometer is also compact in size and efficient in energy usage and also inexpensive [4]. These features make accelerometers highly desirable for installation into tires in the market. In terms of characterization of contact features, the carcass lateral deflection can be obtained by double integrating the lateral acceleration signal. This lateral deflection can be correlated to specially developed tire mathematical models to develop relationships between sensed signals and various tire dynamic characteristics.

However, the accelerometer is very sensitive to the noise generated from the road surface and contains rotational, vibrational and gravitational accelerations. So, it is difficult to extract characteristics of interest from the signals which requires advanced signal processing techniques. Moreover, APOLLO project [3] revealed that acceleration seems to be disadvantageous over global deflection or strain to estimate wheel forces, after conducting comprehensive studies on the wheel force estimation.

To measure the strains in the contact patch of a rolling tire, many kinds of strain sensors have been developed on different measuring principles. Piezo electric material has been largely adopted to measure the strain. Among the piezo materials, Polyvinylidene Fluoride is widely used for tire sensors because this polymer based sensor provides high flexibility and strong compatibility with tire materials (rubber). In [5, 6],

PVDF based strain sensor was developed and attached to the innerliner to measure the bending and the longitudinal deformation of the tread ring.

Another type of strain sensor utilizes the Surface Acoustic Wave (SAW) device, which consists of a piezoelectric substrate with metallic structure, i.e., inter digital transducer (IDT) as a sensor element for measuring physical quantities, and a local radar transceiver. The local radar transceiver transmits a Radio Frequency (RF) burst (request unit) to the antenna of IDT which stimulates a wave due to the piezo electric effect. Using the second set of IDT, the SAW is reconverted into electrical RF output signal (response signal) which is received again by an antenna of the local transceiver. The features of this returning signal such as amplitude, frequency and phase will deliver the information of the physical characteristics of where IDT was installed. In [7], a passive sensor connected to request unit by RF link was developed based on the combination of the conventional SAW device and RF request technology. In [8], the deformation of the tread was measured using SAW sensor for the purpose of friction estimation. In this application, a pin was inserted into the tread element acting as a lever, which is connected to the SAW elements located on the innerliner so that the tread deformation in the contact induces a change in the sound acoustic wave. SAW based sensor is fully passive without requiring power supply and ideal for wireless communication, but it is difficult to install multiple SAW sensors in one tire due to their operational fundamentals.

In the application of capacitive type sensors, the steel wire belt of tire is considered as an electrical condenser, which provides varying capacitance when the space between steel wires in the belt change due to tire deformation. In [9, 10], an oscillating circuit was installed in the tire to measure this capacitance change, which was related to the strain of tread ring. In [11], multiple spectral features of the output signals of capacitive sensors are utilized to improve the accuracy of strain measurement. To make capacitive sensors more appropriate for tire applications, ultra-flexible epoxy resin based sensors were developed assuring low stiffness and high elongation of sensor itself [12]. A drawback of this type of sensor is that a capacitance change is also accompanied with a temperature change inside the tire, requiring temperature correction.

In [13], magnetic sensor based on Hall Effect was employed to measure the tread deformation. A permeant magnetic was inserted into the tread rubber and its movement due to tread deformation during tire rolling induce potential voltage, which was monitored by the Hall sensor mounted just 1mm above the magnet. Inserting the pair of the magnetic and Hall sensors into the tread rubber requires special processing during the tire manufacturing and can affect tread stiffness. The strains of sidewall were also measured with magnetic sensors for the purpose of wheel force estimation in [14], which will be delivered in detail in the following section.

Strain sensors are preferred to accelerometers because they can be directly related to tire deflection and operational conditions. As a result, they seem to have more potential when it comes to estimation of wheel forces. APOLLO project [3] claimed that strain sensors have merit over the accelerometers for wheel force estimation. Also, the noise level of strain sensors is generally lower than the accelerometer noise and measured value is not affected by the tire rotational speed. As a drawback of strain sensors, they are more likely to be detached from the tire under large deformation. Also, if their stiffness is considerably different from the tire stiffness, the measured strain can be distorted. Some types of strain sensors require a correction for temperature change while others need special processing to be installed into the tire during tire manufacturing, which makes them less desirable for the commercial application.

In this section, diverse kinds of sensors for strain and acceleration have been introduced in terms of merits and demerits for real applications. Although the accelerometer seems to be more promising option in the market, secure attachments, low cost robust electronics and power supply for the life span of a tire are still challenging.

Moreover, an accelerometer can track only one specific point while there are some attempts to measure the strains over the wide portion of tires using piezoelectric films. Thus, tire information is obtained once per revolution of the tire if one accelerometer is used. This causes bandwidth issues with vehicle control unit, which can cause considerable degradation of vehicle control performance, especially if there is a sudden change of the road surface at high speeds. Cheli *et al.* [15] show the effects of the

bandwidth difference on ABS braking performance as compared to the ideal case (without delay). The stopping distance increase by around 2.3% due to this delay, which could be critical for sudden braking applications. This problem can be improved by using multiple accelerometers around the tire circumference which increases the cost and complexity which may be avoided if a continuous strain sensor is used.

### 2.1.2 Sensors for identifying global deformation of tire

To monitor the global deflection of tire, optical sensors have been frequently used [16-20]. In these sorts of measurement systems, a light emitting diode (LED) is attached on the tire innerliner and its light is focused on the position detector on the rim through a lens. The detail description of this device will be followed in the next section with the associated algorithm.

APOLLO project [3] confirmed that for the purpose of wheel force estimation, an optical sensor is the best choice because it can estimate all wheel forces ( $F_x$ ,  $F_y$ ,  $F_z$ ) with good accuracies whereas accelerometers and strain sensors estimated only one or two wheel forces. It is because the measurement includes the sidewall deformation and contact patch deformation as well, both of which are key factors in the tire force generation mechanism. Also, it can measure the deformation directly whereas accelerations and strains need to be manipulated based on physical models to get the global deflection of tire. However, after sever braking, the tire could slip around the rim which causes misalignment between the detector and LED. So adjustment and recalibration of this sensor system are required after test runs. Also, these measurement systems are complex and energy-inefficient. Therefore, optical sensors have been utilized for the purpose of tire research more frequently rather than commercial applications.

Besides the optical sensor, ultrasonic distance sensor was exploited to measure the vertical deformation of a loaded rolling tire in [21]. The ultrasonic sensor was mounted on the base of the wheel and measured the distance from the sensor to the opposite inner wall of the tire. Because this distance is determined based on sonic speed

which is a function of temperature, the temperature inside tire can be calculated inversely as well. This estimation is limited to the vertical deflection only in this application.

G. Erdogan *et al.* [22-25], developed a new measurement device to measure the global tire deflection in the lateral direction based on a piezoelectric sensor and utilized this measurement for the friction estimation. Fig. 2 shows the developed sensor. This sensor is based on the bending motion of a cantilever beam covered with piezoelectric film. One end of this beam is fixed to tire bead which experiences minimum deformation during tire rotation. The other end is attached to a cylinder like component attached to the tire inner liner, which generates low rigidity in the tangential and radial direction whereas high rigidity in the lateral direction so that this structure is sensitive to the carcass lateral deformation only. The measurements were validated with an optical device installed inside tire with good agreements.

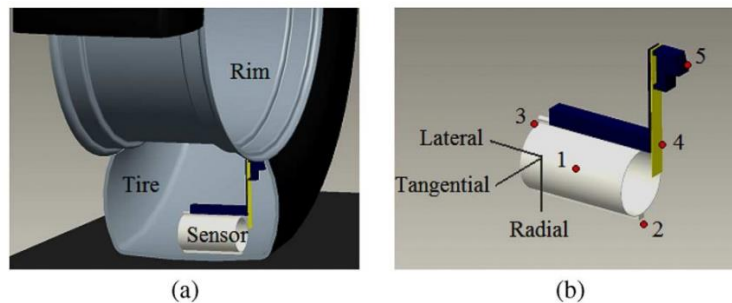


**Fig. 2-2 (a) Sensor location. (b) Designed tire sensor. 1: elastic component, 2: sensor base, 3: slider mechanism, 4: elastic cantilever beam, 5: root of the cantilever beam [23]**

## 2.2 Estimation Methods for Tire Characteristics

For the purpose of the wheel force and contact slippage estimation, three measurement values have been usually exploited: acceleration, strain, and deflection. In this section, estimation algorithms for each of these measurements will be discussed.

### 2.2.1 Estimation based on acceleration measurement

Table 2-1 lists the estimated characteristics and the corresponding parameters used for prediction. Usually the tire features in interest are predicted through simple correlations based on simple mechanisms of tire force generation. Some researchers exploited well-developed tire models to extract meaningful parameters from measurements.

**Table 2-1 Estimated characteristics and related methods based on acceleration**

Estimated Characteristic	Parameters for estimation (Method)	Reference
Contact length (C/L)	Peak to peak distance of signal	[4]
Hydroplaning portion in C/L	Signal shape in contact	[26, 27]
Slip angle (SA)	C/L on shoulder part	[4]
	Amplitude of lateral acc. spaced apart from tread center	[28]
Longitudinal force ( $F_x$ )	Phase shift of signal wave	[29]
	PCA based estimation model	[30]
Test load ( $F_z$ )	Wave width	[29]
	C/L	[4]
	PCA based estimation model	[30]
Lateral force ( $F_y$ )	Integral of lateral acc. (physical model based)	[31-35]
Road classification	PSD, RMS of signal	[4, 36, 37]
Friction	Estimated $F_y$ , $F_z$ , SA (physical model based)	[31-35]

This approach enables us to identify more tire characteristics and to understand the physical meanings of the measured signals. These kinds of approaches are marked as ‘physical based methods’ in the table. Estimation algorithms with acceleration are categorized into four groups based on the scheme of each algorithm: ‘Estimation of contact feature and its application’, ‘Signal processing for road differentiation’, ‘Lateral deflection by double integral of acceleration’, and ‘Statistical approach’.

### 2.2.1.1 Estimation of contact features and its application

The accelerations measured at the innerliner of a loaded rolling tire undergo sudden changes when they enter and leave the contact patch. Therefore, distinctive peaks at the leading and trailing edges of the contact patch are observed regardless of the direction of measured acceleration. The time lag between these two peaks can be an index for identifying the contact length. Although accelerations in any direction can be used for contact length estimation, many researchers have chosen the longitudinal accelerations because they show more distinctive peaks with more straightforward meaning [4, 26, 27, 36, 37].

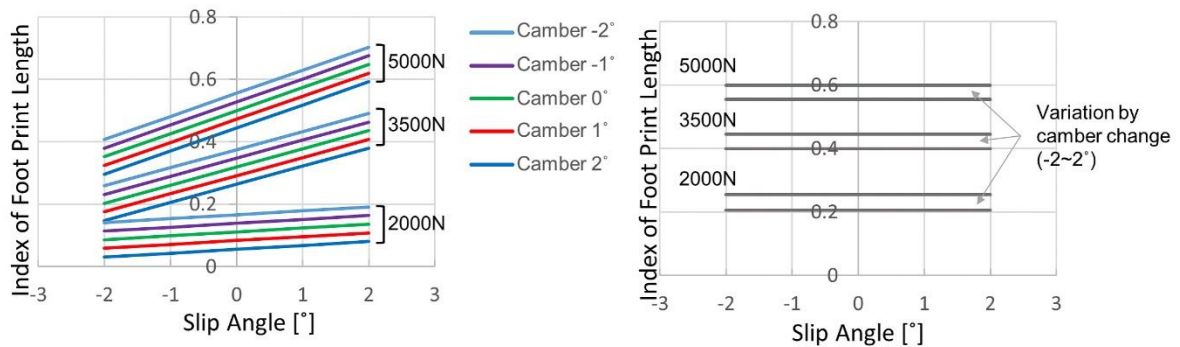


**Fig. 2-3 FL parameter vs slip angle: (a) inner sensor and (b) central sensor as a function of tire load and camber. Adapted from F. Braghin et al., Measurement of contact forces and patch features by means of accelerometers fixed inside the tire to improve future car active control[4], © 2006 Taylor & Francis Publishing**

The contact lengths estimated in this way are also used for the estimations of other parameters like tire forces and slip values. Braghin, F. et al. estimated wheel loads and slip angles based on contact length [4]. The problem using a contact length as a predictor for wheel loads is that contact lengths are also sensitive to other parameters such as slip, camber angle and inflation pressure. To find the robust regressors, they attached three accelerometers along the transverse direction on the innerliner of tread portion corresponding: inner contact (close to a vehicle), center and outer contact, respectively. Force and moment tests on the Flat-Trac test rig were conducted under various combination of slip angles, camber angles and test loads (Fig. 2-3). They found that estimated contact lengths at the center depended on test loads only not sensitive to

slip angles or camber angles. On the contrary, outer and inner contact lengths were very sensitive to slip angles and the relationship between these contact lengths and slip angles was linear up to around two degree of slip angle. Accordingly, the contact length at the center and shoulder (inner and outer) were adopted to estimate test loads and slip angles, respectively. This algorithm was validated thorough indoor and outdoor tests showing good agreements.

US patent US8024087 [28] proposed an estimation algorithm for slip angle, which is similar to [4]. The inventors installed a pair of accelerometers spaced equally apart from the equator line on the inner liner. Instead of using contact patch length, they employed the amplitude of lateral acceleration. This was defined as the difference between the peak values of signal arising near the center of contact patch and the mean value of signal outside contact patch. These amplitudes had a linear relationship with the applied slip angles. Therefore, a linear regression equation in terms of the amplitude of acceleration signal was proposed. The slope and the intercept for this equation turned out to be functions of wheel angular velocities. They also suggested that the wheel angular velocity could be predicted with peak values of the radial acceleration, because they increase monotonically along the wheel angular velocity.

Savaresi, S.M *et al.* utilized angular shifts of the contact patch with respect to the rim under braking or acceleration for the tire force estimation as explained in Fig. 2-4 [29].

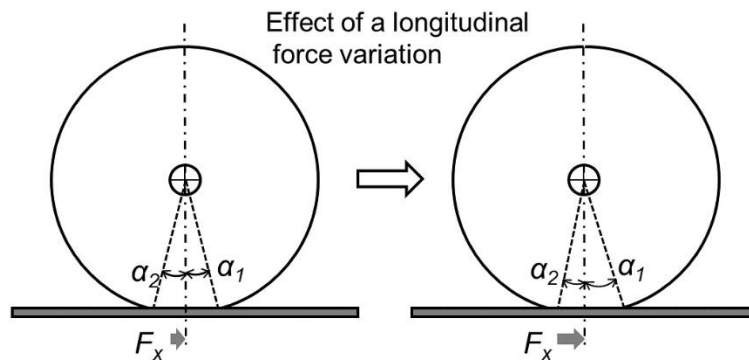


**Fig. 2-4 Effect of a longitudinal force variation. Adapted from S.M. Savaresi et al., New Regressors for the direct identification of tire deformation in road vehicles via 'In-Tire' accelerometers [29], © 2008 IEEE Publishing**

To realize this scheme, they installed a wheel encoder in combination with one radial accelerometer attached to the innerliner of the center tread portion. Using a sensor fusion technique, the acceleration signal along the wheel rotational angle was obtained instead of the travel time. This domain conversion from time to angle removed the effect of wheel rotational frequency on the phase shift. With specially designed contact detection algorithms, absolute angular positions,  $\alpha_1$ ,  $\alpha_2$ , corresponding to the front and the rear edges of contact were extracted. The average ( $\delta\varphi$ ) and difference ( $\Delta\varphi$ ) of these two values were proposed as new regressors for the estimations of the vertical force ( $F_z$ ) and longitudinal tire forces ( $F_x$ ), respectively. These parameters were also affected by vehicle speed due to aerodynamic forces and tire rolling resistance. To remove speed effects, acceleration and braking tests at low accelerations were conducted to find the correction equations. It was also observed that  $F_x$  estimation parameter,  $\Delta\varphi$ , was slightly linked with  $F_z$  as well. Assuming linear relationship between  $\Delta\varphi$  and  $F_z$ , correction factors were obtained to predict accurate  $F_x$  by removing  $F_z$  effect on  $\Delta\varphi$ . Based on validation tests, these two parameters seemed promising to predict the wheel loads and braking forces of each wheel of vehicle during braking and acceleration.

The contact between road and tire is very important not only on the dry conditions, but also on the wet conditions. Especially on the wet conditions, the contact patch is distorted by the wedge like force at the front of contact, which is generated by the inertia of the water entering the contact area. As the vehicle speed increases, this lifting force increases which reduces the contact area and finally hydroplaning occurs. The contact features on the wet road are hard to observe. The footprint tests on the wet road usually have been performed by vehicle tests on the road with a glass plate covered by the water layers. Beneath this plate a high-speed camera is installed to get the foot print image.

Mika Matilainen *et al.* used three axes accelerometers to observe contact features on the wet roads [26, 27]. Acceleration measurements were performed through the vehicle tests on the dry and the wet road at realistic velocities. After observing the longitudinal, lateral, and radial acceleration signals, they concentrated on the longitudinal

signals because it had distinctive peaks at the front and rear contact edges even on the wet road whereas radial and lateral accelerations did not show clear peaks. Moreover, the longitudinal acceleration showed some useful features to characterize road conditions (Fig. 2-5).

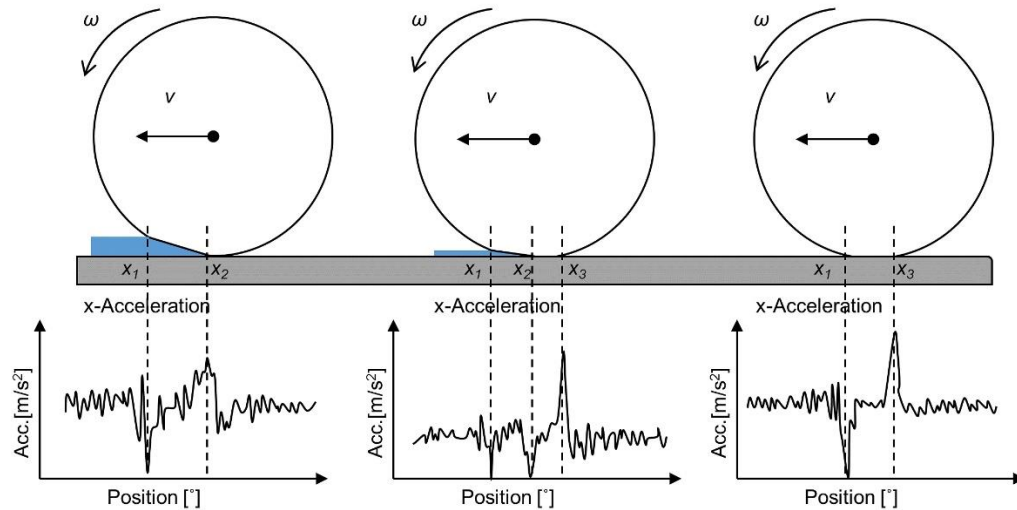


**Fig. 2-5 Determination of the contact length: (a) Full aquaplaning: vehicle velocity=90 km/h; (b) Partial aquaplaning: vehicle velocity=72 km/h; (c) Dry asphalt: vehicle velocity=74 km/h, tyre pressure=2.2 bars. Adapted from M. Matilainen et al., Tyre contact length on dry and wet road surfaces measured by three-axial accelerometer [27], © 2014 Elsevier Publishing.**

On the dry road, the longitudinal acceleration around the contact center was almost flat near zero acceleration and the shape was symmetrical with respect to the contact center under pure rolling condition (c in Fig. 2-5). Two distinct peaks at  $x_1$  and  $x_3$  are observed at the leading and trailing edge on the dry load. When the water film with a depth of 7~8mm existed, the shape of the acceleration signal changed considerably. In the partial hydroplaning, the most noticeable feature is the existence of another negative peak,  $x_2$  within the contact patch, which was assumed to occur when the tire tread hit the road surface breaking through the water film (b in Fig. 2-5). Thus, the real contact length during the partial hydroplaning could be identified with the distance between  $x_2$  and  $x_3$ . Full hydroplaning can be identified by using the radial acceleration. On the dry road, the radial acceleration is almost flat around the contact center because this portion of the tread is in contact with the road surface. On the contrary, under a full hydroplaning, there is no contact area between the tire and the road surface resulting in a non-flat shape of

signal in the contact area. This tendency makes the radial acceleration a good candidate for predicting full hydroplaning. From vehicle tests both on the dry and wet roads under various test conditions, meaningful and reasonable tendencies on contact lengths were observed. Moreover by comparing the test results of worn tires with new tires, this approach was confirmed as promising for hydroplaning prediction [27]. They expanded their research to identify the distorted contact shape on the wet road by attaching more accelerometers to the innerliner along the transverse direction. In this approach, they estimated contact lengths at shoulder, intermediate and center tread ribs on wet surfaces. A high-speed camera was also installed to capture the contact areas for the comparison purposes. The results showed that both methods could identify the phenomena that the contact shape was distorted and the contact area decreased more and more as the test speed increased on the wet road surface. However, for full hydroplaning, the severely distorted contact shape was observed with the optical measurements whereas contact lengths estimated from accelerations distributed evenly from center to shoulder showing less distorted shape. A future study is needed to explain this phenomenon.

#### 2.2.1.2 *Signal processing for road differentiation*

Several researchers have focused on the road differentiation using acceleration measurements as the first step for friction estimation under steady state rolling condition.

Morinaga, H *et al.* differentiates road surfaces using the longitudinal acceleration measured at the inner linear of the center tread portion [37] They noticed that signal powers of measured accelerations within a specific frequency range could be used to identify the road condition. Fig. 6 shows acceleration signals on various road surfaces at 20 km/h of the vehicle speed. On the dry road, the accelerations within contact patch tend to be quite flat ((a) of Fig. 2-6), whereas on the ice road, high frequency accelerations above 2 kHz were observed ((b) of Fig. 2-6) which were generated by skids between the tread blocks and the slippery road surface. On the high friction road surfaces, the tread undergoes shear deformation without slip and these high frequencies in the acceleration

signal are not observed. Therefore, the acceleration levels at high frequencies in the contact patch can be used for the detection of low friction road surfaces, but it could not differentiate snow and ice roads when comparing (b) and (d) of Fig. 2-6. Meanwhile, on the wet surface with a water depth of around 2mm, the high-level accelerations above 1 kHz were observed just before leading edge, which was considered to arise when the tread block hits the water ((c) of Fig. 2-6). Thus, the level of high frequency acceleration just before the leading edge seemed to identify the existence of water film. Moreover, the level of signal powers at this frequency range were used to identify water depth by setting an optimum threshold. For the application in the real world, different band pass filters were designed to extract powers of acceleration signals corresponding to the frequencies of interest for each region of contact. This estimation algorithm classified road status into wet, ice or snow, and dry with a high accuracy rate in validation tests.

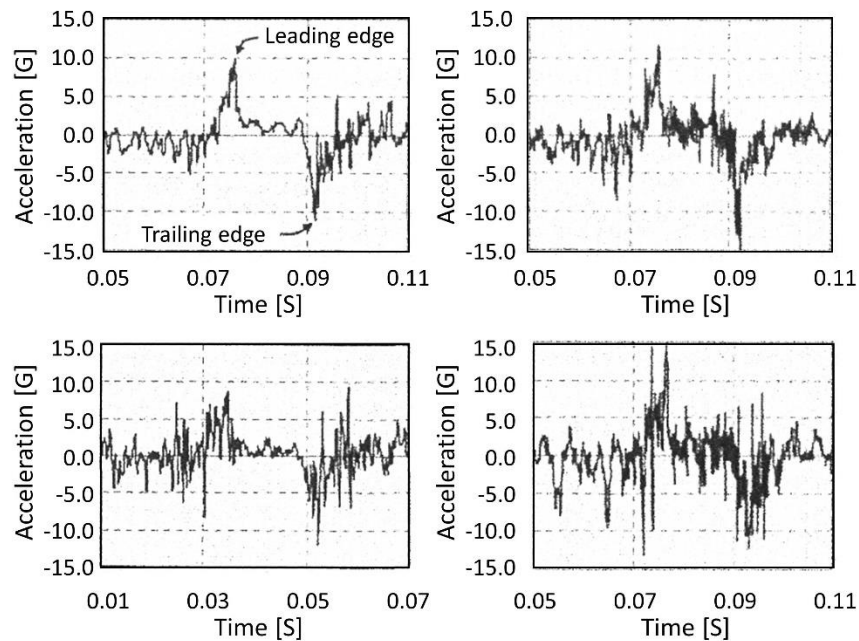


**Fig. 2-6 Acceleration waveform on different road surfaces: (a) Dry asphalt; (b) Ice; (c) Wet asphalt; (d) Snow [37]**

However, because the levels of signal powers are also affected by the roughness of the road surface as well as covered materials (water, ice, snow) as presented in the

following works, more comprehensive research is required for realistic applications based on this methodology.

Braghin, F *et al.* identified the roughness of road surfaces based on the radial acceleration measurements [4]. They found the RMS values of radial accelerations out of contact could differentiate the road roughness from vehicle tests at various speeds (10, 20, 30 km/h.) on three asphalt roads with different roughness. As the roughness of the road surfaces increase, RMS values of acceleration signals also increase. These values also increase along the speed rapidly, so difference of roughness can be identified more clearly at higher speeds.

Niskanen, Arto J., *et al.* employed similar concepts as utilized in [37] to search the potential indicating factors for friction estimation from acceleration signals [36].

They also paid attention to the acceleration signal characteristics in front of the contact patch, but they limited their research to road surfaces with the same macro roughness. Therefore, they tried to find parameters which are more representative of the pure friction phenomena rather than just roughness. They chose concrete and icy roads both of which have smooth surfaces. The vibration level of accelerations is higher on the icy road than concrete road. This is explained by the tire carcass vibration induced by the local slip at the leading edge on slippery roads. Although they used three axis accelerometers on three different locations (center rib, intermediate rib and shoulder block), this phenomenon was more distinctive in the radial and longitudinal accelerations measured at the center rib. They applied a bypass filter to signals measured at the center rib. This filter suppressed the high frequency noise and allowed the signals within 2~5 kHz to pass. This range was considered to be related to friction phenomena. The area under the power spectrum of the filtered signal was proposed as the potential parameter for friction estimation, and the area from icy road was bigger than twice the area on the concrete as shown in the Fig. 2-7.

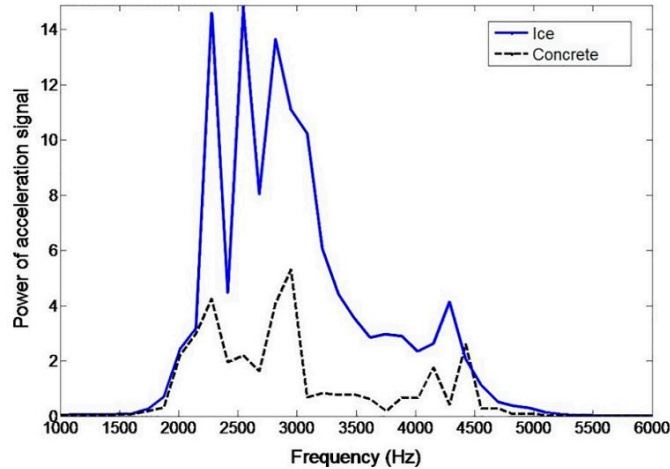


**Fig. 2-7 Power spectrum of the band-pass (2000–5000 Hz) filtered x-axis acceleration signal before contact (2.2 bars, 20 km/h) [36]**

Although the road differentiation using frequency-based analysis of acceleration signal seems promising, more factors should be taken into consideration. Presented analysis were based on the vehicle tests at relatively lower speeds. Considering that the features of acceleration depend on the tire rotation speeds, the validity of presented estimation parameters over a wide range of speeds must be investigated. Moreover, tread rubber characteristics need to be included because viscoelasticity of tread rubber, which is a function of excitation speed, affects the vibration features of tire to some extent.

### 2.2.1.3 Lateral deflection by double integral of acceleration

Another application of acceleration signals is the prediction of the carcass lateral deflection when a tire is subjected to lateral force.

Considering the lateral force is mainly generated by the deformation of the tread ring in the contact patch, lateral deformations of the tread ring in the contact can be used for lateral force estimations. Also, they can be used to characterize tire design properties by introducing physical tire models which make use of carcass deflections. This lateral deformation can be generated by integrating the lateral acceleration twice along the contact length.

As introduced in Section 2.1.2, G. Erdogan *et al.* developed a new measurement device to measure the tire lateral deflection based on a piezoelectric sensor. The measured deflection was utilized for lateral force estimations based on the tire lateral deflection model. Slip angles were also estimated using the kinematic relationship between slip angles and lateral deflection profiles of carcass in the contact region [22-25]. They also expanded this algorithm to be used with acceleration measurements [32]. An FE tire model was developed for the purpose of development and validation of the estimation algorithm. This simulation model was validated by comparing simulated accelerations with measurements from real vehicle tests. Through FEM simulation, lateral deformations at various slip angles were extracted. (Fig. 8)

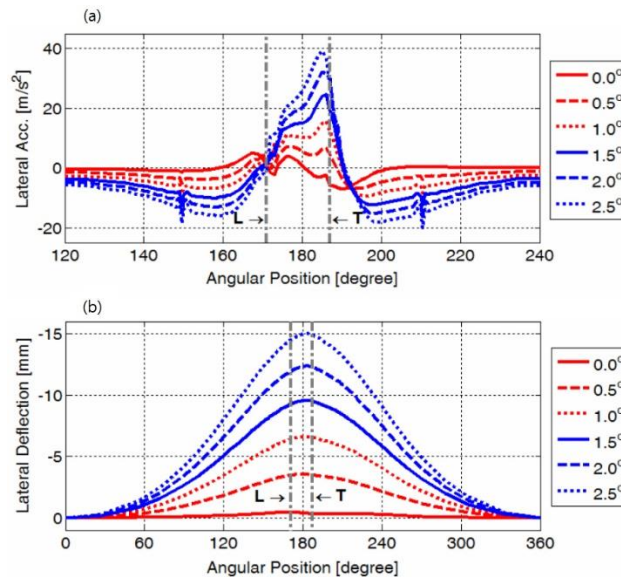


**Fig. 2-8 Lateral (a) acceleration and (b) deflection simulations at different slip angles [32]**

Initial slopes of the lateral deflection curves at the leading edge were proposed as the estimation parameters for slip angles based on the kinematic relationships between slip angle and carcass lateral deflection [38] and this relationship is represented in Eq. (1).

$$\frac{\partial v}{\partial x} = -\alpha \quad (1)$$

where,  $v$  is the lateral displacement of carcass (or tread ring) in the contact patch with respect to its undisturbed location.  $x$  and  $y$  are coordinate axes on the contact patch in the longitudinal and lateral directions, respectively. This relationship only holds on the assumption of steady state pure rolling, no camber, small slip angle and no spin slip. Using this slope of the lateral deflection at the leading edge, slip angles up to two degrees were predicted with a good accuracy. The lateral force was estimated by introducing a simple tire model where the carcass lateral deflection profile ( $y_b$ ) is characterized as a second order polynomial along the contact patch ( $x_b$ ) and its coefficients are compliances corresponding to different deformation modes like bending ( $C_{bend}$ ), yawing ( $C_{yaw}$ ) and lateral shift ( $C_{lat}$ ) as represented in Eq. (2). This carcass deflection model was proposed in developing TREAD Sim model by Pacejka [38].

$$y_b = \frac{F_y}{2C_{bend}} x_b^2 + \frac{M_z}{C_{yaw}} x_b + \frac{F_y}{C_{lat}} \quad (2)$$

The lateral force,  $F_y$  generates the bending and constant lateral deformation of carcass equator line  $y_b$ , which is expressed with the second order and constant terms in this equation. Aligning moment induces asymmetry in the deformation profile through the first order term.  $C_{bend}$ ,  $C_{yaw}$  and  $C_{lat}$  are known stiffness associated with the bending, yaw, and lateral shift, respectively. By fitting this equation to the lateral deflection obtained from twice integrating the lateral acceleration,  $F_y$  and  $M_z$  are estimated. On the assumption of known wheel load, a friction coefficient is estimated from  $F_y$  and  $F_z$  based on the brush type tire model, which is numerically formulated as in Eq. (3) ~ Eq. (5).

$$F_y = 3\mu F_z \frac{\tan(\alpha)}{\tan(\alpha_{sl})} \left( 1 - \left| \frac{\tan(\alpha)}{\tan(\alpha_{sl})} \right| + \frac{1}{3} \frac{\tan^2(\alpha)}{\tan^2(\alpha_{sl})} \right) \quad (3)$$

$$M_z = -\mu F_z \alpha \frac{\tan(\alpha)}{\tan(\alpha_{sl})} \left\{ \begin{array}{l} 1 - 3 \left| \frac{\tan(\alpha)}{\tan(\alpha_{sl})} \right| + 3 \left( \frac{\tan(\alpha)}{\tan(\alpha_{sl})} \right)^2 \\ - \left| \frac{\tan(\alpha)}{\tan(\alpha_{sl})} \right| \end{array} \right\} \quad (4)$$

$$\mu = \frac{2c_{py}a^2}{3F_z} \tan(\alpha_{sl}) \quad (5)$$

In this equation,  $\alpha_{sl}$  is the critical slip angle at which the whole tread elements start to slide, and  $c_{py}$  is the lateral stiffness of the tread.  $\mu$  represents the friction coefficient between tire and road surface and  $a$  is the contact length. By solving these equations for  $\alpha$ ,  $\alpha_{sl}$ , and  $\mu$  simultaneously with estimated  $F_y$  and  $M_z$ , friction value is determined.

This research shows the good example that well-established theory in tire models is integrated with an estimation algorithm based on sensor-measured values, resulting in the expansion of the application of intelligent tires. G. Erdogan also proposed an advanced vehicle control system based on this technology [31]

Hong, S. *et al.* modified, improved and applied this estimation algorithm to real world scenarios [33]. They noticed that the axes system attached to accelerometer body frame is not always aligned to the wheel axes during one full tire rotation because the accelerometer follows the deformed carcass equator line when the tire is subjected to a lateral force. Thus, the lateral deformation obtained through double integrating of the lateral acceleration without a particular manipulation could not be representative of the real lateral carcass deformation. By comparing the lateral deflections from FEM and real accelerometers, they found that even though there was considerable discrepancy in two values out of contact, both have almost same deflection curves in the contact patch. Thus, the previous estimation algorithm based on FEM model [32] was modified to use the acceleration only within the contact patch. In this case, lateral acceleration outside contact patch is set to zero, so zero boundary condition at the leading edge was introduced. Thus Eq. (2) was modified to meet these conditions. In this way, Hong suggested a differential form of the lateral deflection model represented by Eq. (6)

$$\frac{d^2y}{dt^2} = \frac{F_y}{c_{bend}} \left( \frac{dx}{dt} \right)^2 + \left( \frac{F_y}{c_{bend}} x + \frac{M_z}{C_{yaw}} \right) \frac{d^2x}{dt^2} \quad (6)$$

Double integrating this equation with the zero boundary conditions and introducing longitudinal wheel kinematics inside the contact patch yields the following result.

$$y = \iint_{t_l}^t \frac{d^2y}{dt^2} dt dt = \frac{F_y}{2c_{bend}} (x - x_l)^2 \quad (7)$$

where,  $t_l$ , and  $x_l$  are the time and the longitudinal displacement at the leading edge, respectively. By curve fitting of double integrals of lateral acceleration into this simple parabolic equation,  $F_y$  was estimated. Note that we cannot estimate  $M_z$  with this parabolic model, which is essentially required for friction estimation based on the brush model (Eq. (5)). In this estimation scheme, they introduced a tuning parameter related to the pneumatic trail to get  $M_z$ . Validation tests with a real car with different loading conditions showed this algorithm could predict the friction with a reasonable accuracy, but estimated friction was very sensitive to the tuning parameter i.e., the assumed pneumatic trail. This degraded the estimation capability of the algorithm when considerable steering angle was involved. In [34] the same author included the  $M_z$  effects realistically and the results of the new algorithm estimated friction during vehicle tests with large steering inputs.

Matsuzaki, R. *et al.* also used a double integral of lateral acceleration for slip angle and lateral force estimation [35]. Slip angles were estimated in the same way as [32], but for the lateral force estimation, they adopted a simple concept which states that the lateral force developed in the tire contact is simply proportional to the lateral deflection of tread ring in the contact. Thus, double integral within the lateral deflection is used as regressor. In this application, friction was estimated using the model suggested in [38].

$$\mu = \frac{F_y(\alpha)}{F_z(\alpha)} \left\{ 1 - \left( 1 - \frac{\tan \alpha}{\tan \alpha_{sl}} \right)^3 \right\} \quad (8)$$

The critical slip angle ( $\alpha_{sl}$ ) and the friction coefficient ( $\mu$ ) were obtained by simultaneously solving Eq. 8 at two different slip angles ( $\alpha$ ). Validation tests were performed on the indoor test rig at a low speed on the different road surfaces resulting in a good agreement with real friction values.

Accelerations are usually measured in the accelerometer body fixed coordinate, but to utilize measured acceleration for identifying tire deflection, measurements should be expressed in the rim or ground fixed frame. Although Hong [33] revealed that the lateral acceleration expressed in the sensor body fixed frame can be directly used within the contact patch without a coordinate conversion, this approach has its limitation when it comes to applying in out of contact region or utilizing other accelerations in the vertical or longitudinal direction. To fully utilize the acceleration signals to obtain meaningful deformations of tread ring, coordinate conversion matrixes from the sensor fixed coordinate system to another preferred coordinate system are required. The accelerometer tracks a fixed point on the inner liner, which is deformed due to contact forces. Therefore, conversion matrix from accelerometer body fixed frame to other frames should include tread ring deformations. This requires solving complex partial differential equations to get the tire deformations based on acceleration measurements, which makes identification process complex and even more challenging.

#### 2.2.1.4 *Statistical approach*

Due to tire materials as well as response nonlinearities and the complexities in tire structure, estimating the tire dynamic features based on the simple linear relationship is only possible under limited operational and environmental conditions. Moreover, these sorts of estimations use only a few properties of measured signals even though excluded signal features might be meaningful for exact estimations.

To overcome this limitation, the fully statistical model was developed to bridge between the measured signals and longitudinal and vertical force [30]. In this study,

several basis signals or so called ‘features’ were extracted from the radial accelerations by means of Principal Component Analysis (PCA) method. Each extracted signal represented certain characteristics of the original signal, e.g., a typical shape of radial acceleration, accelerations leaving and entering the contact path (feature 1, 2, 3 in Fig. 2-9 respectively). Signal features are orthogonal to each other and play a role as a basis in the linear model to estimate longitudinal forces and vertical loads.

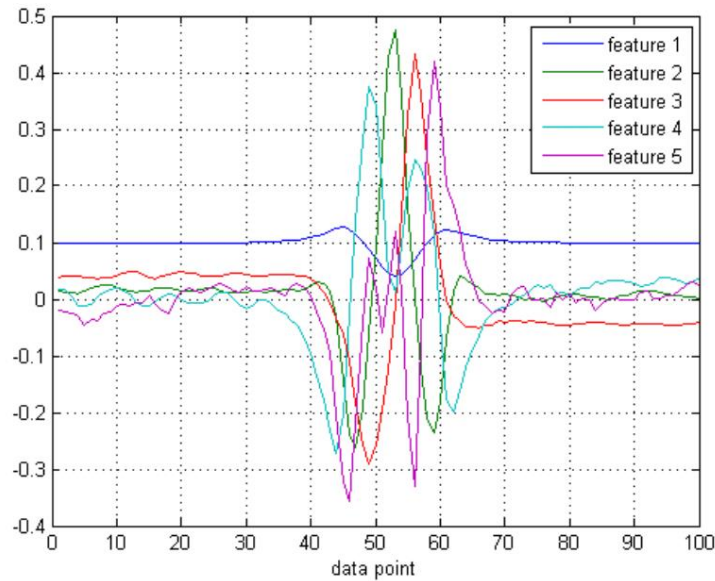


**Fig. 2-9 Features 1-5. [30]**

The linear models are  $F_x = a_0 + \sum a_i p_i$ ,  $F_z = b_0 + \sum b_i p_i$ , where  $p_i$  represents the  $i^{th}$  signal feature and  $a_i$  and  $b_i$  are correlation coefficients. Least square method was used to find the correlation coefficients. Validation tests with a real vehicle were performed and radial accelerations at the inner surface of the tires were measured. Vehicle speeds were used to obtain longitudinal and vertical forces based on the vehicle longitudinal dynamics. Test data were divided in two; one is for identifications and the other is for validations. The estimated forces agreed well with real forces with  $R^2$  of around 0.9.

Most of the estimation studies with acceleration measurements use simple regressions on the confined test results without profound physical theories. Therefore, to guarantee the robust application, extensive tests are required to cover the various test

and environmental conditions, which makes commercial applications difficult. Moreover, far advanced and appropriate statistical models should be adopted to include numerous effects in an efficient way, e.g., neural networks, multivariable regression, fuzzy logic, and so on.

### 2.2.2 Estimation based on strain measurement

Many researchers have chosen the strain sensors especially for the purpose of wheel force estimations. Strains have been measured at the point on the innerliner of the tread near the contact patch. The strains are usually measured in circumferential and lateral directions.

TABLE II summarizes the estimated quantities and the corresponding strain parameters used for estimations. From this table, we can know that strain sensors are actively adopted to estimate wheel forces and slip information. Similar to acceleration based estimation, the strain based algorithms are categorized into four arbitrarily chosen groups of; ‘Estimation of contact features and its application’, ‘Signal amplitude as prediction parameter’, ‘Integral/Derivative of signal as prediction parameter’, and ‘Other methods’.

**Table 2-2 Estimated characteristics and related methods based on strain**

Estimated Characteristic	Parameter for estimation (Method)	Reference
Contact Length (C/L)	Peak to peak distance in strain rate	[37]
Inflation pressure	Const. strain out of contact	[39]
	Axial max. tensile strain	[40]
Velocity	Frequency of peak of strain signal	[39, 41]
Effective radius (→ Slip ratio)	C/L	[42]
Slip angle (SA)	Contact length ratio b/w in & out	[39]

	Circumferential. peak strain rate ratio b/w in & out	[43]
Camber angle effects	Deflection length ratio b/w in & out and Contact length ratio b/w in & out	[37]
	Circumferential. max tensile strain ratio b/w in & out	[43]
Longitudinal Force ( $F_x$ )	Asymmetry in circumferential strain w.r.t. contact center. Integral form. (physical model based)	[44]
	Peak ratio of axial tensile strain b/w front & rear	[41]
	Strains of sidewall	[14]
Test Load ( $F_z$ )	Circumferential max. compressive strain	[42]
	Integral of circumferential strain. (physical model based)	[44]
	Circumferential or axial max. tensile strain	[39, 41]
	C/L	[37, 39, 43, 45]
	Strains of sidewall	[14]
Lateral Force ( $F_y$ )	Contact length ratio b/w in & out	[37]
	Contact length difference and average at in & out	[45]
	Peak ratio of axial tensile strain b/w in & out	[41]
	Strains of sidewall	[14]
Torque	Circumferential. compressive strain ratio b/w front & rear	[42]
Strain signal	Vertical load, vehicle speed (Neural network)	[46]

### 2.2.2.1 Estimation of contact features and its application

The contact length is the primary parameter to be estimated, because it is related closely to other parameters like forces and slip angles. An estimation algorithm of contact length was proposed in [37] by Morinaga, H. *et al.* which has been extensively adopted for contact estimations by other researchers as well. Fig. 2-10 shows the time history of a circumferential strain (the very left) at the innerliner on tread portion and their time

derivatives per one complete revolution of the tire. As shown in the circumferential strain chart, a certain point at innerliner experiences circumferential compression at the leading edge followed by tension near the contact center, and then finally compression at the trailing edge.

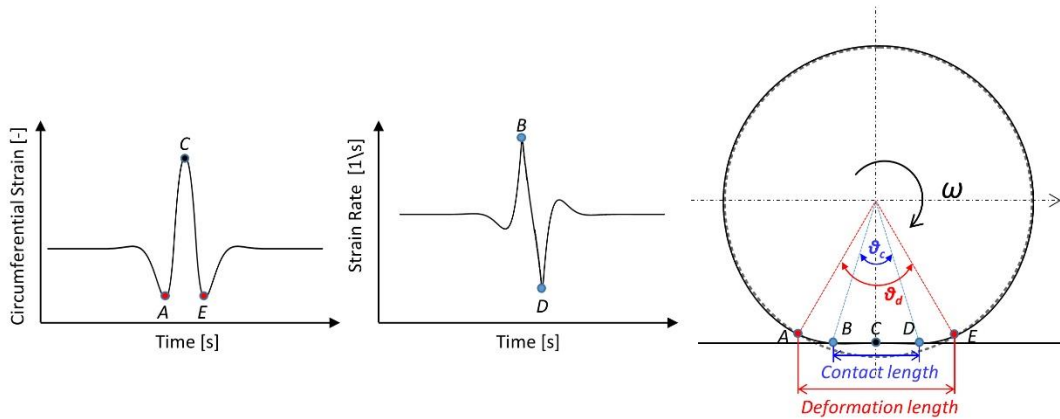


**Fig. 2-10 Characteristics of tire strain time history. Adapted from H. Morinaga et al., *The Possibility of Intelligent Tire (Technology of Contact Area Information Sensing)* [37], © 2006 JSAE Publishing.**

Compressive peaks happen just before and after the contact patch, where the tread deformation towards outside of contact maximizes due to the applied wheel load. In the contact patch, tensile strain becomes dominant due to the bending deflection of tread under the vertical load. The author defined the length between two compressive peaks as 'deflection length' ( $\overline{AE}$ ) because only this region of tire is deflected. Tire contact length also can be determined based on a strain rate, which is the time derivative of the strain. As we can see in Fig. 2-10, strain rate has two distinctive peaks, where the change of strain is maximized. It is because when tread elements enter or leave the contact patch, the strain at the corresponding point on innerliner experiences sudden change. Thus, these two peaks are indicatives of the leading edge and the trailing edge of the contact patch, respectively. Therefore, contact lengths can be estimated from peak to peak distances of the strain rate ( $\overline{BD}$ ).

The shape of the contact patch varies in typical ways as vertical loads or lateral forces change. As test loads increase, contact lengths tend to increase in a linear

relationship up to a point. Therefore, test loads can be estimated based on the contact lengths [37, 39, 43, 45].

If a slip angle is applied to a rolling tire, the contact shape will be distorted into asymmetric, trapezoid like shape. The contact length opposite to wheel heading direction becomes longer whereas the other side becomes shorter. Using this asymmetry in the contact patch under cornering, estimations of lateral force and slip angle have been attempted by several researchers [37, 39-41, 45].

For these experiments, at least two strain gages are attached along the transversal direction (y-direction) on the tire inner linear to measure strain at inner and outer part of the contact path. In [37], 'contact length ratio' is defined as the ratio of the inner contact length to the outer contact length. This parameter was correlated well with the lateral force corresponding to slip angles within  $\pm 8$  degree. However, estimation of slip angles using this parameter is limited to less than 4 degrees, because above a certain amount of slip angle, slip happens across the contact path without distorting the contact shape any more. In [37], for the robust estimation of  $F_y$ , camber angle effects on the contact length ratio were also considered.

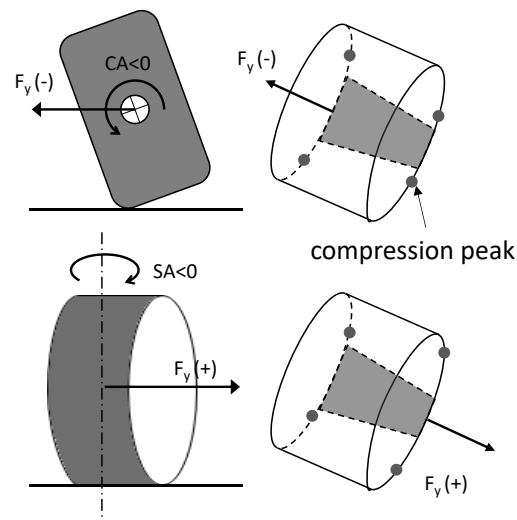


**Fig. 2-11 Drawings of tire deformation. Adapted from H. Morinaga et al., *The Possibility of Intelligent Tire (Technology of Contact Area Information Sensing)* [37], © 2006 JSAE Publishing**

The contact length ratio depended on not only slip angles but also camber angles, so the regression equation for  $F_y$  on the contact length ratio was corrected for camber. The author suggested a compensation method based on the fact that the deflection length ( $\overline{AE}$  in Fig. 2-10) on the longer contact length side ( $\overline{BD}$  in Fig. 2-10) becomes longer as well when camber angle increases, which is contrary to the case as slip angle increases. Fig. 2-11 shows these features conceptually.

Estimation of slip angles and lateral forces were also tried in [39] and [45], respectively using similar concept as [37]. Fig. 2-12 shows the relationship between slip angle and contact ratio indicating that this method can estimate slip angles up to three degrees [39]. In [45], authors used not only contact length difference between inner and outer length but also average contact length as regressors to predict the lateral force. It is thought that the authors intended to include the contact patch area effect on the lateral force as well.

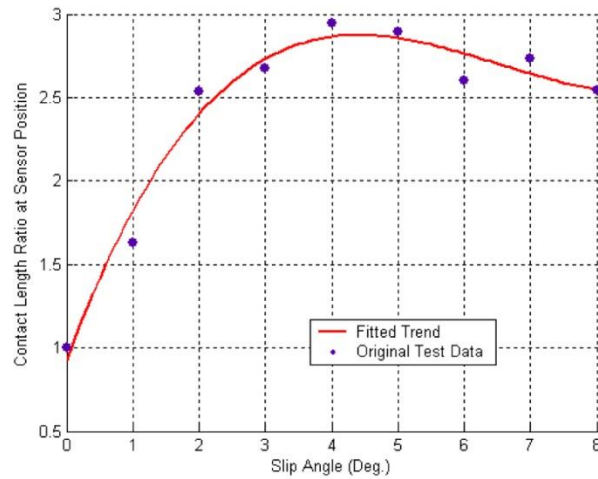


**Fig. 2-12 Contact length ratio at sensor position versus tire slip angle [39]**

Estimated contact lengths were also used for the prediction of an effective rolling radius by considering simple geometry of loaded tire [42, 47]. Once we know the effective radius, slip ratio can be obtained using Eq. (9).

$$slip\ ratio = 1 - \frac{\omega r_e}{\omega_f r_f} \quad (9)$$

where,  $r_e$  is the effective rolling radius of wheel, and  $\omega$  is angular velocity of the driven/braking wheel, which also can be estimated using the occurring rate of strain peaks. The absolute velocity of the vehicle can be calculated by multiplying the radius ( $r_f$ ) and the wheel velocity ( $\omega_f$ ) of the free rolling wheel.

#### 2.2.2.2 Signal amplitude as prediction parameter

Until now, estimation based on contact lengths has been addressed. This approach is the same concept as the one already discussed based on acceleration signal. However, considering forces are generated by the tread deformation and strain is nothing but the ratio of deformed length to undisturbed length, the amplitude of strain signals can be used for force and slip estimation directly. From this point of view, strain measurements could have the merit over acceleration measurements for force and slip estimations.

In [42], Matsuzaki, R. *et al.* adopted circumferential strain sensors to extract tire contact properties. In this study, the authors found that maximum compressive strains have positive, monotonous correlations with test loads. The authors also indicated that the max tensile strain was not appropriate as a regressor, because maximum tensile strains tended to be saturated or even decrease as test load increased further above a certain value of the load. This is because the bending deflection due to the test load becomes constant after total contact between the tire and the road is achieved.

Braking torque was also predicted in this research using the longitudinal strain history under braking, which is shown in Fig. 2-13, where F and T means wheel load and braking torque respectively. Under braking, the tread compression becomes higher just after contact ( $\epsilon_b$ ) than that before contact ( $\epsilon_f$ ) since an accompanied frictional stress, which is roughly symmetric with respect to the center of the contact patch, is added to the stress induced by the vertical load.

The author suggested a synthetic parameter named 'compressive strain ratio',  $r_{fb}$ , to characterize this shape, which is defined as

$$r_{fb} = \frac{\varepsilon_f + \varepsilon_p}{\varepsilon_b + \varepsilon_p} \quad (10)$$

where,  $\varepsilon_p$  is the strain due to tire inflation pressure. This parameter predicted braking torques successfully based on FEM simulation.

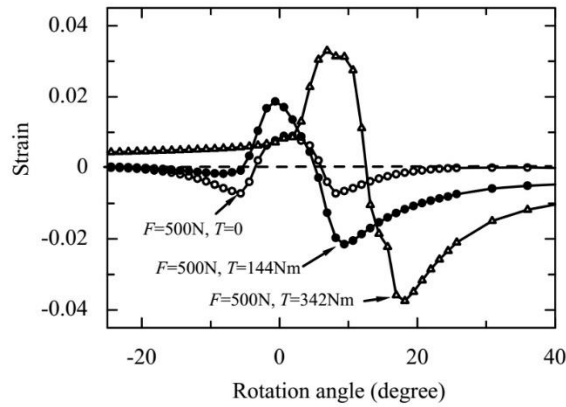


**Fig. 2-13 Strain distribution when braking torque is applied at 0, 144 and 342 Nm. Wheel load  $F_w$  is set to 500 N [42]**

Yang, X. *et al.* adopted a similar concept as in [42] for the longitudinal force estimation [41]. In their work, an FEA tire model was developed to simulate the axial (or lateral) strain at the inner wall of tire tread. Based on the simulation model, an estimation algorithm for tire parameters were suggested. Fig. 2-14 shows the simulation results for axial strains when traction or braking is applied to the tire.

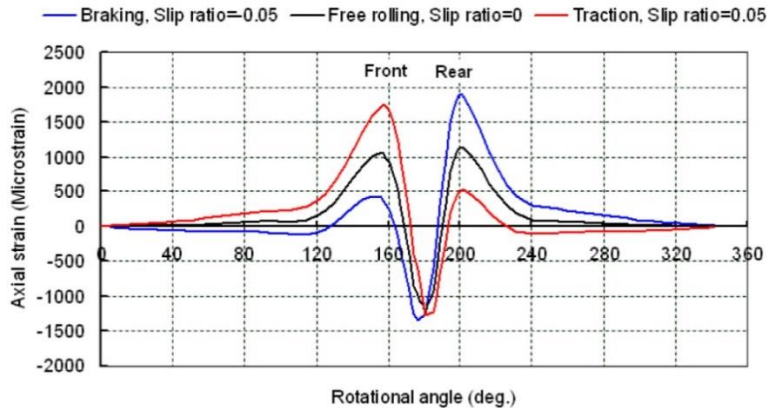


**Fig. 2-14 Axial strain waveform under tire braking, free rolling and traction from FEA [41]**

In the axial strain, there are generally two successive tensile peaks at the leading and trailing edges of contact. They noticed that these two peaks change in a typical way when the tire was subjected to longitudinal forces. They defined the strain peak ratio, i.e., the ratio between the first peak to second one and curve-fitted it to the longitudinal force with a 3<sup>rd</sup> order polynomial regression equation. As to the vertical load estimation, the average of two successive tensile peaks was used as regressor. For the lateral force estimation, two strain measurements at different tread positions, i.e., at the inner and outer contact points are used. The ratio between tensile peaks of measured strains were used as regressors. In their previous work, the vertical load was estimated using the circumferential strain tensile peak instead of the axial direction [39].

#### *2.2.2.3 Integral/Derivative of signal as prediction parameter*

Strain rates have been used to estimate contact lengths as we saw previously, but they can be used for slip angle estimation directly without introducing contact lengths as was done by Go Nagaya in [43]. In this patent, more than one paired circumferential strain gages were attached along the transversal direction. When slip angles were applied, the tread ring in the contact was bent into the direction of road running viewed from the tire. At the leading edge, the tread ring deflection in the outer contact part becomes greater due to the applied slip angle. This means the strain rate in the outer part should be faster than the inner part at the beginning of contact, because the tread element in the outer part travels more distance than inner part during the same period as shown in Fig. 2-15. The ratio of the strain peak rate at inner ( $V_{f1}$ ) to that at outer ( $V_{f2}$ ) at the leading edge of the contact patch had a linear relationship with slip angle, so the inventor used this parameter for the slip angle estimation. This method is differentiated from the estimations using contact length ratios in the point that it uses only the first positive peak of the strain signal. A good correlation was obtained from indoor and outdoor tests using this algorithm and this algorithm worked for the relatively broad range of slip angles (0~7.5 degree).

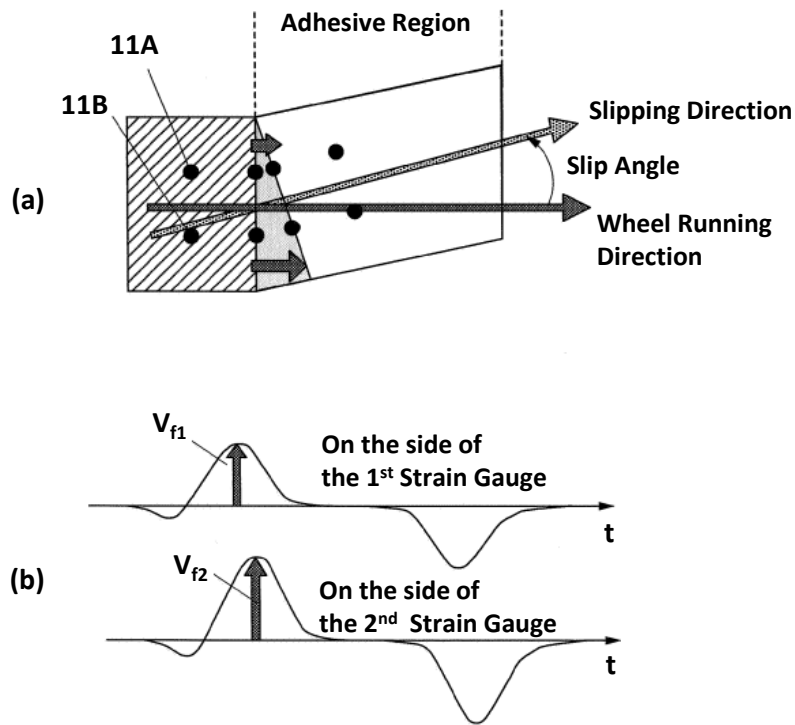


**Fig. 2-15 Relationship between deformation of tread ring and deformation speed wave form at the time of entering in the leading edge [43]**

This algorithm has the merit over the slip angle estimation based on contact length because it can minimize the noise effects arising from road surfaces. Since the slope of correlation equation also depends on the test load, its effect needs to be corrected. The inventor noticed that the slope of the correlation equation was lineally changing along test loads, and test loads was estimated based on average contact lengths similar to other works. In this way, load effects on correlation equations were corrected. Also, a pair of extra strain gages are attached to the inner linear corresponding inner and outer tread shoulders to correct the effect of camber angles on slip angle estimations. The author found that the ratio of maximum tension at inner shoulder to that of outer shoulder mainly depended on the applied camber angles. In this way, the inventor suggested the robust algorithm for the slip angle estimation, which estimated slip angles up to the relatively high value under various wheel loads and camber angles.

Only a few researchers have used integrals of strain to estimate tire dynamic characteristics. Matsuzaki, R. *et al.* improved his previous research results [42, 47] by developing the force estimation algorithm, which predicted frictional forces and test loads from circumferential strain signals only [44].

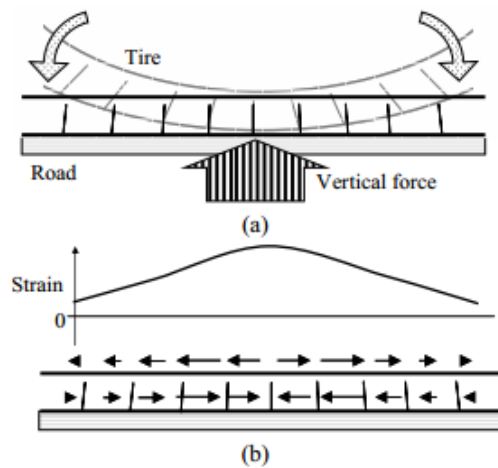


**Fig. 2-16 Cross-sectional deformation and strain distribution of a tire derived from a vertical load: (a) applied load, (b) strain distribution [44]**

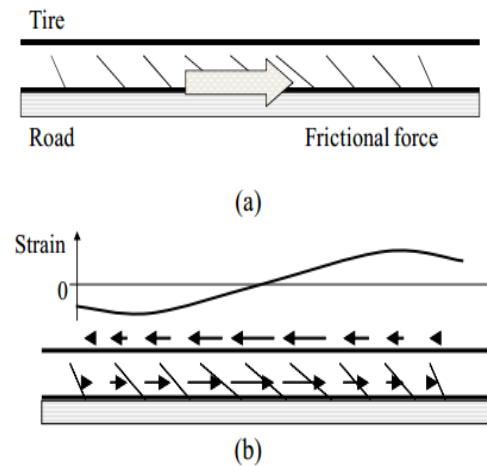


**Fig. 2-17 Cross-sectional deformation and strain distribution of tire derived from the kinetic frictional force: (a) the applied load, (b) the strain distribution [44]**

They introduced a traditional model for the contact strain distribution when braking or acceleration torques are applied to the tire. The authors noticed that the shape of the circumferential stress distribution ( $\epsilon_{ver}$ ) is comprised of three strain components;

strain due to vertical load ( $\epsilon_{ver}$ ), strain due to traction (braking/accelerating) force ( $\epsilon_{fri}$ ) and strain due to flattening force ( $\epsilon_{flat}$ ) (Fig. 2-18).

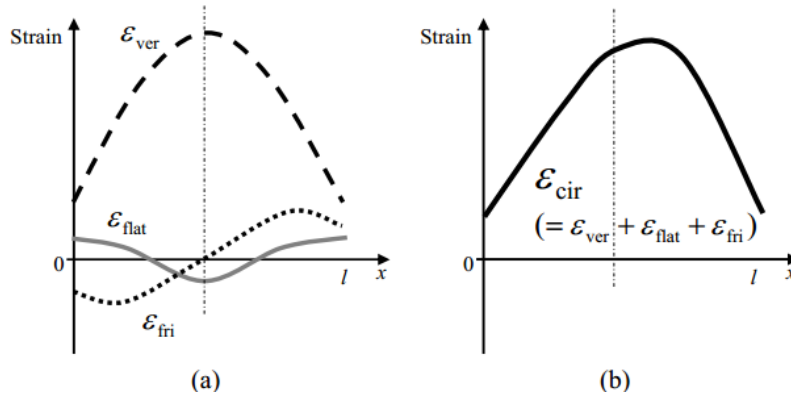


**Fig. 2-18 Strain components and total strain of the circumferential strain of the interior surface of a tire: (a) the strain components (b) the total strain [44]**

$\epsilon_{flat}$  arises because a frictional surface makes the tread element of the loaded tire stretch in the contact plane. However, the authors neglected this strain component because it is much smaller than the other components. The stress distribution along the contact length due to the test load is symmetric with respect to the line perpendicular to the contact patch passing through the contact center Fig. 2-16 whereas the stress distribution due to the braking force is symmetric with respect to the contact center point; in other words, there are compressive stresses in the front of contact patch and tensile stress in the rear, which have almost same distribution shapes with different signs (plus for tension and minus for compression when braking) (Fig. 2-17).

Therefore, integrating the circumferential strain along the contact patch ( $\epsilon_{ver}$ ) can cancel out the frictional component, and this integral can be representative of the vertical deformation of the tread ring due to the applied vertical load. This integral, named as  $E_{vertical}$ , can be used for the test load estimation. Meanwhile, the frictional stress distribution was also obtained using the line-symmetry of  $\epsilon_{ver}$  and the point-symmetry of  $\epsilon_{fri}$  as given in Eq. (11).

$$\begin{aligned}
\varepsilon_{cir} \left( \xi + \frac{l}{2} \right) - \varepsilon_{cir} \left( -\xi + \frac{l}{2} \right) \\
= \left\{ \varepsilon_{ver} \left( \xi + \frac{l}{2} \right) + \varepsilon_{fri} \left( \xi + \frac{l}{2} \right) \right\} \\
- \left\{ \varepsilon_{ver} \left( -\xi + \frac{l}{2} \right) + \varepsilon_{fri} \left( -\xi + \frac{l}{2} \right) \right\} = 2\varepsilon_{fri} \left( \xi + \frac{l}{2} \right)
\end{aligned} \tag{11}$$

where  $l$  is the estimated contact at center length obtained in the same way as [37] and  $\xi$  is a certain location on  $l$ . Similar to vertical estimation parameter ( $E_{vertical}$ ), the frictional force estimation parameter ( $E_{friction}$ ) was obtained through the integration of  $\varepsilon_{fri}$  as given in Eq. (12).

$$E_{friction} = l \int_0^{\frac{l}{2}} |\varepsilon_{fri}(x)| dx \tag{12}$$

Validation was done based on FEM simulations and this estimation method predicted the frictional forces and vertical loads under various wheel loads and braking torques with sufficient accuracy.

As presented in the author's previous work [42], the tensile peak value of a circumferential strain is inadequate for the load estimation but the integration of tensile strains over the contact length seems promising in this work indicating that the width of the tensile strain over contact region is proportional to the test load.

#### 2.2.2.4 Other methods

Throughout this literature review, it is concluded that strain signals in the contact patch has a high potential to estimate tire characteristics like wheel forces and slip quantities. Therefore, if we predict the strain signals during various driving maneuvers, we can gain insight into tire dynamics during driving.

S. KIM *et al.* predicted the lateral strain signals as a function of driving conditions such as wheel loads and vehicle speeds [46]. They characterized axial strain signals and its time derivative, i.e., strain rate, as 'N' or 'M' shape-curves using piece-wise polynomial

curve fitting models and extracted characteristic parameters of these curve shapes (Fig. 2-19).

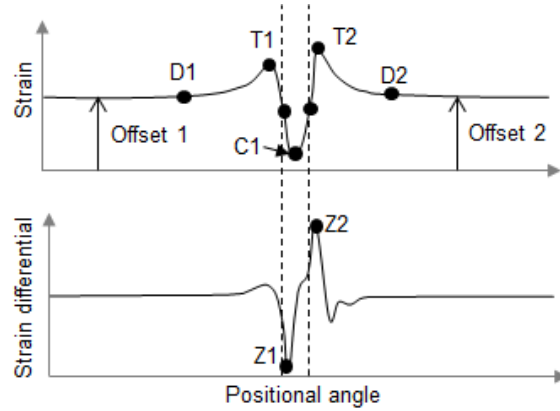


**Fig. 2-19 Standardized shape of tire strain and strain differential and decisive parameters (dots) representing the overall strain shape. Adapted from S. J. Kim et al., Development of a tire model based on an analysis of tire strain obtained by an intelligent tire system[46], © 2015 KSAE Publishing.**

The shape of the lateral strain curve was featured with characteristic parameters,  $D_1$ ,  $D_2$ ,  $C_1$ ,  $T_1$ ,  $T_2$ , which are corresponding offsets, compressive peak and tensile peaks, respectively. The strain differential was characterized with plus and minus peaks ( $Z_1$ ,  $Z_2$ ) representing the front and rear contact edges. Among these parameters,  $Z_1$ ,  $Z_2$ , were estimated using the force balancing equation for the vertical force ( $F_z$ ), as follows:

$$F_z = pbv\Delta t = pb \frac{2\pi r \Delta t}{t_{cycle}} \rightarrow \frac{\Delta t}{t_{cycle}} = \frac{F_z}{2P\pi \cdot br} \quad (13)$$

where  $p$ ,  $b$ ,  $r$ ,  $v$  are contact pressure, contact width, rolling radius, and rolling speed, respectively.  $t_{cycle}$  is the time for one complete rotation of the tire and  $\Delta t$  is a travel time of tread elements crossing over the total contact length, which is representative of  $\overline{z_1 z_2}$ . To predict  $\Delta t$ ,  $b \cdot r$  in Eq. (13) should be determined in advance for various combinations of test loads and speeds. Based on indoor test results, regression equations for  $b \cdot r$  was formulated as 2<sup>nd</sup> order polynomial in terms of  $v$  and  $F_z$ . A neural network model was employed to predict remaining parameters ( $C_1$ ,  $D_1$ ,  $D_2$ ,  $T_1$ ,  $T_2$ ). Authors claimed that this model can be used in HILLS systems to develop advanced vehicle control

algorithms based on the intelligent tire concept, saving time and cost. However, excluding the slip quantities such as slip angle or slip ratio from the estimation process makes this model limited in real applications.

Most research which is based on acceleration or strain data have focused on measurements at the innerliner on the tread, because this point is close to the contact avoiding durability issues. However, the inventor of the patent [14, 48] concluded that the strains at the sidewall could estimate the wheel forces best after investigating capabilities for wheel force estimations with various strain measurements at different positions of the tire: center tread, shoulder tread, bead, and sidewall. Furthermore, he suggested that shear strains at the sidewall were closely linked with longitudinal forces while the radial and circumferential strains at the sidewall were correlated well with lateral and vertical forces, respectively. The inventor also developed a magnetic strain gage comprising magnetic and magneto metric sensors. To capture the strains in different directions on the sidewall, the inventor proposed the special sensor arrays comprising at least three sensors around the sidewall as illustrated in Fig. 2-20. In this application, the direction of sensors are inclined at a preferred angle  $\beta$  with respect to the tire radial direction.

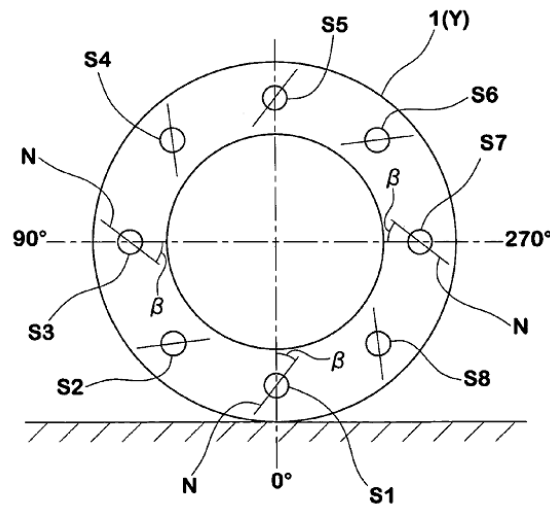


**Fig. 2-20 Strain sensor arrangement[14]**

For prediction of wheel forces in x-,y-,z-directions using sidewall strain measurements, the inventor offered the following correlation equations

$$t_i \equiv A_i * F_x + B_i * F_y + C_i * F_z \quad (14)$$

where  $t_i$  is the tire strain measured at different measuring points  $i$  and  $A_i, B_i, C_i$  are regression coefficients at corresponding positions.

Thus, by solving these equations simultaneously, wheel forces in each direction were obtained.

Most of the literature for contact force estimation based on strain measurements tried to directly link strain measurement to contact forces using simple regression equations obtained from experimental data. However, considering well-defined theoretical tire models [49-51] which define the contact force based on deformations of tread ring and contact patch rather than strains, it is worth trying to acquire the deformations from strain measurements. In this way, we can take advantage of well-established existing tire models and can identify more useful tire characteristics from strain signals.

### 2.2.3 Estimation based on global deflection measurement

As it is mentioned in 2.1.2, global deflections can be generally measured with optical sensors, and their measurements were highly promising for wheel force estimations as confirmed in APOLLO project [3].

A.J. Tuononen developed an optical tire sensor in EC-project, FRICTIO@N [52] and estimated the wheel loads and lateral forces [17]. The sensing system comprised of a two-dimensional position sensitive detector (PSD) attached to the rim, light emitting diode (LED) installed on the innerliner of the tire and a Plano-Convex (PCS) lens installed just before the PSD sensor. The light from the LED was focused through the PCS lens to the PSD which generated 4 channel photo currents varying along the location of LED. With a

transformation algorithm given by sensor manufacturer,  $x$ ,  $y$ ,  $z$  locations were calculated from 4 channel photo currents. Some results are shown in Fig. 21 and Fig. 22.

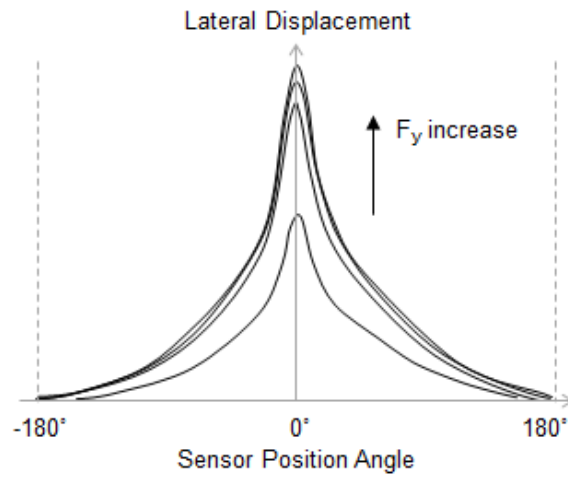


**Fig. 2-21 Lateral displacement of LED at different slip angles. Adapted from A. J. Tuononen, Optical position detection to measure tyre carcass deflections [17], © 2008 Taylor & Francis Publishing.**

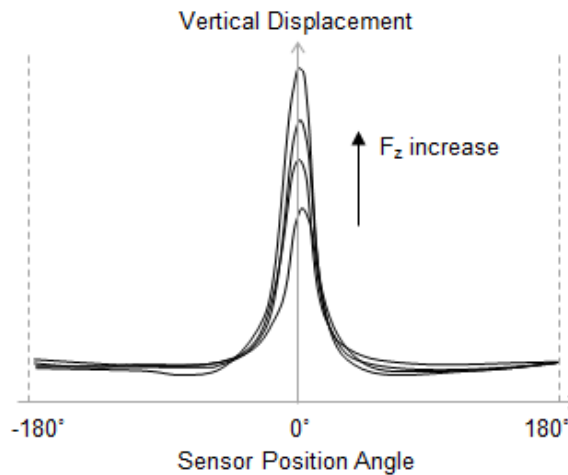


**Fig. 2-22 Vertical displacement of LED. Adapted from A. J. Tuononen, Optical position detection to measure tyre carcass deflections [17], © 2008 Taylor & Francis Publishing.**

The measured lateral and longitudinal deflections around the tire circumference in this way showed physically reasonable shapes (Fig. 2-21), but the vertical deflection curve was too narrow (Fig. 2-22) due to the error from the angular movement of the LED during the one complete rotation of the wheel, which had a non-negligible effect on the

transformation algorithm for vertical deflections. Nevertheless, the peak value of vertical deflection was not distorted by this effect and it was shown that this peak value was promising for  $F_z$  estimations

Simple integrations for the lateral displacement ( $y$ ) and vertical deflection ( $z-z_0$ ) used for the prediction of wheel vertical and lateral forces like Eq. (15) ~ Eq. (16), where  $z$  is the vertical deflection and  $z_0$  is  $z$  value in unloaded situation. Prediction result showed good agreements with  $F_z$  and  $F_y$  measured on the indoor test rig. Note that stiffness constants,  $k_{Fz}$ ,  $k_{Fy}$  are function of the inflation pressure and are not traditional tire stiffness.

$$F_z = k_{Fz} \int_{-180^\circ}^{180^\circ} (z - z_0) d\varphi \quad (15)$$

$$F_y = k_{Fy} \int_{-180^\circ}^{180^\circ} y d\varphi \quad (16)$$

He expanded his work to include real time estimations of wheel loads for a truck [18]. For the purpose of real time estimations, the algorithms in continuous integral form were modified to discretized form. For the estimation of vertical forces, a longitudinal signal amplitude,  $x_{gap}$  was implemented.

To correct the longitudinal force influence on  $x_{gap}$ , the correlation equation included the digital integral of longitudinal deflection,  $\bar{x}$ , which was a regressor for longitudinal force estimations. The regression equations for  $F_x$  and  $F_z$  are shown in Eq. (17) and Eq. (18) respectively.

$$F_x = \bar{x}c_{x,gain} + c_{x,offset} \quad (17)$$

$$F_z = x_{gap}^2 c_{z,parabolic} + x_{gap} c_{z,gain} + c_{z,offset} + [\bar{x} c_{z,gain} + c_{z,offset}] \quad (18)$$

$F_x$  was obtained through a linear equation of  $\bar{x}$  with corresponding regression coefficients ( $c_{x,gain}$ ,  $c_{x,offset}$ ) while  $F_z$  was expressed as a parabolic equation of  $x_{gap}$  and linear equation of  $\bar{x}$  with related coefficients ( $c_{z,parabolic}$ ,  $c_{z,gain}$ ,  $c_{z,offset}$ ).

Real time estimations during vehicle tests equipped with sensor tire were conducted resulting in good accuracies for the longitudinal and lateral force estimations, but under a heavy braking, the vertical force estimation was not reliable.

He also employed this sensor to identify vehicle hydroplaning [16, 20]. From the vehicle tests on the wet road surface with tires equipped with optical measurement system, he noticed that there were particular features in radial and longitudinal deflection curves when compared with those measured on the dry tarmac [16]. The first chart in Fig. 2-23 shows the mean value of the light density, which is representative of radial deflection along the circumferential wheel angle over 10 rotations.

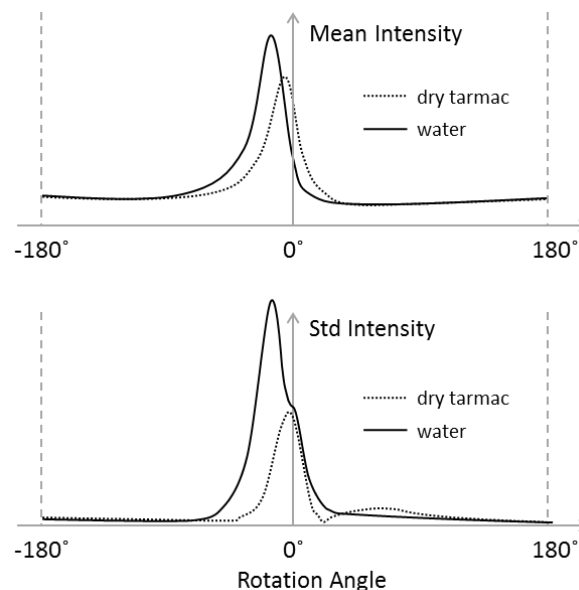


**Fig. 2-23 The mean intensity and standard deviation before and after driving into the water at 110 km/h. Adapted from A. Tuononen et al., Optical position detection sensor to measure tyre carcass deflections in aquaplaning [16], © 2008 Inderscience Enterprise Publishing.**

The radial deflection approaches its maximum value at around zero degree on the dry road, which corresponds to the center of contact. Meanwhile, on the wet road, the peak increases and shifts towards the front of contact patch. It is thought that the inertial effect of water entering the contact patch makes the tread ring deflect ahead of the contact. The second figure shows the standard deviation of intensity over the 10

rotations. On the wet road, this value is kept higher than on the dry tarmac until a certain point and then follows the same curve measured on the dry road. The author proposed that this point could be indicative of a starting point of a viscous contact zone, where the tread partly contacts the road. In this way, the hydroplaning could be identified with this deflection measurements. The author applied this method for the purpose of the real time detection of hydroplaning [20]. The estimation of hydroplaning occurrence for two different types of vehicles was conducted based on the peak shift of the intensity signals and it turned out this algorithm performed well regardless of wheel loads. These series of works conducted by the author are well arranged in his Ph.D. dissertation[19].

As it is presented in the previous section, G. Erdogan *et al.* designed the piezo-effect based sensor (Fig. 2-2) to measure the global deflection of tire and developed the estimation algorithm for lateral force and slip angle, which was finally used for the prediction of the friction coefficients in [22-25]. The slip angle estimation based on this algorithm showed good accuracy within the slip angle range of  $0\sim 5^\circ$  on the indoor test rig. The results of the friction prediction on the two road surfaces are promising providing reasonable friction values for different road surfaces and obtained friction coefficients are generally consistent over the different slip angles:  $1^\circ$ ,  $1.5^\circ$ ,  $2^\circ$ .

### **2.3 Chapter Summary and Discussion**

To identify meaningful characteristics of a loaded rolling tire, tire contact features and global deflections have been measured with different kinds of sensors by a diverse group of researchers. Measurements of accelerations and strains at the tread have been generally exploited to characterize contact features, while measurements of global deflections are usually used for tire force estimations.

For acceleration measurements, three axis MEMS type accelerometers are generally used due to their robustness and size. As to strain sensors, many different kinds of sensors have developed based on diverse measuring principles such as piezo effects, SAW generations, capacitive changes of tire, and magnetic induced Hall effects. These

diverse developments intend to optimize the strain sensors to be installed within/inside tires acquiring durability, wireless data transfers and powerless measurements.

When it comes to wheel force or slip estimations with accelerations or strains, identifying contact lengths have been the basic step for further estimation works. The peak to peak distances of these signals were interpreted into contact lengths and contact lengths at the center could be correlated to the wheel vertical forces [4, 22, 39, 45, 53]. The tire contact lengths at the intermediate portion between center and shoulder of tread were used to estimate slip angles, because they could be representative of distorted contact shapes when the tire is subjected to slip angles [4]. In some applications, a pair of sensors were installed symmetrically apart from the center line and the contact length ratio between inner and outer contact was correlated with the applied slip angles or lateral forces [37, 39-41, 45]. Usually slip angle estimation based on contact lengths are valid in the linear range, i.e., less than 4 degree of slip angles. Slip angle estimations based on the ratio of strain rates between inner and outer side of the contact region seems to cover a wider range of slip angles of around 8 degree [43].

In some research, measured signal peaks were correlated directly to the wheel forces without introducing contact length estimations. These sorts of algorithms were usually found in strain based applications [39, 41, 42], while there is only one application [28] with acceleration measurements among the reviewed literature, where the signal amplitudes were adopted as regressor for the slip angle estimation.

These reviewed algorithms are forms of simple regression equations based on the limited test data under specific test conditions So for robust estimations, it is required to find regressors which are insensitive to other parameters except the parameter of interest [4], or to develop compensation methods to correct the influence of other parameters e.g., camber angle effects on slip angle estimations [37, 43].

The local strains in the sidewall also turned out to be promising for force estimations providing another useful application of strain sensors [14].

Global deflections measured by means of optical sensors were integrated along the tire circumference to estimate the tire forces [17, 18]. Optical sensors have an

advantage of estimating wheel forces [3], but their application has been limited within research purposes because of the recalibration issue after hard braking and complexity in optical sensor-based devices. A series of works [16, 20] were done to capture the hydroplaning occurrence using an optical sensor highlighting its applications in tire research.

It was shown that the global deflections and local strains have been adopted for force estimations more often than accelerations because their physical quantities are closely linked to wheel forces. However, it has been revealed that accelerations are prospective for other applications besides force estimation. Some works exploited acceleration measurements for the special applications such as road differentiations [4, 36, 37], and characterizations of contact patch on the wet road condition [26, 27] by investigating their signal characteristics, which are obtained through appropriate signal processing for each application.

Most of the estimation algorithms presented here depend on simple regression equations without considering much of the complexities of tire dynamics. Some methods just consider the relationship between signal features and tire dynamic characteristics as the black box and employed statistical methods to predict interesting parameters [30, 46].

Some works actively introduced physical models into the estimation process acquiring more physical meanings from the sensor measurements. In the series of works [22-25, 31-33], simple carcass lateral deflection model and brush type tire model are employed for lateral force and friction estimations. In [33], the kinematic model for rolling wheels in the longitudinal direction was developed for understanding of acceleration signals, and was implemented into the process of double integral of acceleration. In [44], the strain distributions in the contact patch under braking was examined based on the classic theory of tire contact, and then the braking forces and test loads were estimated from circumferential strain signals only.

Although, the final goal of these series of works based on physical models is to estimate friction, more tire characteristics can be identified by adopting these sorts of

approaches. Fig. 2-24 illustrates two possible applications of intelligent tire technology; one is for advanced vehicle control (marked green), and the other is for the analysis of tire characteristics (marked blue).

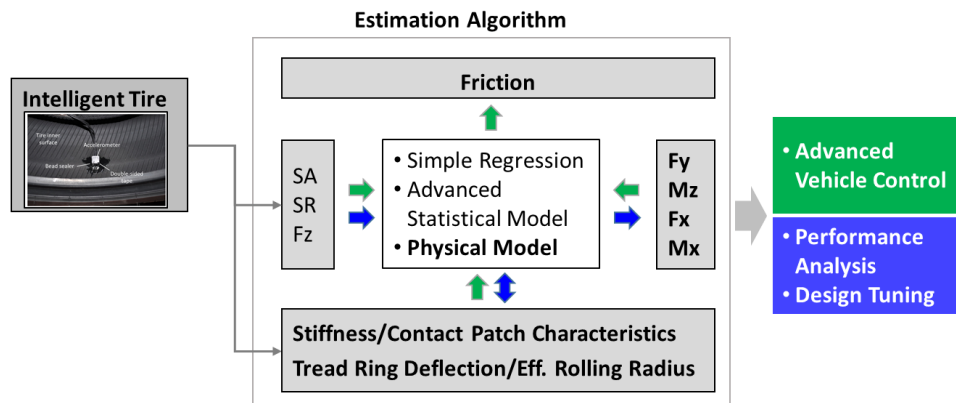


**Fig. 2-24 Possible applications with intelligent tire**

Applications for vehicle control are the main goal of intelligent tire and numerous works have been done in this area whereas applications for the analysis of tire characteristics have been rarely found until now.

Identification of tire dynamic features using intelligent tire is promising because this method can be applied to the real world; the tire characteristics under real driving conditions on the real road. This method can give tire characteristics which cannot be identified on indoor test rigs and can be more closely related to the real vehicle performance. Identifying wet contact patch or occurrence of hydroplaning based on intelligent tire presented earlier show good application examples of intelligent tire for the purpose of tire analysis.

For the purpose of friction estimation, predicting the accurate wheel forces is most important to get the friction coefficient regardless of the estimation methodology. However, if we want to focus on identifying the dynamic characteristics of tire for the analysis of tire characteristics, it is also important to apply well-established physical concepts to analyze sensor measurements. In this way, it is expected to extract crucial

tire characteristics like contact features, stiffness and deformation, which are deeply linked with tire forces and moments, and finally with vehicle performances. This goal can be achieved by employing previously developed tire models or by developing new tire models which actively exploit sensor signals. When choosing or developing tire models for this purpose, their relevance to sensor measurements from the intelligent tire should be carefully investigated first. As for tire models that can be associated with accelerations or global deflections, tire models that can deliver carcass deformation are desirable. Potential existing tire models are TREAD Sim model and stretched ring model [38]. As for tire models associated with strain measurements, strain or stress distributions should be delivered in tire models. In this case, Fiala model [49] and flexible ring models [50, 51], [54] seem promising. Yi, Jingang *et al.* have shown a good example of how to introduce the flexible beam model to develop the strain based intelligent tire [55, 56].

Moreover, advanced tire models can be developed by means of adopting a multiple sensor network. For example, using accelerometers and strain sensors together, we can investigate the lateral deflection and strain distributions in the contact patch. Tire models utilizing both properties can be proposed resulting in identifying more realistic features of tires.

Through this comprehensive review, the authors of this paper have found the potential of the intelligent tire as the analysis tool for tire performance and will conduct research to develop these tools based on the fusion of tire models with intelligent tires.

### 3 STRAIN BASED INTELLIGENT TIRE AND EXPERIMENTATION

In this section, the intelligent tire system for this research will be introduced first. Strain gages are embedded inside the tire near the contact length to catch the contact features of the loaded rolling tire. Sensor embedded tires were tested on the flat belt type test rig in the laboratory. Tire force and moment were measured under diverse test condition while strains were being measured at the same time. Details on the measurement and experimentation are delivered after the explanation the intelligent tire system. Finally, the post-processing of the strain measurement will be followed, which will provide basic parameters for further estimations of tire-road contact features.

#### 3.1 Types and the Principle of Strain Gage Measurement

The types and operation principle of strain gages will be briefly explained in this section.

If an external tensile force or compressive force applied to tire increases or decreases, the resistance of the sensing part inside the sensor proportionally increases or decreases. If the resistance  $R$  changes by  $\Delta R$  because of strain  $\varepsilon$ , the following equation can be written:

$$\frac{\Delta R}{R} = K_s \varepsilon \quad (19)$$

where,  $K_s$  is a gage factor, expressing the sensitivity coefficient of the strain gage. Thus, by measuring the change in  $R$  of the element inside the sensor, the strain can be measured.

Types of strain gages are classified into foil strain gages, wire strain gages, semiconductor strain gages, etc. In this study, foil strain gages were used and their structure is shown in Fig. 3-1. The foil strain gage has a metal foil on the electric insulator of a thin resin, and gage leads are attached to this foil, as shown in the figure. The strain

gauge is bonded to the measuring object (tire innerliner in this study) with a dedicated adhesive. Strain occurring on the measuring site is transferred to the strain sensing element via adhesive and the resin base. For accurate measurement, the strain gauge and adhesive should be compatible with the measuring material and operating conditions such as temperature, etc.

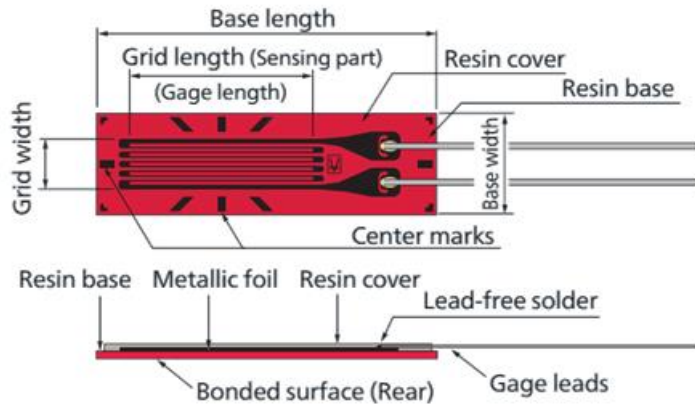


**Fig. 3-1** *Structer of a foil strain gage*

Strain initiated resistance change is extremely small. Thus, for strain measurements, a Wheatstone bridge is formed to convert the resistance change to a voltage change. Referring to Fig. 3-2, if resistances ( $\Omega$ ) are  $R_1$ ,  $R_2$ ,  $R_3$  and  $R_4$  and the bridge voltage ( $V$ ) is  $E$ , If  $R_1 = R_2 = R_3 = R_4 = R$  in the initial condition and using the fact that  $R$  is extremely lager than  $\Delta R$ , the output voltage  $e_0$  can be calculated by Eq. (20).

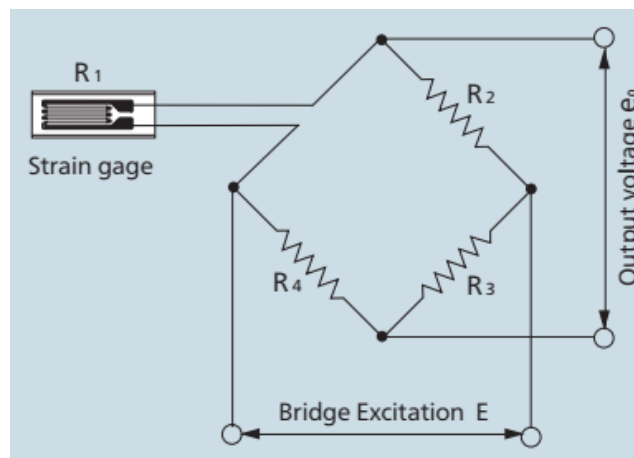


**Fig. 3-2** *Quarter-bridge system*

$$e_0 = \frac{R_1 R_3 - R_2 R_4}{(R_1 + R_2)(R_3 + R_4)} E \approx \frac{1}{4} \frac{\Delta R}{R} E = \frac{1}{4} K_S \varepsilon \quad (20)$$

Thus, an output voltage that is proportional to a change in resistance, i.e. a change in strain, can be measured. This output voltage must be amplified.

### 3.2 Sensor Arrangement inside Test Tire

In this intelligent tire system, five equally spaced strain gages were attached to the tire innerliner in the axial direction. All of them were oriented in the wheel heading direction to measure circumferential strains. One of the five strain gages should be located at the equator line, because it was revealed that the strain measured at the center can be used to estimate basic tire parameters, especially related to in-plane dynamics of tire. Other strain gages attached at off-center positions. One pair of them are located at inner and outer part over intermediate tread portion, equally spaced from the center line. Another pair are located over shoulder tread portion. Sensor measurements at off-centers are expected to provide information on tire lateral dynamics, i.e., out-of-plane dynamics. Fig. 3-3 illustrates the sensor arrangement and their attachment. The tire shown has 5 ribs and sensors are positioned over the tread ribs not grooves, because tread ribs contact the road surface directly and sensors at these positions are believed to measure definite features related to tire-road contact. In this intelligent tire system shown here, the distance between sensors is 30 mm.

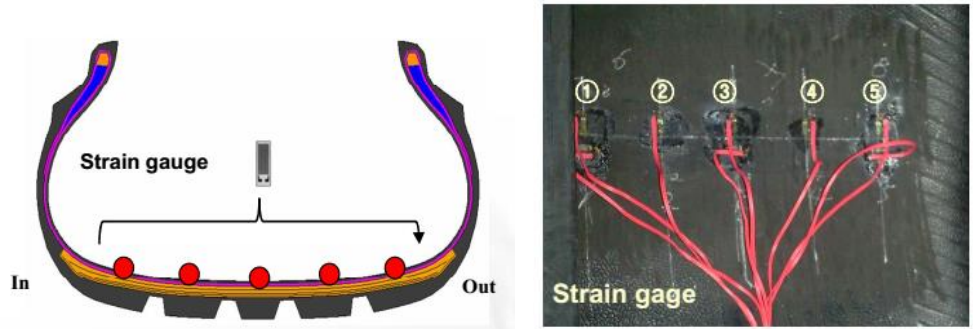


**Fig. 3-3 Intelligent tire system with five strain gage: sensor arrangement in the cross section of tire (left) and sensor attachment on the inner liner.**

Measured signals are wireless transferred to receivers outside the tire using a specially developed transmitter as shown Fig. 3-4.

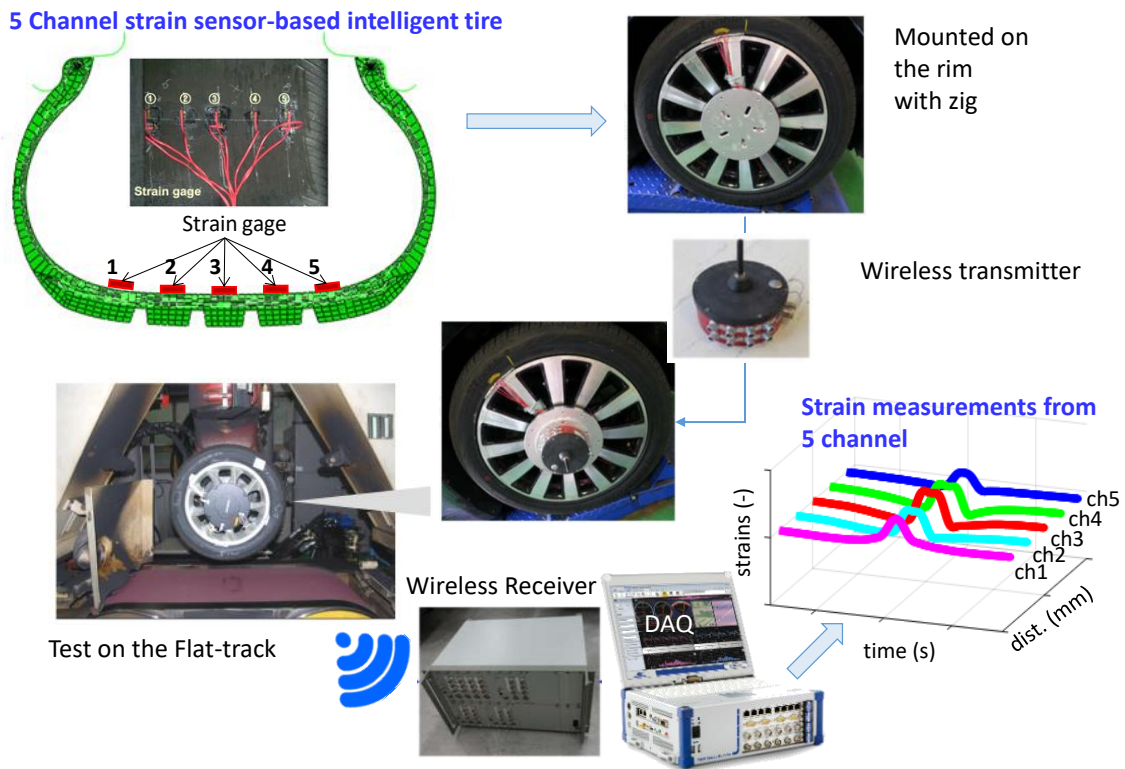


**Fig. 3-4 Hardware setup for intelligent tire system**

### 3.3 Test Information

To apply diverse test driving conditions to the intelligent tire and measure the tire force and moment at the same time, a flat belt type test rig named as Flat-Trac was used (Fig. 3-5). Intelligent tires were test on Flat-Trac under diverse combinations of test conditions like test load, slip angle, camber angle and slip ratio. During test run, strains were measured and sensor measurements were synchronized with the measurement of force transducer installed in Flat-Trac using trigger signals.



**Fig. 3-5 Flat-Trac test rig**

Fig. 3-6 shows typical examples of test conditions and measured forces corresponding to applied test conditions. The plots in the upper row shows applied slip angle time history and measured lateral forces subjected to 5 different test loads. Plots in the lower row are for the braking/acceleration test on Flat-Trace. The tire history of slip ratio for braking (blue line) and acceleration (green line) are plotted in the left chart and longitudinal forces corresponding each slip ratio are shown in the right chart.

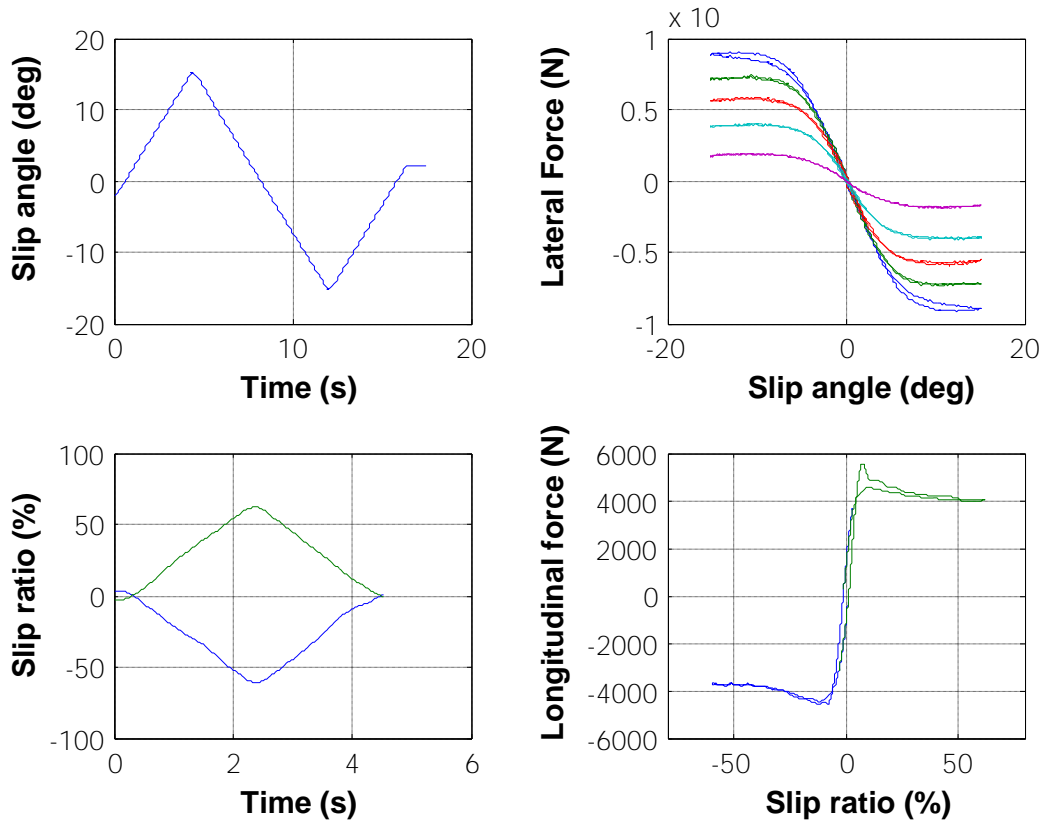


**Fig. 3-6 Examples of Flat-Trac test conditions and force measurements. Upper left is slip angle time history and upper right is corresponding lateral forces. Lower left is slip ratio time history and lower right is corresponding longitudinal forces.**

Two sets of tires in different size were tested under different test conditions as shown in Table 3-1 and Table 3-2 to develop to estimation methods presented over Chapter 3~4. The first test set in Table 3-1 for 235/55R19 tires was designed for cornering situation of the loaded rolling tire, which are not subjected to excessive slip angle. A slip angle was changed from  $-5^{\circ}$  to  $5^{\circ}$  under five different test loads, i.e., 25% to 175% of a reference test load. Based on this test set, test load and slip angle and their combed effects on the strain measurements will be explored and the estimation method for lateral force will be studied. Tests were done for three different tires in this test set, which have the same size sharing the same mold but have different belt constructions. The second test set in Table 3-2 includes the variation of camber angle during the cornering test for tire P235/60R18; three different camber angles were applied for each slip angle sweep test. From this test set, the camber angle effects on strain measurement and how to

include this effects into the lateral force estimation can be studied. Finally, pure braking and acceleration tests were conducted for the same tire; for acceleration, slip ratio increase from zero to 60% and decrease to zero again and for braking, it changed vice versa. Based on this test results, how strain measurements represent tire tractions will be examined and related parameters will be tried to estimate.

The inflation pressure was set to 2.3 bars for these test sets, which is the reference pressure set by the OE manufacturer. All experiments were done in the laboratory maintaining the inflation pressure kept at this reference pressure. Test speed, i.e., travel speed of rolling tire, was set to the same value of 65 km/h for all tests.

**Table 3-1 Flat-Trac test conditions for 235/55R19 tire (Test Set 1)**

Load	25%	62.50%	100%	137.50%	175%
SA	-2° → 5° → -5° → 2°				

**Table 3-2 Flat-Trac test conditions for P235/60R18 Tire (Test Set 2)**

Load	100%		
SA	-2° → 15° → -15° → 2°		
CA	0	-4°	4°
Load	100.0%		
SR	0% → 60% → 0%	0% → -60% → 0%	

To develop the identification methods for tire properties related to in-plane dynamics, free-rolling tests were done for a specific tire with strain measurements under various test conditions following the test design Table 3-3. Using the identification results, the lateral force estimation method was updated and validated with slip angle sweep test results for the same tire on Flat-Trac test machine.

**Table 3-3 Flat-Trac test conditions for P195/65R15 Tire (Test Set 3)**

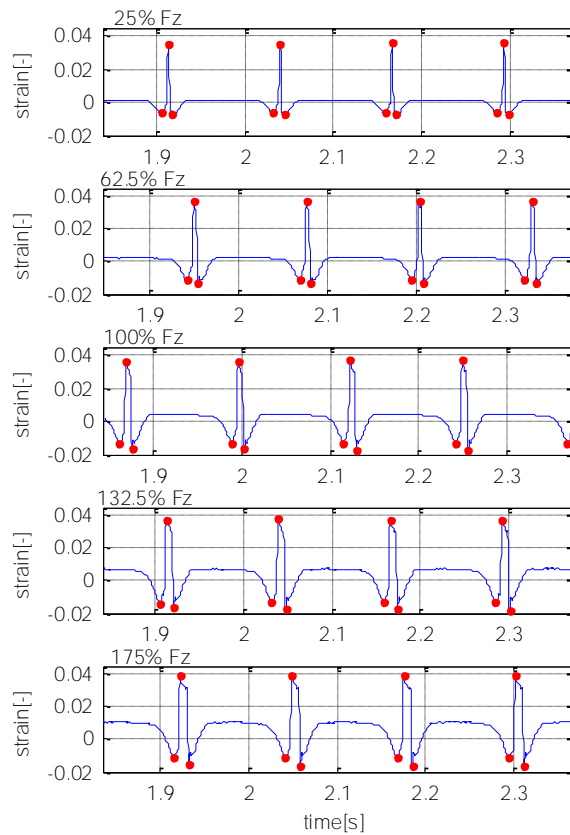
Test Item	Inflation Pressure (bar)	Load	Speed (km/h)	SA (°)
-----------	--------------------------	------	--------------	--------

Straight free-rolling	2.1	100% (4265.9N)	10, 30, 50, 70, 80, 100, 150	0
	2.5, 2.1, 1.7, 1.3	60, 100, 140%	65	0
Slip angle sweep	2.5, 2.1, 1.7, 1.3	60, 100, 140%	65	-2→5→-5→2

### 3.4 Data Processing

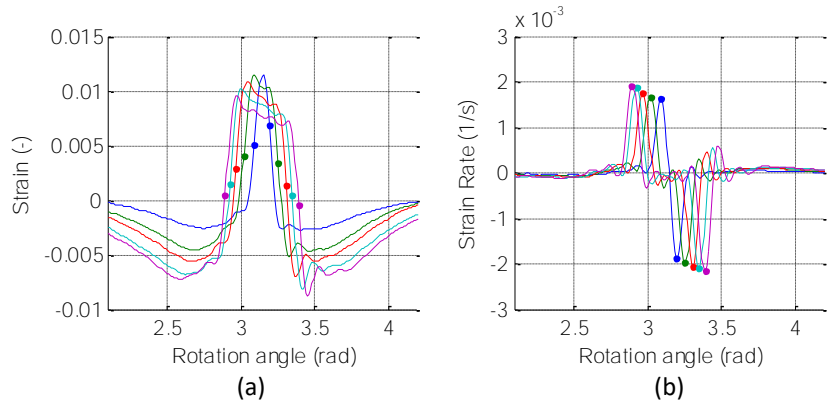
The measured raw signals from strain gage show wide range of frequencies. High frequency components above 1 kHz are usually generated by the vibration behavior of tires. This vibration can be caused by the stick-slip motion of the tread between tire and road surface and the direct excitation due to the road roughness. Thus, these high frequency components of signals can give information on the level of friction and the type of road surface as discussed in the literature review. (Refer to 2.2.1) However, this research focus on the estimation of overall tire contact force rather than frictional phenomena in micro scale. As discussed in the literature review, tire forces are usually identified with the peak information of strains and strain rates during the one rotation of tire. So, low pass filters with hundreds of Hz (200~400 Hz) are applied to the raw signals, which makes sure signals have predominant peak while preserving the information as much as possible.

Fig. 3-7 shows the strain time history of the straight rolling tire under different test loads after applying the low pass filter. Circumferential strains typically have two successive compressive peaks before and after the contact region and they can be used to identify one rotation of tire and wheel assembly. The peak identification algorithm was developed and maximum compressive and tension peaks were marked as solid circles in the graphs shown in Fig. 3-7.



**Fig. 3-7 Time history of circumferential strain under different test loads**

If the rotational speed of the wheel is measured, strain histories can be obtained as a function of rotational angle instead of time. When the wheel rolls without any slip at constant speeds, the rotational speed can be calculated by counting the number of rotations based on the strain measurement. This conversion is only possible when there is no longitudinal slips in the contact patch. This transformation is preferred to find the physical meaning of strain measurements based on theoretical tire models. Fig. 3-8 (a) shows strain measurements as a function of rotation angle for different test loads and strain rate, or time derivative of strain is shown in Fig. 3-8 (b). The peak to peak distance in the strain rate is the indicative of contact length as illustrated in Fig. 2-10.



**Fig. 3-8 Strain and strain rate over the rotation angle under different test loads.**

Peaks of strain rate and corresponding points in the strain were identified and marked as solid circles in both graphs. It is seen from the graphs that as test load increases, the contact length, i.e., peak to peak distance in the strain rate, also increases.

## 4 ESTIMATION OF TIRE-ROAD CONTACT FEATURES USING STRAIN-BASED INTELLIGENT TIRE

Tire-road contact features such as slippage and contact forces can be estimated by utilizing sensor measurements inside the tire. In this chapter, parameter estimations using simple or multivariable regressions were conducted and the brush type tire model was introduced to estimate lateral forces.

### 4.1 Estimation of tire-road contact features using statistical regressions

The features of strain measurements are directly used to estimate tire-road contact features without introducing tire models. Statistical regressions are generally used for this purpose. It is important to extract valid regressors usually which can be done considering simple contact mechanism between tire and road surface.

#### 4.1.1 Contact Length Estimation

The contact length is the primary parameter to be estimated because it is related closely to other parameters like contact forces and slip angles. As addressed in LITERATURE REVIEW (2.2.2.1), an estimation algorithm of contact length was proposed in [37] by Morinaga, H. *et al.*, which has been extensively adopted for contact feature estimations by other researchers.

Based on this method, contact lengths were estimated for test set 1 (Table 3-1) when slip angle is varied. Fig. 4-1 shows strains and their time derivatives (strain rate) in the right part of the figure when slip angle of -4 degree is applied under reference test load. Raw data of strain measurements were filtered through low pass filter and peaks are detected as presented in Fig. 4-1. The schematic view of a tire contact patch when a loaded rolling tire is subjected to negative slip angle is also drawn on the right part of Fig. 4-1 in the SAE coordinate system.  $v$  is wheel velocity vector and the direction  $x$  coincides with wheel heading direction. Slip angle is the angle between  $v$  and  $x$ . In this figure, the slip angle is negative and expressed as  $-\alpha$ . 'ch1' ~ 'ch5' indicate the locations of five strain

gages on the contact patch. At negative slip angles, the contact part on 'ch5' expected to undergo a larger deformation and resultantly, the longest contact length is observed on 'ch5' whereas the shortest length on 'ch1'

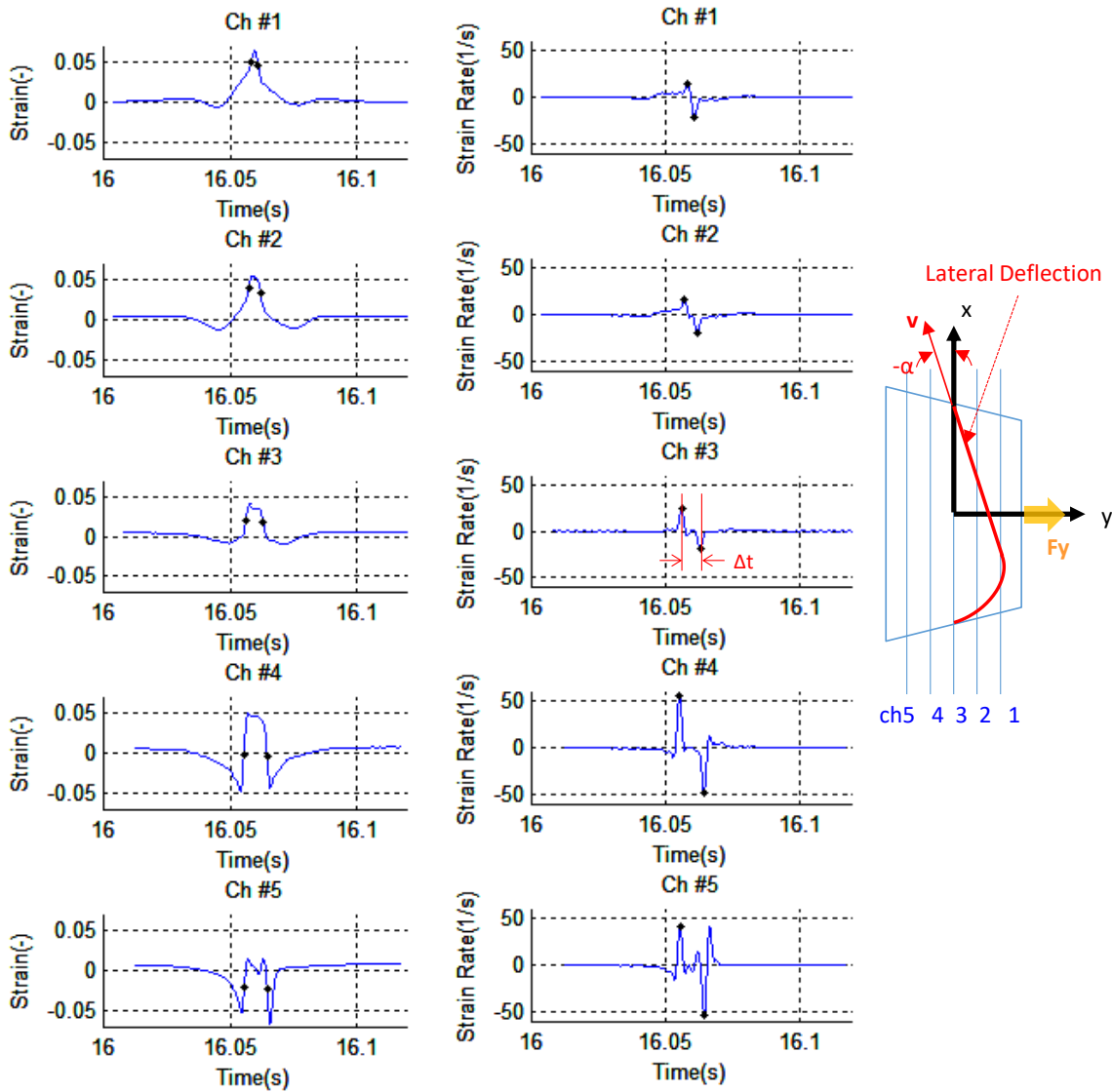


**Fig. 4-1 Strain measurements at  $-4^\circ$  slip angle and schematic view of contact patch**

The contact length at each channel can be estimated by multiplying peak-to-peak time ( $\Delta t$ ) and travel speed ( $|v|$ ) together. As we can expect,  $\Delta t$  becomes longer from channel 1 to channel 5. The results of the contact length estimation are shown in Fig. 4-2.

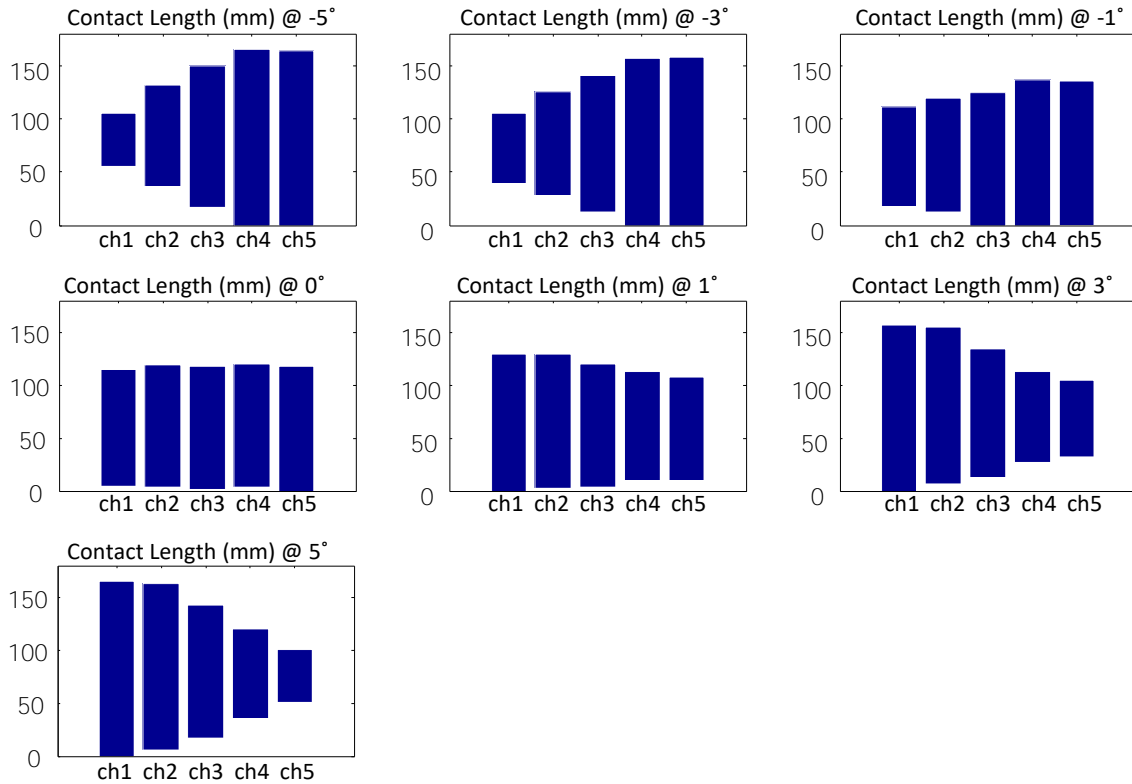


**Fig. 4-2 Estimated contact shapes for different slip angles at 100%  $F_z$**

The results show reasonable contact lengths on each channel when the tire is subjected to slip angle varying from -5 degrees to 5 degrees. From these results, the contact shape and contact area can also be roughly recognized. The contact shape and area under cornering are considered as crucial tire characteristics related to the handling performance of vehicle. Generally, larger contact areas and less distorted shapes under the same cornering condition are believed to contribute to the cornering stability. Considering measurements of the dynamic contact shape of tire in the real driving is very challenging, the intelligent tire with multi-sensors, like presented here, could serve as the alternative tool for tire engineers.

#### 4.1.2 Test Load Estimation

Usually, for the purpose of the friction estimation based on the intelligent tire, test load should be estimated first. In the previous works, test loads were estimated with contact lengths based on the fact that contact length tends to steadily increase as test load increases. However, to achieve robust predictions using the contact lengths, diverse condition effects on contact length such as slip angle and camber angle need to be included. In this research, slip angle effects on contact lengths were investigated. In the left of Fig. 4-3, estimated contact length for each channel is shown for 100% load and the range of applied slip angles. As expected from the previous results of contact length estimation, contact lengths for off-center locations vary considerably as slip angle changes. However, the contact length at the center is kept almost the same over the entire range of applied slip angle. The right chart shows the % standard deviation, which is % ratio of standard deviation of contact lengths to the average contact length as the slip angle varies. At the center (Ch3 in the chart), the contact length varies less than 2.5% (standard deviation). From this observation that the center contact length is insensitive to slip angle variations, it was chosen for test load estimation. Fig. 4-4 represents regression results between contact lengths at the center and the applied test loads; the left chart is the curve fitting results with 2<sup>nd</sup> polynomial equation and the right chart is the residual plot showing residuals at fitted values. Generally, center contact lengths can predict wheel vertical loads with a good precision over the whole operation conditions ( $R^2=0.995$ ), although the prediction quality declines slightly as the test load increase as revealed in the residual plot.

A similar approach was conducted in [4] by F. Braghin *et al.*, in which an accelerometer based intelligent tire was used to estimate contact lengths over various slip angles and camber angles. They also found that the center contact length was insensitive to the change of slip angles and camber angles suggesting it as a regressor for load estimations.

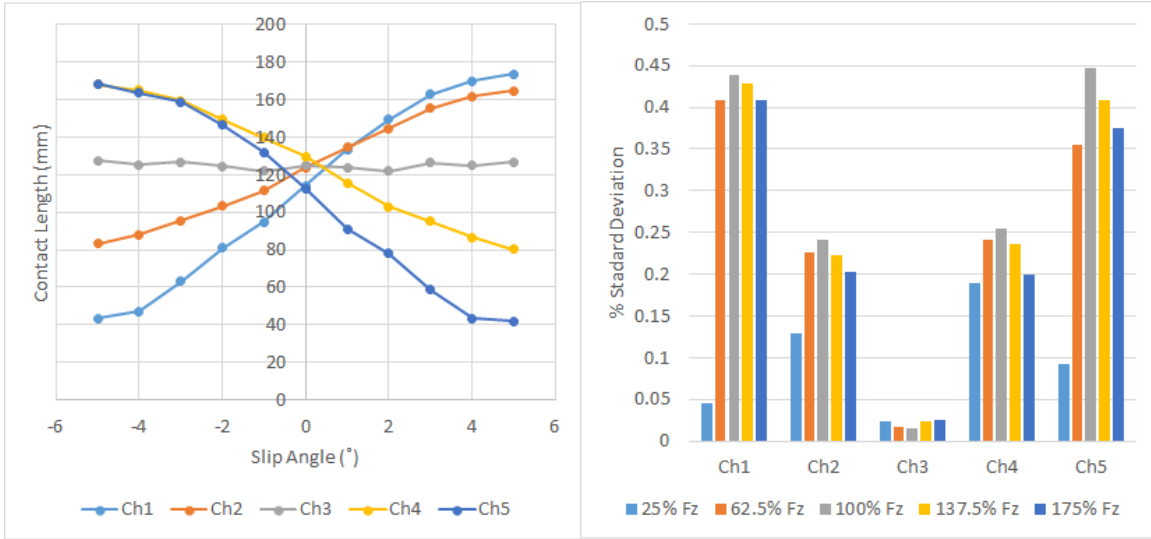


**Fig. 4-3 Contact lengths variation at different slip angles (left) and % standard deviations of contact lengths over various slip angles**

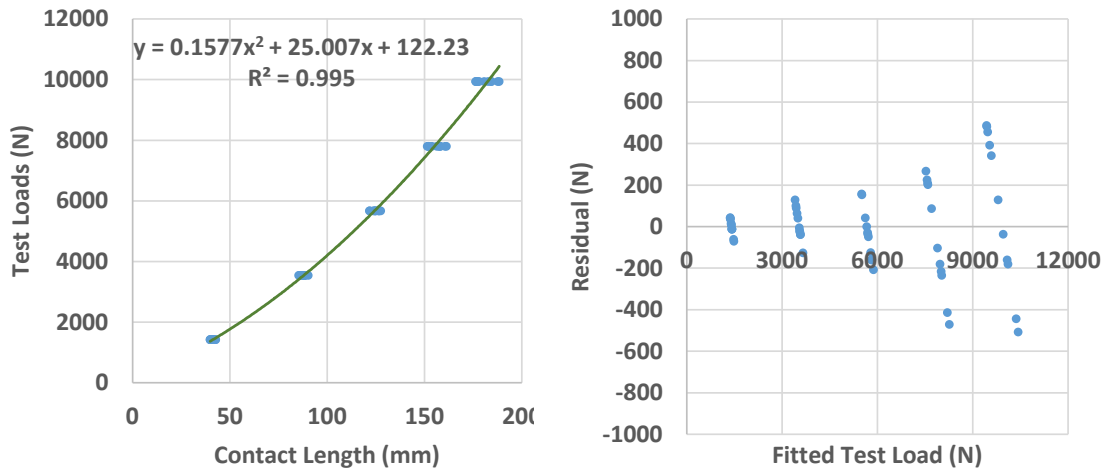


**Fig. 4-4 Regression results between contact lengths and test loads: curve-fitting plot (left) and residual-fit plot (right)**

#### 4.1.3 Slip Angle Estimation

Tire slip angle is one of the crucial variables for tire force generation which is also an input to the algorithm of vehicle stability programs. Thus, several researchers have tried to estimate slip angle using intelligent tire concept. Some researchers have utilized contact lengths estimated at various positions of contact patch; usually inner and outer

sections along the contact width. When the loaded rolling tire is subjected to slip angle, the contact patch is distorted into asymmetric trapezoid-like shape and the amount of asymmetry usually increases as slip angle increases as already shown in Fig. 4-2. Therefore, authors of [4, 37, 39] defined the ratio or difference between two contact lengths measured at inner and outer portions of the contact patch to characterize contact distortions of the cornering tire. However, these approaches were valid to estimate slip angles less than around  $4^\circ$  because, at above this slip angle, slip happens across the entire contact patch without distorting the contact patch further.

Improvement of slip angle estimations was made in the US patent [43] as addressed in the literature review (2.2.2.3). As illustrated in Fig. 2-15, the inventor of that patent suggested the ratio between strain rate peaks at inner side and outer side to cornering as the regressor ( $v_{f1}/v_{f2}$ ) to predict the slip angle. Same method was applied to the test results of test set 1. Strains measured at off-center position, i.e., channel 2 and 4, were used to get the suggested regressor and regression results shown in Fig. 4-5.

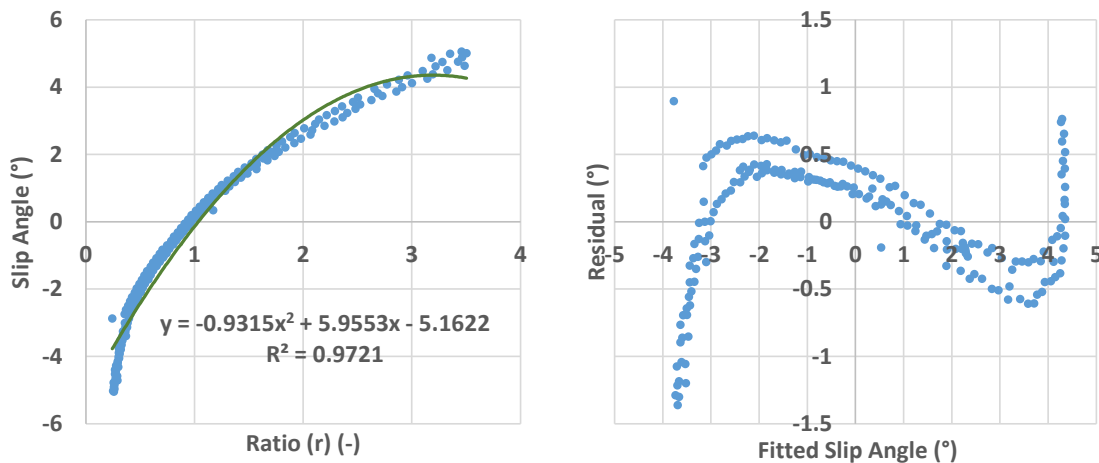


**Fig. 4-5 Regression results between in/out ratio of peak strain rate and slip angle: curve-fitting plot (left) and residual-fit plot (right)**

The left chart shows a positive-monotonous correlation, but it is nonlinear, so a quadratic polynomial was used as a regression model. The residual plot of this regression model shows recognizable patterns and lacks of fit especially at the highest slip angles,

which indicate the goodness of fit is not acceptable. More complex fitting models, e.g., higher order polynomials, are needed.

Since five strain measurements across the contact patch in the axial direction were used in this research, rather than using just two strain measurements, all the measurements were used. After close observations of the strain rate, ‘the slope of peak strain rates’ across the three measurement locations were chosen as the predictor for slip angle estimation. This parameter is illustrated in Fig. 4-6. The left shows the strain signals for channels 2, 3 and 4 and the right chart present their time derivatives. The slope of positive peak strain rates (marked as  $s$  in the chart) can be calculated if we know the distance between sensors. The regression result between this parameter and the slip angle is shown in Fig. 4-7. It needs to be pointed out from the left chart that they have a linear relationship within the slip angle range used in this research ( $-5^\circ \sim 5^\circ$ ). The slope of the linear regression equation ( $-3.1439$  in this case) is expected to represent a physically meaningful parameter rather than just a statistical constant; it could be indicative of the lateral stiffness of the tread ring of the rolling tire when subjected to slip angle. The high value of the coefficient of determination,  $0.994$ , and the randomly distributed residual in the residual fit chart, validate that the linear regression model fits the data well.

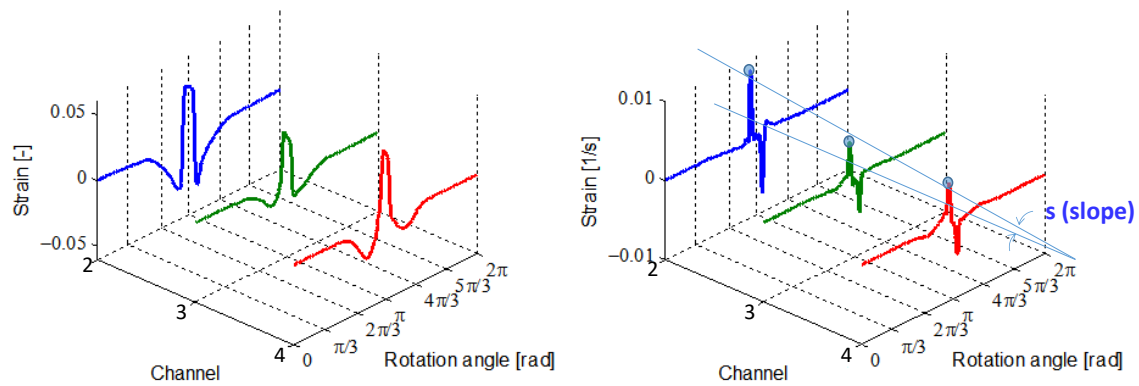


**Fig. 4-6 Strains at three channels (right) and their derivatives with the synthetic parameter ( $s$ ) for slip angle estimation**

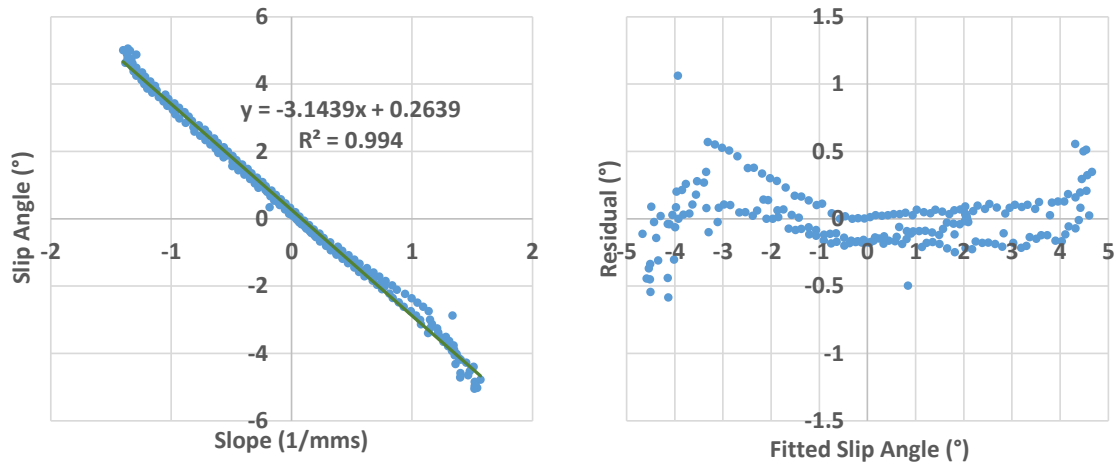


**Fig. 4-7 Regression results between slope of peak strain rate and slip angle: curve-fitting plot (left) and residual-fit plot (right)**

Using this newly suggested approach, slip angles were estimated continuously during the slip angle sweep test and the results are shown in Fig. 4-8. The correlation results are good regardless of the applied test loads, but prediction quality is degraded at lower test loads. At the lower test loads, contact deformation induced by slip angle becomes smaller, which makes their relationships unclear.

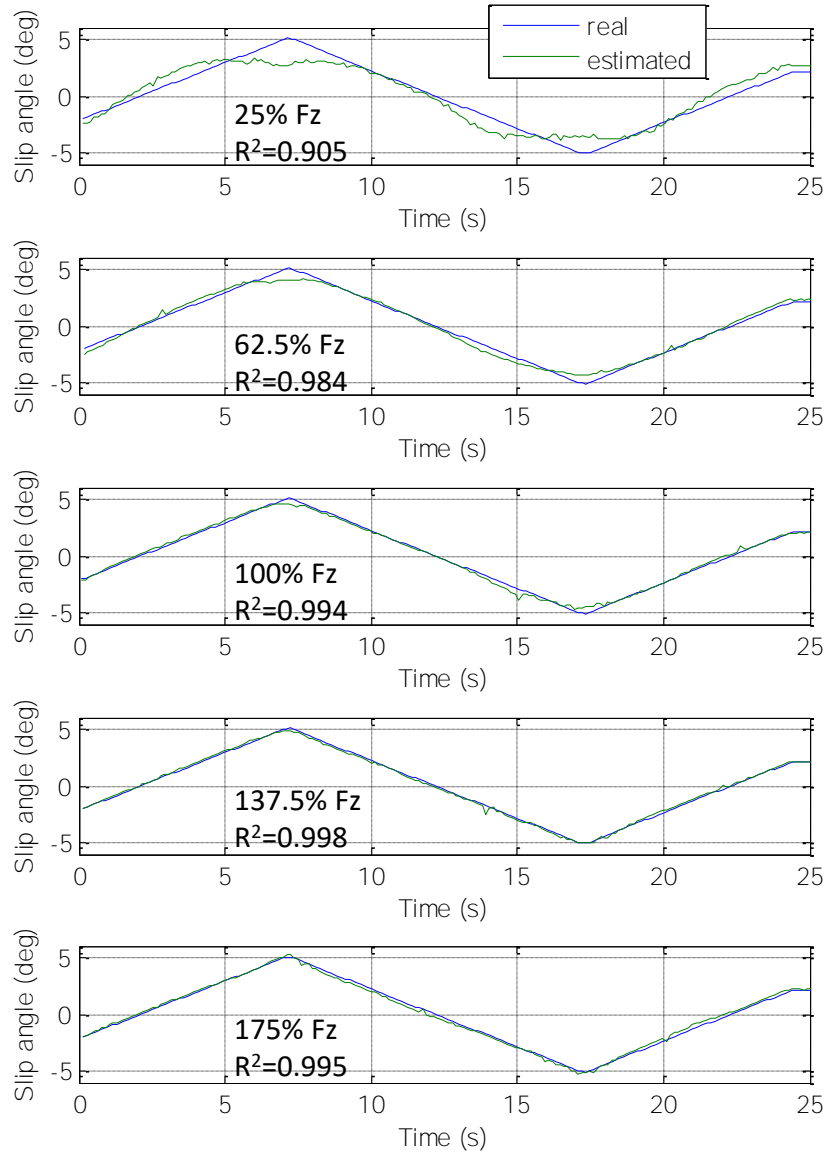


**Fig. 4-8 Slip angle estimation results for whole slip angles under different test loads**

#### 4.1.4 Lateral Force Estimation

Multivariable regressions were developed to estimate the lateral force for various test loads and camber angles. To keep the nonlinearity associated with lateral force to a minimum, the range of slip angle for estimation was limited to  $[-5^\circ \ 5^\circ]$  for both set as illustrated in Fig. 4-9.

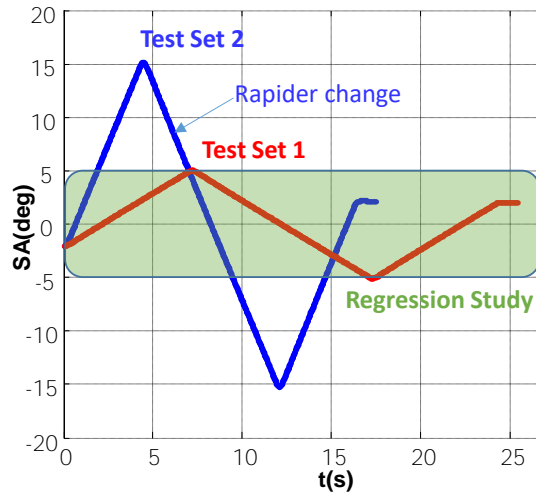


**Fig. 4-9 Slip angle time history for test set 1 and 2**

To choose the regressors which have some physical meanings and show consistent trends when test conditions vary, measured data were closely examined to find candidates meeting these requirements. Candidate regressors were suggested and are shown in Fig. 4-10.

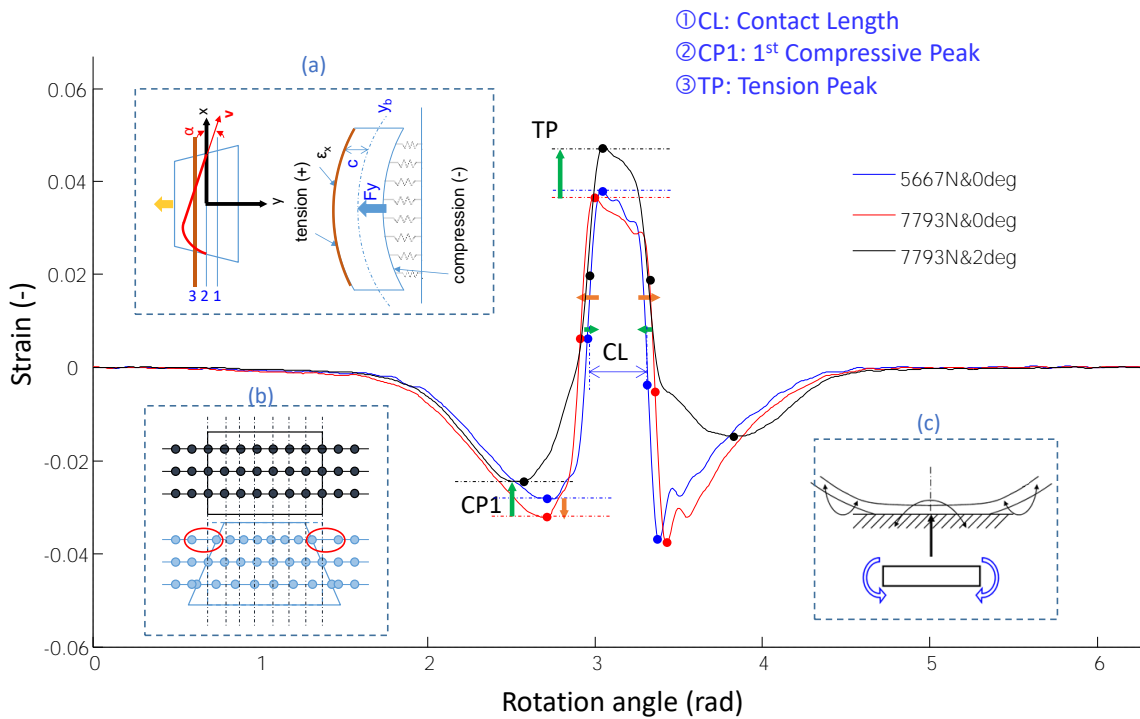


**Fig. 4-10 Combined effects of slip angle and test load on circumferential strain measured at ch3; slip angle:  $0^\circ \rightarrow 2^\circ$ ,  $F_z$ : 100%  $\rightarrow$  137.5%.**

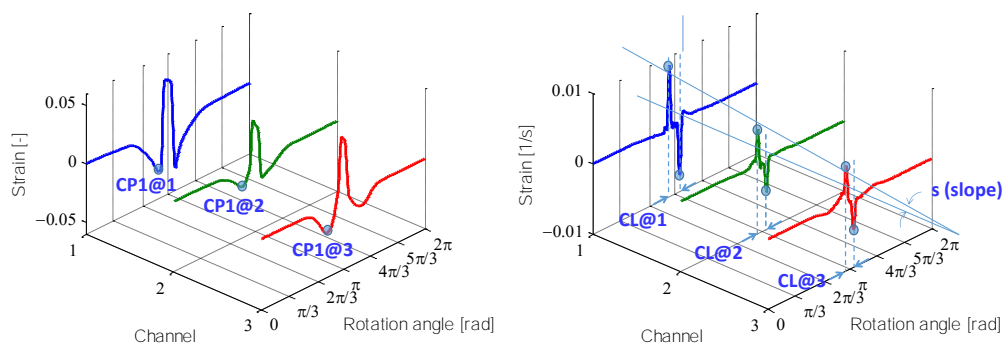
This figure illustrates the combined effects of test load and slip angle on the strain measured at channel 3. The green arrow and orange arrow show effects of slip angle and test load, respectively.

As was discussed in the previous chapter, the contact length, marked as 'CL' in the figure, at each channel shows consistent trend as slip angle varies. Considering the lateral force increases monotonically as the applied slip angle increases, especially within the linear range of slip angle ( $-4^{\circ}\sim 4^{\circ}$ ), the contact length is expected to be one of the effective predictors which can be extracted from the strain measurements. As presented in the review chapter, Section 2.2, many researchers have chosen contact lengths at various positions in the lateral direction for the lateral force estimation. As can be seen in Fig. 4-10, the contact length at inner contact region (channel 3) tends to decrease as slip angle increases in the positive direction. As expected, it also decreases as test load decreases, which make it difficult to differentiate which test condition between test load and slip angle affects the variation of contact lengths.

The peak tension ('TP') arising in the contact region also shows specific trends when the slip angle changes. The tension of the inner part, measured with the strain sensor of channel 3, due to cornering force undergoes higher tension when (+) slip angle is applied as illustrated in (a) of Fig. 4-10. This can be explained using the concept discussed in [49] where, the tread band of the tire was modeled as a beam. When this beam is subjected to a vertical force, both tension and compression are induced at off-center locations by the lateral bending motion of the beam. Under the situation illustrated, the tread band corresponding to channel 3 is subjected to tension due to the lateral force featuring the higher tension peak. When test load increases, this peak tension tends to decrease slightly regardless of the measurement position. However, the trend of the peak tension is very hard to understand because they are governed by the complex contact mechanism between the tire and the road surface such as friction, pressure distribution, local sliding and so on. Thus, the peak tension is given relatively less priority than other predictors.

The last parameter of interest is the first compressive peak marked as 'CP1'. The absolute value of compressive peaks generally increases as the tire vertical deformation increases, i.e., the applied vertical load increases which can be explained by the bending deflection of the ring as conceptually illustrated in (c) of Fig. 4-10. Another interesting trend for this parameter was observed when the applied slip angle changed. Due to cornering, the inner part of the tread undergoes less compression just before the contact (refer to (b) of Fig. 4-10). The tread band at the outer part subjected to elongation and vice versa at the inner part. Also, due to the lateral force transfer, the inner part subjected to the relatively smaller vertical load. These two factors combined to decrease the compressive peak at the inner part, i.e., channel 3. The compressive peaks are very sensitive to the change of slip angle as we can see in Fig. 4-10; the change in the slip angle from 0° to 2° induces considerable change of the compressive peak (marked as green arrow near CP1) while the 37.5% change in test load causes relatively minor changes (marked as orange arrow near CP1). In this research, only the first compressive peak was adopted for the estimation study discarding the second peak because sometimes strains don't have distinctive compressive peaks near the trailing edge, which could be due to the slippage, especially when the tire is subjected to slip angle.

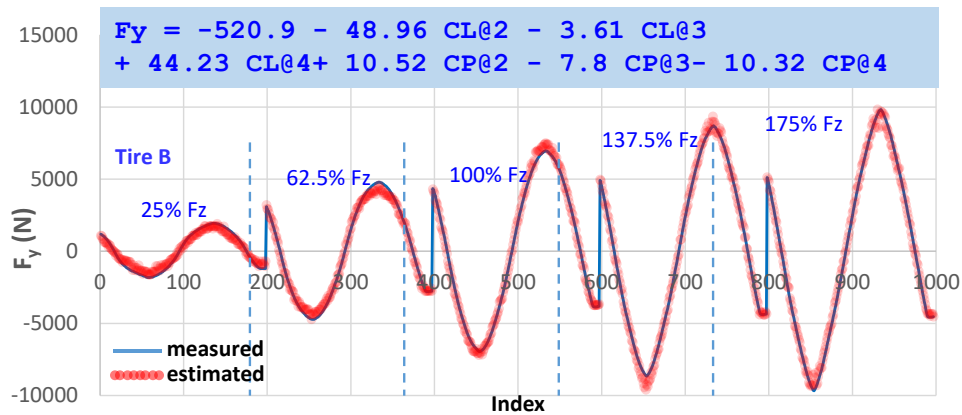
Therefore, six regressors were chosen for the regression study: three contact lengths and three compressive peaks measured at the center and both off-centers. They are marked in Fig. 4-11 with abbreviations.



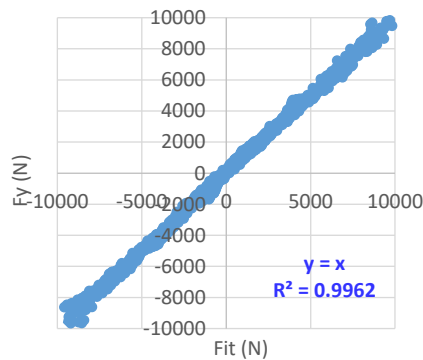
**Fig. 4-11 Six regressors for multi-variable regression study**

The measured location is expressed as '@ channel number'. The tension peaks were neglected due to reasons mentioned previously.

A multivariable regression model was implemented in the statistical software, MINITAB. For the test set 1, lateral forces were predicted based on the six regressors for various test loads and slip angles for the three tires used in this research. A linear multivariable regression model was proposed without any interactions between the variables. Around 1000 measurements for lateral forces for each tire were used for this regression study. The regression model and the fitting results are shown in Fig. 4-12. The  $R^2$  value for this fitting is 0.996 (Fig. 4-13) while a regression just using three contact lengths or compressive peaks gives  $R^2$  value of 0.991. For all 5 different test loads, the regression model predicts well except that under lowest load and the highest load associated with larger slip angles, the prediction accuracy was slightly reduced.



**Fig. 4-12 Regression model for test set 1 and fitting results**



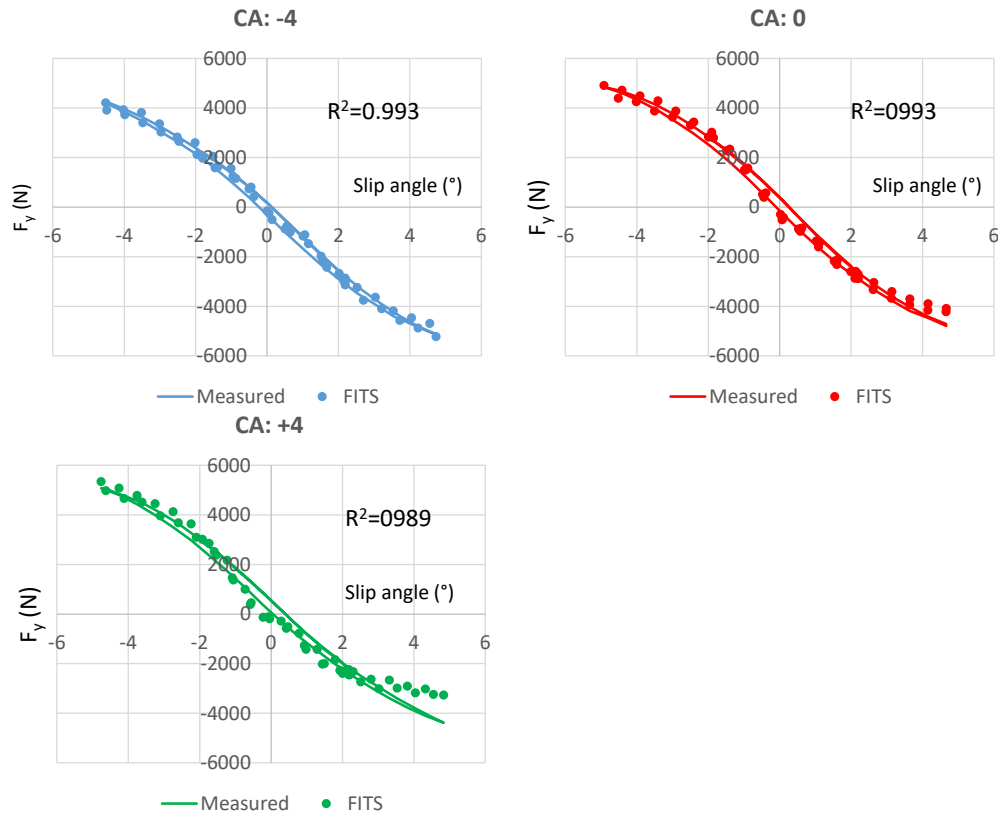
**Fig. 4-13 Goodness of fit for test set 1**

Table 4-1 shows the statistics such as regression coefficients and P-values corresponding to each term, i.e., regressor, for the three different tires. Regardless of the type and size of the tires, the goodness of the fit is high enough as indicated by high  $R^2$  values. P-values indicate the effectiveness of each regressor and smaller value mean more contribution to the regression. Based on these values, it is understood that regressors extracted from off-center measurements are more effective than those from the center for both, the contact lengths and the compressive peaks. A pair of coefficients corresponding to the off-center values are similar in magnitude with opposite signs. For different tires, the coefficients of the same term remains within  $\pm 20\%$ , which indicates the robustness of this predictive model.

**Table 4-1 Statistics table of regression for test set 1**

Term	Coefficients			P Value			R <sup>2</sup>		
	Tire A	Tire B	Tire D	Tire A	Tire B	Tire D	Tire A	Tire B	Tire D
Constants	73.5	-520.9	-606.8	0.288	0.000	0.000			
<b>CL @ Ch2</b>	<b>-49.5</b>	<b>-48.96</b>	<b>-59.66</b>	<b>0.000</b>	<b>0.000</b>	<b>0.000</b>			
CL @ Ch3	11.94	-3.61	5.67	0.000	0.279	0.887			
<b>CL @ Ch4</b>	<b>44.72</b>	<b>44.23</b>	<b>58.22</b>	<b>0.000</b>	<b>0.000</b>	<b>0.000</b>	99.26%	99.62%	99.60%
<b>CP1 @ Ch2</b>	<b>16.462</b>	<b>10.524</b>	<b>11.991</b>	<b>0.000</b>	<b>0.000</b>	<b>0.000</b>			
CP1 @ Ch3	-3.92	-7.799	-1.534	0.033	0.000	0.125			
<b>CP1 @ Ch4</b>	<b>-11.836</b>	<b>-10.320</b>	<b>-10.669</b>	<b>0.000</b>	<b>0.000</b>	<b>0.000</b>			

In the test set #2, the test load is the same for all test runs but different camber angles were applied for each test run. For each test run, the camber angle was kept constant while slip angle was varied from  $-15^\circ$  to  $15^\circ$ . The regression results are shown in Fig. 4-14. The regressors still predict the lateral forces very well when the camber angle is applied as evident from the  $R^2$  values. As we can see in Fig. 4-9, the slip angle changes faster which results in less number of data points of strain measurements, which is partially responsible for the reduction of the accuracy of the estimation.



**Fig. 4-14 Regression results for lateral force estimation under different camber angles**

**Table 4-2 Statistics table of regression for test set 2**

Term	Coefficients			P Value		
	CA: -4	CA: 0	CA: 4	CA: -4	CA: 0	CA: 4
CL @ Ch4	17.5	-29.2	-35.6	0.092	0.04	0.104
CL @ Ch5	-21.7	-5.2	39.5	0.154	0.762	0.118
CL @ Ch6	-20.0	-17.9	1.47	0.095	0.315	0.878
<b>CP1 @ Ch4</b>	<b>30.25</b>	<b>30.43</b>	<b>50.00</b>	<b>0.001</b>	<b>0.000</b>	<b>0.000</b>
CP1 @ Ch5	52.5	31.1	-1.9	0.124	0.169	0.938
<b>CP1 @ Ch6</b>	<b>-38.75</b>	<b>-22.38</b>	<b>-17.6</b>	<b>0.000</b>	<b>0.000</b>	<b>0.005</b>

Again, Table 4-2 shows the statistics of regressions for test set #2. The compressive peaks at off-center locations are still valid factors for the regression but contact lengths are no longer effective. This can be explained by the combined effects of slip angles and

camber angles as illustrated in Fig. 4-16. Fig. 4-15 shows the shape of contact patch conceptually when the camber or slip angle is applied. The sign convention follows SAE coordinate system. When negative camber is applied, the contact patch deforms such that the contact length at channel 3 becomes longer whereas the contact length at channel 1 becomes shorter. This is the similar effects as the negative slip angle has on the contact patch. Thus, the already elongated contact length at channel 3 due to the negative camber angle would not increase anymore even though slip angle increases in the negative direction, i.e., the elongation is saturated.

Fig. 4-16 shows this trend clearly. The contact length estimated at channel 3 increases when negative camber angle is applied. As slip angle increases in negative direction, the contact length at channel 3 increases and then is saturated. Same trend is observed at the contact length at channel 1 which is subjected to positive camber angle. Even though the slip angle increases, the contact length increases to some extent then it saturates. On the contrary, the contact length at channel 3 under the positive camber angle dose not shorten anymore as the slip angle increases and the same trend is observed on the contact length at channel 1 subjected to both negative slip and camber angle.

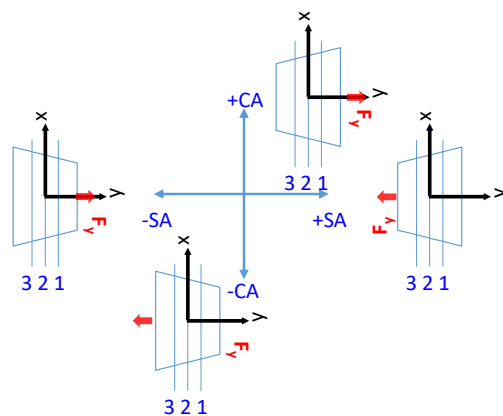


**Fig. 4-15 Conceptual shapes for contact patch subjected to slip and camber angles**

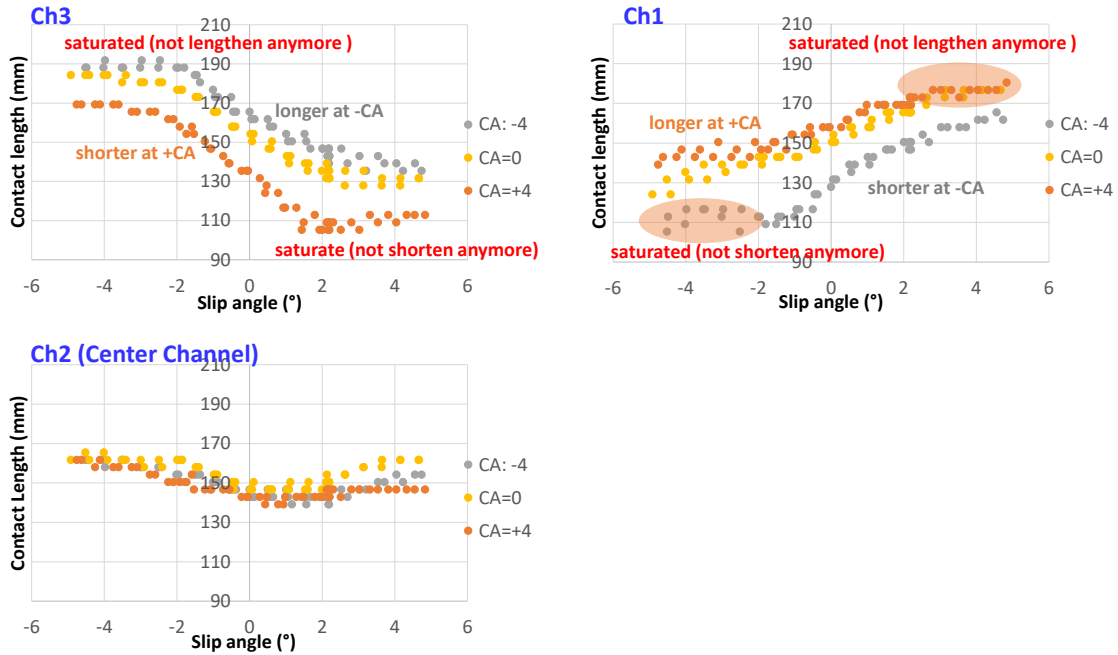


**Fig. 4-16 Combined effects of slip angle and camber angle on contact lengths**

The saturation of the contact length at off-center locations due to the combined effects of slip and camber angles makes the contact length a less effective factor for the regression model. To sum up, although the contact lengths at off-center locations have been considered as very effective predictors for the lateral force estimation, they cannot play a role in lateral force estimations when camber angle is applied. However, the compressive peaks of strains at off-center locations are more suited for predicting the lateral force for various rolling conditions subjected to vertical load, slip angle as well as camber angle.

#### 4.1.5 Slip Ratio Estimation

The slippages of the accelerated or decelerated are very important because this quantity is one of the crucial factors fed into the algorithm of vehicle control systems. In this section, the slip ratio when the wheel is subjected to driving or braking was estimated utilizing strain measurements. Driving and braking tests were conducted on Flat-Trac test rig while strains are measured at the innerliner simultaneously.

Fig. 4-17 shows the time history of measured strains for three different situations: braking, driving and free rolling. During the same time interval, more revolutions are observed for driving condition (Fig. 4-17 (a)) vice versa for braking (Fig. 4-17 (b)). The rotational velocity of the wheel can be simply calculated by dividing  $2\pi$  by peak to peak time of any compressive peak, i.e., the first or second peak. By observing the shape of strains under different rolling condition, characteristics were found which can differentiate the rolling conditions: braking, free rolling and driving. When the tire is freely rolling, the amount of two compressive peaks are almost same as shown Fig. 4-17 (c).

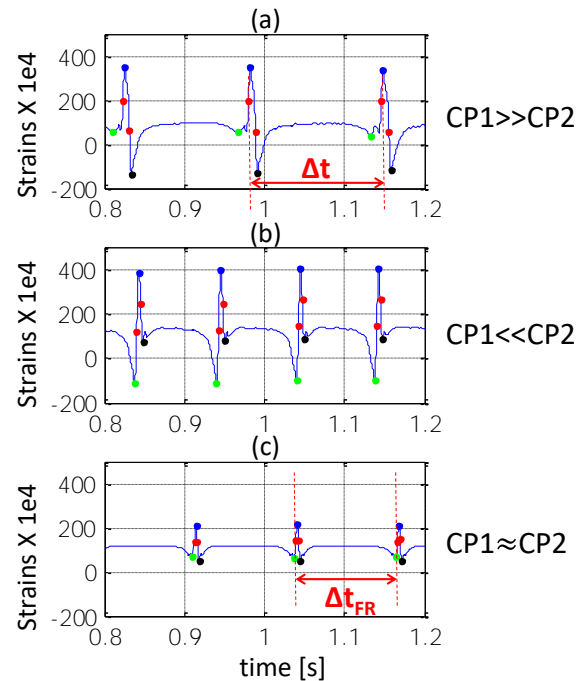


**Fig. 4-17 Strain measurements under various rolling condition: braking (a), driving (b), free rolling (c)**

Under braking, the absolute value of the second peak become larger and vice versa for the first compressive peak. When the tire is subjected braking, the shear deformation of tread elements arise heading to rear direction which contribute to the higher compression just after the trailing edge. The opposite phenomena arise when the tire is accelerated. Thus, by comparing the magnitude of the first and second peak, the rolling condition can be identified theoretically. However, validations for this differentiation

method need to be done on the real road surface with diverse braking/driving maneuvers. Also, the threshold of the difference in first and second compressive peaks should be determined based on expansive experimental data.

A slip ratio of the wheel can be calculated by Eq. (21) where  $\Omega$  is a rotational velocity of wheel subjected to brake or acceleration, which can be simply calculated as mentioned before.  $R_{eff}$  is the effective rolling radius of tire and  $v$  is a vehicle travel speed. Thus, the numerator of Eq. (21) is the difference of the travel speed between the wheel and the vehicle.

$$Slip\ Ratio = \frac{\Omega R_{eff} - v}{v} \quad (21)$$

The effective rolling radius,  $R_{eff}$  can be calculated from the strain measurement in the free rolling wheel under assumption that the vehicle travel speed is already known. Under the free rolling condition, because there is no slip between tire and road surface, the wheel travel speed should be the same as the vehicle speed. From this relationship, Eq. (22) can be induced.

$$R_{eff} = \frac{v}{\Omega_{FR}} \quad (22)$$

Once  $R_{eff}$  is obtained, using Eq. (21), slip ratio can be calculated and estimation results are shown. The estimated slip ratio from the strain measurements are compared with values recorded during Flat-Trac tests in Fig. 4-18. The estimated slip ratios agree with measured ones with high accuracy. More accurate estimation is expected for the acceleration case because more data point can be collected from the strain gage in the same time.

In the real application, the effective rolling radius can be collected during normal driving of the car without any accelerating or decelerating. Once there is considerable difference between first and second compressive peak is detected for the specific wheel,

the rotational velocity of the wheel is calculated based on the previously estimated effective rolling radius. And then, the slip ratio can be easily calculated in real time using Eq. (22).

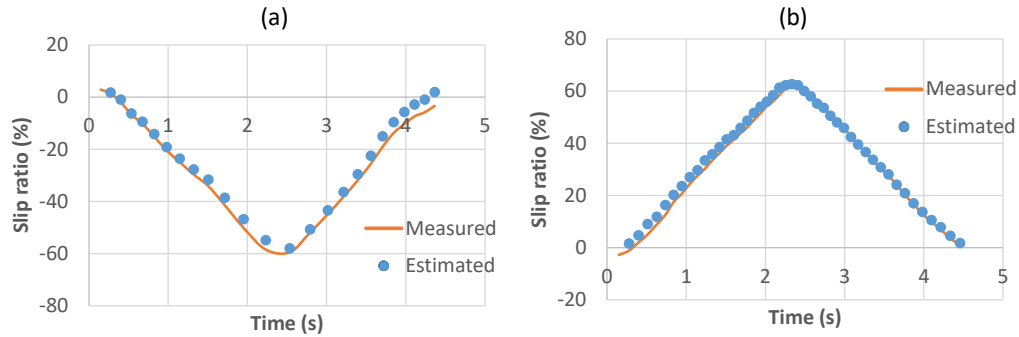


**Fig. 4-18 Slip angle estimation by use of strain measurement**

## 4.2 Model Based Estimations of Lateral Force

One of the desired parameters to be estimated is the tire contact force because the exact and continuous monitoring of tire contact forces can improve the performance of vehicle controls for lateral dynamics. Moreover, tire characteristics in the real driving conditions can be extracted if physical tire models are incorporated in the estimation procedure. The latter can be useful for the analysis of tire performances in real applications, which is sometimes difficult using indoor test results. G. Erdogan *et al.* showed a good example of how a physical tire model is incorporated into estimation process based on intelligent tire system [22-25]. He introduced the lateral carcass deflection model presented in [38] to estimate lateral force and self-aligning moment.

In this study, the similar approach was adopted but a different tire model was chosen considering available parameters from our intelligent tire systems. As presented earlier, contact length, vertical load, and slip angle were estimated based on simple statistic approaches. To utilize this information effectively, the Brush tire model was chosen in this research. Fig. 4-19 illustrates the estimation scheme using the Brush tire model. Previously estimated parameters are input to this tire model. Under the assumption that some other parameters such as cornering stiffness, friction coefficient

between tire/road and pressure distribution are already known, lateral force can be estimated through this suggested model.

The Brush tire model consists of a row of elastic bristles which represent the combined stiffness of carcass, belt and tread elements as illustrated in FIG. 13.

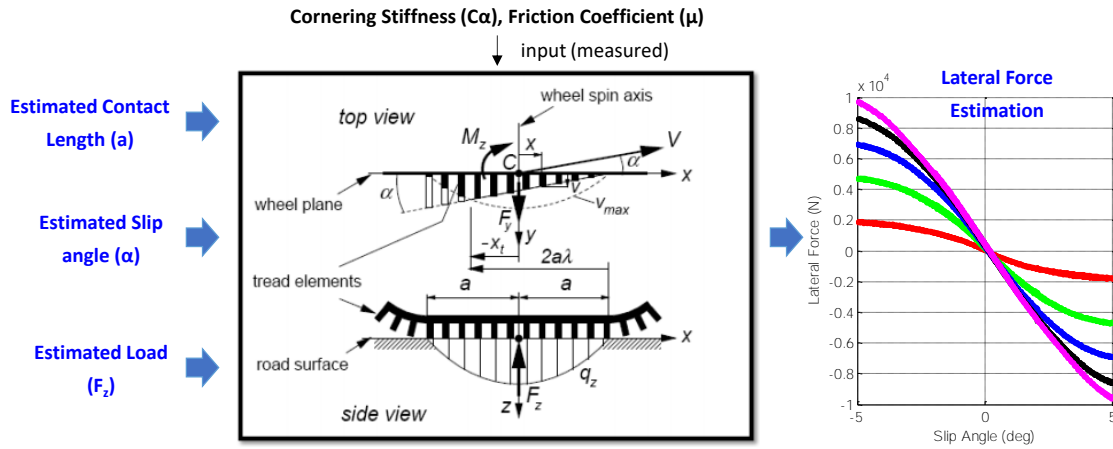


**Fig. 4-19 Scheme for lateral force estimation based on Brush tire model**

When the rolling tire is subjected to a specific slip angle ( $\alpha$ ) under the vertical load ( $F_z$ ), the bristles inside the contact patch experience bending deformations and sliding against the road surface in the lateral direction. One-dimensional contact zone is defined as  $-\overline{aa}$  where  $a$  is half of the contact length. From the leading edge to a certain critical point ( $x_t$ ), bristles adhere to road surface without sliding. This region is called the adhesion region which is represented by  $2a\lambda$  in the figure, where  $\lambda$  is a scaling factor introduced for convenience. In this region, the lateral force is generated due to the resilience of deformed bristles. After this critical point and up to the trailing edge, bristles start to slide to their undisturbed positions. This region is called the sliding region, where sliding friction is the main cause of the lateral force. As the slip angle increases, the adhesion region reduces while sliding region increases. Above a critical slip angle ( $\alpha_{sl}$ ), full sliding happens across the contact area.

In the Brush tire model, the lateral force can be determined based on the following equation, when  $|\alpha| < \alpha_{sl}$

$$F_y = c_{py} \int_{x_t}^a (a - x) \tan \alpha dx + \mu \int_{-a}^{x_t} q_z(x) dx \quad (23)$$

where,  $\mu$  is the friction coefficient between the tire and the road and  $c_{py}$  is the bristle stiffness in the lateral direction.  $q_z(x)$  is one-dimensional pressure distribution, which satisfies the following relationship.

$$F_z = \int_{-a}^a q_z(x) dx \quad (24)$$

The first term of eq. (23) is the lateral force due to the deformation of bristles and the second term is the force component caused by the sliding of the bristles.  $x_t$  can be determined using the fact that at this point the adhesive force is equal to the sliding friction force, which can be expressed by the following equation.

$$c_{py}(a - x_t) = \mu q_z(x_t) \quad (25)$$

$c_{py}$  can be determined considering the case when a small slip angle is applied so that full adhesion is in effect;

$$c_{py} = \frac{C_\alpha}{2a^2} \quad (26)$$

where,  $C_\alpha$  is the cornering stiffness.

The friction coefficient,  $\mu$ , would also be determined based on the measured lateral force if the applied slip angle was large enough so there is a peak associated with the lateral force.

$$\mu = \frac{F_{yp}}{F_z} \quad (27)$$

where,  $F_{yp}$  is the peak lateral force. However, in this research, the slip angle is limited to less than 5 degrees, so magic formula tire model was used to extract  $F_{yp}$ . Fig. 4-20 shows curve-fitting results using the Magic Formula and the main parameters mentioned before.

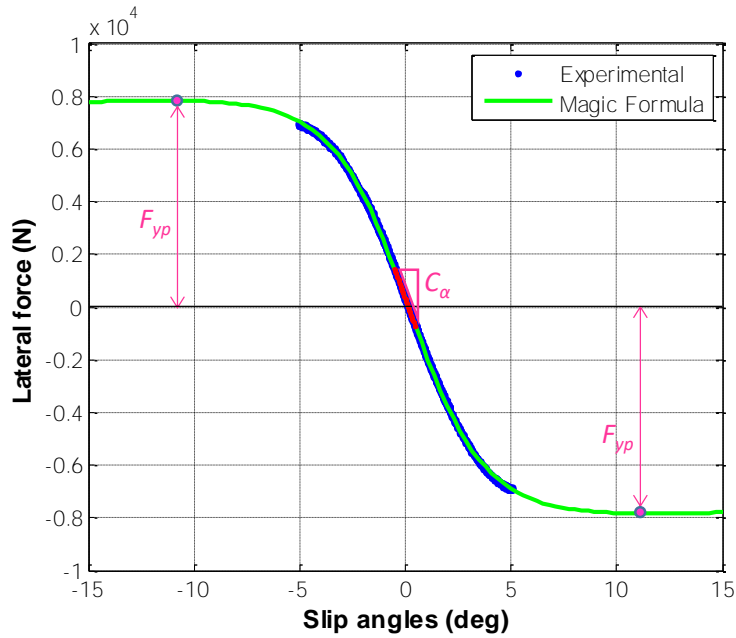


**Fig. 4-20 Magic Formula fitting on measured lateral force with characteristic parameters**

The one-dimensional pressure distribution across the contact length is given using the following equation.

$$q_z(x) = q_{0,n} \left( 1 - \left( \frac{x}{a} \right)^2 \right)^{\frac{1}{n}} \quad (28)$$

where,  $n$  is shape factor and  $q_{0,n}$  is a pressure at the center of the contact patch. By adjusting  $n$ , the shape of the pressure distribution curve changes from a more convex shape to less convex i.e., flat. From measurements and literatures, it was found that as test load increases, the one-dimensional pressure distribution tends to vary from more convex shape to less convex or even concave shape. Based on this phenomenon, pressure distribution is simulated as shown in Fig. 4-21 using Eq. (28) and adjusting the shape factor,  $n$ , for each test load.

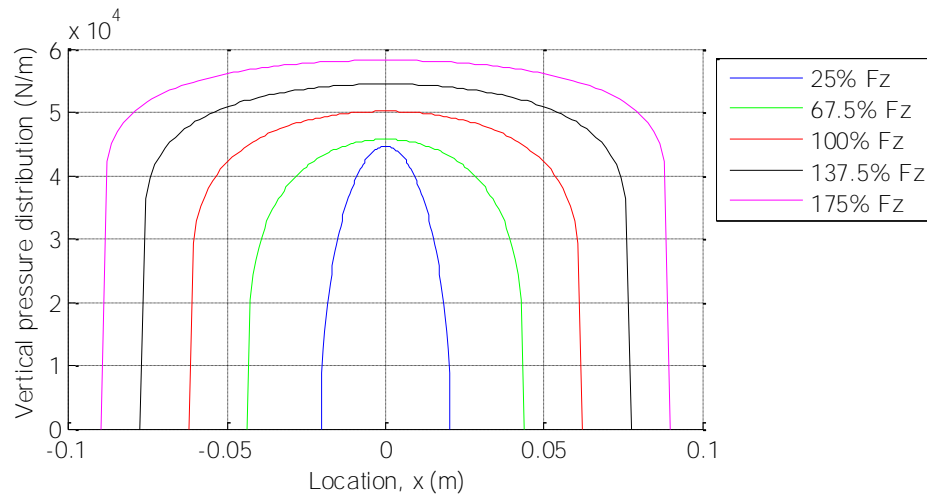


**Fig. 4-21 Assumed one-dimensional pressure distributions at different test loads.**

Estimated parameters ( $a$ ,  $\alpha$ ,  $F_z$ ) and assumed-known parameters ( $C_\alpha$ ,  $\mu$ ,  $q_z(x)$ ) are inputs to the Brush tire model and finally, lateral forces at different loads are estimated. The estimation results are shown in Fig. 4-22, where experimental data is shown with solid lines while estimated data are shown using dotted lines.

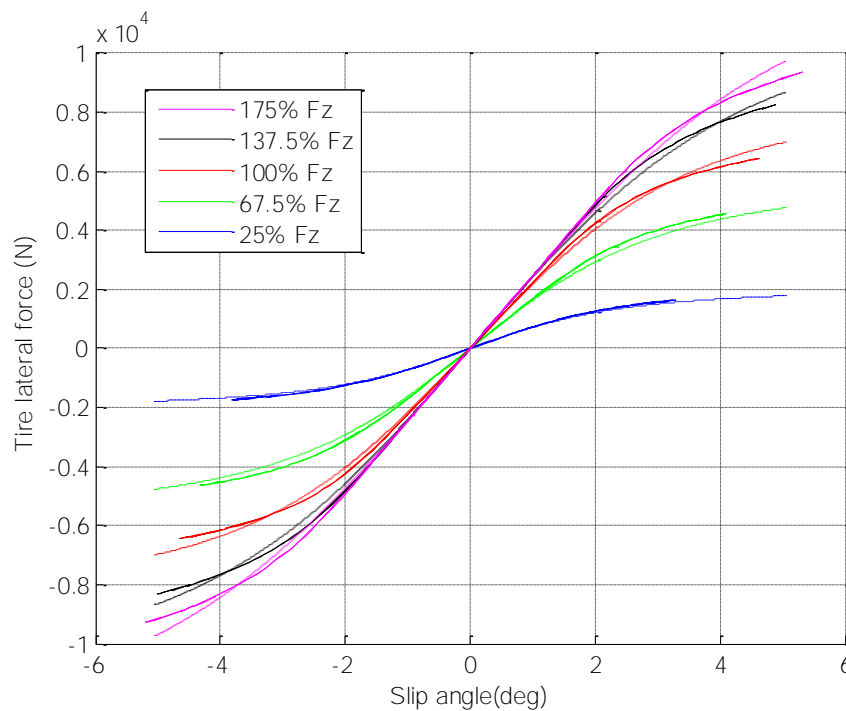


**Fig. 4-22 Lateral force estimation results.**

Generally, they agree well with good accuracies. However, at the higher slip angles and higher test loads, the prediction quality becomes worse. It is thought that the Brush tire model has its limitations when severe, nonlinear deformations of the contact patch become dominant. Also, at the higher slip angles, the friction induced force is the main component of the lateral force. The use of a simple friction model with arbitrarily assumed pressure distributions may cause this degradation of prediction as well.

It should be noticed tire characteristics assumed known, such as cornering stiffness and friction coefficients, are considerably dependent on the test conditions like the test load, inflation pressure, camber angle, etc. Magic formula tire model also defines these tire characteristics as functions of test loads and camber angles. Therefore, it is expected that the cornering stiffness and the peak lateral force would have good correlations with the center contact length, which was used as the regressor for the load estimation. Fig. 4-23 shows the regression results for cornering stiffness and peak lateral force, where regressor is the contact length identified by strain measurements.

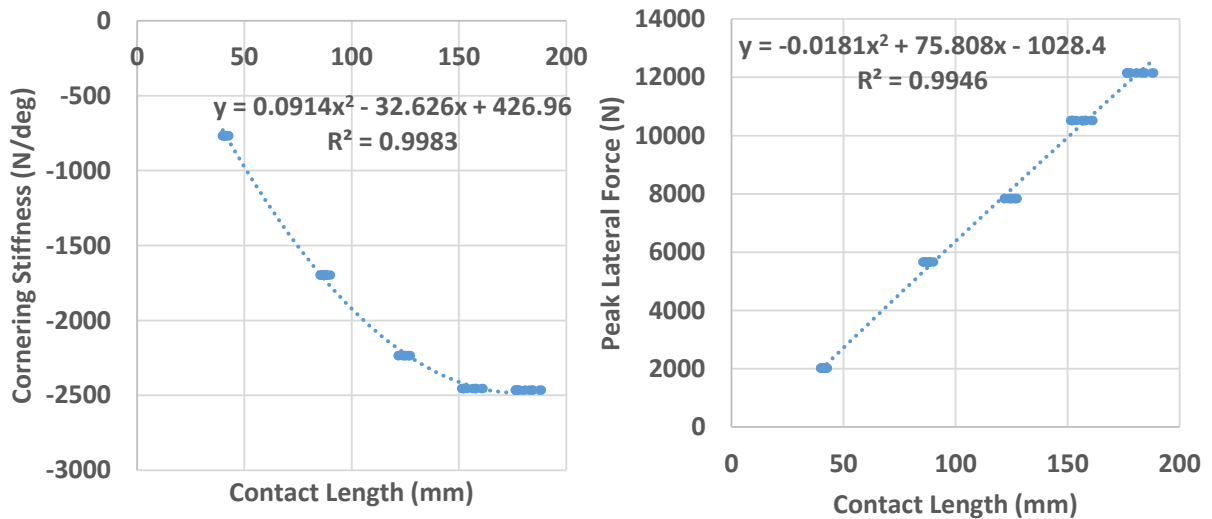


**Fig. 4-23 Curve-fitting between cornering stiffness with estimated contact length (left) and peak lateral force and estimated contact length (right)**

### 4.3 Chapter Conclusion

In this chapter, several tire-road contact features are estimated using the strain gage based intelligent tire when the tire is subjected to different vertical loads, slip angles, slip ratios and camber angles. Five strain gages are attached to the innerliner above the tire tread and they are distributed in the axial direction covering from inner to outer part of the contact patch.

Well-validated estimation methods from previous studies were adopted to predict contact patch length. Because of the five measurements of strains across the contact patch in the axial direction, contact lengths at five different positions were obtained which allowed rough estimates of contact shapes under various slip angles. Estimation results show expected variations in contact shapes as the slip angle changes.

The vertical load can be estimated from contact length based on the fact that they have the steady and positive correlation within the common operation conditions; the contact length increases as the vertical load increases. Through detail investigation of the contact lengths at various slip angles, it is revealed that the contact length at the center of the contact patch is insensitive to slip angle changes whereas heavily depending on the vertical load. Thus, test loads were predicted using the center contact length with a simple regression model and results showed good agreements.

Slip angles are estimated based on the variations of strain rates across the contact width. It is proposed that the slope of the peak strain rate over the five positions along the contact width be used. Estimation shows the newly-suggested regressor has a linear relationship with slip angle, while the work using the similar method proposed by other researcher shows a nonlinear relationship. It is expected that the slope of the linear regression equations can be representative of the tread ring stiffness but more study and validations are required.

Lateral contact forces were also estimated for various test loads and camber angles using multivariable regressions. Contact lengths and the first compressive peaks of strains measured at off-centers were used as regressors and they can predict the lateral force exactly for various test loads. However, when the camber angle is applied, the

contact lengths are not valid factors for regression anymore due to the saturation of the contact length due to the combined effects of the slip angle and camber angle. The compressive peaks are revealed to be still valid for the lateral force estimation even when the camber angle is applied.

By comparing the successive compressive peaks of strains measured inside the straight rolling tire, the rolling status was identified as braking, accelerating or free rolling. Using the rotational velocities of the free rolling wheel or driven/decelerating wheel, the slip ratios were estimated accurately

Using estimated parameters related to lateral dynamics of wheel, a new estimation method for the lateral force was proposed. A well-defined theoretical tire model was incorporated into the estimation process for the purpose of characterizing tire physical features. To fully utilize the estimated parameters, the Brush tire model was adopted with the assumption that some other input parameters are already known, which are tread stiffness, contact pressure distribution, and friction coefficient. Estimation results show good agreement especially in the linear range, i.e., at smaller slip angles and under lower vertical loads. In this study, estimations were mostly done by using simple regressions induced from confined experimental results. To be applied in the real world, estimation algorithms should work successfully on diverse driving and environmental conditions. To achieve this challenging goal, more advanced statistical methods should be presented based on extensive pre-test results covering diverse operation and road conditions.

The estimation method for lateral force based on the Brush tire model revealed the possibility to extract tire physical characteristics such as pressure distribution or tread stiffness with the assumption that the lateral force is already known. Overall, it is expected that in the future study on tire characterization based on intelligent tires, diverse types of tire models will be attempted considering different sensor types, sensing locations and number of sensors.

## 5 INVESTIGATION ON CIRCUMFERENTIAL CONTACT MECHANISM USING STRAIN MEASUREMENTS

The intelligent tire system promising to use sensed measurements from intelligent tire for the analysis of tire from the point of view of the tire design engineer. This is because the accelerations or strains measured near the contact patch have ample information on tire characteristics. To achieve this goal, well-established theories in tire models can be incorporated into the process of identification of tire characteristics. A few previous researchers have adopted this approach to estimate tire parameters. Erdogan *et al.* [32] obtained the carcass lateral profile by double integrating the acceleration in the lateral direction measured at the innerliner and introduced the lateral carcass deflection model [38] to estimate the lateral force and the self-aligning moment. These estimated parameters were finally used as inputs to the brush type tire model to obtain the friction coefficient. This work was advanced further by Hong *et al.*, who applied this method to real world scenarios by taking the tire deformation effects on measured acceleration into consideration [33]. Matsuzaki *et al.* also used the double integral of lateral acceleration to obtain the lateral profile of carcass line, which was correlated with lateral force [35]. In these works, identification of the lateral deformation was used for the estimation of the lateral force with the assumption that the lateral stiffness of tire is known.

In this chapter, a modified flexible ring model is introduced to identify the characteristics related to in-plane dynamics of the tire. As the name implies, this model represents the tread band of the tire as a flexible ring, which is supported by the viscoelastic sidewall elements (between the ring and the wheel). Flexible ring models are widely used to analyze the vibration properties as well as to solve the circumferential contact problems between the tire and the road surface. As to the contact problem, tread elements should be included to account for the boundary conditions between the tire and the road surface. Yamagishi and Jenkins [57-59] studied the circumferential contact problem of the belted radial tire by considering the tread rubber as distributed springs along the outer layer of the circular ring. In their study, they assumed the contact angles to be known whereas they are usually unknown in real applications. The ring was

separated into the free region and the contact region. Governing equations are solved separately for each region by finding numerical solutions of differential equations. The arbitrary constants were determined by symmetry conditions of the static tire and continuity conditions at contact edges. There were convergence issues, so they used a singular perturbation method to get the approximate solution. Gong [50] used the same boundary conditions but solved the contact problem with a more advanced ring model which includes the circumferential stiffness and damping of the sidewall, and dynamic effects of a free rolling tire on the flat road. Rather than solving the equation using conventional methods, modal expansion method was used considering the flexible ring as one unit. After considerable numerical manipulations, he calculated the ring deformation and the contact pressure distribution under the assumption that the contact angles were known. For the case of unknown contact angles, other information such as the vertical deformations or loads were used instead and the solution process was repeated until one of the contact angles met the required boundary condition at the corresponding edge. And then, another iteration process was conducted to find the other contact angle while keeping the previously found contact angle as constant. It needs to be pointed out that finding contact angles sequentially is likely to make some error because the fixed contact angle from the first iteration should be affected when the other contact angle varies thorough the second iteration process. In other words, they need to be determined simultaneously. Yu *et al.*, derived the motion of equation for the rolling tire contacting with the frictionless flat surface tire similar to Gong's work but simplified one was derived by neglecting the rotational inertial effects [60]. The equation was solved analytically for the contact and free region each like Yamagishi's work but the contact angle was identified with boundary conditions which are also based on the same contact model as used by Yamagishi and Gong.

Kim [61] introduced a more realistic compatibility condition for the tread elements for the circumferential contact problems of the free rolling tire on the flat surface by referring the friction modeling [62]. He introduced the shear deformation of the tread and distributed moments along the beam axes due to the shear deformation of the tread.

Therefore, the boundary condition became complex and nonlinear, making it impossible to find an analytical solution. So, he introduced a two-step solution: first, the boundary conditions were linearized and approximate solutions were found like Gong's approach. Second, exact solutions were obtained through iterative process from the approximate solutions using the exact, non-linear compatibility conditions of the tread.

As was shown, solving the equations of the motion for the flexible ring model while satisfying the boundary conditions simultaneously is complex with numerical difficulties. Also, it is difficult to obtain some of the model parameters for flexible ring such as the bending stiffness of tread band and sidewall stiffness. Modal analysis has often been used to get the tire parameters and static test results on indoor test rigs are also used. However, conducting the modal tests and interpreting the results for parameterization of the tire are challenging especially for the contact problems where the tire is rolling with a finite contact with the road. Also, model parameters obtained from the static-indoor test results may not reflect tire characteristics in the real driving scenario. Moreover, when tread elements are introduced, the tread stiffness should be estimated, which does not exactly correspond to the modulus of the tread rubber but a synthetic value determined by the bending stiffness of the tread band, the rubber modulus as well as some geometrical values such as the tread thickness and the beam width as discussed in [57].

In this research, the contact problem was solved based on the combination of strain gages measurements, finite element modeling and the flexible ring model. The rest of the paper is organized as follows: Testing method is discussed in the next section, which is followed by the simulation method of the circumferential strains. And then, circumferential contact problems were solved for three different tires by using both suggested method and conventional method for the validation purpose. Discussions and conclusions are given at the end.

## 5.1 ESTIMATION OF RADIAL DEFORMATION OF THE TREAD BAND USING STRAIN MEASUREMENTS

### 5.1.1 The relationship between deformations of tread band and strains at inner liner

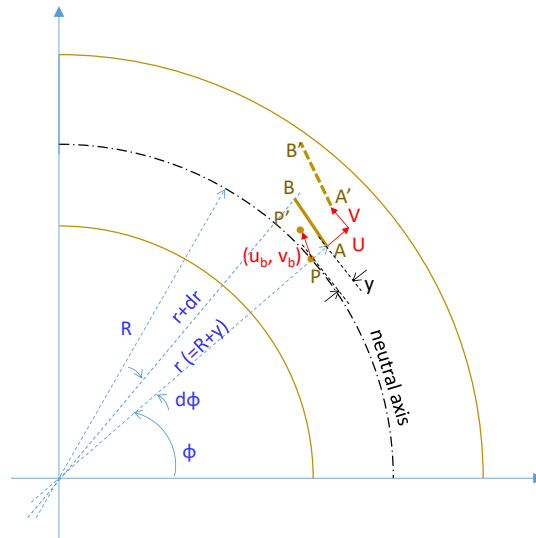


**Fig. 5-1 The location of two neighboring points before and after ring deformation**

Fig. 5-1 illustrates the flexible circular ring. The radius from the center to the neutral axis of the beam is  $R$ . During deformation, Point  $P$  on the neutral axis at  $(R, \phi)$  in polar coordinate system moves to  $P'$  by  $u_b$  and  $v_b$  in the radial and tangential directions, respectively. At the same time, two neighboring points  $A$  and  $B$  located off of the neutral axis move to  $A'$  and  $B'$ , respectively. The location of  $A$  and  $B$  before deformation is  $(\phi, r)$  and  $(\phi+d\phi, r+dr)$ , respectively and  $A$  is apart from the neutral axis by  $y$ , i.e.,  $r=R+y$ . The deformation of  $A$  is defined as  $U$  and  $V$  in the radial and tangential directions, respectively.

With these definitions, the strains in the element  $\overline{AB}$  can be written as [50, 63]

$$\epsilon_{\phi\phi} = \frac{1}{r} \left( U + \frac{\partial V}{\partial \phi} \right) + \frac{1}{2r^2} \left( V - \frac{\partial U}{\partial \phi} \right) \quad (29)$$

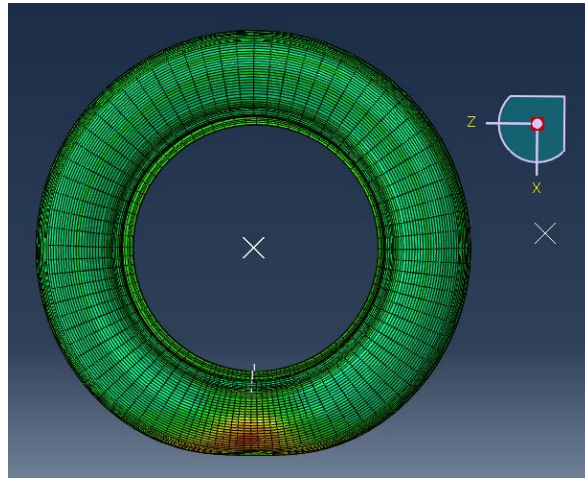
$$\epsilon_r = \frac{\partial U}{\partial r} \quad (30)$$

$$\gamma_{r\phi} = \frac{1}{r} \frac{\partial U}{\partial \phi} + \frac{\partial V}{\partial r} - \frac{V}{r} \quad (31)$$

Because a thin beam is considered, Bernoulli-Euler assumption is valid and the cross-section of the beam remains plane and normal to the neutral axis. Using this assumption, the circumferential strain can be related to  $u_b$  and  $v_b$ , which are the radial and circumferential deformations of the neutral axes, respectively. The relationship is written as the following equation.

$$\epsilon_\phi = \frac{1}{R} \left( u_b + \frac{\partial v_b}{\partial \phi} \right) + \frac{y}{R^2} \left( \frac{\partial v_b}{\partial \phi} - \frac{\partial^2 u_b}{\partial \phi^2} \right) + \frac{1}{2R^2} \left( \frac{\partial u_b}{\partial \phi} - v \right)^2 \quad (32)$$

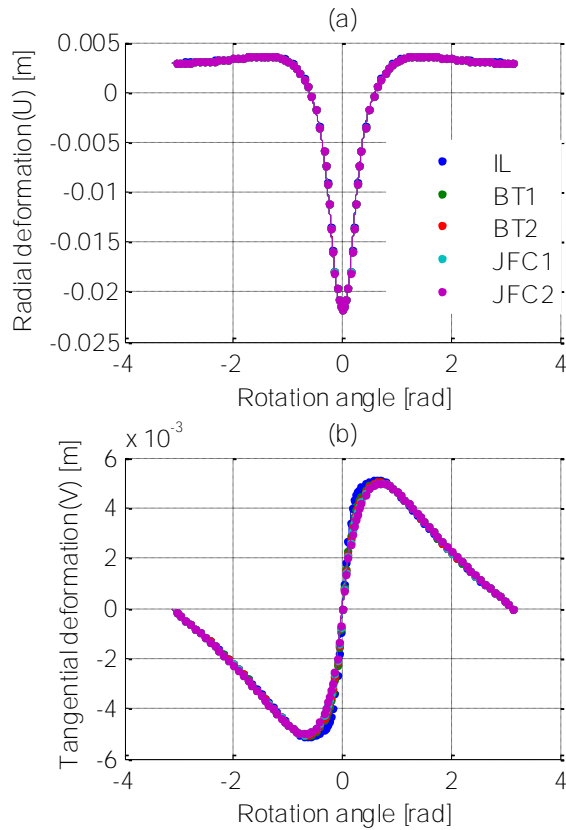
To validate Eq. (32), FEM simulation was conducted and the graphical deformation is shown in Fig. 5-2.



**Fig. 5-2 FEM simulation results for tire subjected to vertical force on the flat road**

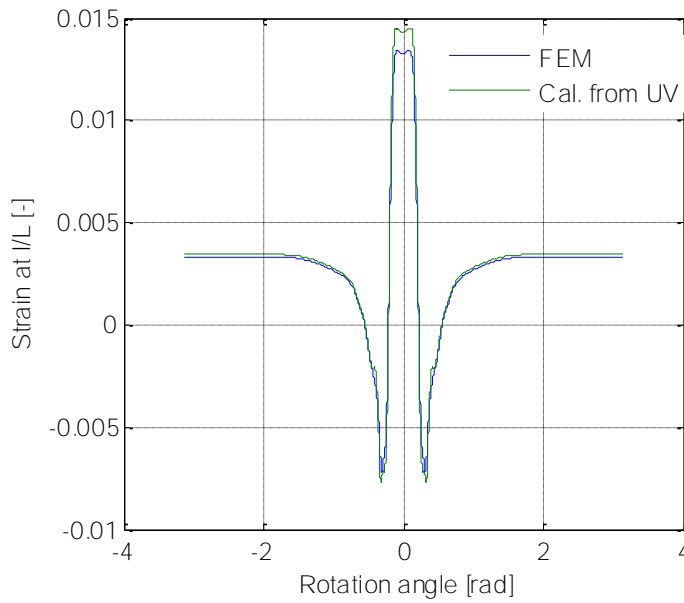
This simulation was conducted for a 215/60R16 size tire pushed against a flat road surface. The inflation pressure was 2.14 bars and the vertical load of 4765N was applied. The deformation of each layer was extracted and was converted to get the corresponding radial-tangential displacements ( $U$ ,  $V$ ).

Fig. 5-3 shows the radial and tangential deformations of each layer (IL: innerliner, BT1, 2: steel belt 1 and 2, JFC1, 2: reinforcement layer 1 and 2). The radial deformations are identical but tangential deformations differ slightly among layers; inside layers, e.g., innerliner, tend to deform more in the contact region.



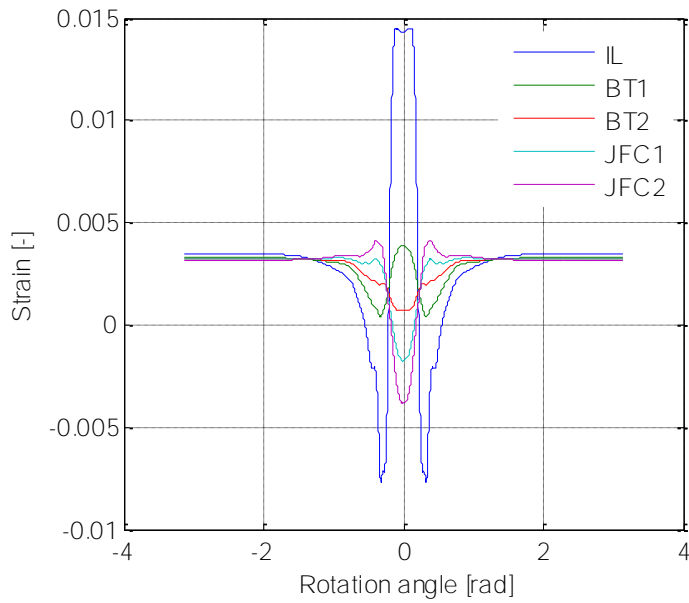
**Fig. 5-3 Radial (a) and tangential (b) deformations of each tire layer**

Fig. 5-4 compares circumferential strains obtained by different methods: one is simulated using FEM and the other is calculated using Eq. (29) using the deformation of the innerliner ( $U$ ,  $V$ ). Though the strain from FEM shows a slightly higher tension in the contact, the calculated one shows almost identical results. So, modeling the tire tread band as a homogeneous ring can represent the circumferential strain of the tire.



**Fig. 5-4 Strains directly from FEM simulation and by calculating from U, V**

Strains at each layer are calculated using their deformations and are shown in Fig. 5-5. The strain at innerliner (IL) shows the high tension within the contact patch and compression arising just before and after contact patch is the same as in the experimental measurements shown in Fig. 3-7. The second reinforcement layer, JFC2 (relatively in the outer part,) shows opposite trends. The first and second belts (BT1, BT2, respectively), show the smallest strains overall, which means that they hardly shorten or elongate during the tire deformation. So, their positions can be regarded as the neutral axis of the ring as was also suggested in [57]. In this research, the first belt is chosen as the neutral axis and its deformations are represented by  $u_b$ ,  $v_b$ , the radial and tangential deformations, respectively.



**Fig. 5-5 Strains at each layer of tire**

Using these values and to check the validity of Bernoulli-Euler assumption, the innerliner strain was calculated using Eq. (32) and the results are shown in Fig. 5-6. The strain calculated using the deformation of the belt ( $u_b, v_b$ ) is the same as the one using the deformation of the innerliner ( $U, V$ ).

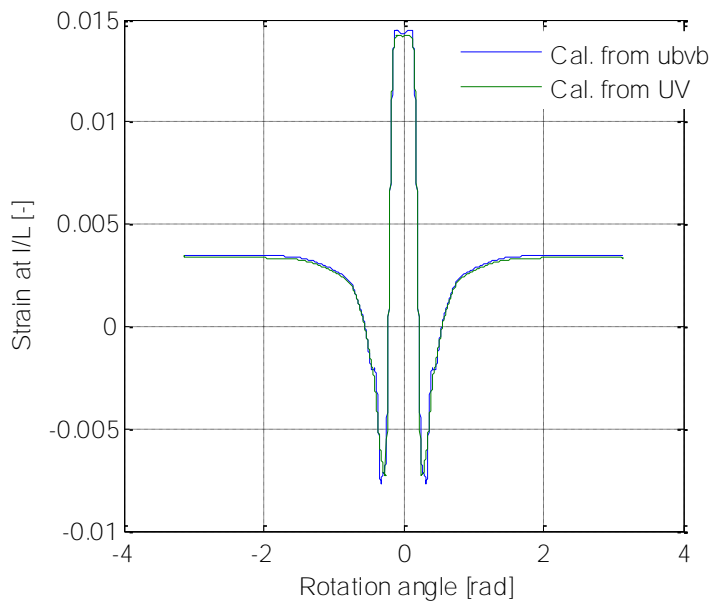


**Fig. 5-6 Strains calculated from IL deformations ( $U, V$ ) and from BT1 deformations ( $u_b, v_b$ )**

Thus, the position of the neutral axis is determined as the location of the first belt line and Bernoulli-Euler assumption is confirmed to be valid for the belted radial tire.

Due to the inflation pressure and the centrifugal force for the rolling tire, usually, tire layers have a small amount of pretension even when they are not in contact with the road surface. This pretension causes the offset in the strain measurement as shown in Fig. 3-7. However, this offset in the measurement is also affected by test sequence, temperature and sensor drift. Thus, when analyzing strain measurements, this offset is usually removed, which means the circumferential elongation of the tire is not used.

The first and third term in Eq. (32) correspond to the circumferential elongation of the ring and second term is induced by its bending motion. So, if just the bending induced strain is of interest, Eq. (32) can be reduced to:

$$\epsilon_{\phi} = \frac{y}{R^2} \left( \frac{\partial v_b}{\partial \phi} - \frac{\partial^2 u_b}{\partial \phi^2} \right) \quad (33)$$

For most of the steel belted radial passenger tires, the inextensibility assumption is also valid, which says that the length of the neutral plane of the ring is constant during deformation. This assumption can be written as:

$$\frac{\partial v}{\partial \phi} = -u_b \quad (34)$$

Substituting Eq. (34) into Eq. (33) gives the final form of the circumferential strain equation:

$$\epsilon_{\phi} = -\frac{y}{R^2} \left( u_b + \frac{\partial^2 u_b}{\partial \phi^2} \right) \quad (35)$$

Fig. 5-7 compares strains using different equations: using full strain equation, Eq. (32), then shifted to zero ('strain w/o offset'), using Eq. (33) ('app. strain 1'), and using Eq. (35) ('app. strain 2'). Some discrepancies are observed in the compression region when comparing original strain and approximated ones. However, since this region will not be directly used in the identification process proposed in this research, reduced equations

are still considered to be valid. There is no difference between Eq. (33) and Eq. (35) confirming the inextensibility assumption. In this research, Eq. (35) will be used for the identification of the radial deformation of the belt in the Section 3.2.

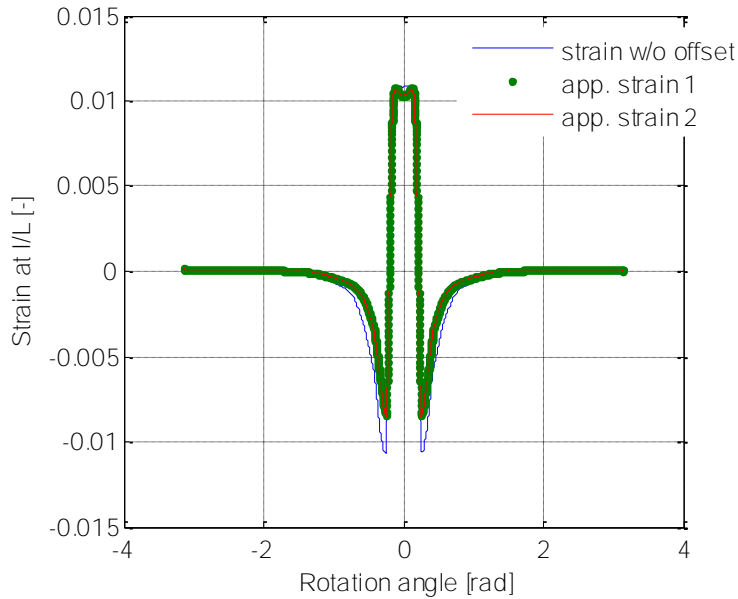


**Fig. 5-7 Comparison of strains calculated by using different equations.**

### 5.1.2 Estimation of radial deformation from strain measurement

One of outputs of the flexible ring model is the radial deformation of the tread band especially at the neutral axis. So, if it is possible to estimate the radial deformation of the belt (or neutral axis) from the strains measured at the innerliner, the strain based intelligent tire can be successfully integrated into the contact problem using the flexible ring model.

The simplest form of the strain-deformation relationship, Eq. (35), is an ordinary differential equation for the spatial variable  $\varphi$ . This can be simply solved if we know the strain measurement by using finite difference method (FDM) and strain measurements as input. This ODE can be discretized using FDM such that;

$$\frac{y}{(\Delta\phi R)^2} u_{bi-1} + \frac{y}{R^2} \left(1 - \frac{2}{\Delta\phi^2}\right) u_{bi} + \frac{y}{(\Delta\phi R)^2} u_{bi+1} = -\epsilon_{\phi_i} \quad (36)$$

In this equation, each point 'i' corresponds to a measurement point and  $\Delta\phi$  is the incremental step of  $\phi$  for discretization. Because Eq. (35) is a second order ODE, two boundary conditions are required. In this research, these boundary conditions are determined based on the compatibility conditions for tread to contact the flat road, which is suggested by Yamagishi [57] and shown in Fig. 5-8.

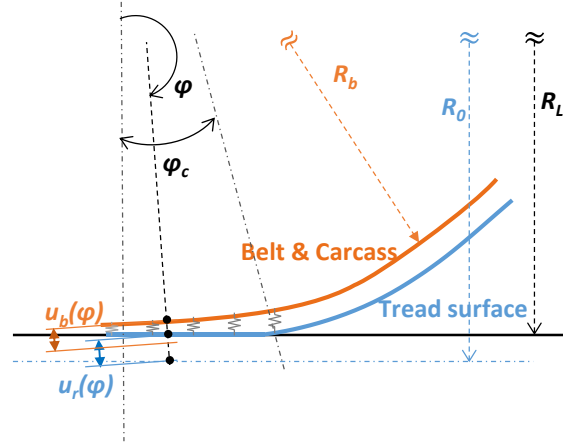


**Fig. 5-8 Flexible ring model including tread elements, adapted from [57]**

In this concept, the deformed tire against the flat surface is considered and tread elements are modeled as radial springs of which stiffness is  $k_t$ .  $R_0$  is the overall radius of the undeformed tire and  $R_L$  is the loaded radius. The pressure distribution can be obtained by multiplying tread deformation and tread stiffness ( $k_t$ ). The tread deformation can be determined by the difference between the radial deformation of tread band ( $u_b$ ) and the total deformation of the tire ( $u_r$ ), i.e.,  $u_b - u_r$  where  $u_r$  is obtained from the loaded tire geometry as shown in the following equation.

$$u_r(\phi) = -d_0 + R_0(1 - \cos(\pi - \phi)) \quad (37)$$

where,  $d_0 = R_0 - R_L$ .

From the strain rate peak values (refer to Fig. 3-8), the leading and trailing contact angles ( $\phi_{c,l}$ ,  $\phi_{c,t}$ ) were identified and the corresponding total radial deformations ( $u_r$ ) were calculated using Eq. (37). At both edges of the contact patch, the pressure should be zero, which means the amount of ring deflection ( $u_b$ ) becomes the same as the total radial deformation of the tire ( $u_r$ ). Thus, the boundary conditions can be written as shown in Eq. (38).

$$\begin{aligned} u_b(\phi_{c,l}) &= u_r(\phi_{c,l}) = -d_0 + R_0(1 - \cos(\pi - \phi_{c,l})) \\ u_b(\phi_{c,t}) &= u_r(\phi_{c,t}) = -d_0 + R_0(1 - \cos(\pi - \phi_{c,t})) \end{aligned} \quad (38)$$

As was mentioned previously, in this research, a simple flexible ring model was considered for the static tire subjected to vertical force only. Thus, tread band deformation is symmetrical with respect to the center point of contact patch and the strain profile at the innerliner should also be symmetrical. However, the pressure distribution of the loaded rolling tire is asymmetrical due to rolling resistance. Thus, the radial deformation and the circumferential strain become asymmetrical, especially in the contact region. To obtain meaningful information on tire characteristics from strains using this static ring model, symmetrical shaped strains are preferred. Therefore, measured strains were approximated to become symmetric using Fourier cosine series expansion.

Eq. (36) shows a set of discretized linear equations for unknown variables,  $u_{bi}$  ( $i=2\dots n-1$ ) as shown in Eq. (39).

$$\begin{bmatrix} b & c & 0 & 0 & 0 & \dots & 0 \\ a & b & c & 0 & 0 & \dots & 0 \\ 0 & a & b & c & 0 & \dots & 0 \\ 0 & \dots & \dots & \dots & \dots & \dots & 0 \\ 0 & \dots & \dots & a & b & c & 0 \\ 0 & \dots & \dots & 0 & a & b & c \\ 0 & \dots & \dots & 0 & 0 & a & b \end{bmatrix} \begin{bmatrix} u_{b2} \\ u_{b3} \\ u_{b4} \\ \dots \\ u_{bn-4} \\ u_{bn-3} \\ u_{bn-2} \end{bmatrix} = \begin{bmatrix} \epsilon_{\phi 2} - au_{b1} \\ \epsilon_{\phi 2} \\ \epsilon_{\phi 4} \\ \dots \\ \epsilon_{\phi n-4} \\ \epsilon_{\phi n-3} \\ \epsilon_{\phi n-2} - au_{bn} \end{bmatrix} \quad (39)$$

where,  $u_{bi}$  are radial deformations of the contact patch corresponding to each measured strain data point. a, b and c coefficients are provided in Eq. (40):

$$a = \frac{y}{(\Delta\phi R)^2}, \quad b = \frac{y}{R^2} \left(1 - \frac{2}{\Delta\phi^2}\right), \quad c = \frac{y}{(\Delta\phi R)^2} \quad (40)$$

In Eq. (39),  $u_{b1}$  and  $u_{bn}$  are pre-determined from boundary conditions given by Eq. (38). This discretization concept is illustrated in Fig. 5-9.

This set of linear equations, Eq. (39) can be easily solved to find  $u_{bi}$  by using a linear solver.

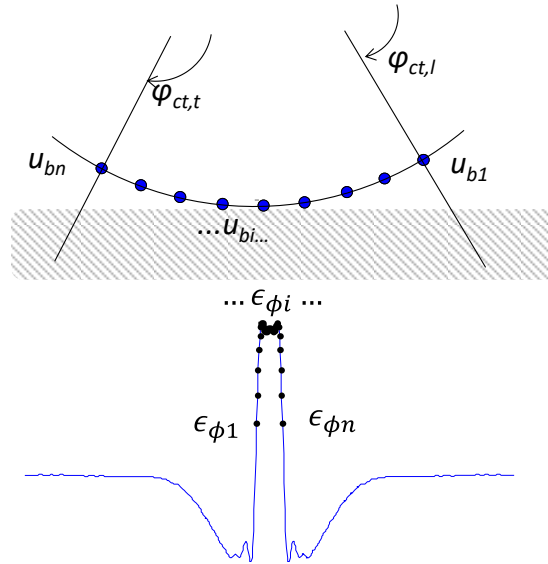


**Fig. 5-9 Discretization of radial deformation based at strain-measurement points**

The estimated radial deformations are plotted in Fig. 5-10. Notice that the deformation is estimated only within the contact patch. As test load increases, the radial deformation and the contact length increase as well.

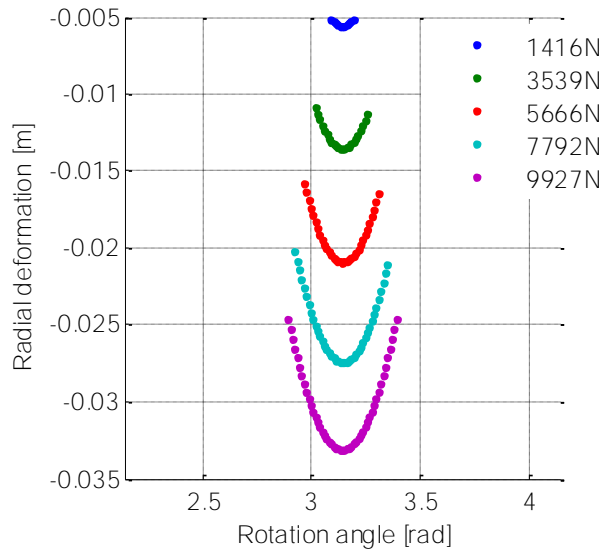


**Fig. 5-10 Radial deformations at different vertical loads estimated from strain measurements**

To check the accuracy of the solution, strains were recalculated from the solution ( $u_{bi}$ ) and compared with Fourier approximations of real measurements. This is shown in Fig. 5-11. Both methods agree with high accuracy.

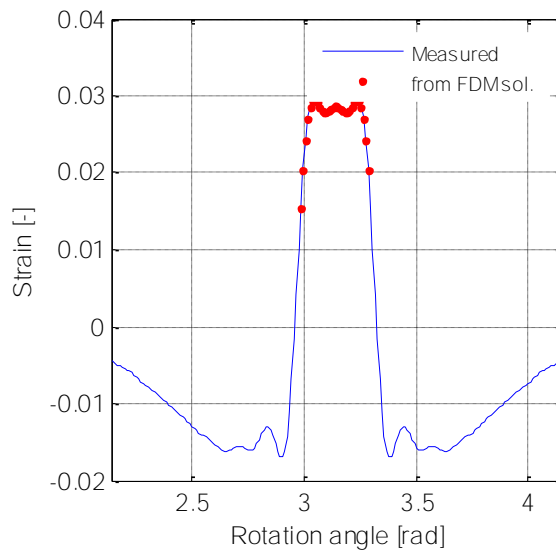


**Fig. 5-11 Convergence of FDM solution at  $F_z=5666N$**

## 5.2 APPLICATION OF STRAIN MEASUREMENT FOR CIRCUMFERENTIAL CONTACT PROBLEMS

A simple flexible ring model was introduced to be used with the strain measurement and the conventional method for contact problems was reviewed briefly. And then, a newly suggested method for solving the circumferential contact problem is described.

### 5.2.1 Flexible Ring Model

In the current study, a simple flexible ring model presented in [64] was used to obtain the deformation of the tread band. Fig. 5-12 illustrates a tire model comprising a circular beam and series of radial springs. The circular beam, with radius  $R$ , represents the tread band and the radial spring models the sidewall and air pressure.  $EI_b$  is the bending stiffness of the circular beam in unit of  $\text{Nm}^2$  and  $K_u$  is the stiffness per unit length of a radial spring in unit of  $\text{N/m}^2$ . A point load  $P$  is applied at the bottom of the ring.  $u_b(\varphi)$  is the radial deformation and positive sign means a radial-outward deformation.

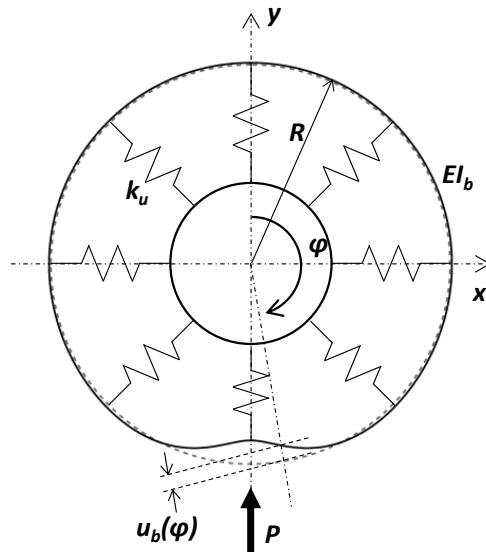


**Fig. 5-12 Flexible ring model subjected to a point load, adapted from [64]**

Assuming static equilibrium for an infinitesimal element of the circular beam, the equation for the tread band deformation can be written as:

$$\frac{d^5 u_b}{d\phi^5} + \frac{2d^3 u_b}{d\phi^3} + \lambda_b \frac{du_b}{d\phi} = 0 \quad (41)$$

where,

$$\lambda_u = \sqrt{\frac{R^4 k_u}{EI_b} + 1} \quad (42)$$

Eq. (43) is the solution to Eq. (41) with the boundary conditions: zero slopes at  $\varphi=0, \varphi=\pi$ , equilibriums of shear forces and external forces at  $\phi=0, \phi=\pi$ , and no rotational movement of the ring.

$$u_{(b)r\phi}(\phi) = P(\bar{C}_0 + \bar{C}_1 \cosh(\alpha\phi) \cos(\beta\phi) + \bar{C}_4 \sinh(\alpha\phi) \sin(\beta\phi)) \quad (43)$$

in which,

$$\bar{C}_0 = \frac{R^3}{2EI_b \pi \lambda_u^2} \quad (44)$$

$$\bar{C}_1 = \frac{R^3 (\alpha \cosh(\pi\alpha) \sin(\pi\beta) + \beta \cos(\pi\beta) \alpha \sinh(\pi\alpha))}{2EI_b \alpha \beta (\alpha^2 + \beta^2) (\cos(2\pi\beta) - \cosh(2\pi\alpha))} \quad (45)$$

$$\bar{C}_4 = \frac{R^3 (\beta \cosh(\pi\alpha) \sin(\pi\beta) - \alpha \cos(\pi\beta) \alpha \sinh(\pi\alpha))}{2EI_b \alpha \beta (\alpha^2 + \beta^2) (\cos(2\pi\beta) - \cosh(2\pi\alpha))} \quad (46)$$

where,

$$\alpha = \sqrt{\frac{\lambda_u - 1}{2}}, \quad \beta = \sqrt{\frac{\lambda_u + 1}{2}}$$

Fig. 5-13 illustrates the flexible ring deformed by the distributed force, in which  $p(\varphi_p)$  is the contact pressure distribution along the contact length. The contact angle is denoted by  $\Delta\varphi_c$ .  $u_b(\varphi; \varphi_p)$  is the radial deformation of the ring at  $\varphi$  contributed by  $p(\varphi_p)$ .

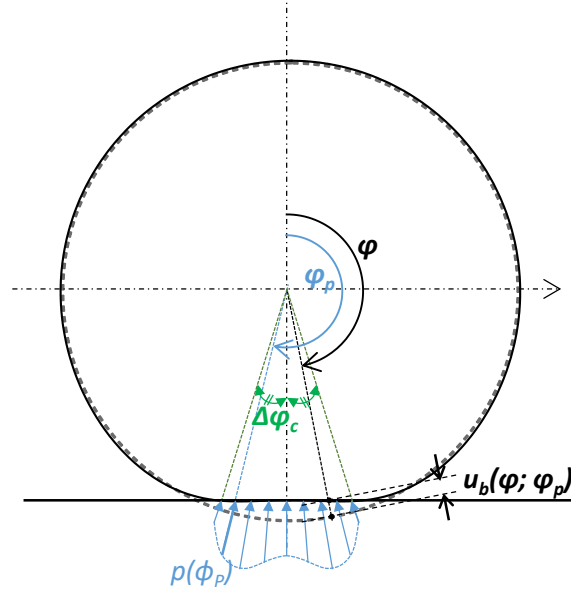


**Fig. 5-13 Flexible ring model when subjected to distributed load**

For the deflection of the tire subjected to distributed contact pressure,  $u_b(\varphi)$  is determined by integrating Eq. (43) as shown in Eq. (47).

$$u_b(\varphi) = \int_{\pi-\varphi_c}^{\pi+\varphi_c} p(\varphi_p) \bar{u}_b(\varphi; \varphi_p) R d\varphi_p \quad (47)$$

where,  $p(\varphi)$  is the contact pressure distribution along the contact length,  $\varphi_c$  is contact angle,  $\bar{u}_b(\varphi; \varphi_p)$  is the radial deformation of the ring at  $\varphi$  contributed by  $p(\varphi_p)$ , which can easily be obtained by shifting the solution function, Eq. (43), by  $\varphi_p$ . Thus, since tire parameters and pressure distribution are known, the radial deformation of the tread band can be calculated analytically.

To solve the contact problem using the ring model, the same contact model as presented in Section 5.1.2 was used. The pressure distribution was calculated by multiplying the tread deformation ( $u_b - u_r$ ) by its stiffness ( $k_t$ ) (refer to Fig. 5-8):

$$p(\phi) = k_t(u_b(\phi) - u_r(\phi)) \quad (48)$$

By substituting Eq. (48) into Eq. (47) and integrating,  $u_b(\phi)$  can be found. To solve this equation, it was discretized as is shown in Eq. (49).

$$u_b(\phi) = \sum_{j=1}^{N_\phi} [k_t(u_b(\phi) - u_r(\phi))] \bar{u}_b(\phi; \phi_{pj}) R \Delta\phi \quad (49)$$

where,  $N_\phi$  is the number of elements within the contact patch and  $\Delta\phi$  is the incremental angle for discretization. Simplifying, Eq. (49) is expressed as:

$$k_t \bar{U}(\bar{u}_b - \bar{u}_r) R \Delta\phi = \bar{u}_b \quad (50)$$

In this expression,  $\phi$  ranging between  $[0, 2\pi]$  is discretized into  $\phi_1, \phi_2, \dots, \phi_{N_t}$ , where  $N_t$  is number of discretized points and is determined by dividing  $2\pi$  by  $\Delta\phi$ .  $\bar{u}_b$  and  $\bar{u}_r$  are  $N_t \times 1$  vectors for tread band and total tire deformation, respectively.  $\bar{U}$  has  $N_T \times N_\phi$  dimension and its  $(i, j)$  element is  $\bar{u}_b(\phi_i; \phi_{pj})$ .

By collecting Eq. (50) for  $\bar{u}_b$ , the following equation is obtained:

$$\bar{u}_b = \left( \bar{U} - \frac{1}{k_t R \Delta\phi} I \right)^{-1} \bar{U} \bar{u}_r \quad (51)$$

Using Eq. (51), ring deformation can be obtained. However, the contact angle  $\phi_c$  is still unknown. This is determined through the iterative procedure until the two tread deformation constraints are satisfied. First, the tread rubber cannot be stretched, in other words, the pressure from Eq. (48) must be positive. Second, the tread rubber cannot be compressed into zero or negative thickness as discussed in [50]. This constraint can be mathematically written as:

$$0 < u_b - u_r < \tau \quad (52)$$

where,  $\tau$  is the tread thickness and  $u_r = d_0 - R_0(1 - \cos(\pi - \phi))$  from Eq. (37).

Usually, the second constraint is satisfied when realistic tire parameters are used. Therefore, first constraint is the only one which must be satisfied through the iterative

process.as illustrated in Fig. 5-14. This Iterative process continues until all of the points in the contact patch meet this constraint and contact angles are found.

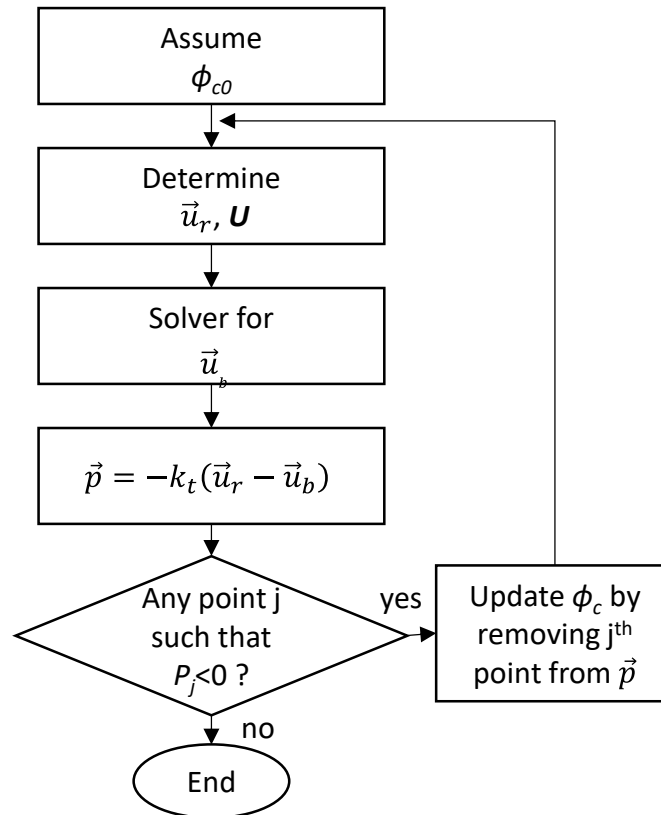


**Fig. 5-14 Flow chart to simulation for flexible ring model**

The stiffness parameters,  $EI$ ,  $k_u$ ,  $k_t$  are determined by using the error minimization method between estimated vertical load and the applied vertical load, which is the same approach suggested by Kim [64].

### 5.2.2 Solving the contact problem using strain measurement

The shape of the radial deformation of the ring is dominated by the applied pressure distribution. In this suggested method, the profile of contact pressure was adjusted so that the radial deformation from the flexible ring model (which doesn't have tread elements) can be fitted to that estimated from strain measurements. On the contrary, in the conventional contact problem, the pressure distribution is identified using

the tire-road contact model during the numerical solution. For the purpose of representing arbitrary shapes of pressure profiles, a numerical model was proposed as shown in Eq. (53).

$$p(x) = p_0 \left( 1 + S \left( x \frac{a_1 + a_2}{2} \right) \right) \left( (x - a_1)(x - a_2) \left( \frac{S_f}{5000} + \left( x - \frac{a_1 + a_2}{2} \right)^2 \right) \right)^{\frac{1}{n_p}} \quad (53)$$

where,

$a_1, a_2$ : contact length in [m] from the center to leading and trailing edges, respectively.

$S$ : Shape factor for the asymmetric distribution

$S_f, n_p$ : shape factors for diverse curvatures in the pressure distribution

$$p_0 = F_z / \int_{a_1}^{a_2} \left( 1 + S \left( \phi - \frac{a_1 + a_2}{2} \right) \right) \left( (x - a_1)(x - a_2) \left( \frac{S_f}{A} + \left( x - \frac{a_1 + a_2}{2} \right)^2 \right) \right)^{\frac{1}{n_p}} dx$$

This numerical expression for the pressure distribution is update form suggested in [65] to generate the both of concave and convex shape profile. In this study, only symmetric pressure distributions are assumed, so the shape factor  $S$  is set to zero. Fig. 5-15 illustrates the effects of  $n_p$  and  $s_f$  on pressure distribution shapes.  $a_1, a_2$  are known from the peak to peak values of the strain rates and  $p_0$  can also be calculated once other shape parameters are set under known load,  $F_z$ . Thus, only  $S_f$  and  $n_p$  need to be determined through the optimization process which tries to minimize the difference between the radial deformations identified from the strain measurements and calculated by the flexible ring model.

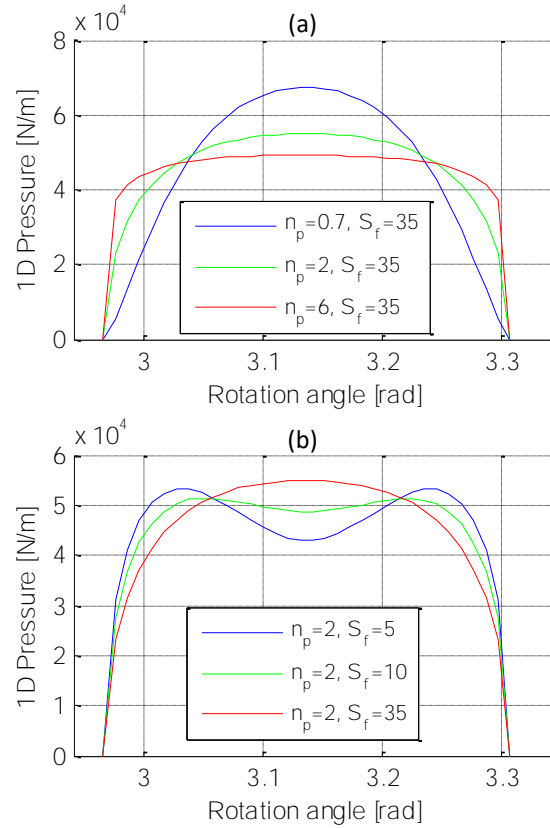


**Fig. 5-15 Realization of one dimensional pressure distribution for diverse shape factors: (a) effects of  $n_p$ , (b) effects of  $S_f$**

The stiffness parameters for this ring model cannot be directly measured since they are pressure and load dependent and have different layers. Identifying these values is a challenging task. In this research, these parameters were determined through the optimization process. The optimization formula to identify the pressure distribution and model parameters is written as follows:

$$\text{Find } EI_b, k_u, n_p, S_f, \text{ such that Min. } \sum_{i=1}^5 \left\| \bar{u}_{Sim}^{(i)} - \bar{u}_{FDM}^{(i)} \right\|^2$$

where,  $\bar{u}_{FDM}$  is known value from strain measurements by FDM,  $\bar{u}_{Sim}$  can be calculated by using Eq. (51) and  $i$  represents the different test loads. The tire parameters and shape factors,  $(EI_u, k_u, n_p, S_f)$ , are design variables in this optimization scheme.  $EI_u$ ,

is assumed to be constant over the entire load range whereas  $k_u$  has the load dependency as suggested in [66];

$$k_u = Ae^{Bd_0} \quad (54)$$

Therefore, using this methodology, the pressure distribution and tire parameters can be estimated based on the combination of the flexible ring model and strain measurements.

### 5.3 Estimation Results for Tire Parameters and Characteristics

The test results of the experimental set shown in Table 3-1 were used again. Since this study aims at characterization of in-plane dynamics, experimental data at zero slip angle was chosen. The inflation pressure and test speed were set to 2.3 bars and 65 km/h, respectively for all tests. The measured strains along time,  $t$ , was converted to along the rotational angle, which was possible the tire rolls at constant speed without any longitudinal slips as mentioned in Section 3.4.

Strain measurements were performed for three different P235/55R19 passenger tires to validate the proposed method based on strain measurements. These tires had the same specifications except for the belt constructions: LTR belt with 27° belt angle (spec A), PCR belt with 27° belt angle (spec B) and PCR belt with 30° belt angle (Spec D). Geometrical parameters ( $R$ ,  $R_0$ ,  $R_l$ ) and stiffness parameters ( $El_b$ ,  $k_u$ ,  $k_t$ ) were needed for this simulation. Loaded rolling radius,  $R_l$ , was measured on the Flat-Trac test rig. Unloaded radius of tire,  $R_0$ , was determined by extrapolating the loaded rolling radius at zero test load. The radius of the ring,  $R$ , is the distance between wheel center and neutral plane of the circular bream.  $R_0$ ,  $R$  and  $y$  are shown in Fig. 5-16.  $y$  is determined such that the position of the neutral axis is located at the first belt position as discussed in Section 5.1.1 but slightly adjusted for different tests in order to match the simulated strain to the measured strain, which slightly varies among test runs, even for the same tire.

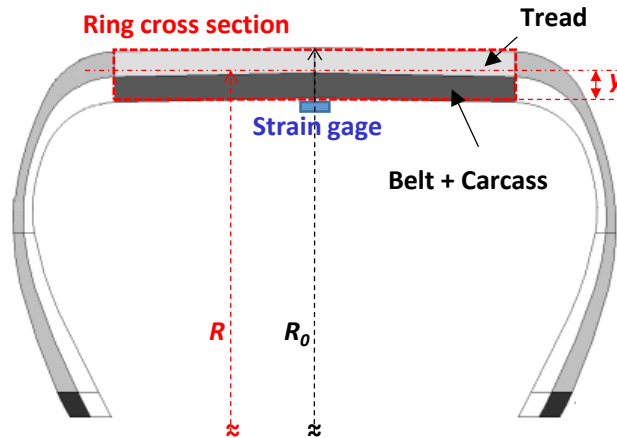


**Fig. 5-16 Geometrical parameters of tire for simulation**

Fig. 5-17 compares the radial deformations from the proposed method using optimization (shown as ‘from opti.’ in Fig. 5-17), from the conventional method using the flexible ring model (shown as ‘from model’ in Fig. 5-17) and identified from real strain measurements using FDM. (shown as ‘from strain’ in Fig. 5-17).

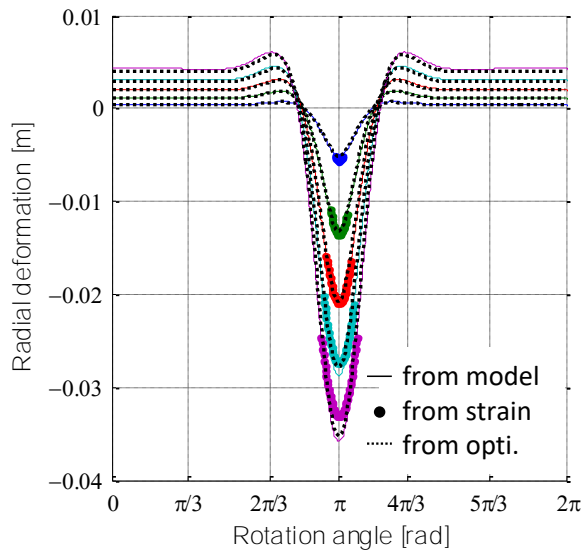


**Fig. 5-17 Radial deformations estimated by different methodologies: based on flexible ring model, strain measurement and optimization**

The proposed method results agree well with the conventional method. However, they both show discrepancies when compared to the one estimated from measurement

at the highest load. The new and conventional methods use the same flexible ring model and it might not represent the tire deformation properly under higher loads, i.e., the deflection becomes large. The tire models used in simple and static methods, did not include the circumferential elements of the sidewall, frictional effects between the tire and the road, nor the shear tread deformation. More discussions on this will be delivered later.

Fig. 5-18 presents the contact length obtained from various methods. Static footprints ('F/P test' in Fig. 5-18) were measured on the indoor static test rig at somewhat different test loads but the entire range of test loads overlap with those of the Flat-Trac test making comparisons possible. The center contact length from the foot print test was chosen for the comparison with the other methods

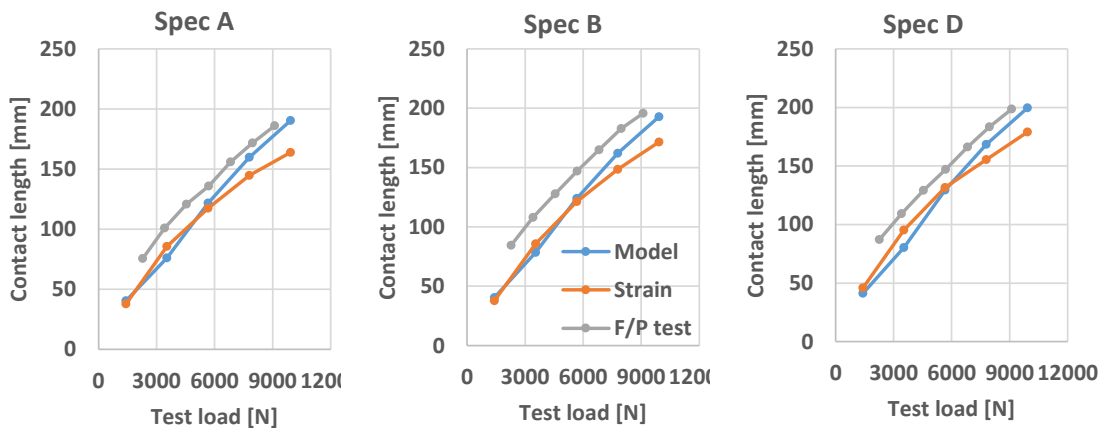


**Fig. 5-18 Comparison of contact lengths obtained from different methodologies**

The measured contact lengths are always longer than the estimated ones. When it comes to the flexible ring model simulation ('Model' in Fig. 5-18), the main input parameter is the vertical deformation of the loaded tire. This deformation was measured on the Flat-Trac test rig at 65 Km/h. The vertical stiffness of the rolling tire is expected to be higher than that of the static tire because the dynamic modulus of the rubber is higher, making the rolling tire stiffer. Fig. 5-19 compares the vertical deformations as a function

of the test load; one was measured on the static test rig; the other on the Flat Trac test rig.

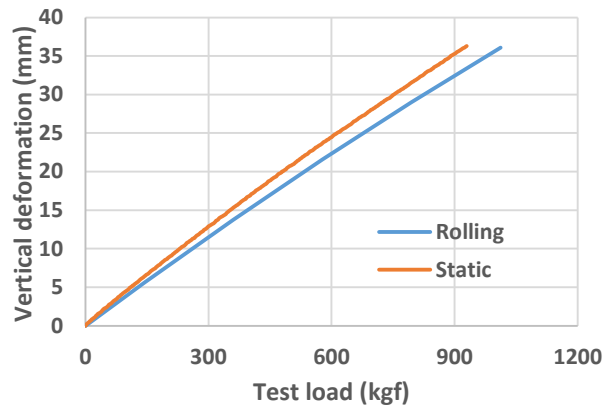
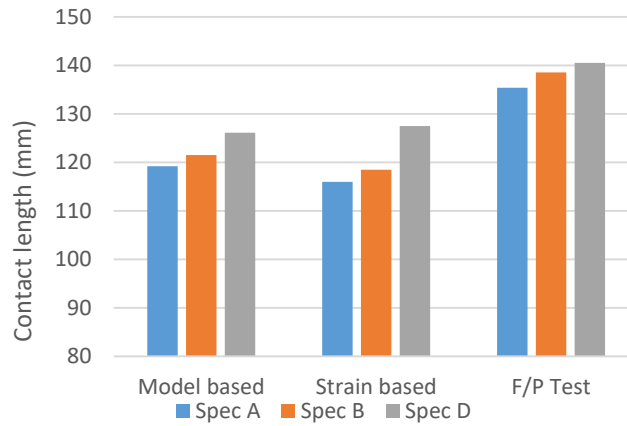


**Fig. 5-19 Vertical deformations versus test load for rolling and static tire**

The shorter contact length due to higher vertical stiffness of the rolling tire would be compensated by the slippery road surface assumed in the model (no frictional force), since the slippery road surface tends to contribute to longer contact lengths. It is observed that the contact length from simulation ('Model' in Fig. 5-18) increases rapidly as the test load is increased. As the test load increases, the frictional force also increases which makes the contact length increase less as observed in the other cases ('FP test' and 'Strain' in Fig. 5-18). The contact length estimated from the strain measurement ('Strain' in Fig. 5-18) shows similar load dependency to the footprint measurements. The shorter contact length from this method can be explained by the dynamic stiffening effect since strain was also measured inside the rolling tire. Moreover, the centrifugal effect of the rolling tire causes the tire to "lift" vertically away from the road surface at higher speeds.

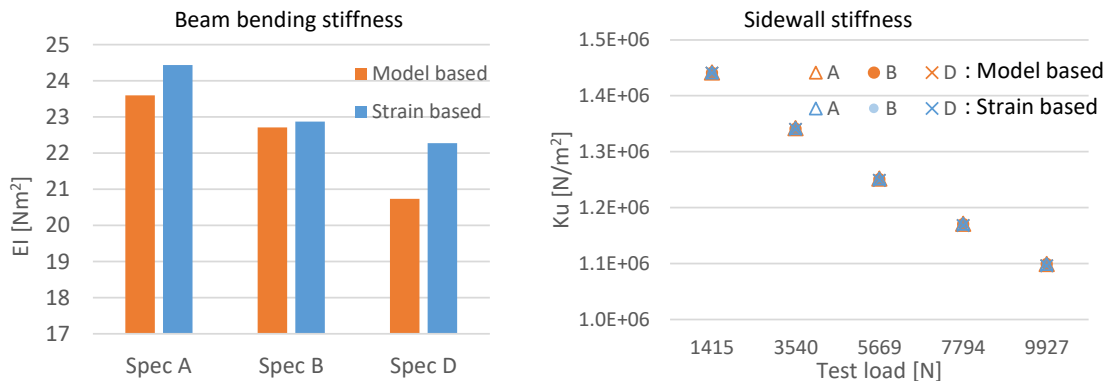
Fig. 5-20 compares the contact lengths of different tires obtained from different methods. Center contact lengths at the reference load are compared. For all cases, Spec D has the longest contact length whereas Spec A has the shortest. All methods demonstrate the expected trend when the belt stiffness varies from stronger (Spec A) to weaker (Spec D). However, the contact length for Spec D is slightly longer than other specs when contact lengths are measured on the static foot print test rig, whereas it is much longer when estimated from strain measurements. This phenomenon could be due to the

difference in contact features between the rolling and static tires, especially when the tire has lower belt stiffness (Spec D).



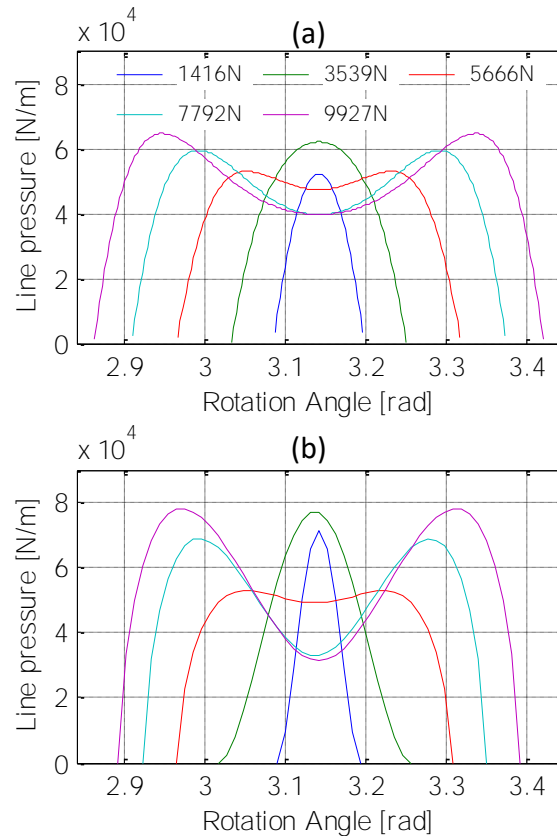
**Fig. 5-20 Comparison of contact lengths at reference test load for different tire specifications**

Fig. 5-21 shows the estimated stiffness parameters from the flexible ring model which includes the optimization with strain measurements. Both identification methods deliver the same ranking for  $EI_b$ : Spec A > Spec B > Spec D. This can be expected based on the belt construction of each tire. However, sidewall stiffness is almost the same regardless of estimation methods and tire specs because the tires only differ in the belt construction.



**Fig. 5-21 Estimated stiffness parameters for different tire specifications using different methodologies**

However, it was noticed that the sidewall stiffness seems less influential in the objective function because it varied less from the initial value during the optimization process. The validity of the sidewall stiffness estimation should be repeated using tires with sufficiently different sidewall stiffness. One dimensional pressure distribution for both methods are shown in Fig. 5-22: Fig. 5-22 (a) is the result of the flexible ring model and Fig. 5-22 (b) from the optimization method based on strain measurements. Both of them show typical tendency that the pressure distribution changes from convex to concave shape as test load increases, which was also discussed in [64]. The strain based method showed more dramatic curvature change.



**Fig. 5-22 Estimated one dimensional pressure distribution under different test loads: (a) based on flexible ring model only, (b) based on optimization results (flexible ring model + strain measurements)**

Fig. 5-23 compares the pressure distribution of each tire estimated from both methods at the reference test load. As observed from the comparison of contact lengths,

Spec A shows the highest-pressure distribution whereas the lowest one is observed for Spec D, regardless of the estimation method used.

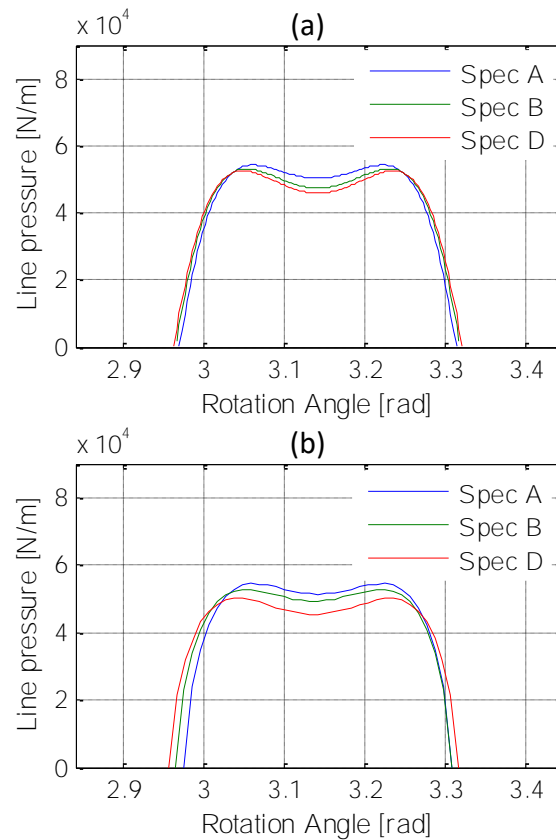


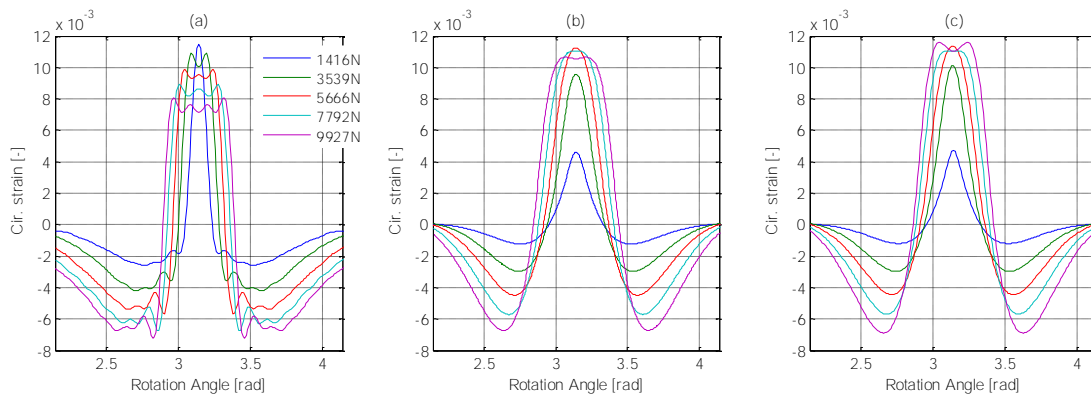
**Fig. 5-23 Estimated pressure distributions at reference test load for different tire specifications: (a) based on flexible ring model only (b) based on optimization results (flexible ring model + strain measurements)**

Further validation is needed to secure the strain-based estimation method for contact lengths and contact pressure distribution with a specially designed test device or FEM simulation, which can deliver the contact features of the rolling tire at high speeds.

## 5.4 Discussions

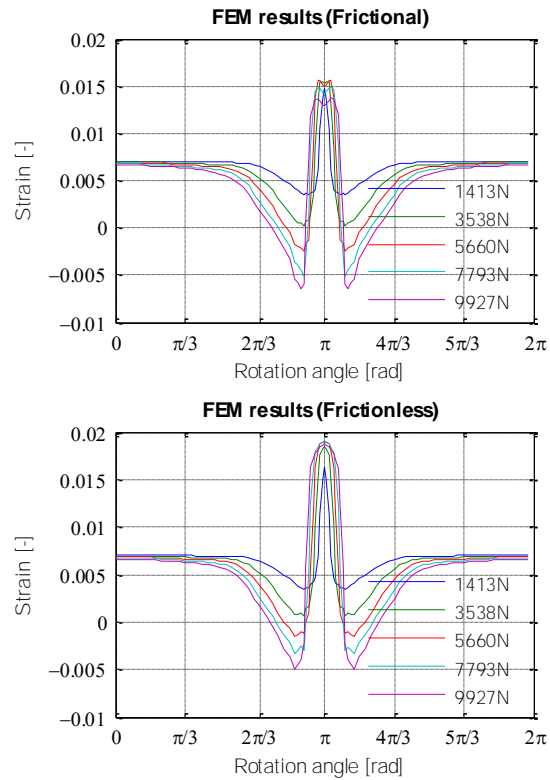
Fig. 5-24 (a) presents measured strains and Fig. 5-24 (b) and (c) show the calculated strains based on radial deformations using conventional method and the proposed method, respectively. Comparing the experimental measurements with the

simulated strains from both methods, they share the same features as the experimental data when test load increases. The peak compression and the width of strain response curve increase consistently as the test load increase. However, discrepancy is observed when it comes to the tension in the contact region. In the experimental data, the tension in the contact area monotonically decreases as the test load increases whereas simulation results present increasing tension when test load increases, specifically from 1416N to 5562N. Diverse factors can contribute to this disagreement but the most likely cause is the nonexistence of friction between the tread and the road surface in the simulation.



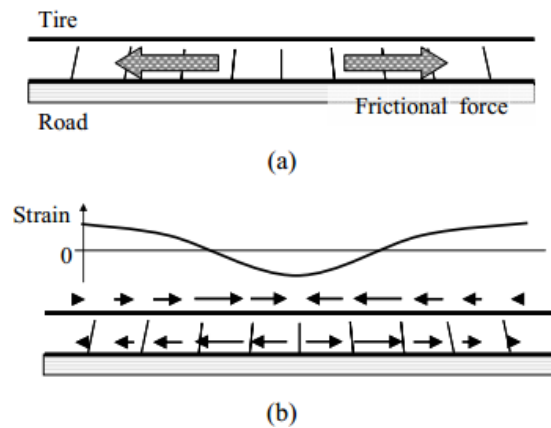
**Fig. 5-24 Circumferential strains from simulation and measurements: (a) measured strain, (b) simulated strain from conventional flexible ring contact model (c) simulated strain from new method using strain measurements**

Fig. 5-25 shows finite element model (FEM) simulation results of circumferential strains calculated at the innerliner for a 215/60R16 size tire. Although the tire of FEM model is different from the tires used in this study, simulation results show the general effects of the frictional force on circumferential strains. The upper chart shows the simulation results when the static tire is subjected to a vertical load on the frictional surface with the friction coefficient of 0.5. The same simulation is repeated with the coefficient of zero and the results are shown in the lower chart. Comparing both, it is obvious that the results which includes friction have more similar features to experimental data; as the test load increases, the tension in the contact region decreases



**Fig. 5-25 FEM simulation results for circumferential strains**

Fig. 5-26 explains the effects of frictional force on circumferential strains [44]. The frictional force causes tips of the tread elements adhering to the road surface to move outward in the circumferential direction. This leads to bending deformation of tread elements inducing compressive horizontal forces in the tire inner layers.



**Fig. 5-26 Cross-sectional deformation and strain distribution of a tire derived from the static frictional force: (a) the applied load (b) the strain distribution [44]**

As a result, the tension induced from the bending motion of the ring is slightly reduced in the contact region.

It should also be mentioned that even though the optimization results of the suggested method for the radial deformation are very close to those estimated from strain measurements as presented in Fig. 5-17, there are still considerable differences in the case of strains. This indicates that the strains are very sensitive to the shape of the radial deformation because they depend on the first and second derivative of the radial deformation on  $\varphi$ . Thus, if the model is not complete enough to describe the real strains of the tire, utilizing the radial deformation is a more effective way to identify tire characteristics as presented here rather than trying to fit the simulated strains directly to the measured ones.

## 5.5 Chapter Conclusion

In this chapter, tire parameters related in-plane dynamics were estimated by incorporating a simple flexible ring model into the parameter-identification process based on strain measurements. To accomplish this complex task, based on FEM simulation, the strain-deformation differential equation for the radial deformation of the tread band was developed first, which can effectively represent strain measurements while it is simple enough for application purposes. In this approach, measured strains were used as the input to the model. Finite Difference Method (FDM) was used to solve the equation with the appropriate boundary conditions. A simple-static flexible ring model was developed and combined with this estimated radial deformation in order to identify contact characteristics between the tire and the road (road is assumed to be flat). This contact problem is solved by using optimization and adjusting the pressure distribution such that the radial deformation from the model fits that of the previously estimated one from strain measurements. During this process, related parameters such as the bending stiffness of the ring and sidewall stiffness are also determined.

For the validation purpose, strains are measured at the innerliner for three tires with different belt structures. Contact characteristics were identified by proposed

method utilizing strain measurements. A conventional method, which use flexible ring model and tread-road contact model was also introduce for the comparison purpose. In this method, tire parameters are estimated by the error minimizing technique between the estimated load and the measured load. The bending stiffness of the tread band and sidewall stiffness estimated from both methods agree well with small differences. The estimated pressure distribution from both methods shows similar tendency presenting more convex shape under higher loads.

However, the flexible ring model needs to be developed further to include the frictional effects to explain the features of measured strains more closely especially for higher test loads. Also, experimental measurements of the footprint features of a rolling tire at high speeds are required to confirm the validity of the proposed identification method.

In this chapter, the static tire model was used for the contact problem, so the identified pressure distribution is symmetric shape. Also, it cannot handle with the inertial effects, dynamic stiffening effect of rolling tire nor damping effects. In the following chapter, dynamic tire models will be used combined with the information from strain measurements.

## 6 ESTIMATION OF TIRE DYNAMIC CHARACTERISTICS

In the previous chapter, the contact problem was solved by use of the strain measurements, which doesn't require any tread-road contact model. However, the static model was used which cannot represent the dynamic characteristics of the rolling tire at high speeds. Thus, the dynamic pressure distribution or damping characteristics of the tire cannot be identified.

In this chapter, estimation of dynamic tire parameters and pressure distributions based on strain measurements, are investigated. To achieve this goal, different flexible ring models were studied [67], modified and implemented: one has a simple contact model considering the pressure distribution in the radial direction only and the other has more advanced contact model by including the shear deformation of the tread. By comparing the simulation results, an appropriate model was chosen.

For validation and application purposes, strains were measured inside the loaded rolling tire subjected to different loads, different inflation pressures as well as different speeds. Information from strain measurements were fed into the model to estimate the model parameters. Simulated strains from the ring model were compared to the measured ones and used to identify the damping characteristics of the tire. Finally, the estimated dynamic pressure distribution, was used in the Brush tire model to predict the lateral forces and the results were compared with the results from the classical Brush tire model.

Through this work, the potential issue in numerical implementation of the flexible ring model was improved by satisfying the boundary conditions at both edges simultaneously. A novel approach to identify sidewall stiffness and damping of a rolling tire was proposed by introducing strain measurements to flexible ring tire model. Finally, the Brush model was improved by the use of identified pressure distribution from the flexible ring model.

## 6.1 Flexible Ring Model for Rolling Tire

Fig. 6-1 illustrate the advanced flexible ring model which can describe the behavior of the rolling tire. The circumferential sidewall elements were included as well as the damping effects. Three different external forces were considered: two forces acting at the neutral axis of the ring in the radial and circumferential directions ( $q_u, q_v$ ) and the moment in wheel axial direction ( $q_\beta$ ). The translational deformation of the tread band is expressed as  $u$  and  $v$  in the radial and transversal direction respectively, which are same as  $u_b$  and  $v_b$  in Section 5.2.1, but the subscript 'b' is omitted for the simplification purpose. To consider the external moment on the tread band, new deformation variable ' $\beta$ ' is introduced, which are the rotation angle of the tread band.

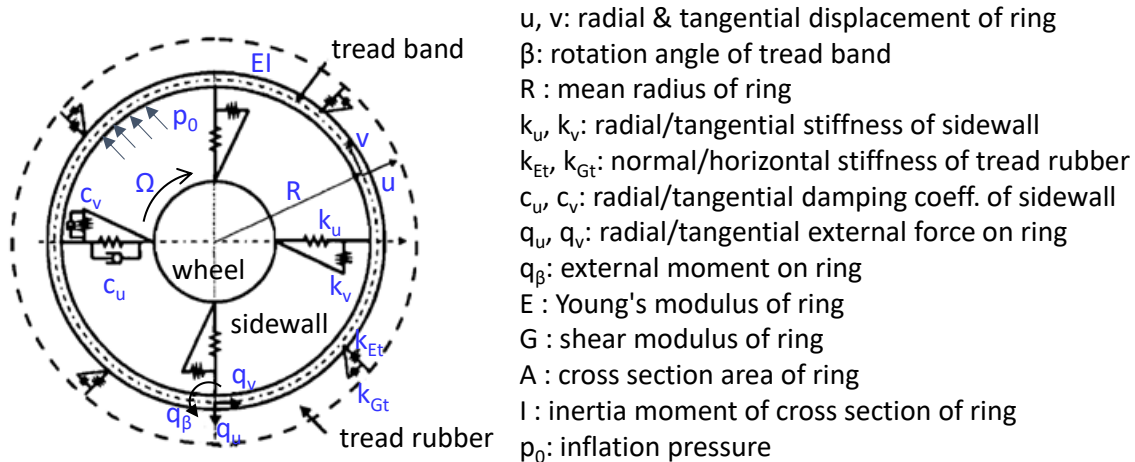


**Fig. 6-1 Flexible ring model for rolling tire with circumferential components**

It is assumed that the springs are connected to the middle surface of the ring. This model has one degree of freedom allowing the wheel angular speed ( $\dot{\theta}_r$ ) to vary around its mean value. The variation of the wheel angular speed was assumed to be small such that the equation of motion can be linearized. The torque  $T$  is applied to the wheel axis to roll the tire at the given rotation speed  $\Omega$ . The pressurized air pressure in the pneumatic tire is very important to the tire functions, it should be modeled properly in the ring model. Inflation pressure effects were introduced by varying sidewall stiffness ( $k_u, k_v$ ) along the inflation pressure and the pretension ( $\sigma_\theta^0$ ) in the circular ring. This

pretension is also caused by the centrifugal force due to rotation. The deformation of the tread band should be parallel to the wheel plane and be uniform over the tire width so that the dynamics of the tire-wheel system is represented as a two-dimensional problem.

The equation of the motion was originally driven by Gong using Hamilton's principle [50] and modified in this research by neglecting the translational motion of the wheel and including the external moment on the ring ( $q_\theta$ ) referring [61]. In the derivation two axes frames were used: one is attached to the ring rotating together ( $X^*Z^*$ ) and the other is the inertial frame ( $XY$ ). The derivation was performed in the rotational frame ( $X^*Z^*$ ) and the ring deformation at the rotation angle  $\vartheta$ , are expressed with variables  $u$ ,  $v$ ,  $\beta$ . Notice that the rotation angle  $\vartheta$  is defined in the rotational axes system ( $XZ$ ) and  $\phi$  is used in the fixed coordinate system.

Various energy components were introduced to derive the equation based on Hamilton's principle such as:

- S1: Strain energy stored in the tread band (pretension,  $\sigma_\theta^0 A$ , considered)

$$S_1 = \int_0^{2\pi} \frac{1}{2} \left[ 2\sigma_\theta^0 A \left( u + \frac{\partial v}{\partial \theta} \right) + \frac{\sigma_\theta^0 A}{R} \left( v - \frac{\partial u}{\partial \theta} \right)^2 + \frac{E}{R} \left\{ A \left( u + \frac{\partial v}{\partial \theta} \right) \right\} \right] d\theta \quad (55)$$

- T1: Kinetic energy of the ring body

$$T_1 = b \int_0^{2\pi} \int_{-t_0/2}^{t_0/2} \frac{1}{2} \rho R |\dot{\gamma}|^2 dy d\theta \quad (56)$$

where,

$$\dot{\gamma} = (\dot{w} - v\Omega)\vec{n}_r + \{\dot{v} + (R + u)\}\vec{n}_\theta$$

- T2: Kinetic energy of the wheel due to rotation.

$$T_2 = \frac{I_r (\Omega + \dot{\theta}_r)^2}{2} \quad (57)$$

- S2: Elastic energy of stored in the sidewall

$$S_2 = \int_0^{2\pi} \frac{1}{2} [k_v (v - R\theta_r)^2 + k_u u^2] r d\theta \quad (58)$$

- Energy dissipation in the sidewall due to non-conservative viscous damping forces in the sidewall

$$D = \int_0^{2\pi} \frac{1}{2} (c_u \dot{u}^2 + c_v \dot{v}^2) r d\theta \quad (59)$$

- $\delta E_1$ : Virtual work done by extensional forces ( $q_u, q_v, q_\beta$ )

$$\delta E_1 = \int_0^{2\pi} (q_u \delta u + q_v \delta v + q_\beta \delta \beta) R d\theta + T \delta \theta_r \quad (60)$$

- $\delta E_2$ : Virtual work done by the inflation pressure ( $p_0$ )

$$\delta E_2 = \int_0^{2\pi} p_0 b \left[ \left( 1 + \frac{1}{R} \left( \frac{\partial v}{\partial \theta} + u \right) \right) \delta u - \frac{1}{R} \left( \frac{\partial w}{\partial \theta} - v \right) \delta v \right] R d\theta \quad (61)$$

The total virtual work is

$$\delta E = \delta E_1 + \delta E_2 \quad (62)$$

Hamilton's principle reads that the time integral over any interval of the sum of virtual kinetic energy change and virtual work vanishes when the virtual displacements are made from configuration of the actual motion and when the final configurations are given:

$$\int_{t_i}^{t_e} (\delta T + \delta W) dt = 0 \quad (63)$$

or, using Lagrangian function, it can be written as:

$$\int_{t_i}^{t_e} (\delta L + \delta E) dt = 0 \quad (64)$$

where,  $t_i$  and  $t_e$  are the times at the initial stage and the final stage over the virtual work process.  $L$  is the Lagrangian function and for this system is this can be calculated by;

$$L = T_1 + T_2 - S_1 - S_2 \quad (65)$$

The Euler-Lagrange equations for our ring model is now derived as:

$$\frac{\partial}{\partial t} \frac{\partial L}{\partial \dot{u}} + \frac{\partial}{\partial \theta} \frac{\partial L}{\partial u'} - \frac{\partial^2}{\partial \theta^2} \frac{\partial L}{\partial u''} - \frac{\partial L}{\partial u} + \frac{\partial D}{\partial \dot{u}} = Q_1 \quad (66)$$

$$\frac{\partial}{\partial t} \frac{\partial L}{\partial \dot{v}} + \frac{\partial}{\partial \theta} \frac{\partial L}{\partial v'} - \frac{\partial L}{\partial v} + \frac{\partial D}{\partial \dot{v}} = Q_2 \quad (67)$$

$$\frac{\partial}{\partial t} \frac{\partial L}{\partial \beta} - \frac{\partial L}{\partial \beta} = Q_3 \quad (68)$$

$$\frac{\partial}{\partial t} \frac{\partial L}{\partial \dot{\theta}_r} - \frac{\partial L}{\partial \theta_r} = Q_4 \quad (69)$$

where,  $Q_1 \sim Q_4$  are generalized forces:

$$Q_1 = \int_0^{2\pi} R \left( q_u + \left( 1 + \frac{v' + w}{R} \right) p_0 b \right) d\theta \quad (70)$$

$$Q_2 = \int_0^{2\pi} R \left( q_v - \frac{w' - v}{R} p_0 b \right) d\theta \quad (71)$$

$$Q_3 = \int_0^{2\pi} R q_\beta d\theta \quad (72)$$

$$Q_4 = T \quad (73)$$

Using Bernoulli-Euler assumption and inextensibility of the ring (Eq. 34), deformation variables have the following relationship with each other.

$$u = -\frac{\partial v}{\partial \theta} \quad (74)$$

$$\beta = \frac{1}{R} \left( v - \frac{\partial u}{\partial \theta} \right) \quad (75)$$

After substituting energy components Eq. (55~59) and generalized forces Eq. (70~73) into Euler-Lagrange equations Eq. (66~69) and simplifying by eliminating the deformation variables,  $u$ ,  $\beta$  by use of Eq. (74~75), the final governing equation can be derived as following:

$$\begin{aligned} & -\frac{EI}{R^4} \left( \frac{\partial^2 v}{\partial \theta^2} + 2 \frac{\partial^4 v}{\partial \theta^4} + \frac{\partial^6 v}{\partial \theta^6} \right) + \frac{\sigma_{\theta}^0 A}{R^2} \left( v + 2 \frac{\partial^2 v}{\partial \theta^2} + \frac{\partial^4 v}{\partial \theta^4} \right) - \frac{p_0 b}{R} \left( v + \frac{\partial^2 v}{\partial \theta^2} \right) \\ & - c_w \frac{\partial^2 \dot{v}}{\partial \theta^2} + c_v \dot{v} - k_u \frac{\partial^2 v}{\partial \theta^2} + k_v (v - R\theta_r) \\ & + \rho A \left[ \ddot{v} - \frac{\partial^2 \dot{v}}{\partial \theta^2} - 4\Omega \frac{\partial \dot{v}}{\partial \theta} + \Omega^2 \left( \frac{\partial^2 v}{\partial \theta^2} - v \right) \right] = q_v + \frac{\partial u}{\partial \theta} + \frac{1}{R} \left( q_{\beta} + \frac{\partial^2 q_{\beta}}{\partial \theta^2} \right) \end{aligned} \quad (76)$$

$$I_r \ddot{\theta}_r + 2\pi k_v R^3 \theta_r - R^2 \int_0^{2\pi} k_v v d\theta = T \quad (77)$$

Under free rolling condition,  $T=0$  and Eq. (77) is reduced to  $R\ddot{\theta}_r = \int_0^{2\pi} v d\theta$ , which simply relate the windup rotation angle  $\vartheta_r$  with the tangential displacement  $v$ . Details on how to derive equations can be found in [50] and [61].

## 6.2 Boundary Condition for Tread-Road Contact

To solve the contact problems using flexible ring models, appropriate contact models between the tread and road are required. In this study, two different boundary conditions were used to figure out their effects on the strains as well as to choose more appropriated model for the application purpose.

The previously used contact model for the static flexible ring model was again used with dynamic models. The tread elements were modeled as radial springs attached outside the ring at the center line. The contact pressure applied in the radial direction only as presented in Fig. 6-2 and can be calculated by Eq. (78). This assumption means that there are horizontal shear stresses along the contact patch which are always directed toward the center of the contact patch. Akasaka [68] claimed that “This friction force occurs in the process of extending the tread arc to conform to the flat surface of the road way”, as illustrated in Fig. 6-3 .

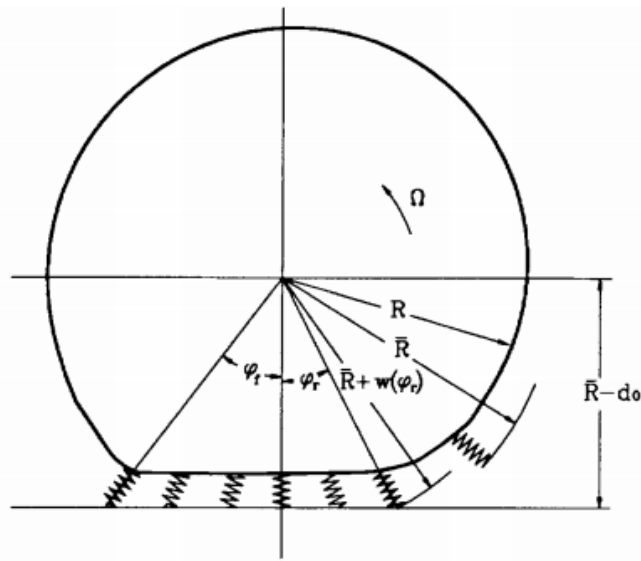


**Fig. 6-2 Tread elements models as radial spring [50]**

$$q_u(\phi) = k_t(u(\phi) + d_0 - \bar{R}(1 - \cos \phi)) \quad (78)$$

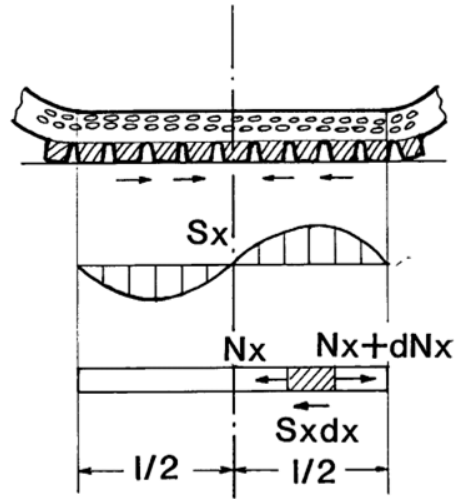


**Fig. 6-3 Distribution of friction force on the tread surface in contact with the roadway [68]**

Although this can explain the contact phenomenon of the solid tire, this assumption might not be adequate for the pneumatic tires. Experimental results show that the frictional forces arise outward of the contact, which is the attribute of pneumatic tires with steel belts. The conceptual friction force distribution is illustrated in Fig. 6-4 by Pottinger [69].

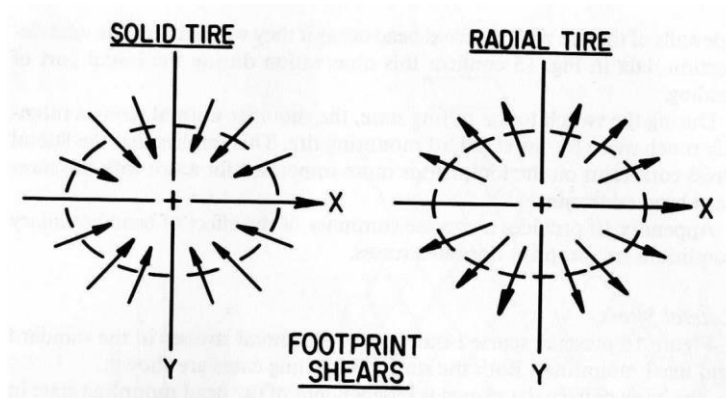


**Fig. 6-4 Directions of shear stress for radial pneumatic tire compared to solid tire [69]**

Kim introduced more advanced compatibility condition for the contact between the rolling tire and the flat road by considering the shear deformation of the tread

elements [61] and this compatibility model was originally suggested in [62]. He also introduced the exact definition of the free rolling and included it in deriving compatibility equations of the tread elements. Fig. 6-5 shows the geometry of the deformed (solid line) and undeformed (dotted line) flexible ring model with the tread elements. During the deformation due to the normal loading,  $P_0$  (on the tread band) and  $Q_0$  move to the deformed positions  $P$  and  $Q$  respectively. The curvature change is considered through  $\eta$ , the declination angle between the normal to the ring and vertical plumb line.  $\eta$  related to the rotation angle  $\beta$  of the tread band cross section by  $\eta = \phi + \beta$ .  $\hat{n}_r, \hat{n}_\theta$  are unit vectors in the radial and tangential directions at points on the treadband axis and  $\hat{n}, \hat{t}$  are unit vectors in the normal and tangential directions of the tread band axis.  $\hat{i}, \hat{k}$  are unit vectors along  $x$  and  $z$  axis respectively in the inertial frame.

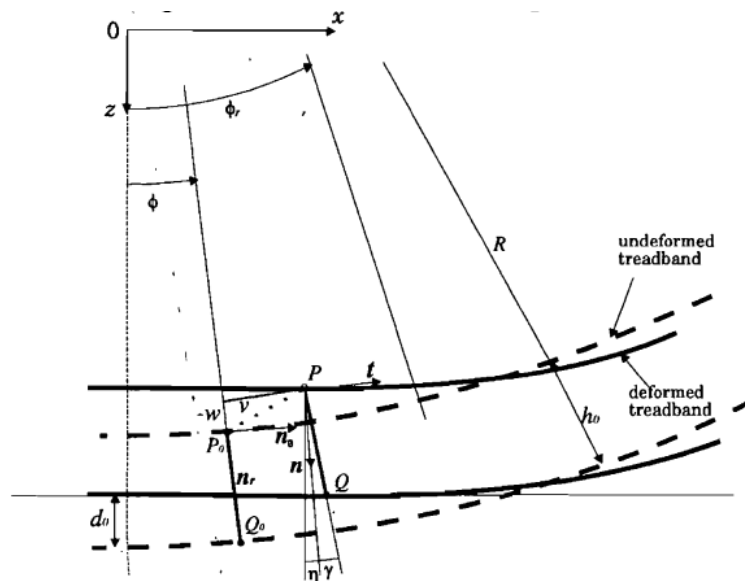


**Fig. 6-5 The geometry of the treadband and tread rubber in undeformed and deformed state [61]**

The tread thickness and shear deformation, i.e.,  $h(\varphi)$  and  $\gamma h(\varphi)$  expressed in  $\hat{n} \hat{t}$  coordinate system was derived using two boundary conditions for the loaded rolling tire; Point  $Q$  in the contact region should be located on the road surface and should travel at the same speed as the rolling tire for the pure rolling without any slippages. Thus, the loaded radius  $R_l$  and the effective rolling radius  $R_e$  were used in boundary conditions. After

the vector analysis for Point  $P$  and  $Q$  with introduced constraints,  $h(\phi)$  and  $\gamma h(\phi)$  are derived as functions of tread band deformations, i.e.,  $u, v, \eta$ .

$$\begin{aligned} h(\phi) &= R_l \cos \eta + R_e \phi \sin \eta - (R + w) \cos(\phi - \eta) + v \sin(\phi - \eta) \\ \gamma h(\phi) &= -R_l \sin \eta + R_e \phi \cos \eta - (R + w) \sin(\phi - \eta) + v \sin(\phi - \eta) \end{aligned} \quad (79)$$

The normal pressure and shear stress on the tread surface are

$$\begin{aligned} f_n(\phi) &= K_{Et}(h(\phi) - h_0) \\ f_t(\phi) &= K_{Gt}\gamma h(\phi) \end{aligned} \quad (80)$$

where,  $K_{Et}$  and  $K_{Gt}$  are the normal and shear stress of tread rubber per unit length of tread band. The external force distributions to the ring in the radial and tangential direction ( $q_u, q_v$ ) and the moment ( $q_\beta$ ) are obtained from  $f_n$  and  $f_t$  thorough the following coordinate transformation.

$$\begin{Bmatrix} q_u \\ q_v \\ q_\beta \end{Bmatrix} = \begin{bmatrix} \cos(\phi - \eta) & \sin(\phi - \eta) \\ -\sin(\phi - \eta) & \cos(\phi - \eta) \\ 0 & h(\phi) \end{bmatrix} \begin{Bmatrix} f_n(\phi) \\ f_t(\phi) \end{Bmatrix} \quad (81)$$

### 6.3 Implementation of Models

#### 6.3.1 Model response to general concentrated line forces

To solve the problem, modal expansion methods were used by use of the periodic nature of the treadband displacements in terms of the angular coordinates,  $\vartheta$  and  $v$  can be expanded to the following Fourier series.

$$v(\theta, t) = \sum_{n=0}^{\infty} a_n(t) \cos n\theta + b_n(t) \sin n\theta \quad (82)$$

where, the generalized coordinates  $a_n(t)$  and  $b_n(t)$  are:

$$a_n(t) = \zeta_n \cos \omega_n t, b_n(t) = \zeta_n \sin \omega_n t, \quad (83)$$

in which,  $\omega_n$  are natural frequencies of the tread band and  $\zeta_n$  are modal participation factors

Substituting Equation (82) into Equation (76) and using the orthogonality of trigonometrical function for the integration over  $[0, 2\pi]$  gives the matrix form for the set of linear second order ordinary differential equations for  $n \geq 1$  as follows.

$$\begin{bmatrix} m_n & 0 \\ 0 & m_n \end{bmatrix} \begin{bmatrix} \ddot{a}_n \\ \ddot{b}_n \end{bmatrix} + \begin{bmatrix} c_n & g_n \\ -g_n & c_n \end{bmatrix} \begin{bmatrix} \dot{a}_n \\ \dot{b}_n \end{bmatrix} + \begin{bmatrix} k_n & 0 \\ 0 & k_n \end{bmatrix} \begin{bmatrix} a_n \\ b_n \end{bmatrix} = \begin{bmatrix} \xi_n \\ \eta_n \end{bmatrix} \quad (84)$$

where the elements related to tire characteristics are determined as:

$$\begin{aligned} m_n &= \rho A(n^2 + 1), & g_n &= -4\rho A n \Omega, & c_n &= c_v + c_w n^2 \\ k_n &= \left( \frac{EI}{R^4} n^2 + \frac{\sigma_{\theta}^0 A}{R^2} \right) (1 - n^2)^2 - \frac{p_0 b}{R} (1 - n^2) + k_v + k_w n^2 \\ &\quad - \rho A (1 + n^2) \Omega^2 \end{aligned} \quad (85)$$

The generalized forces of physical forces and moments are

$$\begin{aligned} \xi_n &= \frac{1}{\pi} \int_0^{2\pi} \cos n\theta \left( q_v + \frac{\partial q_u}{\partial \theta} + \frac{1}{R} \left( q_{\beta} + \frac{\partial^2 q_{\beta}}{\partial \theta^2} \right) \right) d\theta \\ \eta_n &= \frac{1}{\pi} \int_0^{2\pi} \sin n\theta \left( q_v + \frac{\partial q_u}{\partial \theta} + \frac{1}{R} \left( q_{\beta} + \frac{\partial^2 q_{\beta}}{\partial \theta^2} \right) \right) d\theta \end{aligned} \quad (86)$$

Before considering the finite contact problem, the solution for the concentrated line contact needs to be induced. These concentrated forces can be described as follows

$$\begin{aligned}
q_u(\theta, t) &= -Q_u \delta(\theta - (\phi_0 - \Omega t)) \\
q_v(\theta, t) &= Q_v \delta(\theta - (\phi_0 - \Omega t)) \\
\frac{q_\beta(\theta, t)}{R} &= Q_\beta \delta(\theta - (\phi_0 - \Omega t))
\end{aligned} \tag{87}$$

where  $\phi_0$  is the location in the fixed coordinate frame, where the concentrate force and moment apply and  $\delta(\theta - (\phi_0 - \Omega t))$  is the Dirac delta function to describe the impulse force. The generalized forces are now determined by integrating. These generalized forces Eq. (87) and the expression for the modal coefficients Eq. (82) are substitute into Eq. (84). By using the undermined coefficient method, the coefficients,  $a_n$  and  $b_n$  are determined and the tangential deformation of the tread band subjected to concentrated line forces are obtained as:

$$\begin{aligned}
v(\phi) &= \sum_{n=1}^{\infty} \left[ \bar{A}_n (Q_v + (1 - n^2) Q_\beta \cos n(\phi_0 - \phi + \gamma_n)) \right. \\
&\quad \left. + n \bar{A}_n Q_u \sin n(\phi_0 - \phi + \gamma_n) \right] \\
u &= -\frac{\partial v}{\partial \theta}, \quad \beta = \frac{1}{R} \left( v - \frac{\partial u}{\partial \theta} \right)
\end{aligned} \tag{88}$$

where,

$$\begin{aligned}
\bar{A}_n &= \frac{1}{\pi \sqrt{(\bar{M}_n - \bar{G}_n)^2 + \bar{C}_n^2}}, \quad n\gamma_n = \tan^{-1} \frac{\bar{C}_n}{\bar{M}_n - \bar{G}_n}, \\
\bar{M}_n &= k_n - m_n (n\Omega)^2, \quad \bar{G}_n = (n\Omega)g_n, \quad \bar{C}_n = (n\Omega)c_n
\end{aligned} \tag{89}$$

By integrating this equation with respect to  $\varphi_0$  for arbitrary forces and moments distribution can give the tread deformations of the tire with the finite contact with the road surface.

### 6.3.2 Tread compatibility model: radial deformation only

If we assumed that the contact pressure are directed to the center of the wheel always as assumed by Akasaka [68],  $Q_v$  and  $Q_\beta$  become zero and Eq. (88) is reduced to

$$u(\phi) = \sum_{n=0}^{\infty} n^2 \bar{A}_n \cos n(\phi_0 - \phi + \gamma_n) Q_u \quad (90)$$

By superposing the deformation for concentrated load along the finite contact length, the final deformation for the finite contact can be determined. The contact force  $q_u(\phi)$  are distributed along the ring circumference from the front contact angle  $\phi_f$  to rear contact angle  $\phi_r$  as shown Fig. 6-2. The resultant radial deformation of the trade band due to the finite contact can be found by integrating Eq. (90) for  $\phi_0$  over  $[\phi_f \phi_r]$ :

$$\begin{aligned} u(\phi) &= \int_{\phi_f}^{\phi_r} \sum_{n=0}^{\infty} A'_n \cos n(\phi_0 - \phi + \gamma_n) q_u(\phi_0) d\phi_0 = \\ &= \sum_{n=0}^{\infty} A'_n [\alpha_n \cos n(\phi - \gamma_n) + \beta_n \sin n(\phi - \gamma_n)] \end{aligned} \quad (91)$$

where,  $A'_n = n^2 \bar{A}_n$  and

$$\alpha_n = \int_{\phi_f}^{\phi_r} q_u(\phi) \cos(n\phi) d\phi, \quad \beta_n = \int_{\phi_f}^{\phi_r} q_u(\phi) \sin(n\phi) d\phi \quad (92)$$

$q_u(\phi)$  is determined using Eq. (78). Combining Eq. (91), Eq. (92) and Eq. (78) gives the set of equations for  $\alpha_n$  and  $\beta_n$  as shown in the following equation.

$$\begin{aligned} \sum_{j=1}^N \left[ \begin{aligned} &\alpha_j A'_j \int_{\phi_f}^{\phi_r} \cos(i\phi) \{ \cos j(\phi - \gamma_j) - \cos j(\phi_r - \gamma_j) \} d\phi \\ &+ \beta_j A'_j \int_{\phi_f}^{\phi_r} \cos(i\phi) \{ \sin j(\phi - \gamma_j) - \sin j(\phi_r - \gamma_j) \} d\phi \end{aligned} \right] - \frac{1}{k_2} \alpha_i \quad (93) \\ &= \bar{R} \int_{\phi_f}^{\phi_r} \cos(i\phi) (\cos \phi_r - \cos \phi) d\phi \end{aligned}$$

$$\sum_{j=1}^N \left[ \alpha_j A_j' \int_{\phi_f}^{\phi_r} \sin(i\phi) \{ \cos j(\phi - \gamma_j) - \cos j(\phi_r - \gamma_j) \} d\phi \right. \\ \left. + \beta_j A_j' \int_{\phi_f}^{\phi_r} \sin(i\phi) \{ \sin j(\phi - \gamma_j) - \sin j(\phi_r - \gamma_j) \} d\phi \right] - \frac{1}{k_2} \beta_i \quad (94)$$

$$= \bar{R} \int_{\phi_f}^{\phi_r} \sin(i\phi) (\cos \phi_r - \cos \phi) d\phi$$

here,  $i=1 \sim N$  ( $N$ : total mode number used) and we have  $2N$  of linear equation for  $\alpha_i, \beta_i$ . Notice that  $d_0$  in Eq. (78) no longer exists in this equation by using the following constraint equation.

$$d_0 = \bar{R}(1 - \cos \phi_r) - u(\phi_r) \quad (95)$$

which says that the tread deformation should vanish at the rear contact angle.

Eq. (94~92) can be expressed as matrix form:

$$\begin{bmatrix} \mathbf{A} & \mathbf{B} \\ \mathbf{C} & \mathbf{D} \end{bmatrix} \begin{Bmatrix} \vec{\alpha} \\ \vec{\beta} \end{Bmatrix} = \begin{Bmatrix} \vec{E} \\ \vec{F} \end{Bmatrix} \quad (96)$$

where  $\vec{\alpha} = [\alpha_1, \alpha_2, \dots, \alpha_N]$ ,  $\vec{\beta} = [\beta_1, \beta_2, \dots, \beta_N]$ .

The size of matrixes  $A \sim D$  are  $N \times N$  matrixes and  $\vec{E}, \vec{F}$  are  $N \times 1$  vectors. Their elements can be calculated by integrating Eq. (94~95) and this integration can be done analytically if the contact angles are known. Once the coefficients are determined, a linear solver is adopted to get the modal coefficients  $[\alpha_1, \alpha_2, \dots, \alpha_N], [\beta_1, \beta_2, \dots, \beta_N]$ . Finally, Eq. (91) is used to obtain the radial deformation which is substituted into Eq. (78) consequently resulting in the radial pressure distribution.

In this way, if both contact angles are given, the contact problem can be solved easily. However, when contact angles are unknown as usual in general applications, a

repetition process is needed to identify contact angles which satisfy the boundary conditions. At the rear contact edge, the boundary conditions are automatically met by introducing Eq. (95). However, at the front, the constraint, i.e.,  $d_0 = \bar{R}(1 - \cos \phi_f) - u(\phi_f)$  may be violated. For the static tire, the contact is symmetric and contact angles have the same value with the opposite sign and the constraints are automatically met at the front angle also. For the rotating tire, the treadband deformation is not symmetric anymore with respect to vertical axes because of the damping characteristics of the tread and sidewall and the maximum radial deformation move backward. Gong [50] identified two contact angles sequentially: first solution process was repeated until  $\phi_r$  meets the required boundary condition Eq. (95) And then, another iteration process was conducted to find  $\phi_f$  while keeping the previously found contact angle as fixed. This sequential determination of contact angles is likely to generate some error because the fixed contact angle from the first iteration should be affected when the other contact angle varies through the second iteration process.

In this implementation, these two contact angles were found simultaneously by regarding the boundary conditions are set of non-linear equations for unknown  $\phi_f, \phi_r$  as described in following:

$$\begin{aligned} f_1 &= d_0 - \{\bar{R}(1 - \cos \phi_f) - u(\phi_f)\} = 0 \\ f_2 &= d_0 - \{\bar{R}(1 - \cos \phi_r) - u(\phi_r)\} = 0 \end{aligned} \quad (97)$$

MATLAB subroutine for non-linear equation solver, 'fsolve' was used by providing functions  $f_1, f_2$  which include the whole implementation of the flexible ring models. In this way, the contact angles are determined while satisfying the boundary constraints simultaneously. The flow chart for the suggested implementation is presented in Fig. 6-6.

To validation of this implementation, simulations were performed for same numerical examples from literature and the results are shown in Fig. 6-7. The simulation result for the contact pressure was overlaid on the measured ones at each tread rib and simulated ones by Yamagish [57] ('Yamagish' in the chart) and Gongs [50] ('Modal

Expansion Method' in the chart) in chart (a). The simulation result is very close to Gong's results with slight difference. Using Jenkin's numerical example [59], a simulation was done and compared with Gong's results for the same numerical example in Fig. 6-7 (b). Both implementations provide almost same pressure profiles but slight differences are observed near the contact center. This could be caused by some parameters unclearly presented in literature or by the different implementations to find contact angles as previously mentioned. Both represent the concavity in the contact pressure when the tire is subjected to the large vertical deformation. ( $d_0=4\text{cm}$ ).

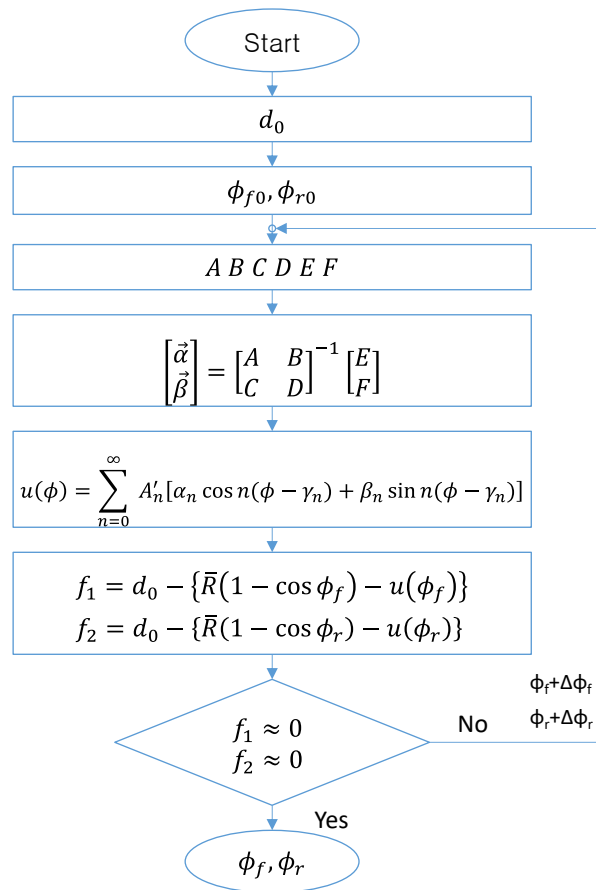


**Fig. 6-6 Flow chart of flexible ring model simulation for free rolling tire (considering radial pressure distribution only)**

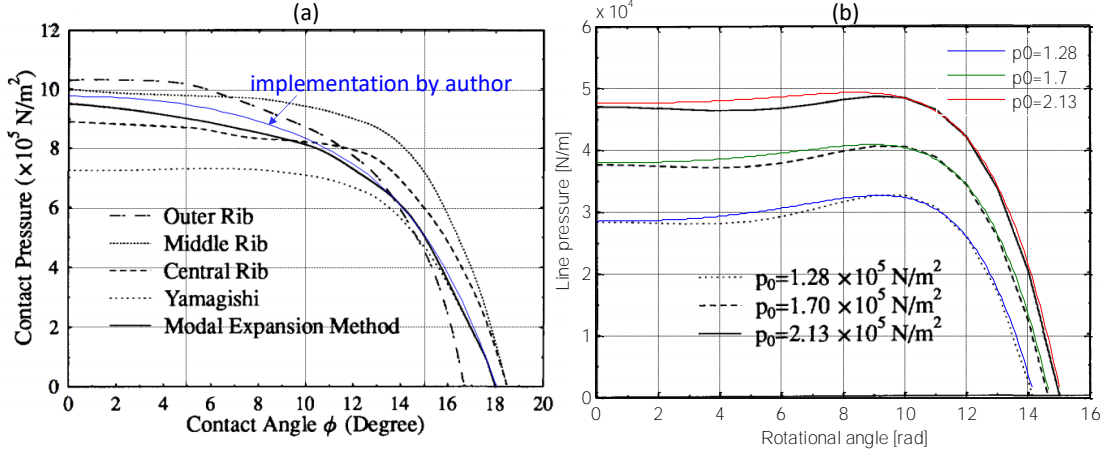


**Fig. 6-7 Validation of the implemented simulation results with those from literature: comparison with Yamagishi and Gong's results (a), comparison with Gong's results (b)**

### 6.3.3 Tread compatibility model: normal and shear deformation

To consider the tread shear deformation and external moments induced by the frictional force, all components of Eq. (88) are needed. By superposing deformations due to the concentrated forces and moments over the contact area, in other words, integrating Equation (98) along  $\varphi_0$  over  $[\varphi_f, \varphi_r]$ , the ring deformations due to the distributed forces in the contact patch are obtained:

$$v(\phi) = \int_{\phi_f}^{\phi_r} \sum_{n=0}^{\infty} \left[ (\alpha_{n1}\bar{A}_n - \alpha_{n3}n\bar{A}_n) \sin n(\phi - \gamma_n) \right. \\ \left. + (\alpha_{n2}\bar{A}_n + \alpha_{n4}n\bar{A}_n) \cos n(\phi - \gamma_n) \right] \quad (98)$$

$$u(\phi) = \frac{\partial v}{\partial \phi}, \quad \beta(\phi) = \frac{1}{R} \left( v - \frac{\partial u}{\partial \phi} \right)$$

where,

$$\begin{aligned}
\alpha_{n1} &= \int_{\phi_f}^{\phi_r} \left( q_v(\phi) + (1 - n^2) \frac{q_\beta(\phi)}{R} \right) \sin n\phi \, d\phi \\
\alpha_{n2} &= \int_{\phi_f}^{\phi_r} \left( q_v(\phi) + (1 - n^2) \frac{q_\beta(\phi)}{R} \right) \cos n\phi \, d\phi \\
\alpha_{n3} &= \int_{\phi_f}^{\phi_r} q_u(\phi) \cos n\phi \, d\phi \\
\alpha_{n4} &= \int_{\phi_f}^{\phi_r} q_u(\phi) \sin n\phi \, d\phi
\end{aligned} \tag{99}$$

If we know the contact force and the moment distributions, the coefficients  $\alpha_{n1} \sim \alpha_{n4}$  are obtained by directly integrating these force and moment distribution using Eq. (99). However, in the real application, these quantities are usually unknown and should be identified during the solving procedure. Similar approach presented in the previous section was made to manage this problem. Substituting Eq. (98) into Eq. (79) and using Eq. (80~81) successively,  $q_u$ ,  $q_v$ ,  $q_\beta$  are expressed as modal parameters  $\bar{A}_n, \gamma_n$  and unknown coefficients  $\alpha_{n1} \sim \alpha_{n4}$ . Substituting these expression into Eq. (99), the set of  $4N$  equations are given for  $4N$  unknowns  $\alpha_{n1} \sim \alpha_{n4} (n=1 \dots N)$ .

In the previous problems, corresponding equations (Eq. (93) and Eq. (94)) are linear for unknown coefficients  $\alpha_n, \beta_n$  by assuming the radial-only contact pressure distribution which was expressed as the linear equation of  $u$  only (refer to Eq. (78)). However, in this problem, the equations are totally nonlinear including trigonometric functions of  $\eta$  and products of  $\alpha_{n1} \sim \alpha_{n4}$ .

To solve this problem, two step approach is uses as suggested in [61]; In the first step, approximate solution is found using linearized equations for the compatibility relations in Eq. (79), which leads to set of  $4N$  equations for unknowns  $\alpha_{n1} \sim \alpha_{n4}$ . In the second step, using these linearized solutions, approximate tread band deformations are calculated using Eq. (98) and force and moment distributions are calculated using the nonlinear boundary conditions Eq. (79~81). By directly integrating these force distributions,  $\alpha_{n1} \sim \alpha_{n4}$  are updated so are the tread ring deformations  $v, w, \beta$ . This iterative procedure repeated until desirable accuracy of the convergence is achieved.

If the tread deformation quantities  $v$ ,  $w$ ,  $\beta$  are negligible compared to the ring radius  $R$ , the compatibility conditions Eq. (79) and the conversion matrix equations Eq. (81) can be linearized leading to linear expressions for the force and moment distributions:

$$q_u(\phi) \approx K_{Et} \begin{bmatrix} (-h_0 + R_l + R_e \eta \phi) \cos \phi - (R + u) \cos^2 \phi \\ -\left(R\eta - \frac{v}{2}\right) \sin 2\phi + (R_l - h_0)\eta \sin \phi \end{bmatrix} - K_{Gt} \begin{bmatrix} (R_l \eta - R_e \phi) \sin \phi + (R + u) \sin^2 \phi \\ -\left(R\eta - \frac{v}{2}\right) \sin 2\phi + R_e \eta \phi \cos \phi \end{bmatrix} \quad (100)$$

$$q_v(\phi) \approx K_{Et} \begin{bmatrix} (h_0 - R_l - R_e \eta \phi) \sin \phi + \frac{(R + u)}{2} \sin 2\phi \\ + (R\eta - v) \sin^2 \phi + (R_l - h_0)\eta \cos \phi - R\eta \cos^2 \phi \end{bmatrix} - K_{Gt} \begin{bmatrix} (R_e \phi - R_l \eta) \cos \phi - \frac{(R + u)}{2} \sin 2\phi \\ + (R\eta - v) \cos^2 \phi + R_e \eta \phi \sin \phi - R\eta \sin^2 \phi \end{bmatrix} \quad (101)$$

$$q_\beta(\phi) \approx K_{Gt} h_0 [-R_l \eta + R_e \phi - (R + u) \sin \phi + (R\eta - v) \cos \phi] \quad (102)$$

Note that  $R_e$  and  $R_l$  can be expressed as the tread deformation at the contact edge using the compatibility condition Eq. (79). Under the free rolling condition, the tread deformation should vanish at the front contact angle:  $h(\phi_f)=0$ ,  $\gamma h(\phi_f)=0$ . These two equations can be solved for  $R_e$  and  $R_l$ :

$$R_e = (h_0 \sin \eta(\phi_f) + (R + u(\phi_f)) \sin \phi_f + v(\phi_f) \cos \phi_f) / \phi_f \quad (103)$$

$$R_l = h_0 \cos \eta(\phi_f) + (R + u(\phi_f)) \cos \phi_f - v(\phi_f) \sin \phi_f \quad (104)$$

These expressions for  $R_e$  and  $R_l$  should be linearized properly also. These expressions are substituted into the Eq. (100~102) such that  $q_u$ ,  $q_v$ ,  $q_\beta$  are expressed as the linear combinations of  $\alpha_{n1} \sim \alpha_{n4}$ . Approximate  $q_u$ ,  $q_v$ ,  $q_\beta$  are substituted into Eq. (99)

again giving set of linear equations of  $4N$  with  $4N$  unknowns  $\alpha_{n1} \sim \alpha_{n4}$ . Their coefficients and constant terms are the functions of  $\varphi_f$  and  $\varphi_r$ , like Eq. (96) in the previous section:

$$\begin{Bmatrix} \vec{\alpha}_1 \\ \vec{\alpha}_2 \\ \vec{\alpha}_3 \\ \vec{\alpha}_4 \end{Bmatrix} = \begin{bmatrix} Y^{11} & Y^{12} & Y^{13} & Y^{14} \\ Y^{21} & Y^{22} & Y^{23} & Y^{24} \\ Y^{31} & Y^{32} & Y^{33} & Y^{34} \\ Y^{41} & Y^{42} & Y^{43} & Y^{44} \end{bmatrix} \begin{Bmatrix} \vec{\alpha}_1 \\ \vec{\alpha}_2 \\ \vec{\alpha}_3 \\ \vec{\alpha}_4 \end{Bmatrix} + \begin{Bmatrix} \vec{c}_1 \\ \vec{c}_2 \\ \vec{c}_3 \\ \vec{c}_4 \end{Bmatrix} \quad (105)$$

The elements of  $N \times N$  matrix,  $Y^{ij}$  and  $N \times 1$  vector  $\vec{c}_i$  can be calculated by integrating if we know both contact angles. However, this time, the integrands become very complex combinations of trigonometric functions making integrating them analytically impossible. Instead, numerical integrations are required and it takes considerable time. Once, matrix and constant vector  $\vec{c}$  are obtained, the set of equation, Eq. (105) can be solved using linear solver. When contact angles are unknown, iterative process continue until the normal deformation at both contact edges become zero. Kim[61] also solved this problem by identifying the contact angles sequentially similar to Gong. In this implementation, the problem are again regarded as a set of non-linear equations as described in the following:

$$\begin{aligned} f_1 &= R_l - \left\{ h_0 + \left( R + u(\phi_f) \right) \cos \phi_f - v(\phi_f) \sin \phi_f \right\} = 0 \\ f_2 &= h(\phi_r) - h_0 = 0 \end{aligned} \quad (106)$$

The first equation comes from Eq. (104) and second one says the tread thickness at the rear edge should be same as the undeformed tread thickness.

As mentioned previously, these approximated solutions are input to get the exact force distributions satisfying non-linear constraints then by directly integrating these external forces, updated deformations are obtained. This process continues until differences in deformations between the previous step and current step become small enough to meet the required accuracy. This two-step solution process is shown in Fig. 6-8.

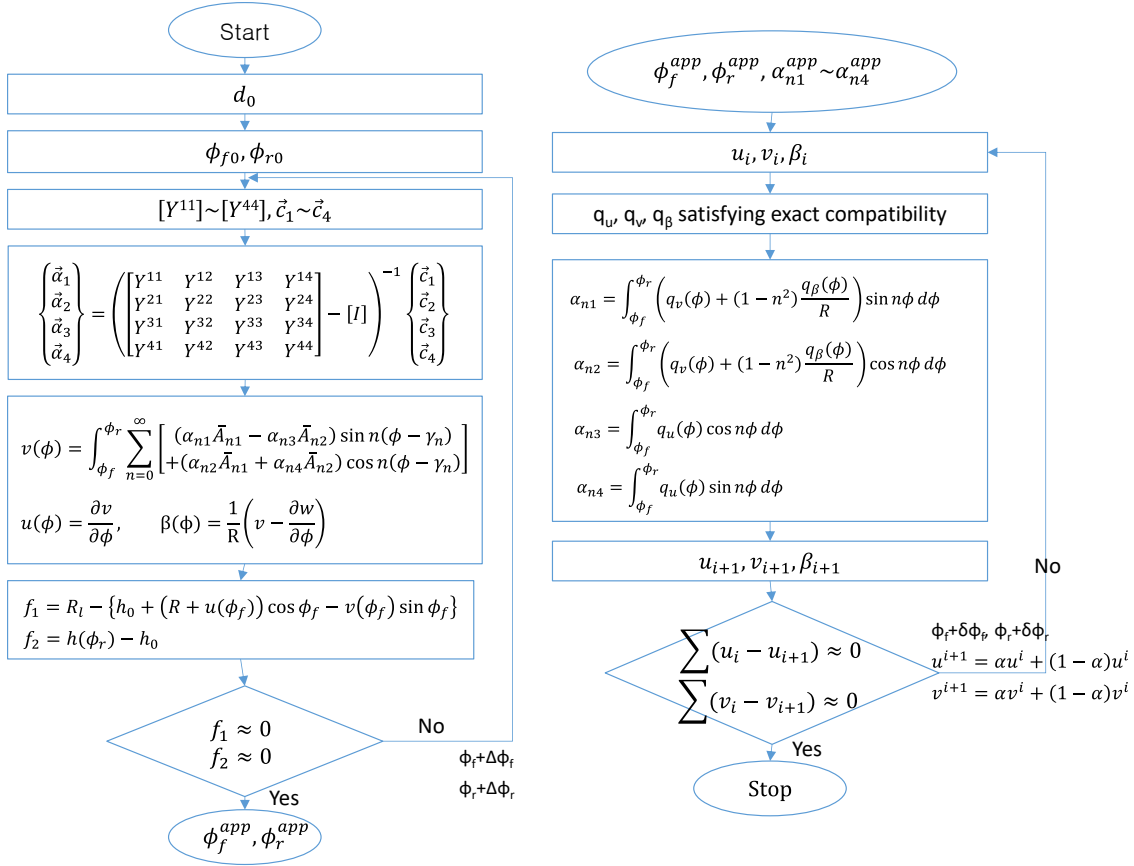


**Fig. 6-8 Flow chart of flexible ring model simulation for free rolling tire (considering normal and tangential pressure distribution)**

Sliding can occur in the rear part of contact area even for the free rolling situation and this can be considered using this model in the second stage of solution. Assuming Coulomb friction law, sliding will arise when the ratio to tangential to normal traction exceeds the value of the friction coefficient  $\mu$ . In the case of sliding, the kinematic constraint for the free rolling (Eq. (79)) is not applicable any longer. The boundary condition on the shear traction is now:

$$\tau \leq -\mu|\sigma| \text{ when } V_s = 0 \text{ and } \tau = -\mu|\sigma|\text{sgn}(V_s) \text{ when } |V_s| > 0$$

where,  $V_s$  is the local sliding velocity and 'sgn' function is introduced to indicate the direction of sliding.  $\tau, \sigma$  are contact stress distributions in the normal and tangential to the road surface, respectively. By comparing the tractive ratio  $\tau/\sigma$  with any finite value

of friction coefficient  $\mu$ , the starting point of sliding region along the contact patch is determined. In the sliding region, the tractive force is calculated by simply multiplying  $\sigma$  with  $\mu$ .

#### 6.4 Comparison of Simulation Results for Different Boundary Conditions

Simulations with two different compatibility conditions were conducted for the comparison purposes. Tire parameters are listed in Table 6-1 which are determined from [61] with slight modifications.

**Table 6-1 Model parameters for implementation and comparison**

$\bar{R}$ (m)	0.3125	$EI$ (Nm <sup>2</sup> )	1.144
$R$ (m)	0.30	$k_{Et}$ or $k_t$ (N/m <sup>2</sup> )	7.5E+07
$h_o$ (m)	0.0125	$k_{Gt}$ (N/m <sup>2</sup> )	2.5E+07
$b$ (m)	0.165	$k_u$ (N/m <sup>2</sup> )	6.24E+05
$\rho A$ (kg/m)	3.16	$k_v$ (N/m <sup>2</sup> )	2.18E+05
$p_o$ (bar)	1.32	$c_{ea}$ (Ns/m <sup>2</sup> ) (or $\lambda$ )	400 (0.04)
$\Omega$ (rad/s)	59	$\mu$	0.65

When only considering the radial deformation of the tread elements (referred to as ‘simple contact model’), the sidewall damping is included directly in Eq. (84) by introducing a non-dimensional modal damping coefficient  $\lambda$ :

$$c_n = 2\lambda\sqrt{m_n k_n} \quad (107)$$

The normal pressure and tangential stress are shown in Fig. 6-9 using different contact models when the vertical deflections,  $d_o$ , is 4.5 cm set as relatively high. When considering both tread deformation in normal and tangential directions (referred to as ‘advanced contact model’), tangential stress directs outward as expected as shown in Fig. 6-9 (a). When considering the radial deformation of tread only, Fig. 6-9 (b), tangential stresses face to the center of the contact patch. The sliding region can be identified when

the advanced contact model was used as shown in the lower chart of Fig. 6-9 (a). Contact angles tend to be smaller when considering the shear deformation of the tread due to the frictional force. For the normal pressure, a strange feature is observed for the simple contact model especially for large  $d_0$ . Generally, it is expected that the normal pressure distribution become concave shape as the vertical deformation increase as we discussed previously. However, a hump is observed in the normal pressure distribution at the contact center for  $d_0=0.045$  in the upper chart of Fig. 1-27. This could be caused by the less realistic assumption that the contact pressure always acts to the wheel center always.

In conclusion, by including the shear deformation of the tread, more realistic pressure distributions can be obtained for sever conditions such as the tire rolls subjected to large deformations or higher vertical loads.

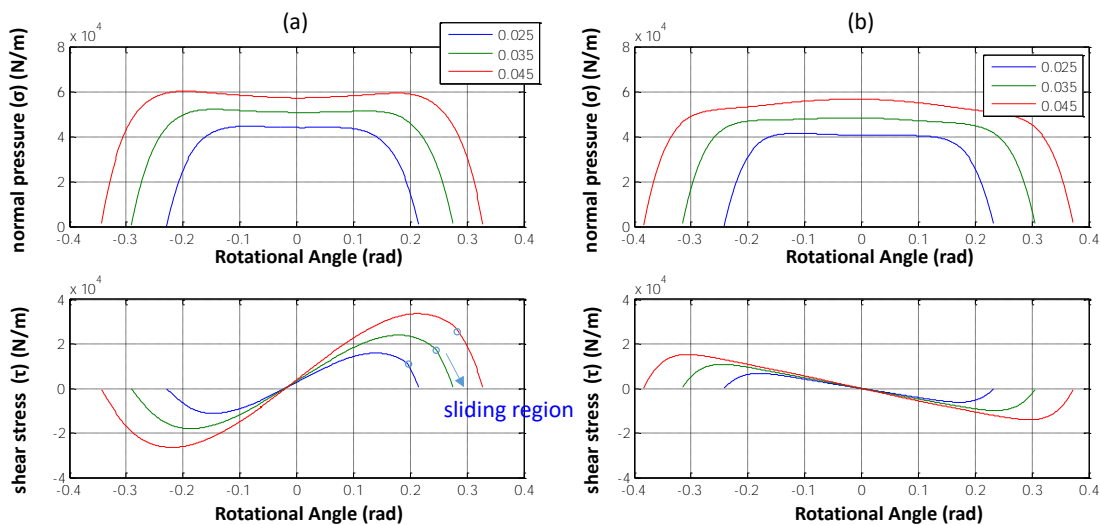


**Fig. 6-9 Normal and horizontal force distribution for different  $d_0$  considering: (a) tread normal & shear deformation, (b) tread radial deformation only ( $d_0$ : 2.5, 3.5, 4.5 cm)**

Using the Eq. (35), the strains are calculated using the simulated treadband deformations and comparison is provided in Fig. 6-10. Both shows almost identical shapes of strains for various vertical deflections although totally different contact models are applied for each case. Both follow the expected trend as the tire vertical deflection increase (or vertical load increase), as we observed previously. The damping affect strains

shapes such that the first compressive peak increase which could be caused by the shift of the pressure distribution forward.

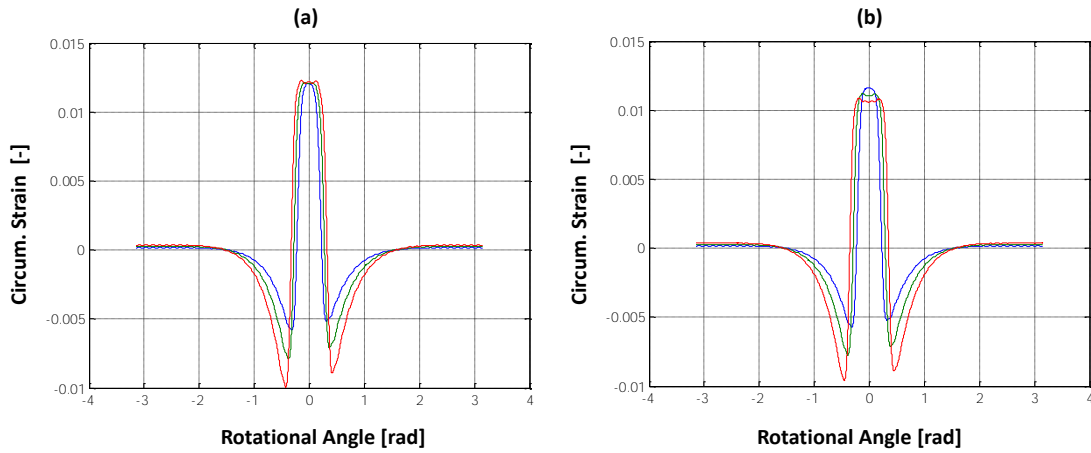


**Fig. 6-10 Circumferential strains at inner line considering: (a) tread normal & shear deformation, (b) tread radial deformation only ( $d_0$ : 2.5, 3.5, 4.5 cm)**

Fig. 6-11 compares the radial and tangential deformation for two contact models. Although there is a slight difference in the tangential deformation around  $\varphi = -0.5$  rad, the radial deformation is almost same regardless contact models used.

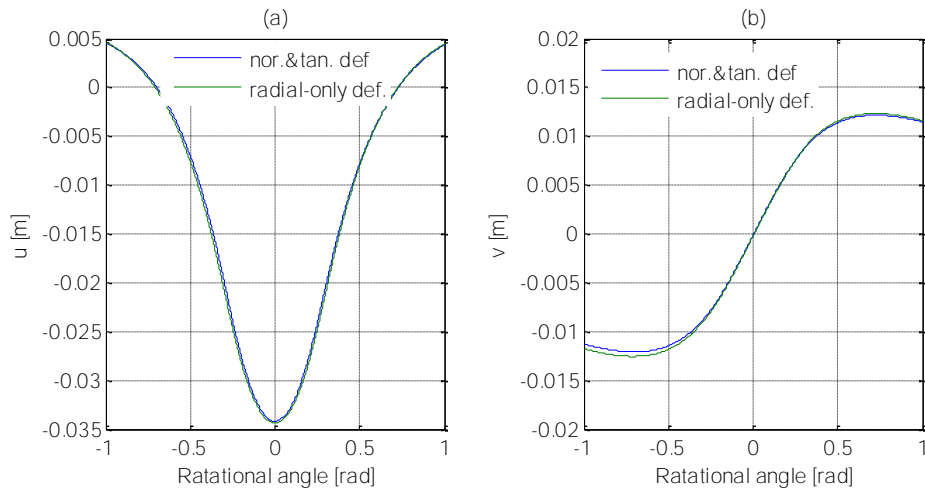


**Fig. 6-11 Radial and tangential deformation a) tread normal & shear deformation, (b) tread radial deformation only ( $d_0$ : 3.5cm)**

Subjected to the same vertical deflection with same model parameters, two contact models give almost identical radial deformation. Due to the inextensibility assumption, the tangential deformations become almost same each other as well. Reminding that the proposed strain equation is only function of  $u$ , strains from different contact models are also expected to be very similar to each other. Both of them fail to show the consistent trend that as test load increases, the peak tension decreases considerably as observed in the experimental data (refer to Fig. 3-8 (a)). More discussion on this issue will be provided in Chapter 7

Fig. 6-12 overlay the strain rate on the pressure profiles to investigate how well simulated strains can identify the contact angles. Although both strain rates identify the contact angles closely, when including tread shear deformation, strain rate peaks coincide contact angles more exactly. Even though the advanced contact model has a merit in that respect, it could be compromised by much longer simulation time. Also, one more parameter, the tread shear stiffness  $k_{GT}$  needs to be estimated. Therefore, the contact model only considering the radial tread deformation was chosen to use for the application purpose in the remaining sections.

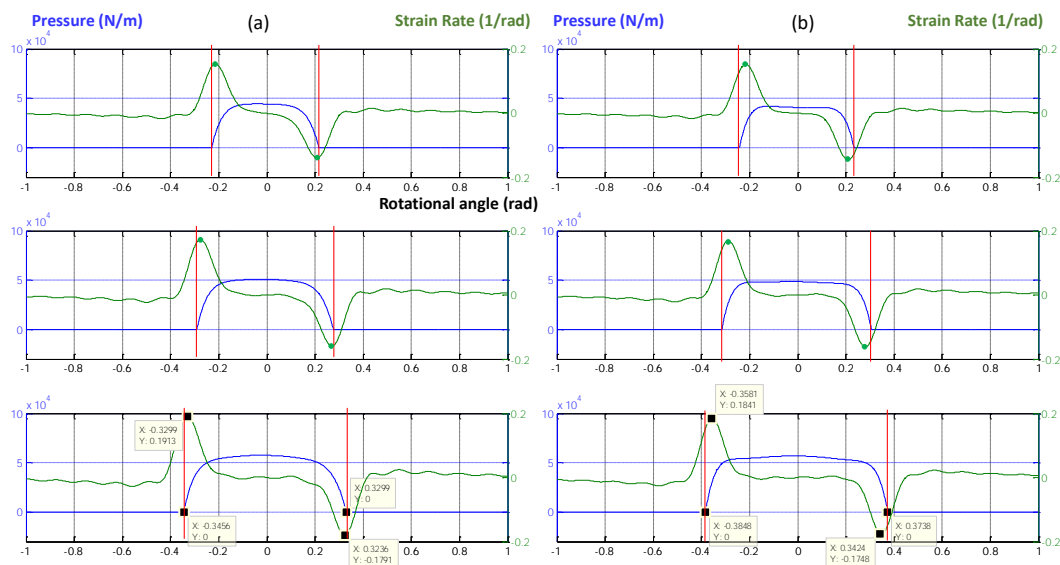


**Fig. 6-12 Identifying contact edges using two different contact models: (a) tread normal & shear deformation, (b) tread radial deformation only (d0: 2.5, 3.5, 4.5 cm)**

## 6.5 Estimation of Dynamic Pressure Distribution and Tire Parameters

In Chapter **Error! Reference source not found.**, the measured strains were used to solve the contact problem by identifying the radial deformations directly from strain measurements. However, this approach is not appropriate for the dynamic rolling case. To adopt this approach, the strain model must be guaranteed to be accurate enough to represent the real measurements. The strain-deformation relationship used in this research was validated using FEM simulation for the static tire pushed against the frictionless road surface. In the static condition or rolling condition at very low speeds, the strains can be assumed to be symmetric. Thus, the simulated strain is believed to represent the real measurements relatively well although it cannot reflect the load dependency of the tension in the contact range well.

The strains measured inside the rolling tire shows considerable asymmetry within the contact patch. The tension achieves its peak value right after the leading edge and continues to decrease until just before the trailing edge, as shown in Fig. 6-13 (a).

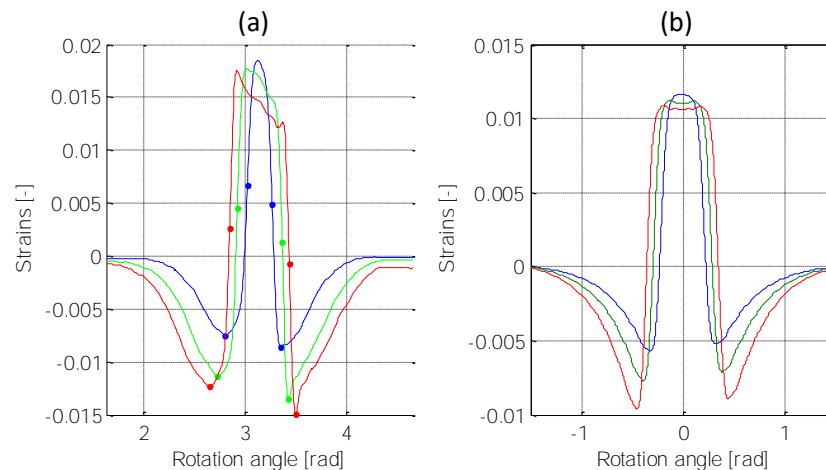


**Fig. 6-13 Measured and simulated strains: (a) measured for 195/65R15 tire (b) simulated using the tire parameters of Table 6-1**

Fig. 6-13(b) was taken from Fig. 6-10 again for comparison which was simulated with a dynamic flexible ring model with damping effects. Even though internal damping

effects cause non-symmetrical pressure distributions, simulated strains have almost symmetrical shapes within the contact patch.

The biased shape of the tension in the measured strain is caused by the complex contact mechanism such as stick-slip phenomena near the rear edge. Thus, without more elaborate and advanced contact models, it is impossible to reproduce same results as the measured strain. Also, the convergence of FDM cannot be guaranteed for the severely biased shapes of real measurements, even if we want to identify the radial deformation directly from the strain measurements, as was done previously.

Because of these limitations, the identification scheme previously used for the static tire was discarded for the rolling tire. Instead, just a few valid characteristics of measured strains were used to be accompanied with ring models; the contact angles at the front and rear edge. The ring model primarily focuses on identifying the contact angles and they are determined in the repeated process requiring the large amount of numerical calculations. Therefore, knowing contact angles makes it easier to solve the circumferential contact problem with the flexible ring model. In real applications, contact angles of the tire rolling at high speeds are hard to measure without the aid of intelligent tire systems.

To build the flexible ring model, some model parameters like geometrical parameters and the bending stiffness of the tread band were defined or estimated for a 195/65R15 tire from Hankook Tire Company. Free rolling tests on Flat-Trac test rig were done under various combinations of test loads, inflation pressures and test speeds while measuring strains at the innerliner using the design of experiment as was shown in Table 3-3. Using the contact angles estimated from strain measurements, sidewall stiffness is estimated for different loads and inflation pressures. The estimation method for tire damping characteristics was suggested based on the combination of simulation results and features of the measured strain profile. With these estimated parameters, flexible ring model was developed and simulated to generate the dynamic pressure distribution.

## 6.5.1 Estimation of Model Parameters

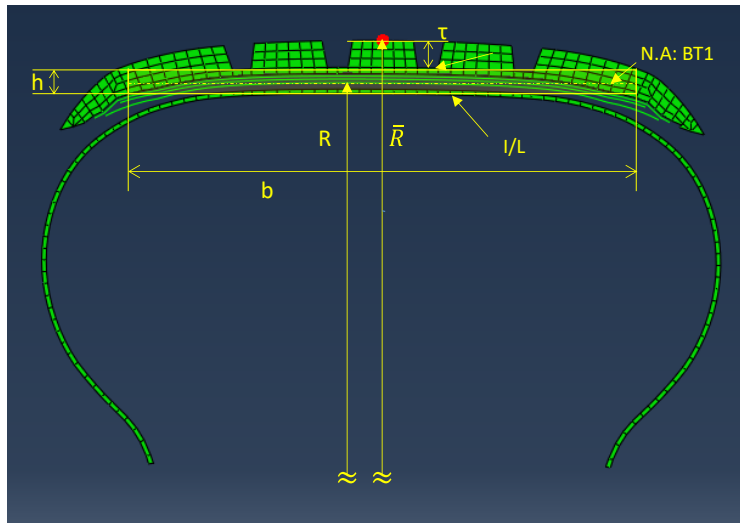
### 6.5.1.1 Geometrical Parameters

Fig. 6-14 illustrates geometrical model parameters. The width of the ring,  $b$ , is determined as the first belt width which also corresponds to the neutral axis. The overall radius of tire,  $\bar{R}$ , is directly measured after inflation. The radius of the ring,  $R$ , and the distance from the neutral axis to the innerliner surface,  $y$ , were calculated using the thickness of each layer. The tread thickness,  $\tau$  is the difference between  $\bar{R}$  and  $R$ .

The tread ring mass,  $m_t$  can be calculated using the following relationship:

$$m_t = \rho A \times 2\pi R \quad (108)$$

Thus,  $\rho A$  can be calculated once  $m_t$  is known.



**Fig. 6-14 Geometrical model parameters**

Zegelaar [70] claimed that a portion of the tire need to be separated from the tread band and considered to belong to the rim, because it moves together with the rim. In Fig. 6-15, the parts rolling attached to rim are considered as two beads and inner half of the side wall. Excluding the sum of masses of these parts from the total tire mass, the

tread band mass can be determined. In this research, 54% of the sidewall mass is assumed to belong to the ring mass [70].

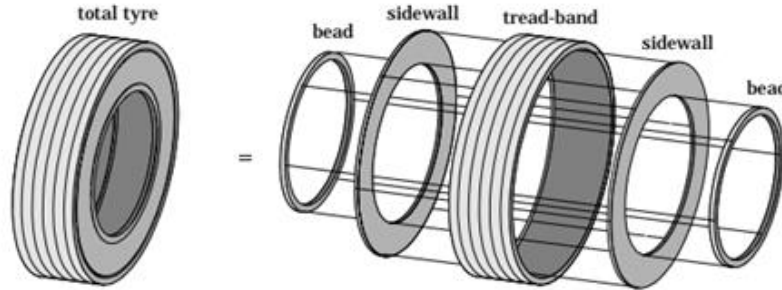


**Fig. 6-15 Decomposition of the tire into five components [70].**

#### 6.5.1.2 Ring bending stiffness and tread stiffness

The bending stiffness is considered to be constant and not affected by the test load, inflation pressure nor speed. This parameter was estimated based on the modal test results and the formulation derived from the flexible ring model. Using the flexible ring model, the natural frequencies of the non-rotating tire are given by [50] :

$$\omega_n = \left\{ \frac{1}{\rho A(1+n^2)} \left[ \frac{EI}{R^4} (1-n^2) - \frac{p_0 b}{R} \right] n^2 (1-n^2) + k_v + k_w n^2 \right\}^{\frac{1}{2}} \quad (109)$$

To measure the natural frequency, vibration tests were conducted where the tire axle is fixed and sinusoidal excitations were applied to the tread in the radial direction and nature frequencies for the 0~3<sup>th</sup> modes were measured for various inflation pressures. The experimental results are compared with the results provided in [50]. The natural frequencies of the tire used for this research show lower frequencies for all the modes.

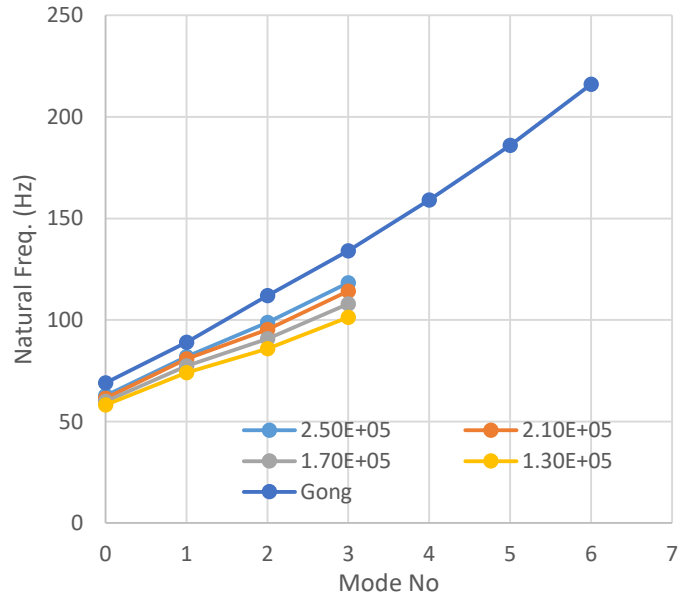


**Fig. 6-16 Natural frequencies from vibration test**

Eq. (109) can be solved for  $EI$ ,  $k_v$ ,  $k_u$  with any three measured natural frequencies for different modes. Using  $\omega_1 \sim \omega_3$ , the set of non-linear equations were solved for  $EI$ ,  $k_v$ ,  $k_u$ . Eq. (109) shows the derived equation for  $EI$  from natural frequencies.

$$EI = \frac{1}{144} R^3 (-12bp_0 + R(\omega_1^2 - 4\omega_2^2 + 3\omega_3^2)\rho A) \quad (110)$$

To minimize the possible effects of inflation pressure on  $EI$ , this value was calculated with the test results for the tire having the lowest inflation pressure, 1.3 bars. Estimated sidewall stiffness, i.e.,  $k_u$  and  $k_v$  will be used as initial guess of optimization routines, which will estimate sidewall stiffness under various inflation pressures and test loads. This process – using model parameters from modal tests as initial guess to refine them– was suggested in [71] for model parameterizations.

The estimation method for tread stiffness was suggested by Jenkin *et al.* [59]. This parameter is determined from Young's modulus,  $E$ , of the rubber, the width of the belt,  $b$ , and the tread thickness,  $\tau$ , as shown by the following:

$$k_t = \frac{Eb}{\tau} \quad (111)$$

The young's modulus of the test tire is 6.58E6 N/m<sup>2</sup> and  $k_t$  is found to be 9.9e7 N/m<sup>2</sup>. Table 6-2 lists measured or estimated model parameters.

**Table 6-2 Estimated model parameters for test tire (P195/65R15)**

$\bar{R}$ (mm)	@ 2.5 bars	317.36	R (mm)	$\bar{R} - \tau$
	@ 2.1 bars	317.20	y(mm)	2
	@ 1.7 bars	316.88	$\rho A$ (kg/m)	3.1529
	@ 1.3 bars	316.72	EI (Nm <sup>2</sup> )	2.13
			$K_t$ (N/m <sup>2</sup> )	99e7

## 6.5.2 Parameter Estimation using Strain Measurements

Remaining model parameters are the radial and tangential sidewall stiffness ( $k_u$ ,  $k_v$ ) and normalized damping coefficient ( $\lambda$ ). These parameters are estimated by using the combination of the flexible ring model and strain measurements. First, assuming the damping coefficient is zero, the radial and tangential sidewall stiffness were estimated through the optimization routine which minimizes the error between estimated and test loads. Second, the flexible ring model was built with estimated  $k_u$  and  $k_v$  and simulations were performed for various damping coefficients. The measured strains were compared with simulated strains for various damping coefficients to identify the damping coefficient of the current system.

### 6.5.2.1 Sidewall Stiffness

In this model, the tangential and radial stiffness of the sidewall represent the pressurized air of the tire, indicating variation of stiffness with tire inflation pressure. It is also claimed that the radial sidewall stiffness tends to decrease as the test load or the

vertical deflection of the tire increases. This relationship, given by Eq. (54), was also used in Section 5.3.

The details of the optimization routine to estimate sidewall stiffness is illustrated in Fig. 6-17. In the previous implementation, a non-linear solver was used to find contact angles under known vertical deflection,  $d_0$  (refer to Fig. 6-6). Now we already know contact angles from the strain measurements but sidewall stiffness need to be estimated. Contact angles are directly input to the flexible ring model removing the repeated process to solve set of equations. Under fixed contact angles, the optimization is performed to find  $k_u$  and  $k_v$  which can minimize the summation of the error between the test load and the estimated load for each test load. The load can be estimated by integrating the pressure distribution obtained from the flexible ring model. Notice that in this implementation, the vertical deflection,  $d_0$  is not used anymore. The vertical deflection of the loaded rolling tire is hard to measure, especially in the real driving situation. Instead, the test load was used here. The undetermined parameter, i.e., internal damping coefficient ( $\lambda$ ) was set to zero in this step.

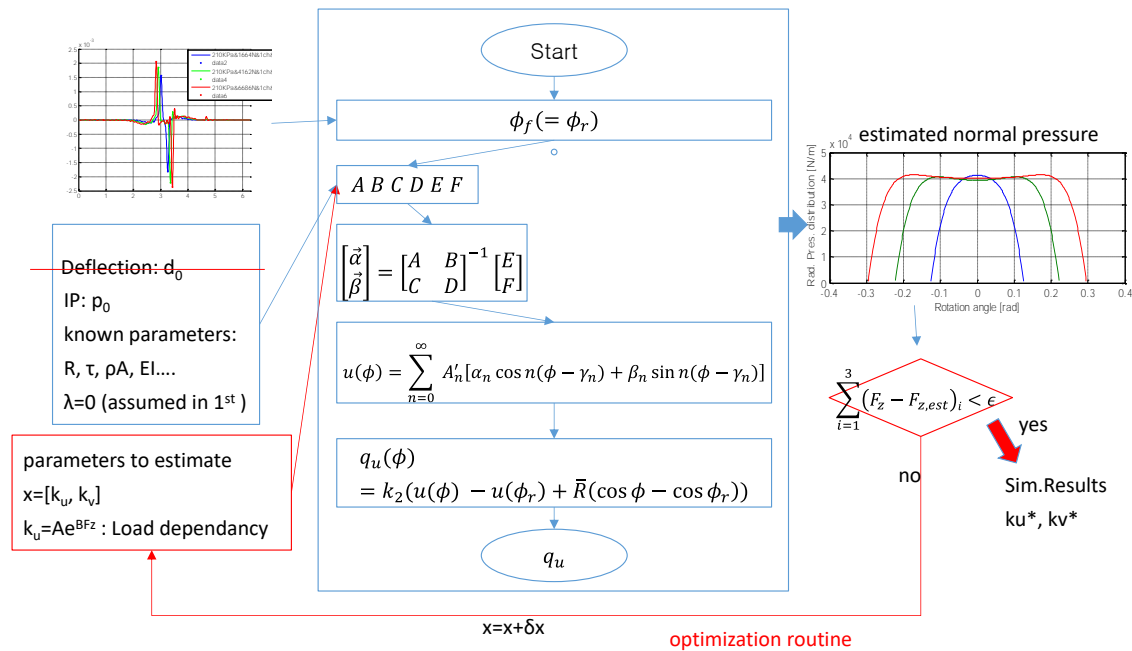
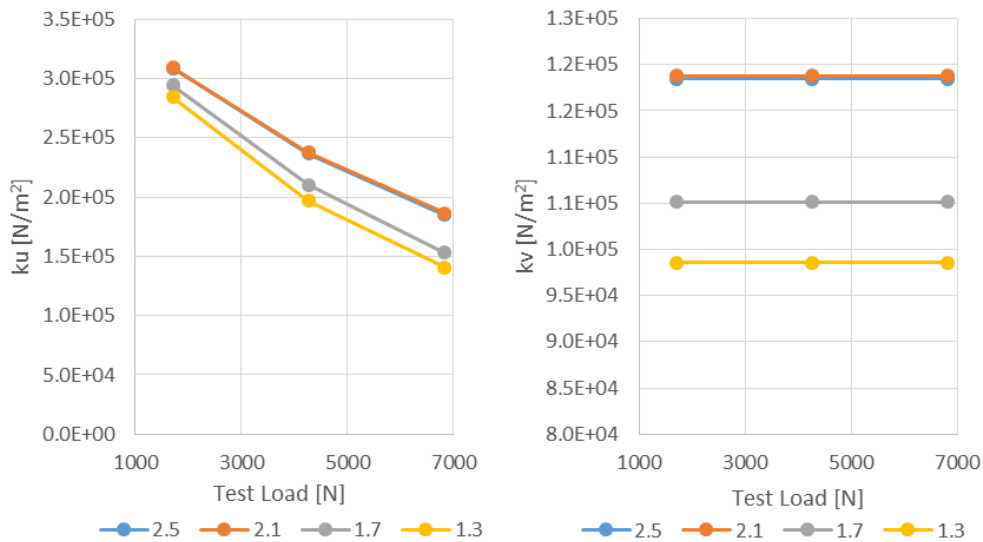


Fig. 6-17 Optimization routing for parameterization

The optimization routine was formulated as following:

- Design variables:  $x=[A, B, k_v]$
  - Objective function  $\sum_{i=1}^{i=3}(F_{z,est}(x) - F_z)_i$
  - Nonlinear constraint:  $(-Ae^{-BF_z})C + k_v < 0$
- Find  $x$  to minimize objective function subject to constraints

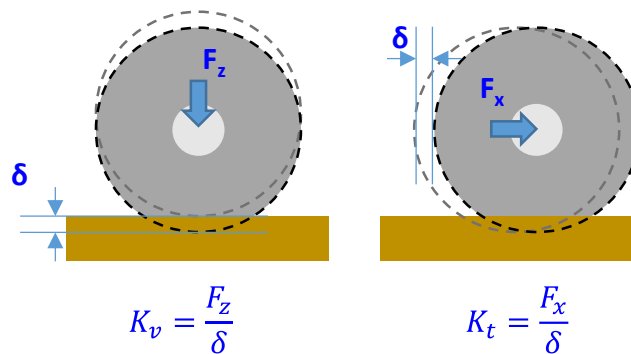
Non-linear constraints were introduced to keep the tangential stiffness lower than the radial stiffness. The weight factor,  $C$  is determined as 0.5 referring to the radial and tangential sidewall stiffness used in literature. Fig. 6-18 shows the results for  $k_u$  and  $k_v$  from the optimization. As expected, both tend to decrease as inflation pressure decreases. However, stiffness measured at 2.1 and 2.5 bars are almost identical. The radial stiffness decreases as test load increases as formulated in Eq. (54).



**Fig. 6-18 Estimated sidewall stiffness**

For the validation purpose, the tire vertical stiffness ( $K_v$ ) and longitudinal stiffness ( $K_t$ ) were measured on the indoor test rig. The conceptual meanings of these parameter are illustrated in Fig. 6-19. Although these parameters represent the total stiffness of the

tire, for the same tire with different inflation pressures, these parameters are expected to represent the inflation pressure effects which are modeled through sidewall stiffness. Especially, longitudinal stiffness could be a better representative for the radial stiffness because the cross-sectional profile of the tire is maintained during the longitudinal force application.  $K_v$  is likely to be governed by not only the inflation pressure itself but also the cross-sectional profile change caused by different inflation pressures. The latter effect cannot be represented by the ring model.



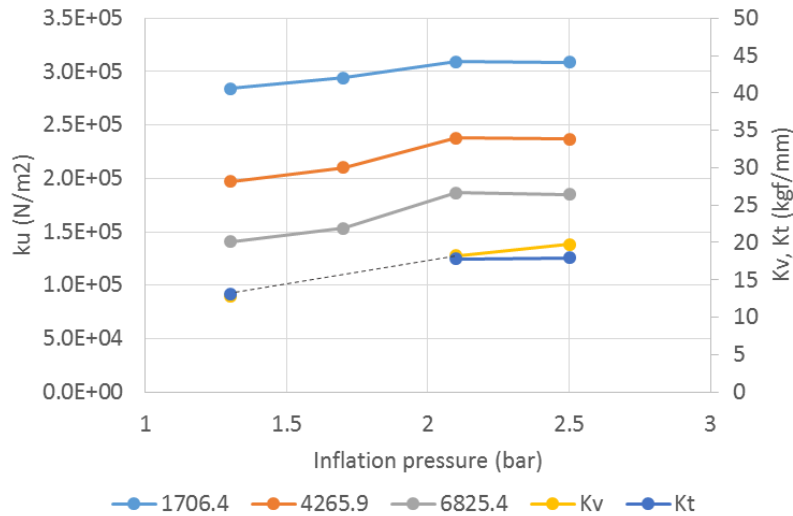
**Fig. 6-19 Tire vertical stiffness ( $K_v$ ) and longitudinal stiffness ( $K_t$ )**

Fig. 6-20 compares the estimated radial stiffness to the vertical and longitudinal stiffness. Stiffness test results at 1.7 bars were not available due to a mistake during testing. Instead, test results for 1.3, 2.1 and 2.5 bars were available. The longitudinal stiffness at 2.5 and 2.1 bars are almost identical and decrease significantly at 1.3 bars, which are similar trend found in the estimation results for  $K_u$ .

Estimations of sidewall stiffness (foundation of the ring) for validations can be conducted more accurately using sidewall stiffness of tires are measured rather than tire total stiffness. In this test, the tread part of tire is fixed by the zig of the test machine and force and moment applied to sidewall only through the axle. The radial stiffness ( $S_v$ ) and torsional stiffness ( $S_\theta$ ) are measured while applying the radial or torsional displacements to the axle. The sidewall stiffness of the ring model,  $k_u$ ,  $k_v$  can be calculated by solving the following equations [70].

$$S_v = 2\pi R(k_w + k_v), \quad S_\theta = 2\pi R^3 k_v \quad (112)$$

Validations of estimated sidewall stiffness will be updated using these test results later.



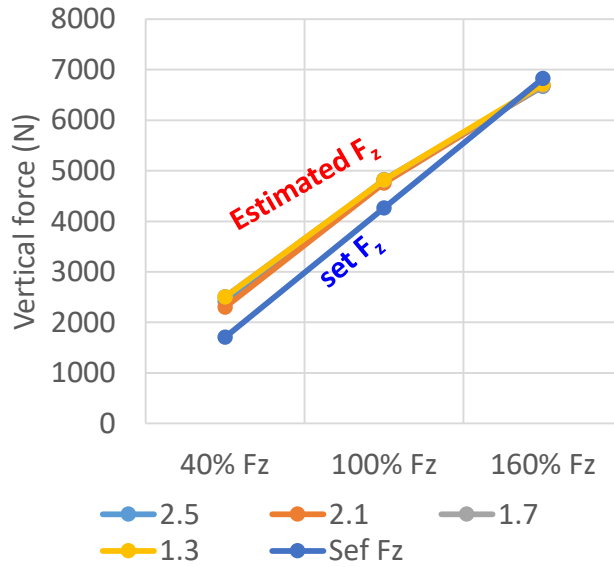
**Fig. 6-20 Comparison of  $k_w$ ,  $K_v$ , and  $K_t$  on various inflation pressure**

Table 6-3 lists model parameters from literature and those estimated in this work.  $EI$  is within the range of the value used other literature. A higher value of tread stiffness was estimated whereas the vertical and longitudinal sidewall stiffness were estimated to be lower. Actually, estimating the exact model parameters are very challenging and validation methods must developed to justify the proposed estimation methods.

Fig. 6-21 shows the error between estimated vertical force and the test load. As test load decreases, considerable discrepancies are observed. The fixed stiffness of the tread and sidewall in tangential direction may cause the error suggesting the load dependences for these stiffness also need to be included.

**Table 6-3 Comparison of stiffness parameters of flexible ring with those from literature**

Parameter	Symbol	Gong [50]	Jenkin [59]	SJ [61]	Zegelaar [70]	HK 195 size
TD Stiffness	$k_t$ (N/m <sup>2</sup> )		9.81E7	5.14E7	7.906E7	9.9E7
Ring Bending Stiffness	EI (Nm <sup>2</sup> )	1.571	1.8829	2	4	2.13
S/W Stiffness in radial	$k_u$ (N/m <sup>2</sup> )	1.16E6	4.36E5 @2.01bar	6.30E5	6.49E6	3.09E5 @2.5bar
			3.48E5 @1.67bar			3.09E5 @2.1bar
			2.62E5 @1.26bar			2.94E5 @1.7bar
S/W Stiffness in tangential	$k_v$ (N/m <sup>2</sup> )	4.70E+05	0	1.89E5	1.93E6	0.98E5~ 1.18E5



**Fig. 6-21 Error between set  $F_z$  and estimated  $F_z$  from optimization**

Using model parameters obtained, flexible ring model simulations were conducted for  $\lambda=0$  and contact pressure distributions are shown in Fig. 6-22. As test load increases, wider pressure distribution is observed. Also, under higher loads, the normal

pressure distribution become slightly concaved. The tangential traction force always points towards the contact center.

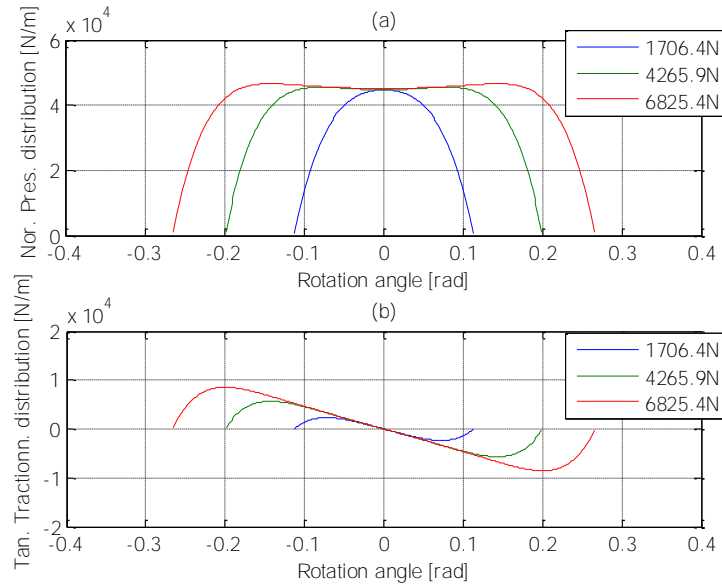


**Fig. 6-22 Estimated pressure distribution under various loads: (a) normal pressure distribution, (b) tangential stress distribution**

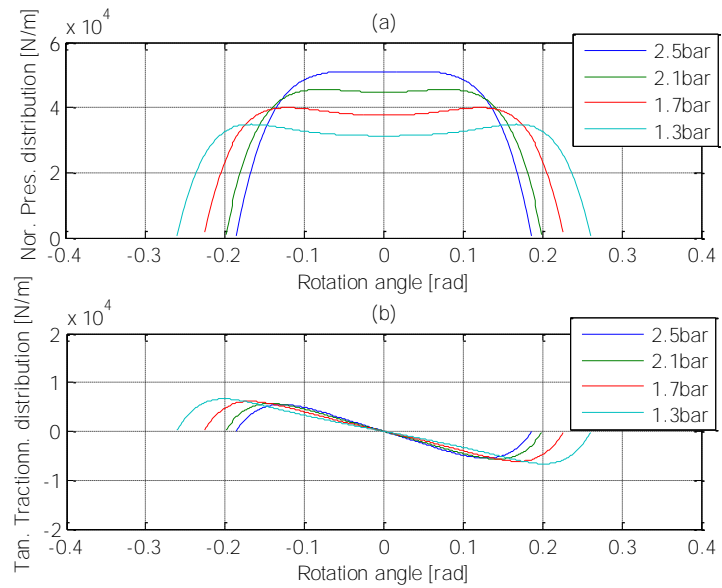


**Fig. 6-23 Estimated pressure distribution under various inflation pressures: (a) normal pressure distribution, (b) tangential stress distribution**

Fig. 6-23 shows the contact pressure distribution estimated from the model under various inflation pressures. As the inflation pressure increases, the normal pressure increases and become a more convex shape. Those trends observed in the normal pressure agree with previous founding by Jenkins [59], Gong[67], and Kim[61].

Using the same model parameters, the flexible ring model with the advanced contact model was simulated and contact pressure distributions from this model are shown in Fig. 6-24. With the same contact angles, higher contact pressures were estimated using this model and more concave shaped normal pressure arose under higher load. Tangential stresses points away from the contact patch.

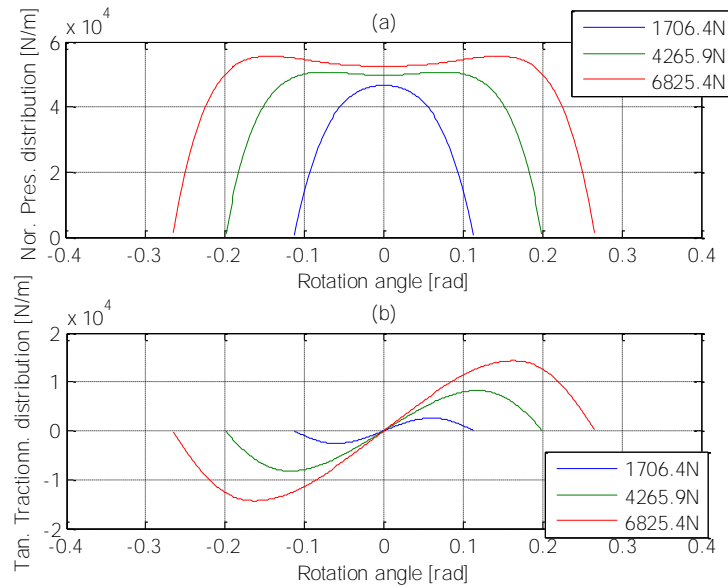


**Fig. 6-24 Pressure distribution using advanced contact model under various test loads ( $\lambda=0$ )**

Using the radial deformation from the ring model, circumferential strains at innerliner and strain rates are calculated and compared with measure ones under various test loads (Fig. 6-25~Fig. 6-26) and inflation pressures (Fig. 6-27~Fig. 6-28). In real measurements, as test load increases the width of the strain profile corresponding to the contact patch increases and compressive peaks also increase. As the inflation pressure decreases, similar trends are observed but the change is smaller than when the test load decreases. The variation in test load from 1706N to 6825.4N has a bigger impact on the

strains than the change of inflation pressure from 1.3 to 2.5 bars. These trends are also shown in the simulated strains for various test loads and inflation pressures. However, generally, the compressive peaks and the widths are smaller than real measurements. It was shown that the peak to peak distance of strain rate is slightly smaller than the contact angle when the simple contact model is used (refer to Fig. 6-12 ).

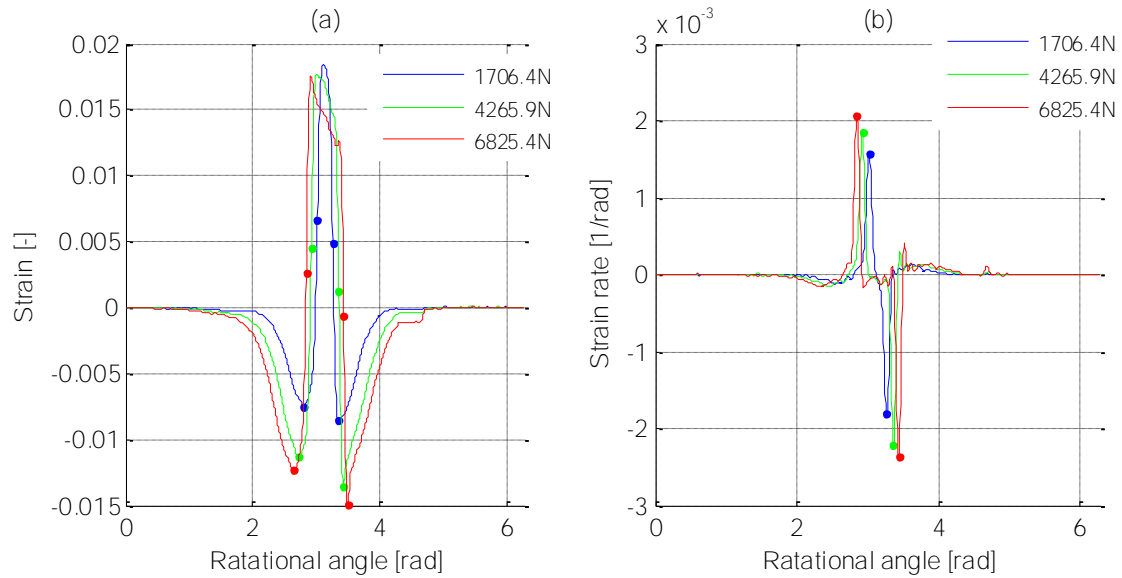


**Fig. 6-25 Measured strains (a) and strain rate (b) under various test loads @ 2.1 bars**

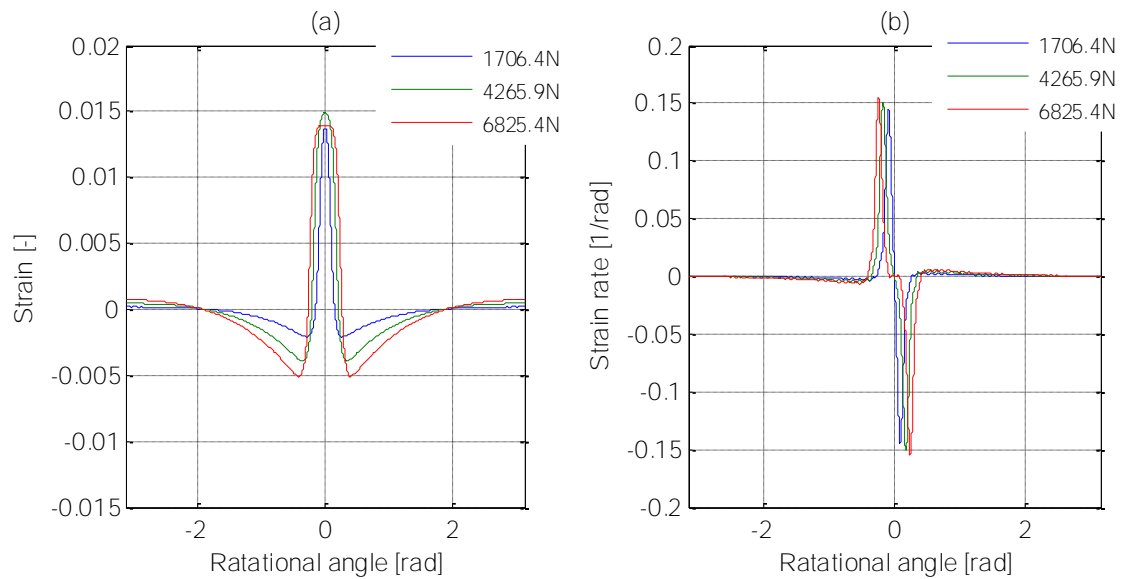


**Fig. 6-26 Simulated strains (a) and strain rate (b) under various test loads @ 2.1 bars**

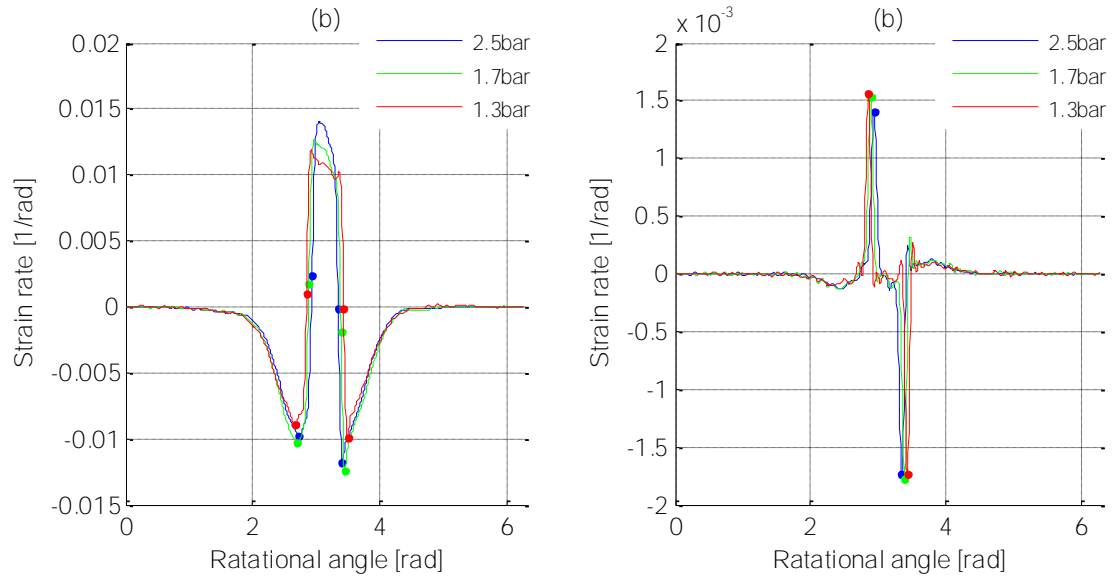


**Fig. 6-27 Measured strains (a) and strain rate (b) under various inflation pressures @ 4265.9N**

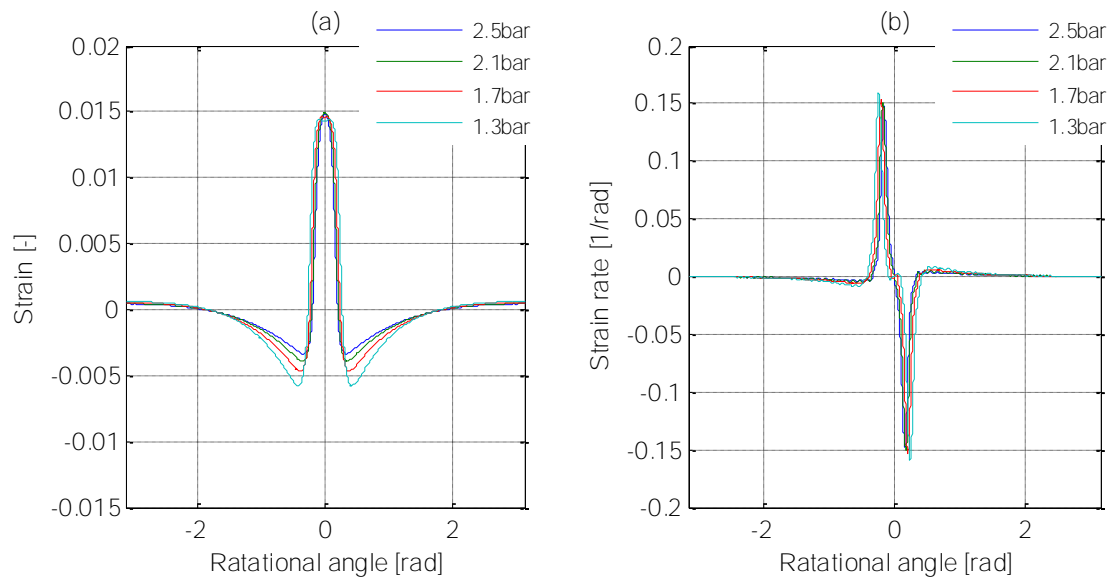


**Fig. 6-28 Simulated strains (a) and strain rate (b) under various inflation pressures @ 4265.9N**

### 6.5.2.2 Damping coefficient

Until now, the model parameters for the flexible ring model have been estimated using various methods except for non-dimensional damping coefficient,  $\lambda$ . To figure out the damping effects on strains, simulations were conducted for various rolling speeds with different damping coefficients ( $\lambda=0, 0.05, 0.1$ ), using the previously built flexible ring model. The simulation results of the contact pressures, strains and strain rates are shown in Fig. 6-29. The damping causes the center of pressure distribution to shift forward of the contact patch. As the damping increases, pressure distribution becomes asymmetrical. Also, as tire rolling speed increases, the damping effects become more obvious. Therefore, high speed combined with large damping will cause more server non-symmetry in the pressure distribution shape. When the rotational speed increases, the whole contact patch shift slightly to the front but the contact length remains almost the same indicating the rolling speed has little impact on the contact length.

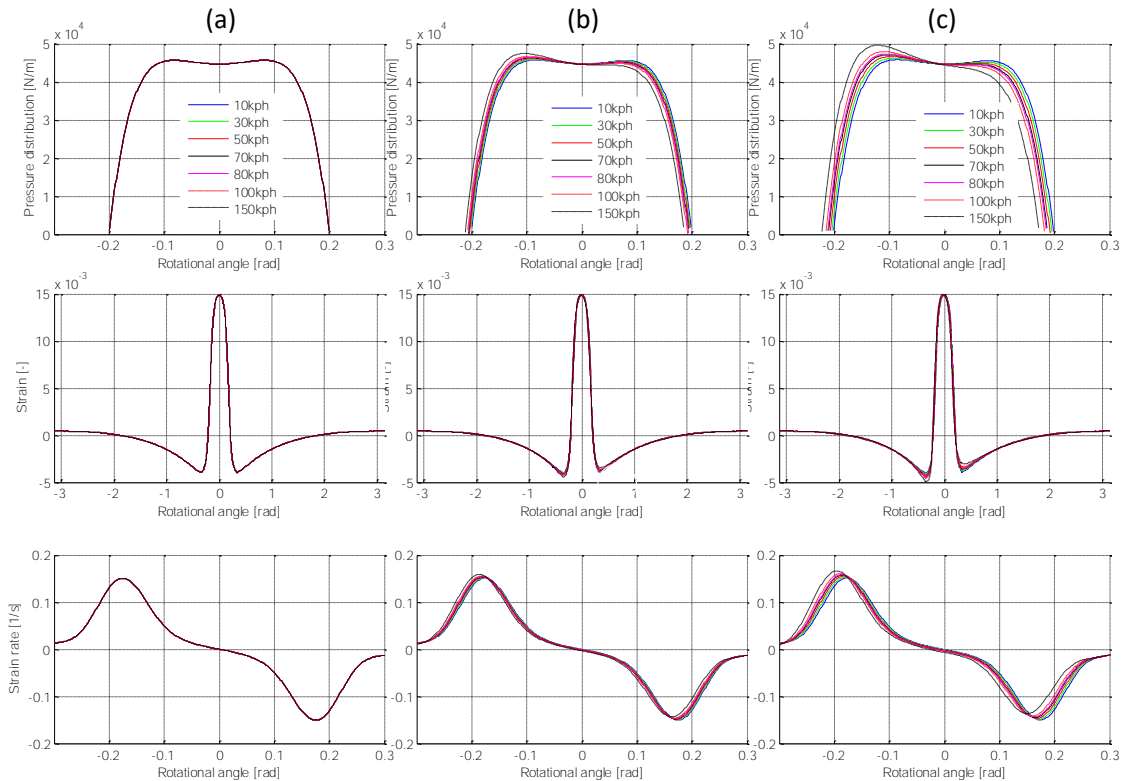


**Fig. 6-29 Damping effect on pressure distributions and strains at ref. test condition.  $\lambda=0$  (a),  $\lambda=0$  (b),  $\lambda=0$  (c)**

The internal damping also affects the shape of the strain curves; as the internal damping increases, the first compressive peak of the strain tends to increase while the second peak decreases. The higher pressure in the front of contact patch induces the higher compression before contact. The opposite explanation applies to the decrease of the compression after the contact. Fig. 6-30 shows the test speed effects on strain measurements for two different tires. As marked with light blue arrows, as test speed increases, the first compressive peak tends to increase as observed in the simulation results. However, for the second compressive peak, this tendency is not obvious. The possible slip in the rear contact region could make the internal damping effects unclear. Note that in both, simulation and experimental results, the positions of compressive peaks and the width of the tension profile is almost the same regardless test speeds.

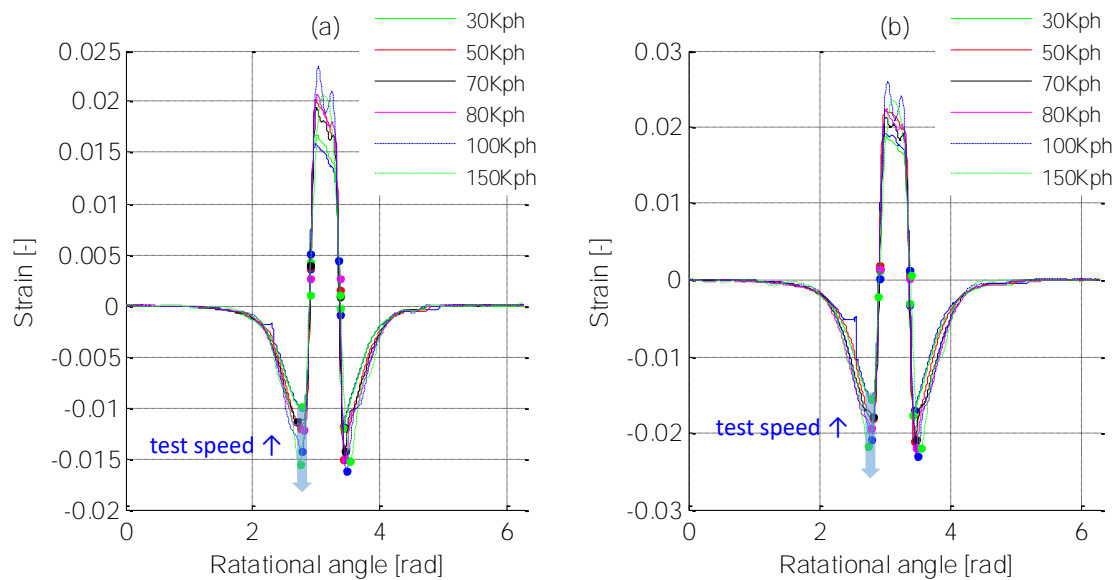


**Fig. 6-30 Test speeds effect on circumferential strains in 195/65R15 tire (a) and 205/55R16 tire (b)**

The shift of contact patch was also observed in strain rates where the first and second peaks move forward of the contact as the test speed increases while the peak to peak distance remains almost the same as shown in Fig. 6-29. Therefore, if the shift of the

contact angles can be found from strain measurements under various rolling speeds, the amount of internal damping would be estimated based on the strain simulation results. The contact angle shift at a specific rotational speed should be measured with respect to the tire at stand still or rolling at very low speeds. Thus, the time history of the strain measurement needs to be expressed on the rotational angle during the increase of the rotational speed. Under the constant speed, conversion from time to rotational angle can be easily done by counting the number of the wheel rotations within a specific time interval, as was done previously. When the angular velocity changes, this method cannot be applied and the rotational angle or its velocity should be directly measured using another sensor. Fig. 6-31 shows time histories of the strain measurements and the rotational speed. The rotational speed begin to increase at  $t=0$  and achieves the target speed after a certain time period. By integrating this speed profile, the rotational angle is calculated and the measured strain can be expressed on the absolute rotational angle rather than test time. By comparing the strain rate peak at stand still with that at a target speed, the contact angle shift can be measured.

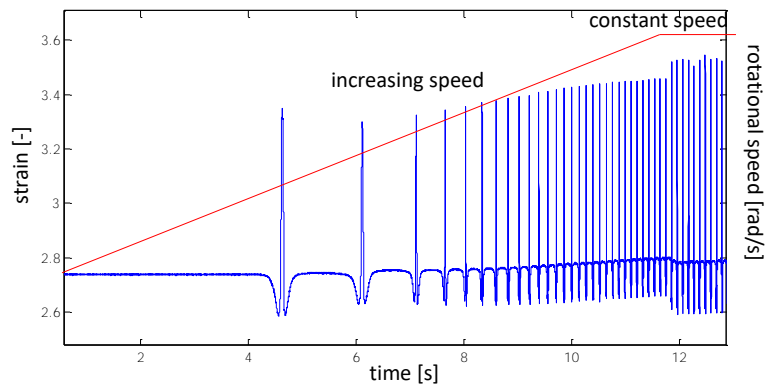


**Fig. 6-31 Strain and rotational speed time history**

However, the rotational velocity is not available from the measurements, therefore, a different method was developed. As was previously observed, the compressive peaks for experimental and simulated results of circumferential strain, are almost the same during the increase of the test speed while the contact patch shifts to the front. In other words, the peaks of the strain rate move forward while the compressive

peaks remain at the same location. Therefore, by measuring the distance between the compressive peaks of strain and the peak of strain rate, the contact patch shift can be represented. Fig. 6-32 illustrates this concept using experimental data. Strains measured at various speeds were plotted such that their second peaks are overlaid. This shift was done to amplify the effects of the test speed. The circled points in this chart correspond to locations of the strain rate peaks at the trailing edge for each test speed. As expected, the location of the strain rate peaks move forward of the contact patch as the test speed increases. The distance between peaks of the strain rate and the compression ( $\Delta\phi_{comp-edge}$ ) can be indicative of the internal damping.

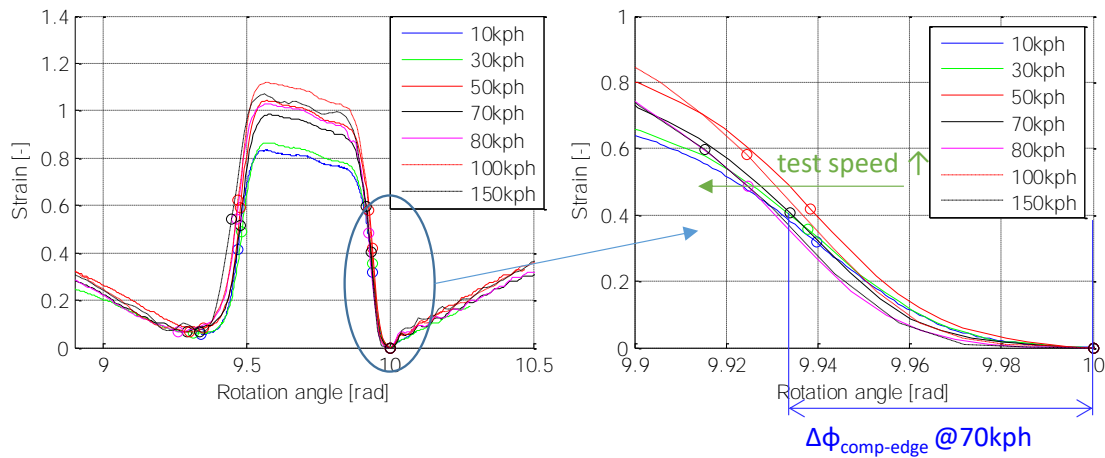


**Fig. 6-32 Identification of contact angle offset in measured data**

The contact angle shift at speed  $V$  with respect to that at 10 kph ( $\Delta\phi_{shift}@V$ ) can be calculated as shown by Equation (113) and Figure 6-33.

$$\Delta\phi_{shift}@v = \Delta\phi_{comp-edge}@v - \Delta\phi_{comp-edge}@10 \quad (113)$$

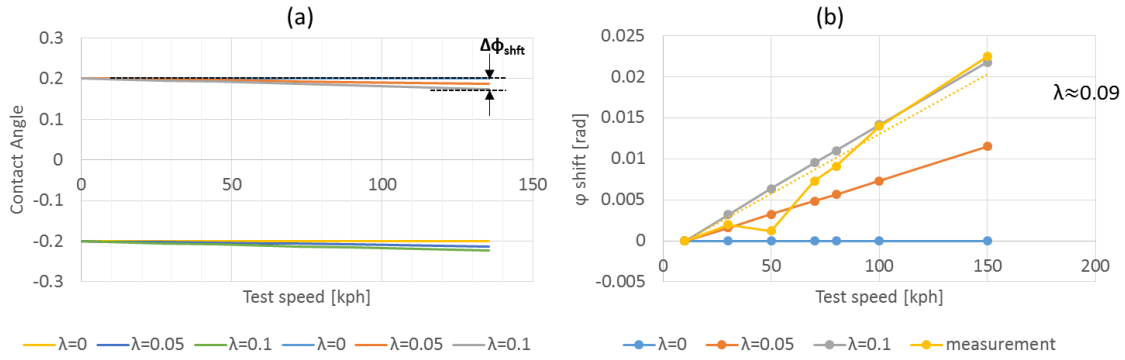


**Fig. 6-33 Estimation of normalized damping coefficient**

Simulations were done for various test speeds for  $\lambda=0, 0.05, 0.1$  and were plotted in Fig. 6-33(a). It is clearly shown as the test speed increases the contact patch shifts to the front and this tendency become more obvious as  $\lambda$  increases. The  $\Delta\phi_{shift}$  is graphically explained in this figure and calculated from the simulation results as well as experimental results, which are shown in Fig. 6-33(b). The trend line of  $\Delta\phi_{shift}$  on the test speed of experimental results is located near the line of  $\lambda=0.1$  and exact reading the graph gave around 0.09 of internal damping coefficient. In this way, the internal damping was identified using strain measurements only. Of course, to identify the contact patch shift exactly, the wheel rotational speed should be recorded simultaneously with strain measurements.

Using the estimated internal damping coefficient, dynamic pressure distributions were finally simulated for various test loads and inflation pressures and simulation results are shown in Fig. 6-34~Fig. 6-35. In this simulation, contact angles are not known, but should be determined by solving the set of nonlinear equations for contact angles similar to the implementation in Section 6.3.2. However, equations were changed because the test load is used as an input to the algorithm instead of the vertical deflection,  $d_0$ . The new set of equations were written as:

$$\begin{aligned}
 f_1 &= F_z - R \int_{\phi_f}^{\phi_r} q_u(\phi) \cos \phi d\phi = 0 \\
 f_2 &= u(\phi_f) - \bar{R}(1 - \cos \phi_f) - \{u(\phi_r) - \bar{R}(1 - \cos \phi_r)\} = 0
 \end{aligned}
 \tag{114}$$

The first equation means that the estimated load is equal to the test load and the second one means that the tread deformations at both contact edges should be the same. In simulation results (Fig. 6-34~Fig. 6-35), the non-symmetry in the contact pressure is now clearly observed; a higher normal pressure arises in the front whereas a lower pressure in the rear of the contact patch. As the test load increases or the inflation pressure decreases, a more concavity is shown in the normal pressure distribution.

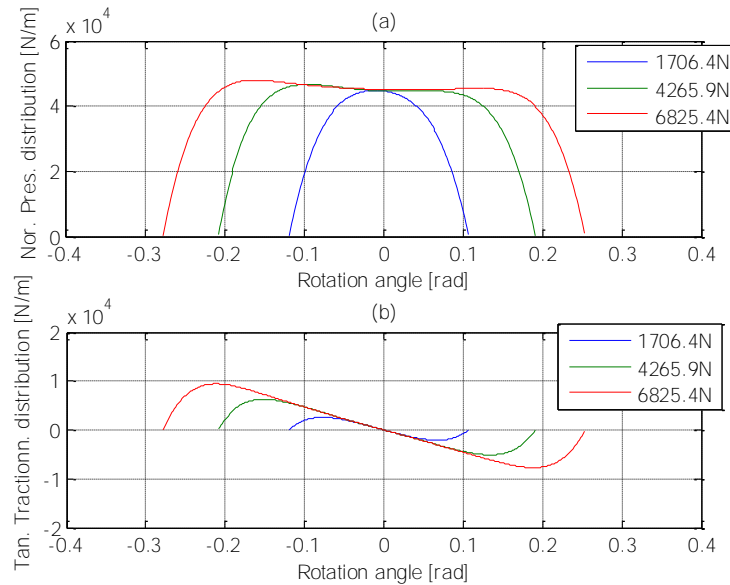


**Fig. 6-34 Pressure distribution using model type I under various test loads ( $\lambda=0.09$ )**

Notice that the inflation pressure effects on the pressure distribution differ from those shown in Fig. 6-7 (b). In this simulation, as the inflation pressure decreases, the contact length increases while the maximum pressure decreases as shown in Fig. 6-35(b). However, the contact path length becomes longer as the inflation pressure increases in the previous simulation results (Fig. 6-7 (b)). In the previous simulation, the same vertical deflection was applied to the tire under various inflation pressures. In order that the high inflated tire is deflected by the same amount as the low inflated tire, the higher vertical load should be applied. The effect of this increase in the vertical load on the contact patch could be bigger than the effect of the increase in the inflation pressure from 1.28 bars to 2.13 bars. In this simulation, the test load is kept the same and the vertical deflection

varies with respect to different inflation pressures, such that the integral of the pressure distribution is identical to the applied vertical force. This is the general situation occurring in indoor tests to measure the vertical stiffness or contact shapes of tires. From experimental results, it is obvious that the low inflated tire has longer contact length and lower contact pressure than the high inflated tire when both are subjected to the same vertical load.

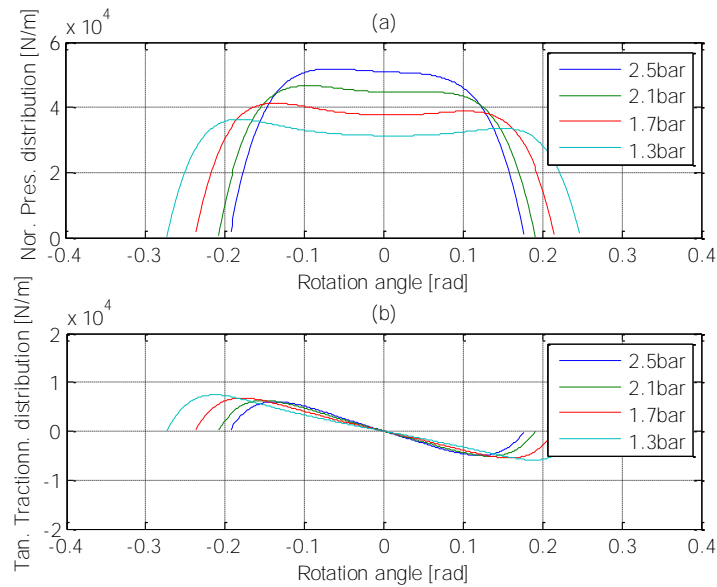


**Fig. 6-35 Pressure distribution using model type II under various test loads ( $\lambda=0.09$ )**

Using the same damping coefficients, simulations were conducted again with the advanced contact model and the results are shown in Fig. 6-36. The concavity of the normal pressure is more severe as the test load increases. The tangential stress points away from the contact center and sliding occurs near the trailing edge. The advanced contact model is thought to provide more realistic pressure distribution.

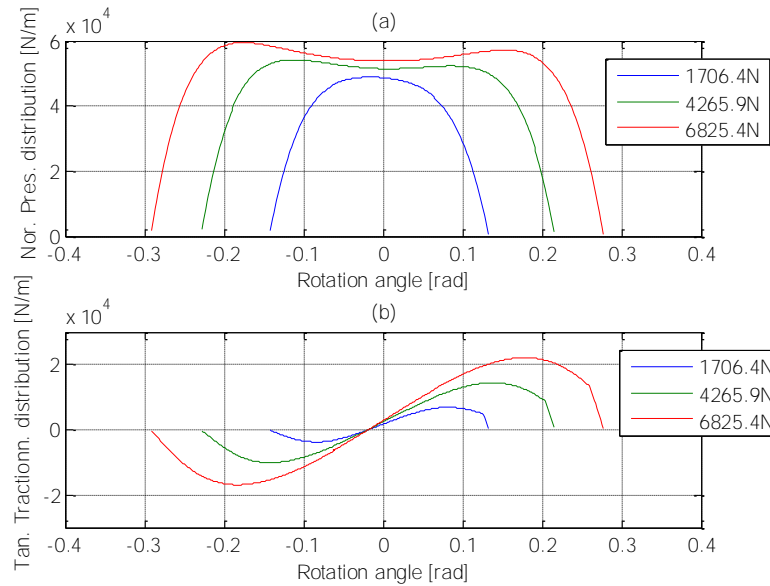


**Fig. 6-36 Pressure distribution using model type II under various test loads ( $\lambda=0.09$ )**

## 6.6 Application for Lateral Force Estimation

Through Section 6.5, various model parameters have been identified step by step and dynamic pressure distributions were obtained finally. This pressure distribution can be utilized for the study of tire wear, traction and so on. In this section, the estimation method for the lateral force proposed in Section 4.2 is updated by use of identified pressure distributions. In the conventional Brush tire model, the pressure distribution is assumed to be parabolic. As was found from the flexible ring model, the pressure distribution is more concaved especially when the tire is subjected to larger vertical deflections. Also, pressure distribution is asymmetrical due to the internal damping effect. Those characteristics of the dynamic pressure distribution affect lateral forces especially in the sliding region (near trailing edge).

In this chapter, the lateral force estimation was performed again using pressure distributions estimated from the developed flexible ring model. The scheme of this estimation is illustrated in Fig. 6-37. Test loads and slip angles can be estimated using the algorithms suggested in Sections 4.1.2-4.1.3. However, they are assumed to be known.

The lateral forces are estimated using parabolic pressure distribution, as is done in the conventional method and using estimated pressure distributions from the flexible ring model. Except for formulating pressure distributions, the same algorithm was used for both cases. Estimated lateral forces were compared with the measured lateral forces collected from Flat-Trac test rig. More test information can be found in Table 3-3.

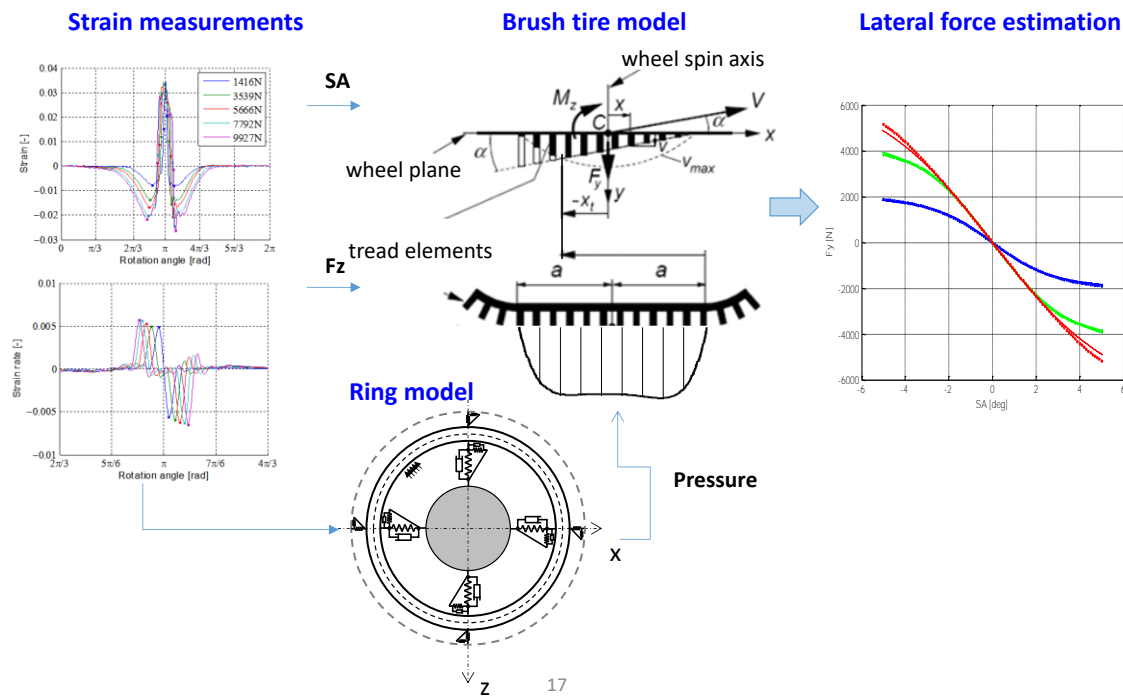


**Fig. 6-37 Estimation of lateral force by use of BM and flexible ring model**

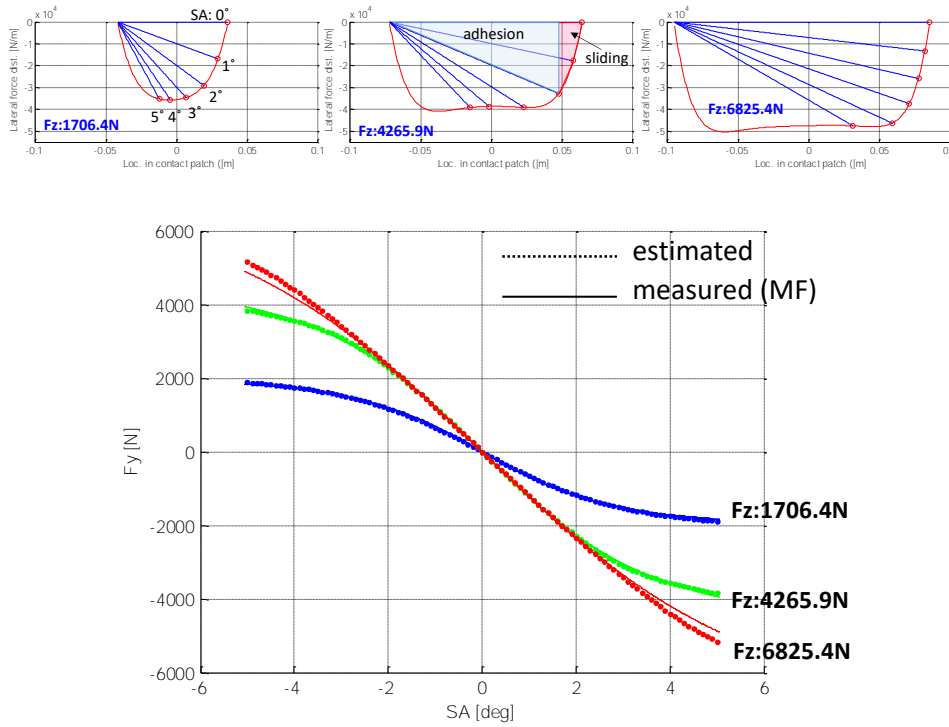


**Fig. 6-38 Lateral force estimations for various test loads using estimated pressure distributions**

The estimation results are shown in Fig. 6-38 and Fig. 6-39 for various test loads and inflation pressures, respectively. The lateral force distribution on the sliding region for each slip angle are also conceptually illustrated in the upper charts in rows. For various test loads, estimated lateral forces agree well with the measured ones except for the case that the higher load and the higher slip angle are applied at the same time (Fig. 6-38). The inflation pressure effect on the lateral force from test results is somewhat nonlinear; the lateral force at 2.1 bars is largest and then it decreases as the inflation pressure decreases. This nonlinear relationship is well represented with estimated lateral forces. Under the lowest inflation pressure, the lateral force was overestimated making the estimation accuracy poor.

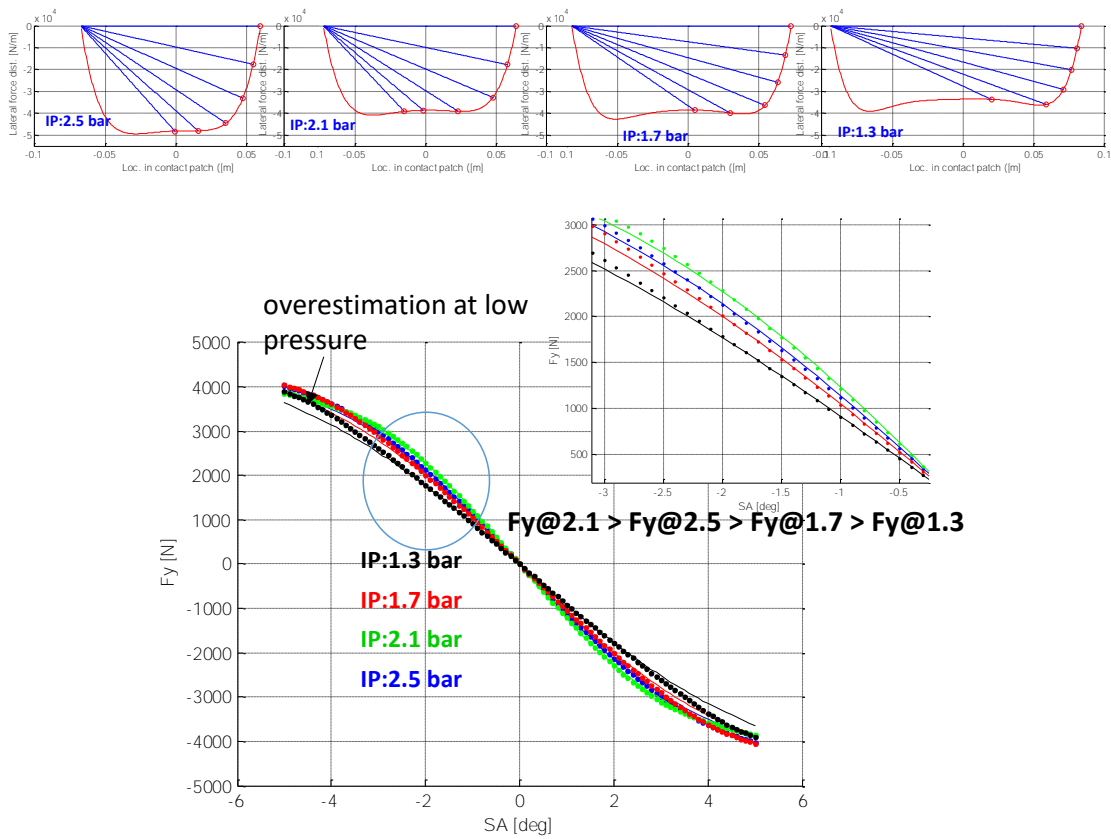


**Fig. 6-39 Lateral force estimations for various inflation pressures using estimated pressure distributions**

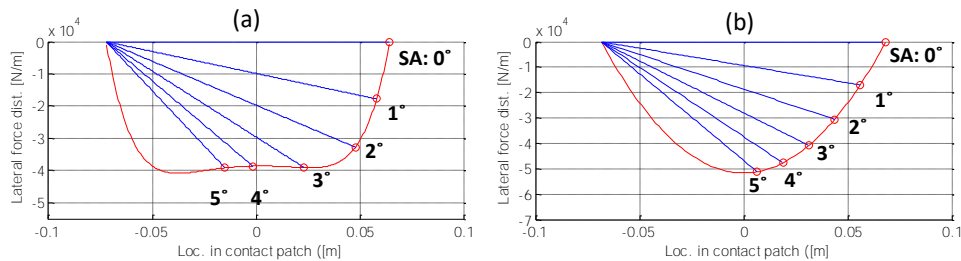


**Fig. 6-40 Comparison of pressure distribution between estimated and parabolic-assumed**

To confirm any improvements of the suggested method over the conventional one, the parabolic pressure distributions were formulated and was fed into the Brush tire model. Fig. 6-40 compares lateral force distributions at different slip angles for both pressure distributions. For the various test loads, the suggested method provides better estimation especially for the slip angle ranging  $0^{\circ} \sim 4^{\circ}$  (Fig. 6-41). The suggested method

shows better estimations when the inflation pressure varies also (Fig. 6-42). Under higher inflation pressures like 2.5 and 2.1 bars, the estimation results of the suggested method show good agreements within  $0^{\circ}\sim 4^{\circ}$  of the slip angle while the conventional method somewhat underestimates lateral forces. When lower pressures are applied, the suggested method shows better estimation results within  $0^{\circ}\sim 3^{\circ}$  of the slip angle than the conventional method. Beyond this range of slip angle, the suggested method overestimates whereas the conventional method underestimates lateral forces; both methods provide poor estimations. Overall, the suggested method can estimate lateral forces more accurately than the conventional method.

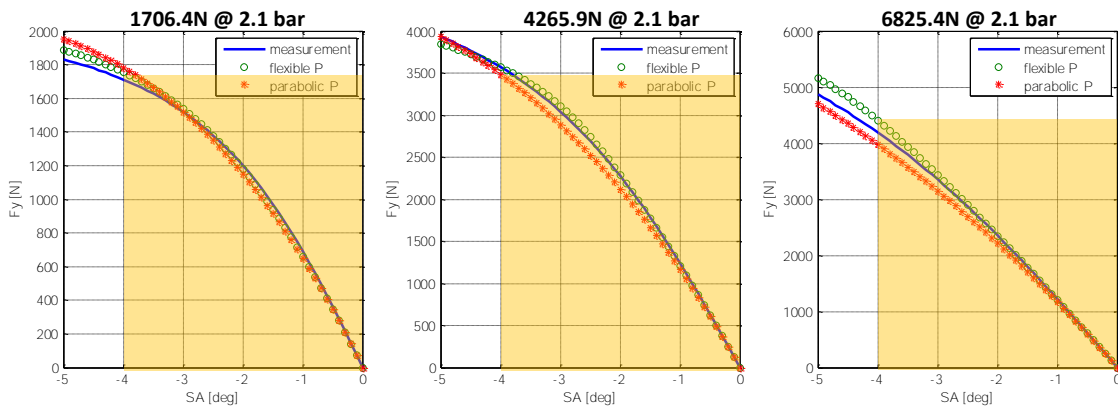


**Fig. 6-41 Comparison of lateral force estimation results between suggested and conventional**

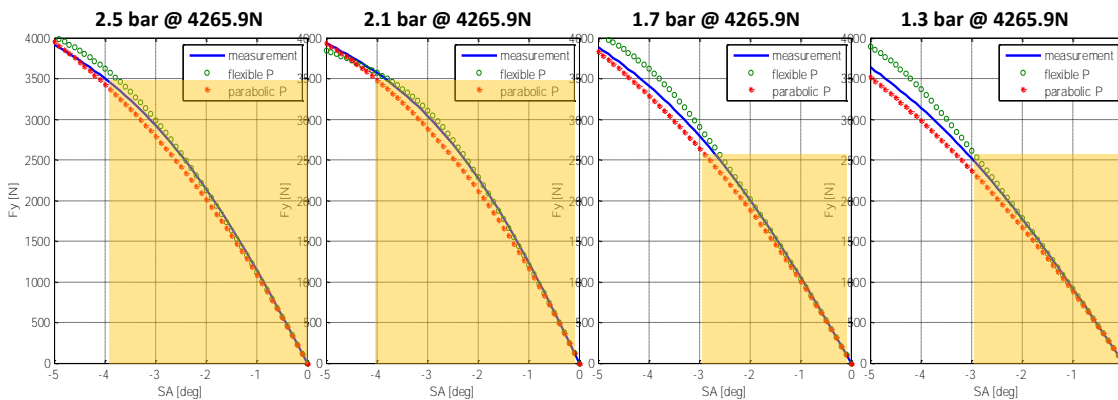


**Fig. 6-42 Comparison of lateral force estimation results between suggested and conventional**

## 6.7 Chapter Conclusion

Advanced flexible ring models were introduced to be combined with measured strains, which can represent rolling tires at high speeds by including the inertial and internal damping effects of the wheel. Two different boundary conditions were used to solve the circumferential contact problems and simulation programs were implemented for each. The simulation results are compared with each other using model parameters from literature.

For the application purpose of these model, strains are measured for free rolling tires under various combinations of test loads, inflation pressures and test speeds. Modal tests were conducted and test results were used to estimate the bending stiffness of the tread band. Contact angles were identified from strain measurements and were input to the simulation of the flexible ring model, which removed the repeated process to identify the contact patch. Sidewall stiffness was estimated based on the optimization routine minimizing the error between test loads and estimated loads obtained from the flexible ring model assuming there is no damping effect.

Using estimated model parameters, damping effects on the circumferential strains were simulated. Based on the simulation results, a methodology to extract damping characteristic from the measured strain was proposed. By comparing this characteristic from measured strains with simulation results, the damping coefficient was roughly estimated for the test tire.

With this estimated damping coefficient, simulation was conducted and dynamic contact pressures (of which shapes are now asymmetric due to the damping effects) are estimated under various test conditions. These estimated pressures were used in the Brush tire model to replace assumed pressure distributions used in the conventional method. Estimated lateral forces using pressure distributions from the ring model agree well with measured values more accurately than the conventional method.

## 7 CONCLUSIONS AND FUTURE WORK

This research was initiated to formulate the methodologies to estimate crucial tire-road contact parameters for advanced vehicle controls and to develop analysis tools to study tire dynamic characteristics by use of the intelligent tire system. In this chapter, the summary of this research and contributions are provided followed by expected future work.

### 7.1 Research Summary

Based on extensive literature survey, the effective sensor network for estimating characteristics related to lateral dynamics of tires was developed; multiple strain gages were attached to the innerliner corresponding to the center and off-center locations for a five-rib tire. The direction of sensors were parallel to the wheel plane to measure the circumferential strains. By investigating empirical results of both strain measurements and Flat-Tract test results, several predictors were suggested and correlated with the tire characteristics such as contact shapes, test loads, slip angles, slip ratios and lateral forces.

The estimation of contact shapes and test loads were based on the contact length estimated from strain signals suggested in [37]. A robust regressor was developed for the test load estimation while slip angle is applied. The tire contact length at the center was found to be a valid regressor for the test load estimation during cornering because it is insensitive to slip angle change. Based on the work of [53], a new synthetic predictor was suggested for slip angle estimation: the slope of peak strain rates over the tire lateral distance. It was correlated linearly with the slip angle with higher accuracy. The method to estimate slip ratios when the wheel is subjected to acceleration or braking was developed by use of the idea from [39, 41].

Multivariable regressions were conducted to estimate lateral force when tire is subjected to slip angle under various vertical loads or camber angles simultaneously. It was shown that regression results agree well with the measurements. The suggested regressors for this multivariable regression (compressive peaks and contact lengths

measured at the center and a pair of off centers) were chosen by considering simple physics of the tire lateral dynamics. Another estimation method for the lateral force was suggested by introducing the Brush tire model. In this application, previously estimated parameters such as test loads, contact lengths and slip angles were input to this model to predict the lateral force. This method predicted lateral forces with high accuracy.

This research also explored another application of intelligent tire system; as a tool for the analysis of tire characteristics. Because sensors are located generally near the contact, the measurements have ample information on the tire-road contact and tire deflections near the contact patch. To utilize these sensor measurements for this purpose, well-define physical tire models need to be incorporated. This approach was utilized in [31-35] where tire lateral dynamic models were included in the estimation process for friction coefficients.

In this research, tire characteristics related to in-plane dynamics were investigated by inclusion of modified flexible ring models. An appropriate strain-deformation relationship was developed and validated based on FEM simulation results. By combining flexible ring model and the proposed relationship, the simulation method to represent the circumferential strain was developed. The contact problem for the static tire or slowly rolling tire was solved using this model. In this case, the strain is regarded as a symmetrical shape, which are well represented by the suggested model. The radial deformation was directly obtained by solving the strain-deformation relationship expressed as an ordinary differential equation using Finite Difference Method (FDM). Tire parameters were identified by fitting the radial deformations from the flexible ring model [64] to those derived from strain measurements. Some model parameters were also determined during this process. Identified pressure distributions and tire parameters for three different tires based on this method agree well with the conventional method which use the flexible ring model with a tread-road contact model. The suggested method has a merit of not including the tread-tire contact model which requires repeated process to determine the contact angle and often face numerical difficulties in satisfying boundary conditions simultaneously.

Identifying dynamic pressure distributions and stiffness of the rolling tire at high speeds is challenging although they need to be deeply investigated to understand their effects on the tire performance like wear, vibration and traction. To do this, flexible ring models which can handle dynamic behavior of the tire were implemented based on [50, 61]. A simple contact model was chosen considering its applicability and capability to represent the measured strains. However, an advanced contact model was also implemented with the flexible ring model to provide more realistic pressure distributions. In the model implementation, the contact angles were determined simultaneously by solving a set of nonlinear equations. This suggested implementation could reduce any potential errors.

The contact angles identified from strain measurements were input to the flexible ring model to identify tire characteristics, which eliminated the repeated procedure to find them. Instead, an optimization routine was incorporated into the solution process to find sidewall stiffness in the tangential and radial directions while minimizing the error between estimated vertical forces and measured ones under the assumption of non-internal damping. As a result, sidewall stiffness and dynamic pressure distribution were estimated. For diverse vertical loads and inflation pressures, simulations were performed and tire characteristics were estimated. The observed trends during variation of the vertical load and the inflation pressure follows those of the experimental results.

Internal damping effects on strains were simulated for various test speeds with different damping coefficients. By comparing measured strains at different test speeds to the simulation results, the internal damping coefficient was roughly estimated. With these set of estimated parameters, the dynamic pressure distributions were obtained where they have asymmetrical shapes due to the inclusion of internal damping effects.

The lateral force estimation based on the Brush tire model was updated by replacing the assumed pressure distribution in the conventional method with estimated ones from the flexible ring model and the predicted lateral forces agreed well with measured ones (better results than the conventional method).

## 7.2 Research Contributions

By conducting this research, the previous applications of intelligent tires are explored and organized to provide reference for any future study.

The suggested arrays of strains gages can be effectively used for the estimation of key tire-road contact parameters for the lateral tire dynamics and with developed estimation algorithms, they can be readily utilized for the real driving scenarios. The parameter estimations using the intelligent tire technology is expected to give more exact quantities and require less time for predictions than traditional indirect methods and can effectively improve vehicle stability control performance.

Among the important contributions of the dissertation is the proposal of the new application of intelligent tires to analyze tire dynamic characteristics by inclusion of well-defined theoretical tire models. Throughout the course of research in this application, the simulation method to represent strain measurements were suggested. This model can give insight to the physical meanings of strain measurement which have been considered as nothing more than inputs to statistical models or machine learning models. Also, more valid and effective features of measured signals can be extracted as predictors for statistical model based on the physical understanding on the strain measurements. The estimated parameters based on the fusion of flexible ring models and strain measurements could very well reflect the characteristics of tires used in the real driving because strain measurements can be conducted in any driving conditions. The proposed identification methods are implemented as a stand-alone program in MATLAB and can be readily used once strain measurements are secured.

Overall, the suggested methodology is a good starting point of new application of sensor measurement for the analysis of the tire physical characteristics. Therefore, the contributions of this research are summarized as:

- 1- Comprehensive literature search
- 2- Multiple strain-based intelligent tire system

- 3- Estimation algorithm for crucial tire characteristics related to lateral dynamics of the wheel
- 4- Simulation model for circumferential strains using FE and flexible ring models
- 5- An enhanced flexible ring model by use of strain measurements
- 6- Methodologies to identify tire parameters by utilizing strain measurements

### **7.3 Future works**

In order that the suggested estimation method to be a more effective tool, further refinement should be warranted as suggested below.

First, the flexible ring model and the strain-deformation relationship need to be modified to represent more realistic features of strain measurements.

As discussed in Section 5.4, current strain simulation methods cannot represent the trend of the measured strain of which tension in the contact region tends to decrease consistently as test load increases. Even though advanced contact models were introduced, which can represent the tread shear deformations and the outward tangential stress, this trend of real measurements could not be duplicated.

Fig. 7-1 illustrates these two contact models conceptually. In the simple contact model shown in (a), the contact pressure always points toward the wheel center. Therefore, the tangential stress is directed to the center of the contact. In the current ring model, regardless of the contact model used, the external forces are assumed to be applied at the neutral axis, which means the inward tangential stress is applied at the neutral axis suppressing the increase of the tension due to the beam bending motion. This effect will grow as the test load increases and a slight drop in the tension was observed as test load increases with this contact model as shown Fig. 7-2 (a). (Fig. 7-2 magnified Fig. 6-10 for the convenience sake.)

When an advanced contact model is used, the tangential stress is directed outward and applied at the neutral axis too even though this tangential force is applied at the tread surface (Fig. 7-2 (b)). The outward tangential force applied at the neutral axis causes more tension as the test load increases, which is opposite to the desired outcome.

Even though the moment  $q_\theta$  due to the offset of applied force from the tread surface to the neutral axis would contribute to the compression at the innerliner through the rotation of the cross-section, this effect is very small because of Bernoulli-Euler assumption. In the contact region, on a flat surface, the neutral axis is almost flat and the cross-section is subjected to be almost normal to the flat surface without any rotation. Resultantly, the advanced contact model fail to duplicate the load dependency of measured strain as shown in Fig. 7-2 (b)

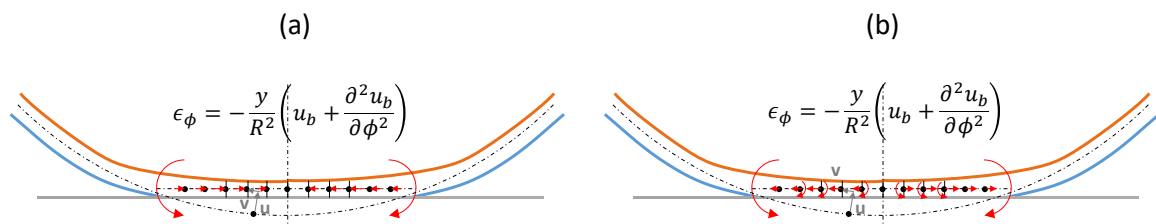


**Fig. 7-1 Tread-road contact model: (a) radial-only-deformation of tread, (b) shear and normal deformation of tread**

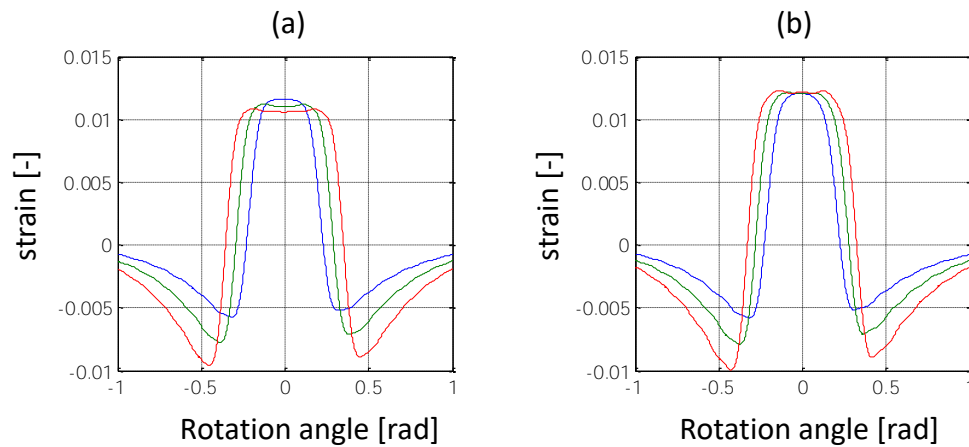


**Fig. 7-2 Simulated strains: (a) radial-only-deformation of tread, (b) shear and normal deformation of tread**

Thus, the compression at the inner surface induced by the rotation of the cross plane is hardly expressed with the conventional ring model. Rather, in the advanced contact model, the tension may increase due to the outward tangential stress assumed to be applied at the neutral axis. By comparing Fig. 7-2 (a) and (b), the load dependency

of the strain is represented by the the simple contact model slightly better than the advanced model. However, the amount of decrease is very small as compared to that of real measurements. To represent this load dependency of strains, the rotation of cross-section due to the outward tangential stress need to be magnified as illustrated in Fig. 7-3. To allow this deformation of the ring, Bernoulli-Euler assumption would be discarded and more elaborated curved beam models need to be adopted. Since the strain-deformation relationship used are also based on this assumption, it needs to be modified without this assumption. This would be beyond the scope of this research.

This paragraph explains a way to advance the strain model. When the tire is pushed on the frictional flat surface, two different modes of the ring deformation take place simultaneously: one is the bending motion arising during the ring is bent to fit into the flat surface and the other is shear deformation due to the tangential contact stress applied at its surface. Let us assume these deformations take place sequentially rather than simultaneously. Thus, we can still use the traditional ring model and calculate the strains for the first stage (bending deformation of the ring). And then, straight beam model can be introduced to model the shear deformation due to the outward tangential stress applied at the outer surface of the beam. For the straight beam under this condition, the strains  $\Delta\epsilon_{\phi,comp}$  at the inner surface could be easily calculated. By superposing the strain induced by bending onto that induced by shear, the resultant strains will be obtained and they are expected to have more obvious load decencies similar to measured strains.

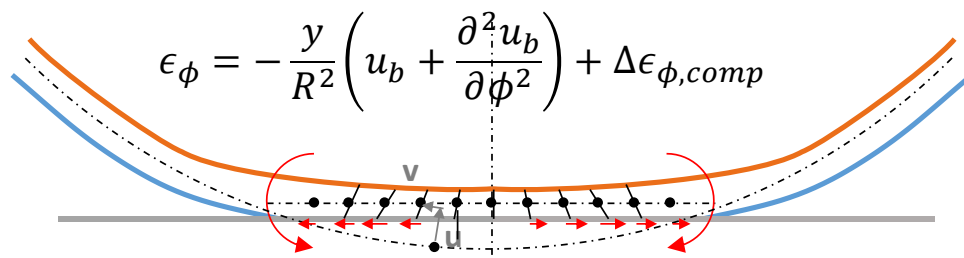


**Fig. 7-3 Proposal of improved model for strain simulation**

This research showed the possibility to obtain the tire deformation from strain measurements. However, it requires a sophisticated and updated flexible ring models as well as strain-deformation relationships as discussed. To validate the current method and update the model, another type of sensors can be installed together with strain gages to measure the radial deformation directly as presented in [72] Fig. 7-4 shows measured in-plane deformations of carcass from this literature using an optical tire sensor system when tire is subjected various test loads. Using these experimental data, assumptions such as Bernoulli-Euler beam and inextensibility would be discussed again especially in the contact patch.

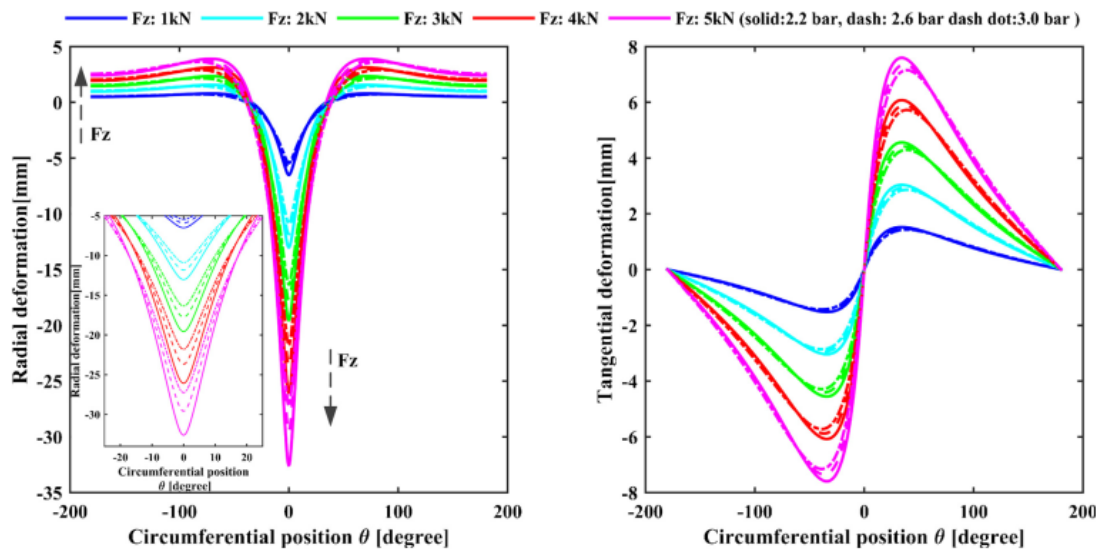


**Fig. 7-4 In-plane tire deformations under different vertical forces with a rotational speed of 100 rad/s: (a) radial deformations and (b) tangential deformations**

Another future work is related to validations. The identified tire dynamic characteristics using this combined method are hard to validate because measuring the characteristics of the rolling tire at high speeds, like contact lengths and pressure distribution, is very challenging. Elaborated FEM models which can handle with simulations of tire rolling at high speeds can be used for validations of this methods.

In this research, tire physical characteristics related to only in-plane dynamics were deeply investigated using the strain measurements. Although these parameters could be related to diverse performances such as vibrations, a ride quality of vehicle as

well as traction, rolling resistance and wear of tire, they cannot directly explain the lateral dynamics of tire which is crucial to analyze handling performances of vehicle. To investigate those characteristics, lateral strains or accelerations measured in the lateral directions can be utilized with appropriate tire models such as Fiala model [49] and TREAD Sim model model [38].

Lastly, the estimation methods for the tire-road contact parameters are developed based on the test results from the indoor rolling test machine. To be applied in the real driving, the estimation methods need to be validated using collected data from the real driving situation. Most strains in this research were measured on the flat surface, so the effects of road unevenness on strains measured at the innerliner should be investigated for real applications. Fortunately, since the flexible ring model can deal with uneven road surfaces somehow, the effects of the uneven road surface can be understood theoretically. Also, the durability of the strain gages needs to be confirmed for the real application and hard ware configurations should be adjusted to be used in the real driving.

From these considerations, followings are suggested as possible future studies within this research scope

1. Validate and apply suggested estimation methods in the real driving situation.
2. Expand the identification study to out of plane dynamics of tire by use of combinations of lateral strains or accelerations with appropriate tire models.
3. Improve the strain model to represent the same load dependency as measured strain has.
4. Improve suggested identification method using the updated model.
5. Validations of model parameters identified by suggested methods using FEM or experiments

## REFERENCE

- [1] Matsuzaki, R., and Todoroki, A., 2008, "Wireless Monitoring of Automobile Tires for Intelligent Tires," *Sensors (Basel)*, 8(12), pp. 8123-8138. 10.3390/s8128123
- [2] Gent, A. N., and Walter, J. D., 2006, "Pneumatic Tire."
- [3] Consortium, A., 2005, "APOLLO Final Report Including Technical Implementation Plan," Technical Research Centre of Finland (VTT).
- [4] Braghin, F., Brusarosco, M., Cheli, F., Cigada, A., Manzoni, S., and Mancosu, F., 2006, "Measurement of contact forces and patch features by means of accelerometers fixed inside the tire to improve future car active control," *Vehicle System Dynamics*, 44(sup1), pp. 3-13. DOI: 10.1080/00423110600867101
- [5] Tomizuka, M., Moon, K. S., Yun, C.-B., Liang, H., Yi, J., Giurgiutiu, V., and Mika, B., 2007, "Tire tread deformation sensor and energy harvester development for smart-tire applications," 6529, p. 65290K. 10.1117/12.721009
- [6] Yi, J., 2008, "A Piezo-Sensor-Based 'Smart Tire' system for mobile robots and vehicles," *IEEE/ASME Transactions on Mechatronics*, 13(1), pp. 95-103. 10.1109/tmech.2007.915064
- [7] Reindl, L. M., Pohl, A., Scholl, G., and Weigel, R., 2001, "SAW-based radio sensor systems," *IEEE Sensors Journal*, 1(1), pp. 69-78. 10.1109/jsen.2001.923589
- [8] Pohl, A., Steindl, R., and Reindl, L., 1999, "The "intelligent tire" utilizing passive SAW sensors measurement of tire friction," *IEEE transactions on instrumentation and measurement*, 48(6), pp. 1041-1046.
- [9] Todoroki, A., Miyatani, S., and Shimamura, Y., 2003, "Wireless strain monitoring using electrical capacitance change of tire: part I—with oscillating circuit," *Smart Materials and Structures*, 12(3), p. 403.
- [10] Todoroki, A., Miyatani, S., and Shimamura, Y., 2003, "Wireless strain monitoring using electrical capacitance change of tire: part II—passive," *Smart Materials and Structures*, 12(3), p. 410.
- [11] Matsuzaki, R., and Todoroki, A., 2006, "Passive wireless strain monitoring of actual tire using capacitance–resistance change and multiple spectral features," *Sensors and Actuators A: Physical*, 126(2), pp. 277-286.
- [12] Matsuzaki, R., and Todoroki, A., 2007, "Wireless flexible capacitive sensor based on ultra-flexible epoxy resin for strain measurement of automobile tires," *Sensors and Actuators A: Physical*, 140(1), pp. 32-42.

- [13] Yilmazoglu, O., Brandt, M., Sigmund, J., Genc, E., and Hartnagel, H., 2001, "Integrated InAs/GaSb 3D magnetic field sensors for "the intelligent tire", " Sensors and Actuators A: Physical, 94(1), pp. 59-63.
- [14] Miyoshi, A., Tsurita, T., and Kunii, M., 2007, "System and method for determining tire force," Google Patents.
- [15] Cheli, F., Leo, E., Melzi, S., and Sabbioni, E., 2010, "On the impact of 'smart tyres' on existing ABS/EBD control systems," *Vehicle System Dynamics*, 48(S1), pp. 255-270.
- [16] Tuononen, A., and Hartikainen, L., 2008, "Optical position detection sensor to measure tyre carcass deflections in aquaplaning," *International Journal of Vehicle Systems Modelling and Testing*, 3(3), pp. 189-197.
- [17] Tuononen, A. J., 2008, "Optical position detection to measure tyre carcass deflections," *Vehicle System Dynamics*, 46(6), pp. 471-481.
- [18] Tuononen, A., 2009, "On-board estimation of dynamic tyre forces from optically measured tyre carcass deflections," *International journal of heavy vehicle systems*, 16(3), pp. 362-378.
- [19] Tuononen, A., 2009, "Optical position detection to measure tyre carcass deflections and implementation for vehicle state estimation," Ph.D. Dissertation.
- [20] Tuononen, A., and Matilainen, M., 2009, "Real-time estimation of aquaplaning with an optical tyre sensor," *Proceedings of the Institution of Mechanical Engineers, Part D: Journal of Automobile Engineering*, 223(10), pp. 1263-1272.
- [21] Magori, V., Magori, V., and Seitz, N., "On-line determination of tyre deformation, a novel sensor principle," *Proc. Ultrasonics Symposium, 1998. Proceedings., 1998 IEEE, IEEE*, pp. 485-488
- [22] Erdogan, G., 2009, "New Sensors and Estimation Systems for the Measurement of Tire-Road Friction Coefficient and Tire Slip Variables," Ph.D. Dissertation, University of Minnesota.
- [23] Erdogan, G., Alexander, L., and Rajamani, R., 2009, "A novel wireless piezoelectric tire sensor for the estimation of slip angle," *Measurement Science and Technology*, 21(1), p. 015201.
- [24] Erdogan, G., Alexander, L., and Rajamani, R., "Measurement of Uncoupled Lateral Carcass Deflections With a Wireless Piezoelectric Sensor and Estimation of Tire Road Friction Coefficient," *Proc. ASME 2010 Dynamic Systems and Control Conference, American Society of Mechanical Engineers*, pp. 541-548

- [25] Erdogan, G., Alexander, L., and Rajamani, R., 2011, "Estimation of tire-road friction coefficient using a novel wireless piezoelectric tire sensor," *IEEE Sensors Journal*, 11(2), pp. 267-279. DOI: 10.1109/JSEN.2010.2053198
- [26] Niskanen, A. J., and Tuononen, A. J., 2014, "Three 3-axis accelerometers fixed inside the tyre for studying contact patch deformations in wet conditions," *Vehicle System Dynamics*, 52(sup1), pp. 287-298.
- [27] Matilainen, M., and Tuononen, A., 2015, "Tyre contact length on dry and wet road surfaces measured by three-axial accelerometer," *Mechanical Systems and Signal Processing*, 52, pp. 548-558.
- [28] Mancosu, F., Brusarosco, M., and Arosio, D., 2011, "Method and system for determining a cornering angle of a tyre during the running of a vehicle," Google Patents.
- [29] Savaresi, S. M., Tanelli, M., Langthaler, P., and Del Re, L., 2008, "New regressors for the direct identification of tire deformation in road vehicles via "in-tire" accelerometers," *IEEE Transactions on Control Systems Technology*, 16(4), pp. 769-780. DOI: 10.1109/TCST.2007.912245
- [30] Krier, D., Zanardo, G. S., and del Re, L., 2014, "A PCA-Based Modeling Approach for Estimation of Road-Tire Forces by In-Tire Accelerometers," *IFAC Proceedings Volumes*, 47(3), pp. 12029-12034.
- [31] Erdogan, G., Borrelli, F., Tebano, R., Audisio, G., Lori, G., and Sannazzaro, J., "Development of a New Lateral Stability Control System Enhanced with Accelerometer Based Tire Sensors," *Proc. ASME 2010 Dynamic Systems and Control Conference*, American Society of Mechanical Engineers, pp. 841-848
- [32] Erdogan, G., Hong, S., Borrelli, F., and Hedrick, K., 2011, "Tire sensors for the measurement of slip angle and friction coefficient and their use in stability control systems," *SAE International Journal of Passenger Cars-Mechanical Systems*, 4(2011-01-0095), pp. 44-58. DOI: 10.4271/2011-01-0095
- [33] Hong, S., Erdogan, G., Hedrick, K., and Borrelli, F., 2013, "Tyre-road friction coefficient estimation based on tyre sensors and lateral tyre deflection: modelling, simulations and experiments," *Vehicle System Dynamics*, 51(5), pp. 627-647. DOI: 10.1080/00423114.2012.758859
- [34] Hong, S., and Hedrick, J. K., "Tire-road friction coefficient estimation with vehicle steering," *Proc. Intelligent Vehicles Symposium (IV)*, 2013 IEEE, IEEE, pp. 1227-1232
- [35] Matsuzaki, R., Kamai, K., and Seki, R., 2014, "Intelligent tires for identifying coefficient of friction of tire/road contact surfaces using three-axis accelerometer," *Smart Materials and Structures*, 24(2), p. 025010.

- [36] Niskanen, A., and Tuononen, A. J., 2015, "Three Three-Axis IEPE Accelerometers on the Inner Liner of a Tire for Finding the Tire-Road Friction Potential Indicators," *Sensors*, 15(8), pp. 19251-19263.
- [37] Morinaga, H., Wakao, Y., Hanatsuka, Y., and Kobayakawa, A., 2006, "The possibility of intelligent tire (technology of contact area information sensing)," *FISITA2006 Trans.*, F2006V104.
- [38] Pacejka, H., 2005, *Tire and vehicle dynamics*, Elsevier. 0080543332
- [39] Yang, X., Olatunbosun, O., Ramos, D. G.-P., and Bolarinwa, E., 2013, "Experimental Investigation of Tire Dynamic Strain Characteristics for Developing Strain-Based Intelligent Tire System," *SAE International Journal of Passenger Cars-Mechanical Systems*, 6(2013-01-0633), pp. 97-108.
- [40] Yang, X., Olatunbosun, O., Garcia-Pozuelo, D., and Bolarinwa, E., 2015, "FE-Based Tire Loading Estimation for Developing Strain-Based Intelligent Tire System," No. 0148-7191, SAE Technical Paper.
- [41] Yang, X., 2011, "Finite element analysis and experimental investigation of tyre characteristics for developing strain-based intelligent tyre system," University of Birmingham.
- [42] Matsuzaki, R., and Todoroki, A., "Intelligent tires for improved tire safety based on strain measurements," *Proc. SPIE Smart Structures and Materials+ Nondestructive Evaluation and Health Monitoring*, International Society for Optics and Photonics, pp. 72952E-72952E-72911. DOI: 10.1117/12.815403
- [43] Nagaya, G., 2006, "Method for estimating tire slip angle and a tire with sensors mounted therein," Google Patents.
- [44] Matsuzaki, R., Hiraoka, N., Todoroki, A., and Mizutani, Y., 2010, "Analysis of Applied Load Estimation Using Strain for Intelligent Tires," *Journal of Solid Mechanics and Materials Engineering*, 4(10), pp. 1496-1510. DOI: 10.1299/jmmp.4.1496
- [45] Jo, H. Y., Yeom, M., Lee, J., Park, K., and Oh, J., 2013, "Development of Intelligent Tire System," No. 0148-7191, SAE Technical Paper.
- [46] Kim, S., Kim, K.-S., and Yoon, Y.-S., 2015, "Development of a tire model based on an analysis of tire strain obtained by an intelligent tire system," *International Journal of Automotive Technology*, 16(5), pp. 865-875. 10.1007/s12239-015-0088-0
- [47] Matsuzaki, R., and Todoroki, A., 2008, "Intelligent tires based on measurement of tire deformation," *Journal of solid mechanics and Materials engineering*, 2(2), pp. 269-280.

- [48] Miyoshi, A., 2009, "Pneumatic tire with specifically arranged strain sensors," Google Patents.
- [49] Fiala, E., 1954, "Seitenkrafte am rollenden Luftreifen," ZVD I, 96, p. Nr. 29.
- [50] Gong, S., 1993, "A study of in-plane dynamics of tires," Ph.D. Dissertation, Delft University of Technology, Delft, Netherlands.
- [51] Zegelaar, P., and Pacejka, H., 1996, "The in-plane dynamics of tyres on uneven roads," *Vehicle System Dynamics*, 25(S1), pp. 714-730.
- [52] FRICTION Consortium, 2009, "Final Report of the EU Project Friction in the Information Society Technologies (IST) Programme," Technical Research Centre of Finland (VTT).
- [53] Nagaya, G., 2006, "Method for estimating tire slip angle and a tire with sensors mounted therein," Google Patents.
- [54] Zegelaar, P., Gong, S., and Pacejka, H., 1994, "Tyre models for the study of in-plane dynamics," *Vehicle System Dynamics*, 23(S1), pp. 578-590.
- [55] Zhang, Y., Yi, J., and Liu, T., 2013, "Embedded flexible force sensor for in-situ tire-road interaction measurements," *IEEE Sensors Journal*, 13(5), pp. 1756-1765. DOI: 10.1109/JSEN.2013.2241051
- [56] Zhang, Y., and Yi, J., 2014, "Static Tire/Road Stick-Slip Interactions: Analysis and Experiments," *IEEE/ASME Transactions on Mechatronics*, 19(6), pp. 1940-1950. DOI: 10.1109/TMECH.2013.2292872
- [57] Yamagishi, K., and Jenkins, J., 1980, "The circumferential contact problem for the belted radial tire," *Journal of Applied Mechanics*, 47(3), pp. 513-518.
- [58] Yamagishi, K., and Jenkins, J., 1980, "Singular perturbation solutions of the circumferential contact problem for the belted radial truck and bus tire," *Journal of Applied Mechanics*, 47(3), pp. 519-524.
- [59] JENKINS, J. T., 1982, "The circumferential contact problem for the belted radial passenger car tire," *Vehicle System Dynamics*, 11(5-6), pp. 325-343.
- [60] Yu, Z.-X., Tan, H.-F., Du, X.-W., and Sun, L., 2001, "A Simple Analysis Method for Contact Deformation of Rolling Tire," *Vehicle System Dynamics*, 36(6), pp. 435-443. DOI: 10.1076/vesd.36.6.435.3543
- [61] Kim, S.-J., and Savkoor, A. R., 1997, "The Contact Problem of In-Plane Rolling of Tires on a Flat Road," *Vehicle System Dynamics*, 27(sup001), pp. 189-206. DOI: 10.1080/00423119708969654

- [62] Klingbeil, W., and Witt, H. W., 1990, "Some Consequences of Coulomb Friction in Modeling Longitudinal Traction," *Tire Science and Technology*, 18(1), pp. 13-65.
- [63] Richards Jr, R., 2000, *Principles of solid mechanics*, CRC Press. 1420042203
- [64] Kim, S., 2002, "A comprehensive analytical model for pneumatic tires," Ph.D. Dissertation, The University of Arizona, Tucson, AZ.
- [65] Chan, B. J.-Y., 2008, "Development of an off-road capable tire model for vehicle dynamics simulations," Virginia Polytechnic Institute and State University.
- [66] Mousseau, C., and Clark, S., 1994, "An analytical and experimental study of a tire rolling over a stepped obstacle at low velocity," *Tire Science and Technology*, 22(3), pp. 162-181. DOI: <http://dx.doi.org/10.2346/1.2139540>
- [67] Gong, S., 1989, "Tire ring model - Literature review," Delft University of Technology, Delft, Netherlands.
- [68] Akasaka, T., Katoh, M., Nihei, S., and Hiraiwa, M., 1990, "Two-dimensional contact pressure distribution of a radial tire," *Tire Science and Technology*, 18(2), pp. 80-103.
- [69] Pottinger, M., 1992, "The three-dimensional contact patch stress field of solid and pneumatic tires," *Tire Science and Technology*, 20(1), pp. 3-32.
- [70] Zegelaar, P. W. A., 1998, "The dynamic response of tyres to brake torque variations and road unevennesses," Ph.D. Thesis, TU Delft, Delft University of Technology.
- [71] Taheri, S., 2015, "A HYBRID SOFT SOIL TIRE MODEL (HSSTM) FOR VEHICLE MOBILITY AND DETERMINISTIC PERFORMANCE ANALYSIS IN TERRAMECHANICS APPLICATIONS," Virginia Polytechnic Institute and State University.
- [72] Xiong, Y., and Tuononen, A., 2015, "The in-plane deformation of a tire carcass: Analysis and measurement," *Case Studies in Mechanical Systems and Signal Processing*, 2, pp. 12-18.